Cell theory of binary and polydisperse hard sphere systems

Voisey, Jeremy Paul

Award date:
2001

Awarding institution:
University of Bath

Cell Theory of Binary and Polydisperse Hard Sphere Systems

submitted by Jeremy Paul Voisey

for the degree of PhD

of the University of Bath

2001

J. Voisey

ProQuest LLC
789 East Eisenhower Parkway
P.O. Box 1346
Ann Arbor, MI 48106-1346

Summary

The phase behaviour of a system of binary hard spheres was calculated over an wide range of diameter ratios, $0.33 \leq \sigma \leq 0.75$ and densities. At each diameter ratio, the thermodynamic properties of a number of different crystalline binary superlattices were calculated using a Lennard-Jones cell model. Equilibrium phase diagrams were derived by combining these solid free energies with accurate fluid equation of states. The resulting predictions were found to be in excellent agreement with extensive simulations performed by Frenkel *et al.* for systems of size ratio $\sigma = 0.6$. The Lennard-Jones model offered two advantages over conventional simulations. First, its computational efficiency enabled accurate calculations to be made over a more extensive range size ratios than previously reported and, secondly the stability of a much wider range of crystalline structures could be explored.

In the second portion of the thesis, the Lennard-Jones cell model was applied to the freezing transition of a polydisperse system of hard spheres. The thermodynamic properties of a polydisperse FCC crystal were calculated using an extension of the Lennard-Jones cell model. A continuous distribution of particle diameters was approximated by a finite number of discrete points. In order to perform the calculation efficiently, symmetry was taken into account and a fast analytical algorithm was used to calculate the pressure and Helmholtz free energy. This model predicted a terminal polydispersity of 0.055.

The stabilities of the polydisperse HCP and FCC structures were compared. The HCP structure was shown be more stable with increasing polydispersity.

Index

Chapter 1 Hard Sphere Freezing

1.1 Hard Spheres, Simulation and Experiment

1.1.1 The Hard Sphere Model.

The hard sphere model of the atom is one familiar to most students of science. Atoms are assumed to posses a finite mass and volume, while interactions are simplified by assuming there are no attractive forces. The only force ever present is an infinite repulsive force when the hard spheres touch (fig. 1.1.1). The only model conceptually simpler is the ideal gas model, where atoms are assumed to posses a finite mass, but no volume. i.e. they are assumed to be points.

By their nature, no model is an exact copy of the system being modelled. Some models are closer to the system than others. The purpose of a model is to give an insight into the behaviour of the system by studying the properties of the model. It may be thought that the hard sphere model is too basic to be of any benefit. Since the conception of the hard sphere model, many more sophisticated models have been considered. Yet the properties of the fundamental hard sphere model still remains an area of investigation.

In recent years new equations of state have been proposed[1-3] for the hard sphere fluid, so that there are, at present, at least twenty two expressions for the equation of state[4] . Pronk and Frenkel[5] have investigated the density of point defects in hard sphere crystals, calculating that, at melting point, the concentration of interstitials is three orders of magnitude lower than the concentration of vacancies. The relative stability of the FCC and HCP crystal structures is still being debated (section 1.3). The nature

of the binary hard sphere fluid equation of state is not fully known (section 3.4). And the random close packing fraction of binary and polydisperse systems is still being investigated[6].

There has been much interest, in recent year, in the kinetics of transitions in hard sphere system. Dixit *et al.*[7] and Wild *et al.*[8] both examined the kinetics of nucleation. While Davidchack and Laird[9] studied the crystal melt interface, finding that the crystal to fluid transition occurred over 2-3 crystal planes.

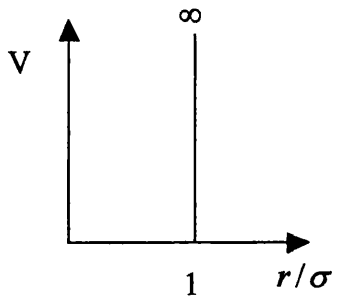

Figure 1.1.1 The hard sphere potential, separation, r, is given in terms of the diameter of the hard spheres. As the spheres touch when $r/\sigma = 1$, the potential jumps from 0 to ∞.

The critical temperature for hard spheres is at absolute zero. This is determined by the total lack of any attractive forces between the spheres. Consequently no liquid phase exists for hard spheres. It was once assumed that hard spheres would not exist in any solid state (ordered crystalline phase or disordered glassy phase). The basis of this assumption was that the hard spheres lacked the cohesive forces thought vital to hold a crystal or a glassy state together. Thus the hard sphere model was initially confined to studies of the fluid phase.

1.1.2 Computer Simulation of the Hard Sphere Model

A model may be classified into one of two categories, physical or mathematical. An example of the former is the use of gelatine balls by Morrell and Hildebrand[10] to model a liquid. The hard sphere model comes into the second category, the properties being defined by a set of equations. Until the 1950's it was only possible to build analytical theories upon such mathematical models[11-15]. Simulation of a mathematical model was impractical due to the number, rather than the complexity, of numerical calculations required.

The advent of programmable computers removed this barrier. Mathematical models were first simulated on computers such as the Los Alamos MANIAC[15,16].

Metropolis *et al.*[15] utilised a simulation method based upon the random movement of particles. The purpose of this "Monte Carlo" method was to randomly sample the configuration space of the system. To do this they used Markov chains, if the random movement of a particle led to an increase in energy of the system it was accepted with probability, $e^{-\frac{\Delta E_k}{kT}}$, where ΔE_k is the change in potential energy of the system. In this way configurations were chosen with probability proportional to $e^{-\frac{E_k}{kT}}$, where E_k is the potential energy of the configuration. Simulating just 244 particles, using periodic boundary conditions, they were able to calculate an equation of state and a radial distribution function for a two-dimensional hard disk system.

Following on from this, Rosenbluth *et al.*[16] simulated a three-dimensional hard sphere system. Using the same Monte Carlo method, they were able to calculate the equation of state of the fluid phase of hard spheres. This initial simulation of 256 hard spheres, again using periodic boundary conditions, produced an equation of state for the fluid

phase. In these early simulations no evidence was found of any fluid-solid phase transition. i.e. there was no evidence of a first order transition in the equation of state.

The Monte Carlo method is restricted to calculating equilibrium properties, as particles trajectories are not calculated. Alder and Wainwright[17] devised a method to exactly calculate the behaviour of a system of particles. Although their molecular dynamical method was later extended to study a system of particles with a Lennard-Jones potential, initial studies were on a system of hard spheres[18]. In this method particle trajectories are calculated exactly. In the hard sphere system, a particle is moved in a straight line at constant velocity until it collides with another particle. When a collision occurs, the velocities of the particles involved are changed accordingly.

These calculations were restricted to systems containing from 4 to 500 particles. In order to represent a macroscopic system with so few particles, periodic boundary conditions were employed. It was found that there were two branches to the equation of state. The system occasionally jumped from one branch to the other. This suggested the possibility of a first order phase transition, although they were unable to observe the two phases in co-existence. It must be remembered that the timescales of these calculations was extremely short (~ 1 nanosecond). For 500 particles it took half an hour to calculate on average, just one collision per particle. Because of this there was some concern that metastable states were being observed. Consequently they were reluctant to suggest that their results were a definite proof of the crystallisation of hard spheres. But their results aroused much interest. Subsequent Monte Carlo simulations upon hard sphere systems using longer calculation times confirmed the existence of two branches to the equation of state[19]. After vigorous debate and further

calculations, including many using density functional theory[20] (for a review see Oxtoby[21]) it was finally generally accepted that hard spheres do undergo a first order phase transition from a fluid to a crystalline phase.

In the solid phase, the structure observed was that of the face centred cubic crystal (FCC – see section 1.3). In this close packed structure each particle is surrounded by a total of twelve neighbours (fig. 1.1.2).

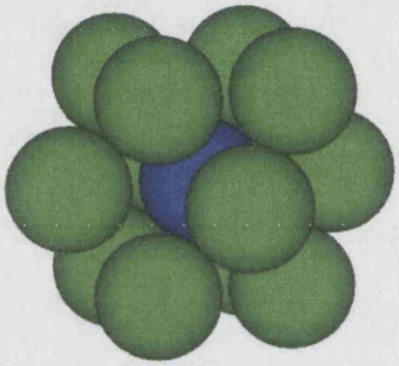

Figure 1.1.2 The first co-ordination shell of neighbours for a particle arranged in an FCC structure.

The suggestion that hard spheres were able to crystallise under suitable conditions was initially cause for scepticism. This was something long held as being impossible. Sceptics correctly argued that the only driving force for such a phase transition would be entropy, but they wrongly assumed that there could not be an increase of entropy on crystallisation.

As the only force between hard spheres is an infinite repulsion upon contact, the internal energy may be ignored. As spheres lack any rotational or vibrational modes only the translational degrees of freedom need be considered. Therefore the entropy of hard spheres depends only upon their ability to explore space. The entropy may be split into two parts, configuartional and correlational (fig. 1.1.3). Configurational

entropy relates to the freedom of the particles to move throughout the entire system and thus alter the overall configuration. This is always lower in the solid phase as spheres are tied to their lattice sites. Correlational entropy relates to the freedom of particles to move in the vicinities of their average lattice sites. The correlational entropy is determined by the nearest neighbours that restrict this localised movement.

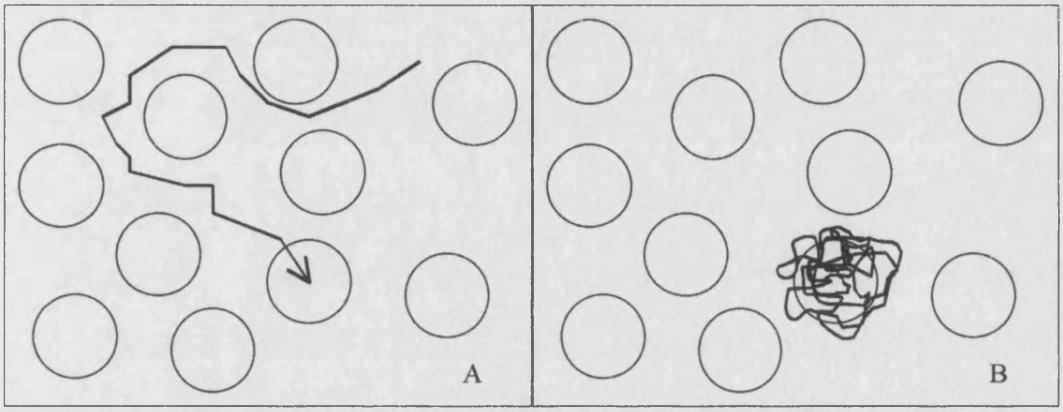

Figure 1.1.3 A) Configurational entropy depends on the ability of the particles to move throughout the entire system and thus alter the overall configuration. B) Correlational entropy depends on the ability of particles to move in the vicinities of their average lattice sites.

Whilst the configurational entropy is always higher in the disordered fluid than in the ordered solid, the correlational entropy may well be higher in the solid. This is the case at high densities when the fluid phase is "crowded". Greater local movement is achieved in the ordered solid phase. At high enough densities the higher correlational entropy in the solid phase offsets the lower configurational entropy, so that, counter intuitively the overall entropy is higher in the ordered solid phase.

1.1.3 Colloidal Systems That Approximate Hard Spheres

Whilst mathematical models may be tailored to exact requirements, they may well be unwieldy. Even with today's computers, simulations are restricted to a limited number

of particles and short time spans. In contrast a great number of particles may be studied using a physical model and there are no great time constraints. Obviously there are advantages and disadvantages with each type of model, but physical models may not be ignored.

Steel ball bearings are amongst the examples of physical models that have been used. Whilst the ball bearings are not exact hard spheres, their behaviour is very similar. Pieranski *et al.*[22] performed some useful simulations using 631 steel ball bearings upon a flat surface to approximate a hard disc system. They were able, for example, to observe a first order phase transition and obtain an image of the pair distribution function.

Another useful physical model is a colloidal system. Colloids are large enough (10-1000nm) to be observed with microscopes. At the same time their smallness allows a large number of colloidal particles to be used at any one time. Meanwhile, the timescale of transitions (these can take days) is also slow enough to allow the observation of nucleation events and meta-stable states. Techniques, such as phase-contrast, allow the structures formed to be examined more easily. Recently confocal microscopy has been used to determine the positions of individual particles beneath the surface of crystals[23].

Hachisu *et al.*[24] examined systems of charged polystyrene colloidal particles, with strongly screened coulombic interactions as an approximation to hard spheres. Other interactions may be modelled, but the hard sphere like interaction is of particular interest. One method to form colloidal hard spheres is to graft of a thin layer of poly(12-hydroxystearic acid) (PHSA) onto poly(methyl methacrylate) (PMMA) spheres[25] (fig. 1.1.4). When two such colloidal particles come into contact the PHSA

"brushes" entangle, generating a steep repulsive potential[26] . Whilst this may not be an exact hard sphere potential it is very close. The refractive index of the suspension medium is matched to that of the colloidal particles. This minimises the Van der Waals forces and also allows light scattering experiments to take place by reducing cloudiness. Pusey[25] observed the occurrence of crystallisation in such systems. Gravitational sedimentation is avoided by slowly rotating the samples so that particles expierience "time-averaged zero gravity"[27].

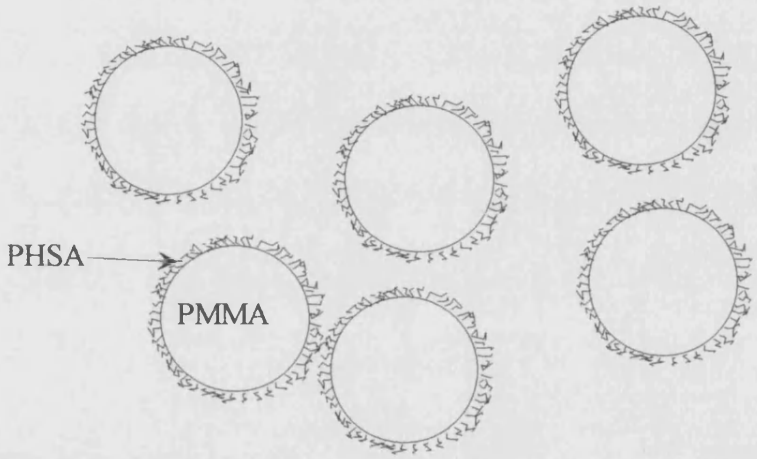

Figure 1.1.4 The thinly grafted layer (~10nm) of PHSA prevents the PMMA spheres from coming too close and is responsible for the hard sphere like repulsive potential.

Experiments on systems of colloidal hard spheres (PMMA grafted with PHSA) have taken place aboard the Space Shuttle Columbia[28]. The purpose of these experiments was to observe the behaviour in the absence of normal gravity. Under the conditions of micro gravity, the colloidal hard spheres crystallised at a faster rate and formed larger crystallites than on earth. Glassy samples, which had failed to crystallise on earth, crystallised in two weeks under microgravity. Crystals were also found to adopt the RHCP structure (see section 1.3). A comparison of crystallisation in gravity and microgravity has been carried out by Cheng *et al*[29].

Elliot *et al.*[30] imaged a nucleating crystal at single particle resolution. Gasser *et al.*[31] were able to examine a nucleating crystal in three dimensions with the use of laser scanning confocal microscopy.

1.2 The Lennard-Jones Cell Model

In order to calculate the properties of a system using statistical mechanics, it is necessary to know how the atoms or particles in that system interact. In a gas, only binary interactions need be considered, as particles are too widely spaced for there to be many multiple encounters. It is relatively easy to model the interaction between just two particles, and so the statistical mechanics is correspondingly easier. However, as the density of the system increases, interactions between groups of particles begin to predominate. It becomes much harder to model the interaction as the number of particles involved increases.

1.2.1 Fundamental Approximations of the Cell Model

Lennard-Jones and Devonshire[32] initially conceived the cell model with denser gaseous systems in mind. Rather than allowing particles to migrate throughout the gas, this model confines atoms to individual cells. This reduces the many body problem down to a number of single body ones. The boundaries of the cell are determined by the positions of the neighbours, which are fixed at their lattice sites.

The lattice chosen for the application of their model was face centred cubic.

One further approximation made was the "smeared" approach, where it was assumed that each atom in its cell was in a spherically symmetrical field (see section 1.2.5).

Without making any specific application there are three fundamental approximations, which will be considered in the following pages, in the cell model of Lennard-Jones and Devonshire. These are:-

1) Single occupancy - Particles are placed in individual cells, which are arranged according to a regular lattice.

2) No co-operative movement – All other particles in the phase are fixed in space.

3) Smeared potential – The particle occupying the cell is in a spherically symmetrical potential field.

Once a model for the interaction of the particle has been chosen, statistical mechanics may be applied to calculate, amongst other things, the equation of state.

1.2.2 The Single Occupancy Approximation

Lennard-Jones and Devonshire derived their cell model on an empirical basis. By deriving it from general statistical mechanics, Kirkwood[33] was able to place it on a firm basis.

The expression for The Gibbs phase integral, Z_N is given by

$$Z_N = \int^{v}\!\!\dots\int^{v} e^{-\beta V_N} \prod_{k=1}^{N} dv_k \,, (1.2.1)$$

where $\beta = \frac{1}{kT}$ and V_N is the potential of the system. In all but the simplest of cases this expression in intractable.

The volume, v, is spanned by a lattice of N cells, $\Delta_1 \dots \Delta_N$. Now the integral over v is replaced by the sum of the integrals over the individual cells. So that

$$Z_N = \sum_{l_1=1}^{N} \cdots \sum_{l_N=1}^{N} \int_{}^{\Delta_{l_1}} \cdots \int_{}^{\Delta_{l_N}} e^{-\beta V_N} \prod_{k=1}^{N} dv_k \,, \quad (1.2.2)$$

where particle k is in cell l_k.

It is not necessary to make the number of cells to be equal to the number of particles. Neither is it imperative that the size of the cells be equal. This step is not, in itself, an approximation.

The approximation is introduced when it is assumed that each cell is occupied by only one particle (in which case the number of cells must equal the number of particles). The Gibbs phase integral becomes

$$Z_N = \int_{}^{\Delta_1} \cdots \int_{}^{\Delta_N} e^{-\beta V_N} \prod_{k=1}^{N} dv_k \,. \qquad (1.2.3)$$

By restricting particles to occupy single cells, which are arranged on a regular lattice, order is imposed on the system. If this model is applied to a disordered fluid state, as was initially intended, there is of necessity a loss of entropy. Calculating the loss in non-trivial and is the downfall of this model, which was initially meant to be one for the fluid state.

There is no intention to resolve this issue here. Rather than attempting to adapt the model to the fluid state, the model is applied to a crystalline state. It could be said that in effect the system has been adapted to the model.

Recently Cottin and Monson[34] have applied cell theory, with some success, to a number of solid systems. They studied binary hard sphere systems with diameter ratios approaching unity (~0.97). These may be expected to form a substitutionally

disordered FCC arrangement of hard spheres. They also used cell theory to study single component and binary Lennard-Jones systems[35]. In both cases they found that there results were in good agreement with Monte Carlo simulations. Cell theory has also been applied to systems of two dimensional hard cyclic hexamers[36] and confined hard spheres[37]

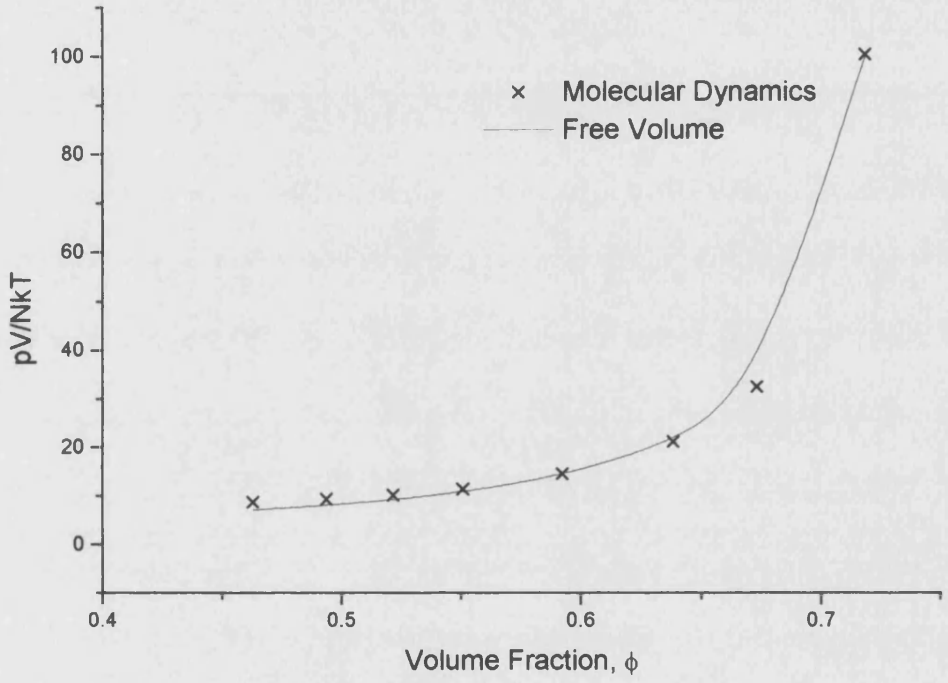

Figure 1.2.1 Equation of state obtained by molecular dynamical calculations[18] (96 particles, solid branch) compared to equation of state obtained using free volume theory[38].

The work of Alder and Wainwright[17,18] in molecular dynamics was an early indicator that cell theory was more applicable to solid than fluid phases. The results from these first molecular dynamical calculations were compared to results obtained using the cell or "free volume" theory. The system under investigation was one consisting of hard spheres. They found that the free-volume theory was "just not applicable" at low densities. Much better agreement was obtained at higher densities in the region of the

solid branch. The results obtained by Alder and Wainwright[18] using a system of 96 particles are compared to calculations using cell theory in fig. 1.2.1.

When applying cell theory to a fluid state, the choice of the lattice was arbitrary. Obviously this is no longer the case for the crystalline state, where the lattice is chosen to match that of the crystal.

In summary the Lennard-Jones and Devonshire cell model has been applied to a system where the single occupancy approximation is a good one.

1.2.3 The No Co-operative Movement Approximation

Even with the single occupancy approximation of the cell model, the Gibbs phase integral is not easily calculated. Even though particles have been restricted to individual cells, it is still a many body problem as all particles are free to move within their own cells.

The second approximation used by Lennard-Jones and Devonshire is that neighbours remained fixed on average at their lattice sites. It is assumed that there is no co-operative movement of particles to be considered. It is this approximation that truly reduces the problem to a single bodied one as the dynamics of each particle is now independent of its neighbours.

Kirkwood[33] states this approximation in a more formal manner. The probability density, P_N is given by

$$P_N = \prod_{k=1}^{N} \varphi(\mathbf{r}_k) \qquad (1.2.4)$$

$$\int_{\Delta} \varphi(\mathbf{r}) dv = 1. \quad (1.2.5),$$

where $\mathbf{r}_k$ is the position vector of particle k and $\varphi(\mathbf{r}_k)$ is the probability density function.

Here, $\varphi(\mathbf{r}_k)$ depends solely on the position of particle k inside its cell. By neglecting co-operative movement it is possible to evaluate the cell configuration integrals, z_k, independently. The Gibbs phase integral is now given by

$$Z_N = \prod_{k=1}^{N} z_k \text{ , where} \qquad (1.2.6)$$

$$z_k = \int_{\Delta_k} e^{-\beta \Phi_k(\mathbf{r})} dv. \qquad (1.2.7)$$

The effective potential for particle k, Φ_k is determined by the fixed neighbours. The important point to note is that the particle in the middle of the cell is now moving in a fixed potential field. It is not too difficult to evaluate the corresponding cell configuration integral using analytical or numerical methods.

Although there is no intention to remove this approximation, it is interesting to note the calculations performed by Hoover *et al.*[39]. Hoover *et al.* pointed out that adjusting the masses of individual particles would not alter the overall properties of a system. Accordingly he made the mass of the particle in the cell to be very small, whilst making that of its neighbours to be great. The lighter particle would naturally move at greater speed than the heavier neighbours, which would effectively be fixed in space. This is equivalent to the cell model. As long as the neighbours are moved eventually

no approximation has been made. To allow for some movement of the neighbours, the average of a fluctuating arrangement of neighbours was taken. It is also noted that this fluctuating cell model is equivalent to a Monte Carlo average, where the neighbours are moved with far less frequency than the central particle. Again it is important that the neighbours are moved eventually. This model was applied by Hoover[39] to both solid and fluid phases of hard spheres.

1.2.4 The Concept of Free Volume

Before a consideration of the third approximation made in the original application of the cell model it is useful to consider the potential that is to be used.

Whilst a variety of potentials may be used, the hard sphere potential is particularly suited to the cell model, as the cell configurational integral,

$$z_k = \int^{\Delta_k} e^{-\beta\Phi_k(\mathbf{r})} dv, \qquad (1.2.8)$$

may be readily obtained.

$\Phi(r)$, the effective single particle potential energy function, takes one of two possible values. r is a vector describing the position of the centre of the particle in the cell, the tagged particle. If the particle in the cell is not overlapping with any of its neighbours then $\Phi(\mathbf{r}) = 0$ and hence $e^{-\Phi(\mathbf{r})} = 1$. Conversely if the tagged particle is overlapping with one or more of its neighbours so $\Phi(\mathbf{r}) = \infty$ and $e^{-\Phi(\mathbf{r})} = 0$. Thus z_k is equal to the volume in which the centre of the tagged particle is free to move about inside the cell. This is known as the free volume, v_f (fig. 1.2.2).

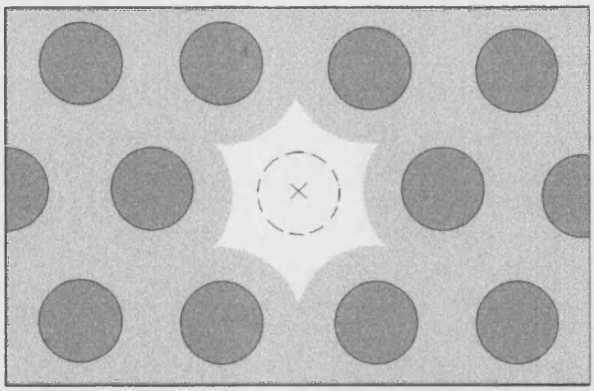

Figure 1.2.2 An illustration of free volume in two dimensions. The tagged particle is marked by the central cross. The neighbours (dark grey) are surrounded by exclusion spheres (light grey). The resulting area (the free volume) marked in white is that accessible by the centre of the tagged particle.

1.2.5 The Smeared Potential Approximation

The third approximation used by Lennard-Jones and Devonshire is the one that is most easily removed.

They used the smeared approximation in their application of the cell model. The smeared approximation is the assumption that the tagged particle was in a spherically symmetrical field. Whilst this might be a useful approximation to make when dealing with more complicated potentials, it is unnecessary with a hard sphere system in view. For a hard sphere system the smeared approximation simply means that the free volume is a sphere.

It is well within the capabilities of modern computers to calculate the exact free volume. When applying the cell model to hard sphere systems, the smeared approximation is unnecessary.

Buehler *et al.*[40] were the first to calculate the exact free volume. They used analytical methods. Still applying the cell model to hard spheres forming a dense gas, Buehler *et*

al. calculated the exact free volume for a particle in a face centred cubic lattice. The walls of the cell were defined by the planes that bisected the lines joining the lattice sites of the tagged particle and those of its neighbours (i.e. a Voronoi polyhedron). The cell thus took on the shape of a dodecahedron. At low densities the tagged particle was free to explore its entire cell, so that the free volume was equal to that of the dodecahedron. As the density increased, it was found the proximity of neighbouring particles prevented the tagged particle from exploring its entire cell. Eventually the movement of the tagged particle was found to be determined solely by the steric hindrance of the neighbours. The shape of the free volume at these densities is that of a dodecahedron with concave sides.

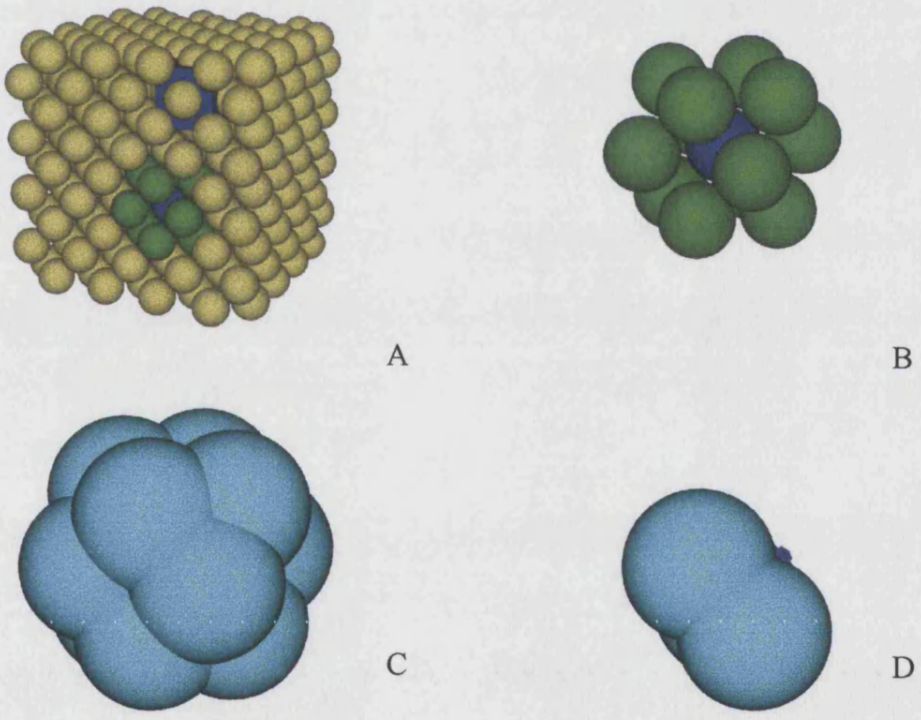

Figure 1.2.3 The tagged particle in an FCC structure (A), coloured blue is surrounded by its nearest neighbours coloured green (B). The corresponding exclusion spheres are shown in cyan (C). The free volume may be seen when most of the exclusion spheres

are cut away (D). At a volume fraction of 0.545 (the volume fraction at which crystals are first formed), the free volume is approximately one quarter of the width of a particle.

A useful concept, when calculating the free volume is that of "exclusion" spheres. In fig. 1.2.3.A, the tagged particle is shown, marked in blue. It is surrounded by its twelve nearest neighbours, highlighted in green. In this case it is only these twelve nearest neighbours that determine the free volume (fig. 1.2.3.B). Note that the volume at the centre of the "cage" is not of interest. It is only the volume accessible to the **centre** of the tagged particle that is of relevance. The surfaces of any two hard spheres are not allowed to overlap; so that the closest those two spheres may approach is determined by the sum of their radii. Therefore the centre of the tagged particle is excluded from a spherical volume surrounding the centre of each neighbour. The radius of this "exclusion" sphere is equal to the sum of radii of the neighbour and the tagged particle (fig. 1.2.4). When determining the free volume it is possible to replace the neighbours with the appropriate exclusion spheres and reduce the tagged particle to a point. The free volume is then equal to that volume remaining at the centre of the arrangement of overlapping exclusion spheres. In fig. 1.2.3.C, the exclusion spheres corresponding to the twelve neighbours are shown in cyan. The free volume, in blue, is seen when some of the exclusion spheres are cut away (fig. 1.2.3.D).

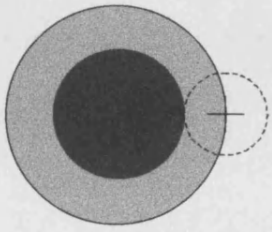

Figure 1.2.4 The radius of the exclusion sphere (light grey) is the sum of the radii of the tagged particle and the neighbouring particle (dark grey).

1.2.6 The Restriction of Particles to Individual Cells

The free volume is normally determined by the neighbouring particles. However, at low densities, a particle may appear to be free to leave the vicinity of its equilibrium lattice site and wander throughout the crystal. If the particle were allowed to do this, then it would be able to leave its own cell and enter into another. This would break the first approximation of single occupancy. It is therefore assumed that each particle will stay inside the confines of its own cell that is centred upon its lattice site. This also ensures that the definition of model does not contradict that of a crystal. i.e. that particles are localised and not free to wander through space. At the freezing densities of monodisperse systems, this consideration may be safely neglected as the neighbours restrict each particle to the vicinity of its lattice site. However in a binary systems where the diameter ratio is small, it is quite possible that a small particle may pass by its neighbours. Hence the restriction of the tagged particle to its own cell becomes important. Buehler *et al.* needed to enforce this restriction, as they were considering systems at low density.

Each cell takes on the form of a Voronoi polyhedron. i.e. The plane that perpendicularly bisects the line joining the particle under consideration to its neighbour defines each face. Within that cell, the tagged particle is always closer to its own lattice site than another's.

1.3 A Comparison of FCC and HCP

It has long been known that spheres can pack into one of two close packed arrangements. These being face centred cubic (FCC) and hexagonal close packed (HCP). These two arrangements are very similar, both being based upon layers of hexagonally close packed spheres (fig. 1.3.1).

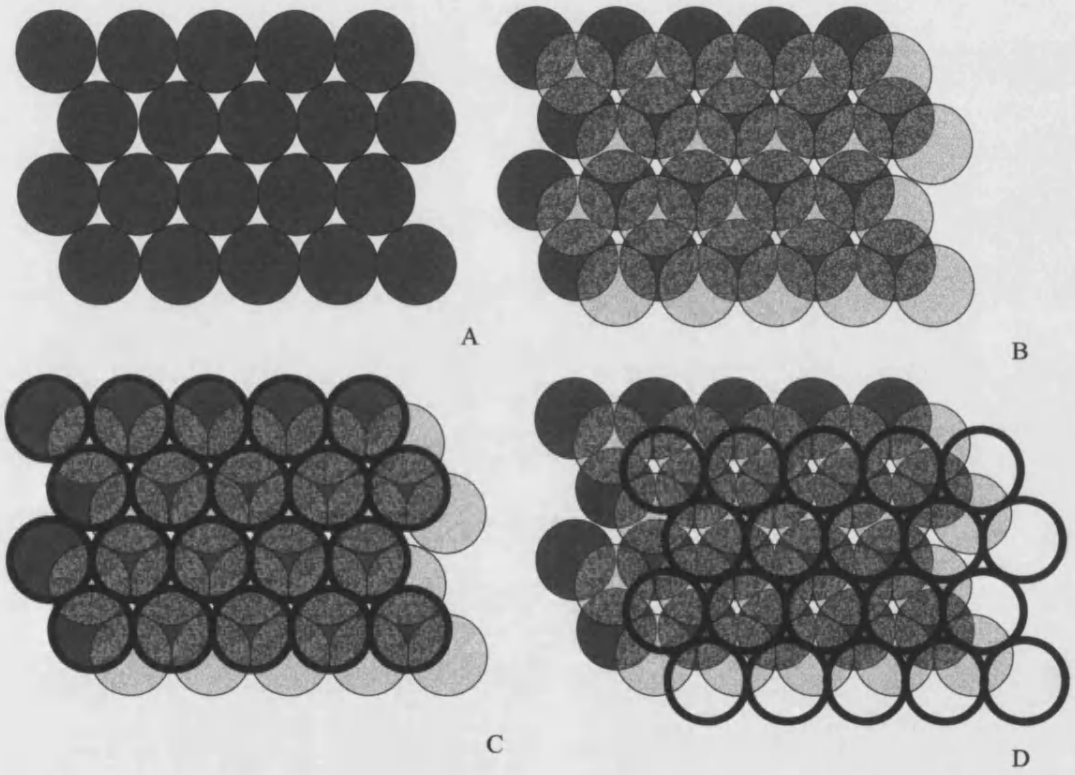

Figure 1.3.1 A) The arrangement of spheres in a hexagonal close packed layer. B) A second layer lies over the interstitial gaps in the first layer. The third layer either lies directly over the first layer (C) – the HCP arrangement or is offset from both the previous layers (D) – the FCC arrangement.

Adjacent layers in both structures are staggered, spheres being placed above the interstitial gaps in the preceding layer. Having placed two layers, there are two options for the position of the third. In HCP (fig. 1.3.2) the third layer lies directly

above the first. In FCC the third layer is offset from the first as well as the second layers. The FCC structure is observed in nature slightly more often than HCP As many as 25% elements crystallise into the FCC structure, with 20% preferring to adopt the HCP structure.

Both these structures as labelled as close packed structures as they have the maximum possible packing fraction obtainable by monodisperse spheres. The fraction of the volume occupied by the spheres in either of these arrangements is $\frac{\pi}{3\sqrt{2}} \approx 0.7405$.

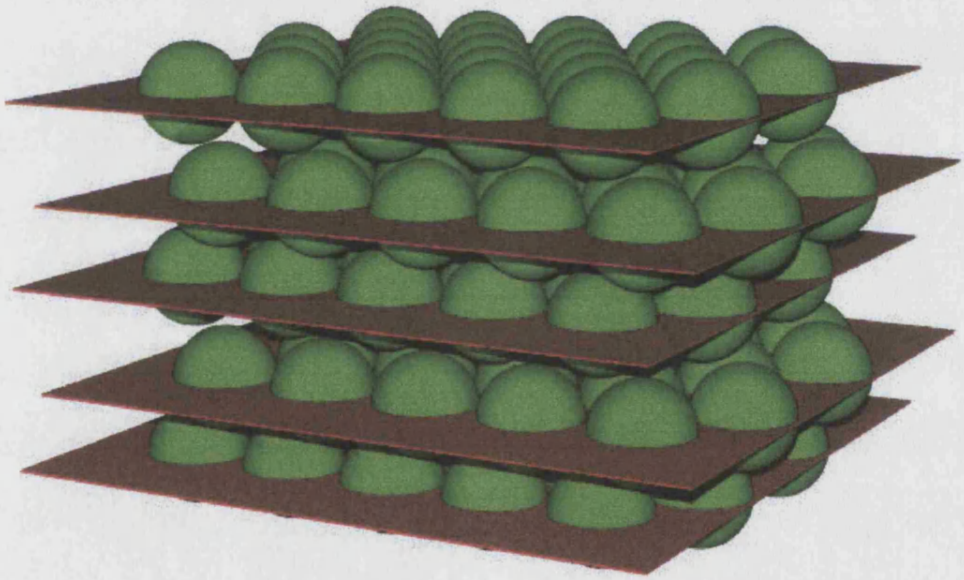

Figure 1.3.2 The hexagonal close packed structure, the close packed layers are marked.

When interatomic forces are present it is understandable that one structure may be favoured above another. What is not so clear is whether any one structure should be the favoured arrangement for hard sphere crystals. Based purely upon packing ability there is no distinction between the two alternatives.

In the majority of calculations involving hard sphere crystals, the preferred choice of structure has been FCC[17,18,40]. This choice has been somewhat arbitrary, being based only upon the slight predominance of FCC in nature.

Should there be no preference for either close packed structure, then a hybrid may form. This is known as the random hexagonally close packed (RHCP) structure. The spheres in the second close packed layer lie over the gaps in the first layer. The spheres in the third layer either lie over the spheres in the first layer (as with HCP) or they may be offset from both the previous layers (as with FCC).

1.3.1 A Comparison Using the Cell Model

The free volume approach of the cell model is incapable of resolving any difference between the two structures. This is not due to a lack of accuracy in the numerical calculation, but rather to the symmetry of the two cells involved.

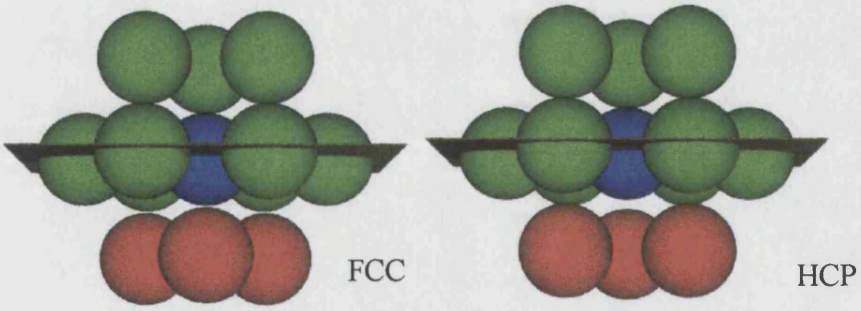

Figure 1.3.3 The arrangement of spheres in the FCC and HCP cells. The tagged particle is shown in blue. The arrangement of the neighbours shown in green is the same in the FCC and HCP arrangements. The only difference is in the positions of the neighbours shown in red. The planes divide the cells in two.

The cell for the FCC structure may be split into two halves. If the lower half is rotated by 60° about the normal to the plane used to split the cell, then the HCP cell is

obtained (fig. 1.3.3). The only difference is the positioning of the spheres marked in red.

To calculate the free volume, the neighbours are replaced with exclusion spheres and the tagged particle is reduced to a point (fig. 1.3.4).

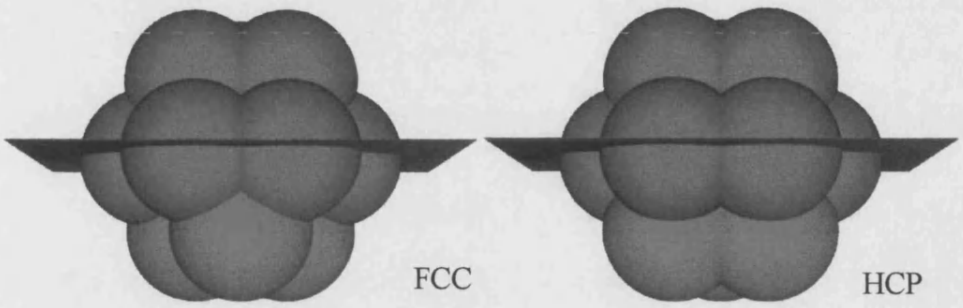

Figure 1.3.4 The arrangement of exclusion spheres corresponding to the arrangement of neighbours in fig. 1.3.3.

The free volume is equivalent to the volume of the vacancy at the centre of the arrangement of resulting exclusion spheres shown (fig. 1.3.5). The shape of the free volume is that of a dodecahedron with concave sides.

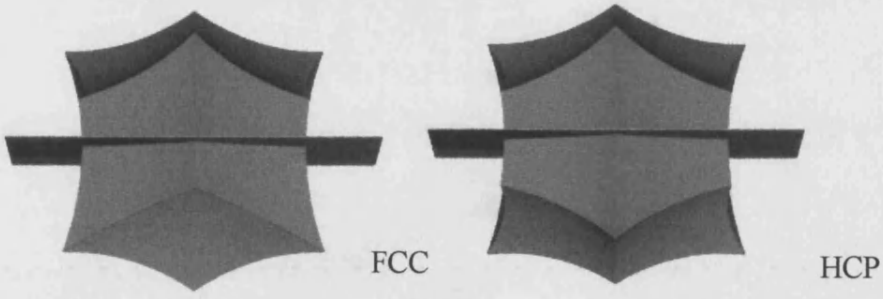

Figure 1.3.5 The free volume for the tagged particles in the FCC and HCP cells.

The shapes of the free volumes for the two cells are different, but they share the same "symmetry" relationship as the original arrangement of neighbours in the cell. i.e. The

free volume for HCP may be obtained by rotating the lower half of the FCC free volume by 60°. This holds true as long as the sides of the free volume shown in red do not extend into the upper half. When this does not occur, then the two halves of the free volume are independent. The geometry of the two arrangements dictates that this is the case. Therefore the quantity of the free volume for the two arrangements is identical. As free energy, in this model, ultimately depends upon this free volume, then no difference in the free energy of the two structures may be found.

1.3.2 A Comparison in Experimental Systems

A preference for the FCC structure has been observed in experiments with colloidal hard spheres[26]. It was observed that crystals that grew quickly formed the RHCP structure, whilst those that grew more slowly formed the RHCP structure, but with FCC regions. It was suggested that the equilibrium structure was FCC, but that the metastable RHCP phase was forming. As the difference between the two structures, if any, is small, the authors were cautious in putting this down to pure hard sphere effects. They speculated that the balanced could be tipped by any Van der Waals forces present.

In the microgravity experiments carried out aboard the Space Shuttle Columbia[28], it was found that colloidal hard spheres formed the RHCP structure. This led them to suggest that any preference for the FCC structure was due to gravity. However it is worth noting that, under microgravity, crystallisation occurred fairly rapidly in these systems. This suggests that the RHCP structure may have formed due to the speed of crystallisation.

1.3.3 A Comparison Using Molecular Dynamics

Woodcock[41] calculated an entropy difference between the two structures using molecular dynamics. By integrating the P-V isotherms for the two arrangements to a common point, he found a free energy difference of 0.005RT between the two structures. FCC being marginally more stable than HCP.

The magnitude of his result, though not the sign was disputed by Bolhuis et al.[42] Using Monte Carlo techniques, they found the free energy difference to be only 0.0009 RT, considerably smaller than the result reported by Woodcock.

Although the size of the difference between the two structures is debated, the fact that FCC is slightly more stable is generally accepted. However any difference is so marginal that under normal experimental conditions no structure will be favoured. In which case the positioning of the third layer relative to the first and second layers will be unpredictable. i.e. RHCP arrangements will form.

The difference between these two arrangements will be considered again in sections 5.1.3 and 9.3. Factors that may influence the difference are the occupation of the octahedral holes in a binary structures and polydispersity.

Chapter 2 Binary Superlattices

It is now well known that a system of monodisperse hard spheres will form a face centred crystal under suitable conditions (section 1.1). Those conditions being high enough density and the absence of sedimentation. There are many different crystals that could, potentially, be formed from a binary system of hard spheres. This is, in itself fascinating, given that the formation of such structures is entropically driven. However, of fundamental interest is the ability to form binary colloidal crystals, as this enables the fabrication of novel nano-scale structures[43] beyond the capabilities of lithography. Applications include, for example, the construction of an electronic device that is able to measure the resistance of a single organic molecule[44]. Photonic[45] materials and biochemical sensors[46] have also been constructed using self-assembling colloidal particles. Further uses may include the manufacture of ceramics and composites or the construction of lithographic templates.

2.1 Initial Observation in a Sample of Gem Opal

Binary superlattices were discovered in a naturally occurring sample of gem opal. Gem opals consist of a close packed array of silica spheres, which are typically uniform in size (in the range of 150-400 nm). In the course of examining some samples of gem quality opal from Brazil, Sanders[47] came across an unusual sample. In this sample, a mixture of silica spheres with two distinct diameters, 362 nm and 210 nm, was found. The ratio of diameters being 0.580.

By examining etched cross sections of the gem opal with an electron microscope, Sanders was able to identify two different structures present within the sample, which he labelled AB_{13} and AB_2. Whilst neither of these structures is simple, the AB_{13}

structure is particularly unusual. The larger spheres, labelled "A", form a primitive cubic lattice, with the smaller spheres forming icosahedral clusters that occupy the centre of each cube. Adjacent icosahedral clusters are rotated by 90° relative to each other. A small sphere at the centre of each icosahedral cluster ensures the stochiometry is AB_{13}. In the AB_2 structure the large spheres form hexagonal close packed layers that lie directly over each other. The small spheres sit in the centres of the triangular prisms formed. Diagrams of both of these structures may be found in section 3.2.2 (AB_{13}) and 3.2.4 (AB_2).

Gem opal is believed to form by the slow, steady precipitation of silica from an aqueous solution[47]. The maximum possible packing fraction of a random arrangement of hard spheres is 0.64. However if the spheres sediment slowly they are able to form close-packed crystalline arrays, with a packing fraction of 0.74. In the monodisperse system the formation of the crystalline phase depends only on the volume fraction of the hard spheres present. In contrast in a binary system the formation of superlattices depends upon the diameter ratio, σ, the mole fractions of the two species present as well as the overall volume fraction. Murray and Sanders speculated that the formation of these phases was dependant on the ability of the hard spheres to pack efficiently[48]. Samples of gem opal with monodisperse particles in the FCC arrangement are common. So Murray and Sanders reasoned that the binary structures formed if the volume fraction of such a structure was higher than that of the two separate FCC structures. As is shown in section 3.2 AB_2 comfortably satisfies this criterion, while the AB_{13} system must be modified slightly to ensure it also fits the criteria. One possible distortion is to assume that the sphere at the centre of the icosahedral cluster was marginally smaller than those at the edge. They argued that the sedimenting

systems maximised their packing fractions in order to minimise their gravitational potential energy.

2.2 Observation in Colloidal Systems

Following on from the discovery of these structures in gem opal, Hachisu *et al.*[49] studied systems of highly charged colloidal spheres using optical microscopy. The repulsive potential was characterized by an effective hard sphere potential. Unable to look much further than the surface of their samples, due to the opaqueness, they were still able to observe a number of superlattices. Amongst these were, the AB_2 and AB_{13} structures already discovered in gem opal. They also discovered two structures that followed the arrangement of ions in the $MgCu_2$ ($\sigma = 0.77$) and $CaCu_5$ ($0.72 \leq \sigma \leq 0.75$) crystals. The potential of the charged colloidal spheres and surface effects may well have influenced the formation of some of these structures, as both $MgCu_2$ and $CaCu_5$ have poor packing fractions (sections 3.2.6 and 3.2.7).

Later, Bartlett *et al.*[50] studied a binary colloidal system with diameter ratio of 0.58. The phase behaviour was studied of a mixture of poly(methyl methacrylate) (PMMA) spheres. By adjusting the densities of the two differently-sized colloidal spheres present, they were able to observe both AB_{13} and AB_2 crystals by optical crystallography. The refractive index of the suspension medium was matched to that of the particles to avoid turbidity and to minimize the attractive van der Waals forces. A phase diagram was constructed from their experimental data. One of the most noteworthy aspects of this study is the time scales involved for crystallization. AB_2 crystals took in the region of five weeks to form (compared to a few hours needed for monodisperse crystals). This introduces the possibility that the formation of binary

superlattices may be kinetically hindered. The structures were identified using powder light crystallography and electron microscopy.

Pusey *et al.*[51] also studied a binary system of colloidal hard spheres (PMMA grafted with PHSA) at a diameter ratio , $\sigma = 0.36$, and observed the formation of AB_6 crystals (section 3.2.8). In more recent studies, Schofield[52] observed the formation of a binary hard crystal with the CsCl structure at a diameter ratio, $\sigma = 0.736$ (section 3.2.9). However the crystals disappeared over time, leading him to suggest that this structure was metastable.

Hunt and Jardine[53] studied a number of binary systems with different diameter ratios. At a diameter ratio, $\sigma = 0.39$, they observed the formation of binary hard sphere crystals with the structure of NaCl or NiAs (sections 3.2.10, 3.2.11 and 5.1.3). At a diameter ratio, $\sigma = 0.52$ they observed the AB_2 and AB_{13} superlattices, whilst at $\sigma = 0.72$ they found that the two phases were immiscible and no superlattices were formed.

2.3 Computer Simulation

Inspired by the observation of superlattices in colloidal systems, Frenkel *et.al.*[54,55] performed an extensive range of computer simulations of binary hard sphere systems ($0.5 \leq \sigma \leq 0.625$). Dependent on the diameter ratio and number densities of the species present, they showed that both the AB_2 and AB_{13} phases could be stable relative to other possible binary phases. Recall that the formation of these complex crystals is entropy driven, this is remarkable given that entropy is always thought of as a force for disorder. They found good agreement between their simulations and the earlier experimental work[56]. The discrepancies that were observed were put down to

kinetic effects, for instance the speed at which nucleation and subsequent growth occurs. They found that AB_2 was stable in the range of diameter ratios, $0.5 \leq \sigma \leq 0.625$ and AB_{13} was stable in the range, $0.54 \leq \sigma \leq 0.625$.

Trizac *et al.*[57] performed simulations of binary systems at the more extreme diameter ratios 0.414 and 0.45. It is at these ratios that the NaCl structure is expected to form (as it has a high packing fraction). In the NaCl structure, the large spheres form an FCC lattice with the small spheres occupying the octahedral vacancies. From their simulations they predicted that under suitable conditions the NaCl phase would be thermodynamically stable relative to other competing phases.

2.4 Summary

The AB_2 and AB_{13} structures are only observed in experiment and simulation within a limited range of diameter ratios. Outside those diameter ratios a rich variety of phases seems possible. The binary superlattices that have been observed in experiment or simulation are summarised in figure 2.1.

The ability of a given structure to pack efficiently is a first guide to the likelihood of that structure forming. For instance, at diameter ratios, $\sigma > 0.8$, the AB_{13} structure has a low maximum packing fraction and would not be expected to form. On the other hand, the FCC structure has interstitial vacancies which may accommodate a sphere of diameter ratio, $\sigma = 0.414$ (octahedral holes). An FCC arrangement of large spheres with the smaller spheres occupying the octahedral holes will have a high packing fraction, when the diameter ratio is near 0.414. This structure, which is formed by NaCl, is a prime candidate for consideration. Although this may be a good "rule of thumb", to properly predict the thermodynamic stability of a particular structure

statistical mechanics is used. Even then, the thermodynamic stability of a given structure under certain conditions is not enough to predict its existence with certainty. Other factors, such as kinetic stability[58,59] may come into play.

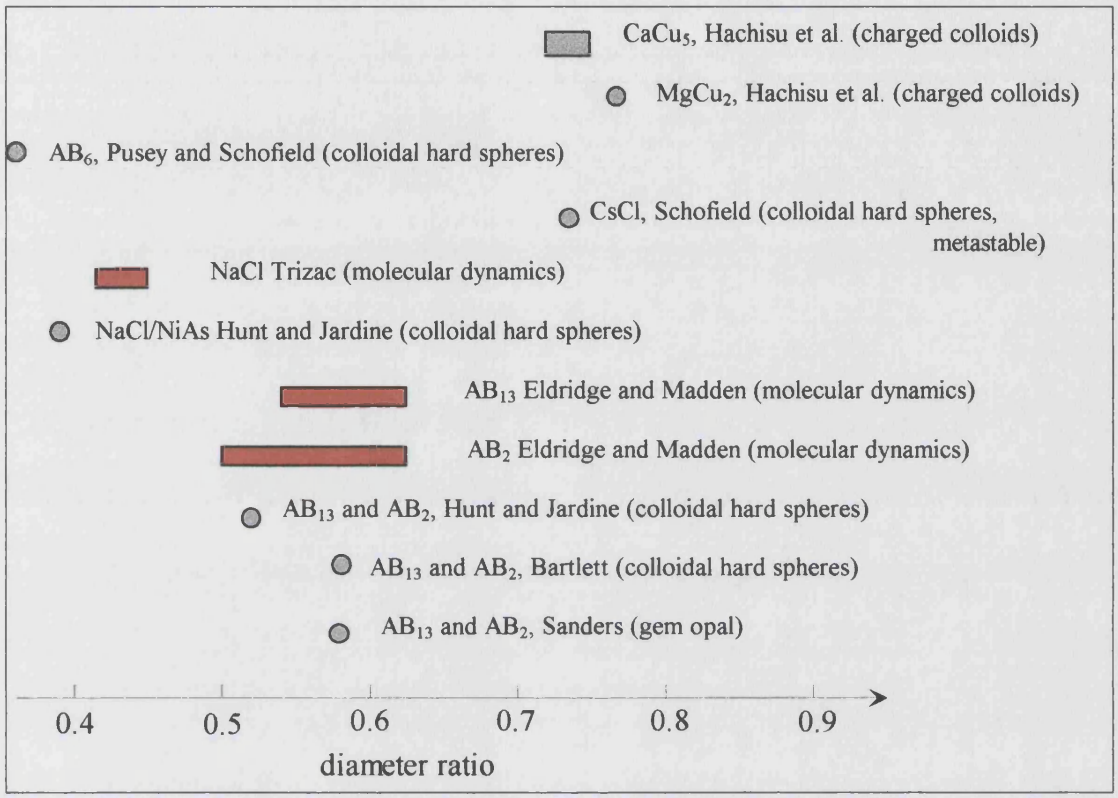

Figure 2.1 A summary of binary superlattices observed in experiment (grey) and simulation (red). The circles mark the diameter ratio at which the superlattice was observed, whilst the rectangles shows a range of diameter ratios.

2.5 Plan of action

In the following section (3.1), the application of statistical mechanics, in particular the cell model, to binary systems is considered. Before any calculations involving the cell model may be carried out, it is necessary to work out the relative positions of the hard spheres in the structure under consideration. These, as well as the close packing fractions, are evaluated in section 3.2. A number of structures are considered, many of

which have been observed in various systems. In section 3.2 an attempt to predict new structures is made. The calculation of the phase behaviour of binary hard sphere systems is considered in section 3.3. The equation of state of the binary fluid is examined in section 3.4. The method used to calculate the free volumes is described in chapter 4 and some general results are given in section 5.1.

The phase diagrams for binary hard sphere systems with a range of diameter ratios are given in section 5.2.

Chapter 3 Theory of Binary Systems

3.1 The Application of the Cell Model

3.1.1 Statistical Mechanics

The theory behind the cell model is considered in the introduction (section 1.2). In this section, the specific application to binary systems is considered.

All the structures considered in this study have stochiometry AB_n, where the large spheres are denoted A and the smaller spheres B. In each case, considered in this thesis, the large spheres are in identical environments. This is also true for the smaller spheres in the majority of instances but it there are exceptions. For instance, the AB_{13} structure, considered in section 3.2.2 in which twelve of the small spheres sit at the verticies in the icosahedral cluster, whilst the thirteenth occupies the centre. Hence this structure may be defined as an $AB'_{12}C$ type. Note that this is not a true ternary structure as the particles labelled B′ and C have the same diameter. To cover all eventualities the denotation AB'_mC_p is used in the following pages. In all cases,

$$n = m + p \qquad (3.1.1)$$

The ratio of the diameters of the large spheres, σ_A to the small spheres, σ_B is defined by

$$\sigma = \frac{\sigma_B}{\sigma_A}. \qquad (3.1.2)$$

Writing the semi-classical partition function,

$$Z_N = \prod_i z_i^{N_i}, \quad (3.1.3)$$

where z_i is the semi-classical partition function of cell type i, for a structure, AB'_mC_p, we have

$$Z_N = z_A^{N_A} z_{B'}^{N_{B'}} z_C^{N_C}, \quad (3.1.4)$$

where z_i is given by

$$z_i = \frac{1}{\lambda_i^3} \int d^3 r e^{-\beta \Phi_i(r)}, \quad (3.1.5)$$

Φ is the potential energy function and λ_i is the thermal wavelength for the particles occupying cell i. λ_i is a scaling factor, whose value does not influence the final results. Hence for convenience we chose to define

$$\lambda_i = \sigma_A \text{ for all } i. \quad (3.1.6)$$

Choosing σ_A, the diameter of the large spheres, as the unit length throughout all calculations, so that all volumes are measured in units of σ_A^3. This leads to the scaled expression for z_i,

$$z_i = \int d^3 r e^{-\beta \Phi_i(r)}, \quad (3.1.7)$$

$$\text{or} \qquad z_i = q_i, \quad (3.1.8)$$

where q_i is the cell configurational integral.

For a hard sphere system, in the cell model, q_i and consequently z_i are equal to the volume in which the centre of the tagged particle is free to move about inside the cell. This is known as the free volume, v_f. Since the volume of each particle type is independent,

$$Z_N = v_{fA}{}^{N_A} v_{fB'}{}^{N_{B'}} v_{fC}{}^{N_C}. \quad (3.1.9)$$

The Helmholtz free energy, A is then given by

$$\frac{A}{kT} = -\ln Z_N. \quad (3.1.10)$$

So that

$$\frac{A}{kT} = -N_A \ln v_{fA} - N_{B'} \ln v_{fB'} - N_C \ln v_{fC} \quad (3.1.11)$$

or

$$\frac{A}{NkT} = -x_A \ln v_{fA} - x_{B'} \ln v_{fB'} - x_C \ln v_{fC}, \quad (3.1.12)$$

where x_i is the mole fraction of particles in cell type i.

The pressure is then obtained from the standard result,

$$p = -\left(\frac{\partial A}{\partial V}\right)_{T,N}. \quad (3.1.13)$$

The volume fraction of the system is a more useful measurement than the volume. The volume fraction is that fraction of the volume occupied by the particles, not including any interstial spaces. The volume fraction, ϕ, is given by.

$$\phi = \frac{N\pi}{6V}\langle\sigma^3\rangle \quad (3.1.14)$$

From this the expression

$$\frac{d}{dV} \equiv -\frac{\phi}{V}\frac{d}{d\phi} \qquad (3.1.15)$$

is obtained. So the pressure is given by

$$p = \frac{\phi}{V}\left(\frac{\partial A}{\partial \phi}\right)_{T,N} . \qquad (3.1.16)$$

Consequently,

$$\frac{pV}{NkT} = -\phi\sum_i x_i \frac{\partial}{\partial \phi}\left(\ln v_{fi}\right)_{T,N} . (3.1.17)$$

This differential is evaluated numerically by the algorithms described in section 5.1.

The Gibbs free energy may now be obtained using

$$\frac{G}{NkT} = \frac{A}{NkT} + \frac{pV}{NkT} \quad (3.1.18)$$

3.1.2 The Excess Helmholtz Free Energy

It is frequently more instructive to split the ideal from the non-ideal terms in the free energy. The excess Helmholtz free energy, A_{ex}, is defined by

$$A_{ex} = A - A_{id} , (3.1.19)$$

where A_{id} is the Helmholtz free energy for an ideal system.

The semi classical partition function for an ideal binary system, Z_{id}^{bin}, is given by

$$Z_{id}^{bin} = \frac{1}{N_A! N_B!} z_{Aid}{}^{N_A} z_{Bid}{}^{N_B}. \quad (3.1.20)$$

The pre-factor accounts for the entropy of mixing two species of different size. We note, in passing that the notation AB'_mC_p is not needed when considering an ideal system as individual small spheres are by definition always indistinguishable. The partition function for the individual species, z_{i-id}, with i = A or B, is given by

$$z_{i-id} = \frac{V^{N_i}}{\lambda_i^{3N_i}}. \quad (3.1.21)$$

Utilising the definition of λ_i (3.1.6) leads to the result,

$$Z_{id}^{bin} = \frac{V^N}{N_A! N_B!}, \qquad (3.1.22)$$

where, as before the volume, V, is measured in units of $\sigma_A{}^3$. The ideal free energy is therefore

$$\frac{A_{id}^{bin}}{kT} = -\ln Z_{id}^{bin}, \qquad (3.1.23)$$

$$\text{or } \frac{A_{id}^{bin}}{NkT} = -\ln V + \frac{N_A \ln N_A - N_A}{N} + \frac{N_B \ln N_B - N_B}{N}. \qquad (3.1.24)$$

Substitution of the expression for the volume fraction,

$$\phi = \frac{\pi}{6V}(N_A + N_B \sigma^3) \qquad (3.1.25)$$

and the mole fractions,

$$x_i = \frac{N_i}{N}, \qquad (3.1.26)$$

yields a final expression for the ideal Helmholtz free energy,

$$\frac{A_{id}^{bin}}{NkT} = \ln\phi - 1 + \ln\left(\frac{6}{\pi(x_A + x_B\sigma^3)}\right) + x_A \ln x_A + x_B \ln x_B . \quad (3.1.27)$$

The excess Helmholtz free energy for a binary system is consequently

$$\begin{aligned}\frac{A_{ex}^{bin}}{NkT} = &-x_A \ln v_{fA} - x_{B'} \ln v_{fB'} - x_C \ln v_{fC} - \ln\phi + 1 \\ &- \ln\left(\frac{6}{\pi(x_A + x_B\sigma^3)}\right) - x_A \ln x_A - x_B \ln x_B\end{aligned} \qquad (3.1.28)$$

3.2 Binary Superlattices

3.2.1 Selection of Candidate Structures

The purpose of the cell model is not to generate binary structures. It is used to determine the stability of a number of possible structures. There are a very large number of possible arrangements within a binary system. Molecular shape and bond angles determine the form of many complex structures. These complex structures are unlikely to be formed by a simple hard sphere system, as was pointed out by Murray and Saunders[48]. Other structures may be ruled out due to steric hindrance. For instance the CaF_2 structure has the smaller spheres occupying the tetrahedral vacancies left by an FCC arrangement of large spheres. At diameter ratios greater than 0.5 the smaller spheres would be too large for the holes, which are ideally suited for a diameter ratio of 0.225.

A good quantitative measure of the likelihood of a particular structure is the maximum packing fraction. When Murray and Saunders examined samples of gem opal containing the AB_2 and AB_{13} structures[48], they speculated that the maximum packing fraction was the deciding factor in the formation of different arrangements. Their hypothesis was that a structure formed if its maximum packing fraction was greater than that of the monodisperse FCC structure. This was based on the postulate that the system attempted to maximise its density.

Comparison of the stabilities of different structures is carried out at constant density. If a structure is capable of packing at a high density, then it follows that by the time the density is reduced the particles will have greater freedom to move about. Hence the free volume will be greater and the Helmholtz free energy lower. For this reason,

the packing fraction is a good indicator of the stability of a structure. For instance, the CaF_2 structure has a packing fraction of only 0.484 at diameter ratio 0.56 whilst AB_{13} has one of 0.735. It is, therefore, not surprising that it is the AB_{13} and not the CaF_2 structure that is found to be more stable at these diameter ratios.

Note that structures are sometimes referred to by their ionic analogues. The "CaF_2" structure refers to the binary hard sphere superlattice having the same structure as the CaF_2 crystal.

When considering a structure, the primary step is the calculation of the close packing curve. i.e. the maximum packing fraction vs. the diameter ratio. The maximum packing fraction occurs at the point where any further increase in the density would result in the overlap of any pair of particles. The minimum distance between pairs of hard spheres is fixed by their diameters. These minimum distances may be expressed in terms of the unit cell dimensions. The constraints on the separation between pairs of particles leads to the minimum possible unit cell dimensions and so to the maximum packing fractions.

To determine whether or not to include a structure at the diameter ratio under consideration, the criterion of a close packing fraction greater than 0.65 was used. i.e. only those structures with a maximum packing fractions greater than 0.65 at the appropriate diameter ratio were included. The volume fraction of 0.65 is approximately halfway between the close packing fraction and melting fraction of FCC. A structure with such a low maximum packing fraction will have a small free volume and thus will be thermodynamically unstable relative to the FCC phases. Naturally, some exceptions were made to this crude selection criterion.

In the following sections all the various binary superlattices used in these calculations are introduced. Whilst the list of structures given is by no means exhaustive, a large number of possible structures have been taken into account. These structures may be broadly classified into four groups according to the arrangement of the large spheres. These being cubic, trigonal prismatic, close packed and body centred cubic (There is a fifth type based upon the diamond lattice, but only one structure adopts this arrangement). Many of the structures have been observed in nature or have been suggested in literature[47-49] as possible arrangements for binary hard sphere systems. However a number of the structures described have not been observed in nature and are put forward as possible arrangements. In this manner, it is hoped a comprehensive collection of arrangements has been generated.

3.2.2 AB_{13} Structure and Close Packing Curve

As AB_{13} has been observed in samples of gem opal, no study would be complete without the inclusion of this structure. Murray and Saunders have calculated the close packing curve. This is one of four structures considered where the larger spheres form a simple cubic array. Two parameters, *a* and *b*, are used to define the unit cell (fig. 3.2.1). The width of the unit cell is given by *a* and the distance of the small spheres from the centre is given by *b*. Note that the unit cell parameter, *b*, is not strictly dependent on *a*. When the spheres forming the icosahedral cluster are quite small, *b* may vary without altering the close packing characteristics. In these cases it is normally assumed that at close packing *b* is at a minimum. The close packing curve for AB_{13} is shown in fig. 3.2.3. It is typical of some of the curves in that it has three branches. Packing is determined, in the first branch by contact between large spheres,

in the last branch by small spheres. In the middle branch it is contact in-between small and large spheres that governs the packing characteristics.

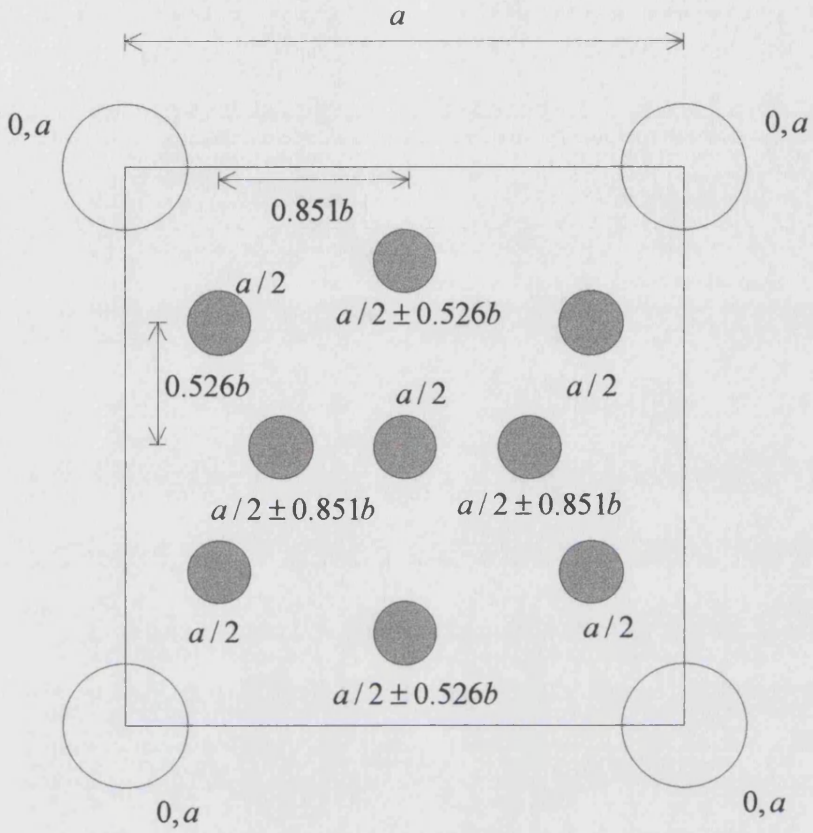

Figure 3.2.1 Diagram showing arrangement of large and small spheres in the unit cell of AB_{13}. The co-ordinates perpendicular to the plane of the diagram are given adjacent to the spheres.

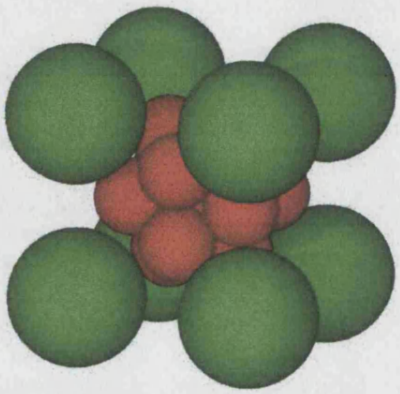

Figure 3.2.2 Unit cell for AB_{13}, showing (001) face.

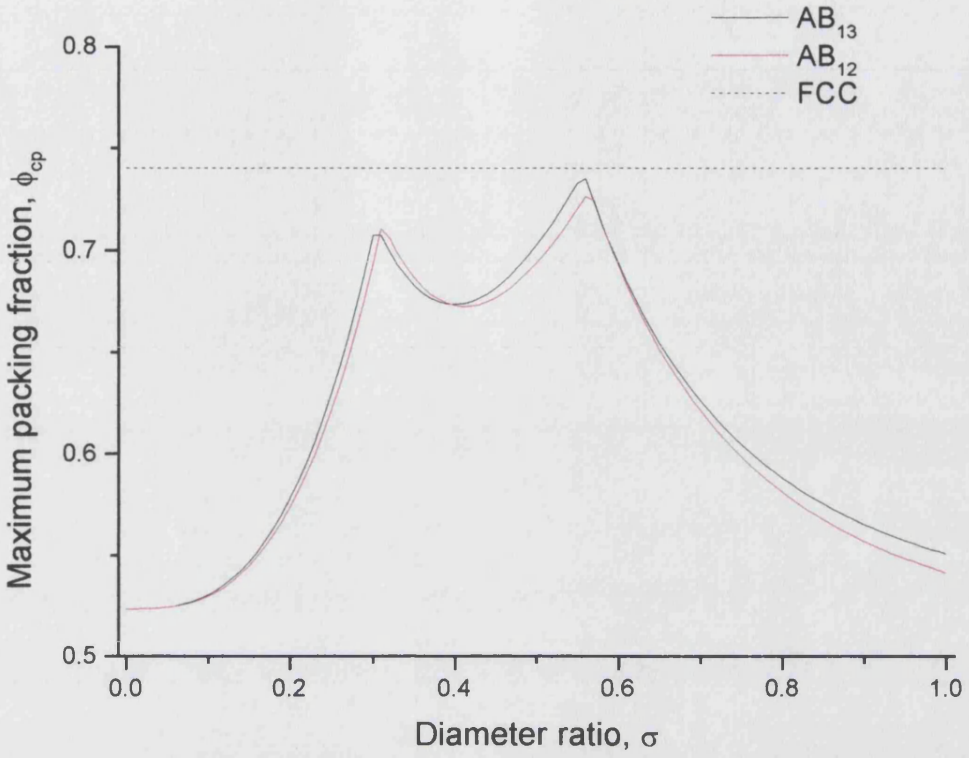

Figure 3.2.3 Close packing curves for AB_{13} and its variant AB_{12} (see section 3.2.3). The dotted line is the maximum packing fraction of a monodisperse FCC crystal.

3.2.3 AB_{12} Structure and Close Packing Curve

This structure is almost identical to AB_{13}, the only difference being the removal of the small sphere at the centre of the icosahederal cluster. It was thought that the removal of the sphere at the centre of the icosahedral cluster would allow the structure to pack more efficiently, by allowing the size of the cluster to be reduced. There is a very small advantage in doing so at low diameter ratios, as may be seen in fig. 3.2.3. However, this advantage is lost at the higher diameter ratios where AB_{13} is actually seen to occur.

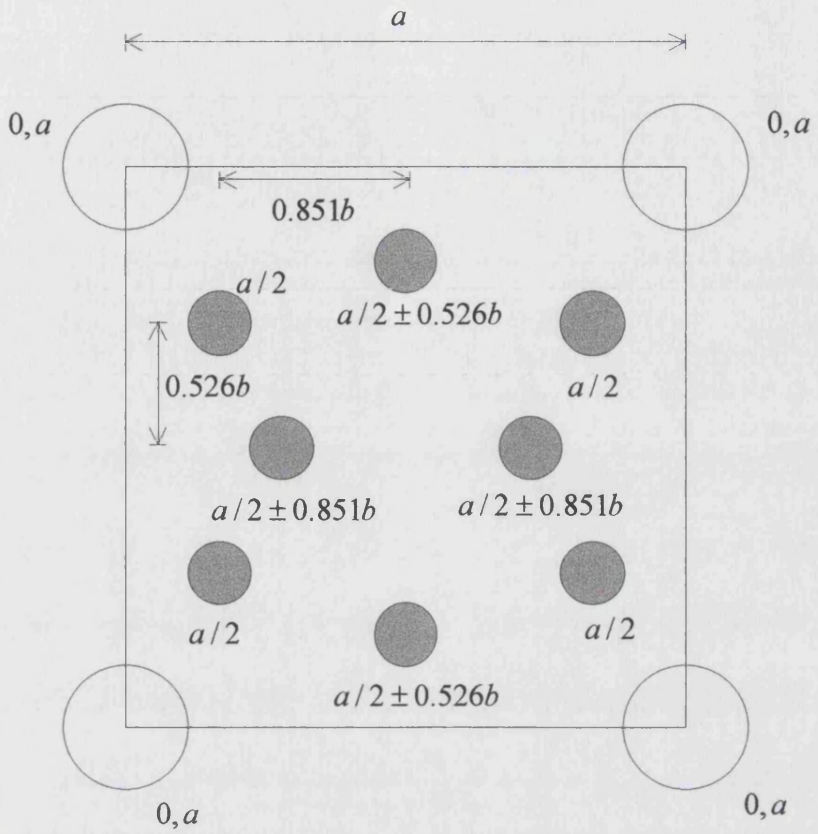

Figure 3.2.4 Diagram showing arrangement of large and small spheres in the unit cell of AB_{12}. The co-ordinates perpendicular to the plane of the diagram are given adjacent to the spheres.

3.2.4 AB_2 Structure and Close Packing Curve

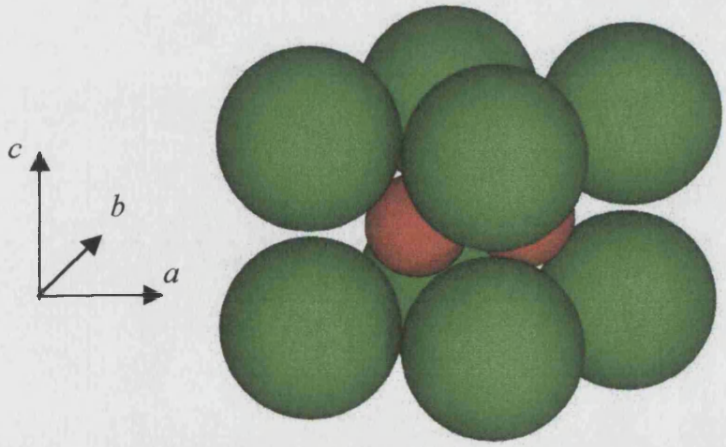

Figure 3.2.5 Unit cell portion of AB_2, (010) face. The large spheres, A, are shown in green, the small spheres, B are shown in red.

The other structure observed by Murray and Saunders is also a vital inclusion. Less complex than AB_{13} it is one of three structures where the larger spheres form a trigonal prism. In this case, the first coordination sphere of large spheres surrounding each small sphere is trigonal prismatic. It is one of the structures explored with the best close packing characteristics having a maximum packing fraction of 0.779 at a diameter ratio of 0.558.

The hexagonal unit cell of AB_2 has two parameters a and c. At the maximum packing fraction, these parameters are dependent upon each other. Murray and Saunders also calculated the close packing curve for this structure. The packing curve for AB_2 does not follow the typical three branch construction of AB_{13}. This is due to the fact that AB_2 has two cell parameters to be minimised. Packing is determined by contacts in the basal plane as well as contacts across the basal plane.

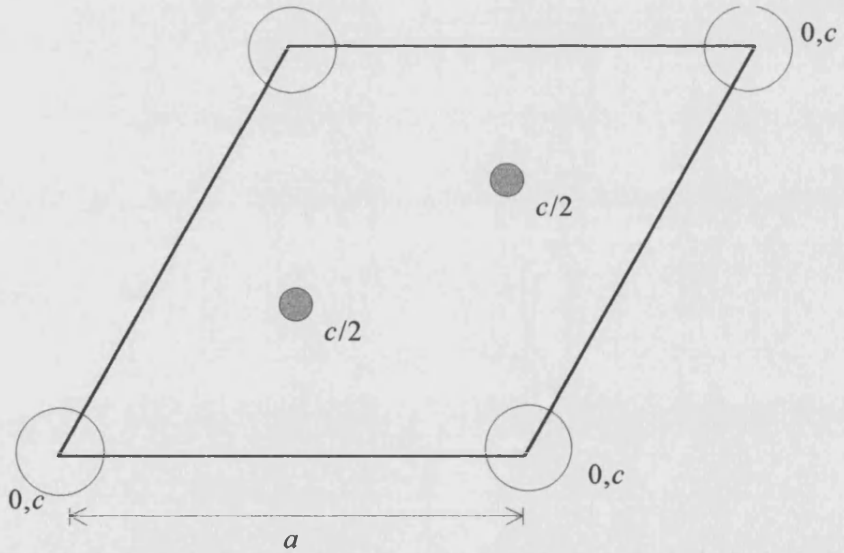

Figure 3.2.6 Diagram showing arrangement of large and small spheres in the unit cell of AB_2. The co-ordinates perpendicular to the plane of the diagram are given adjacent to the spheres.

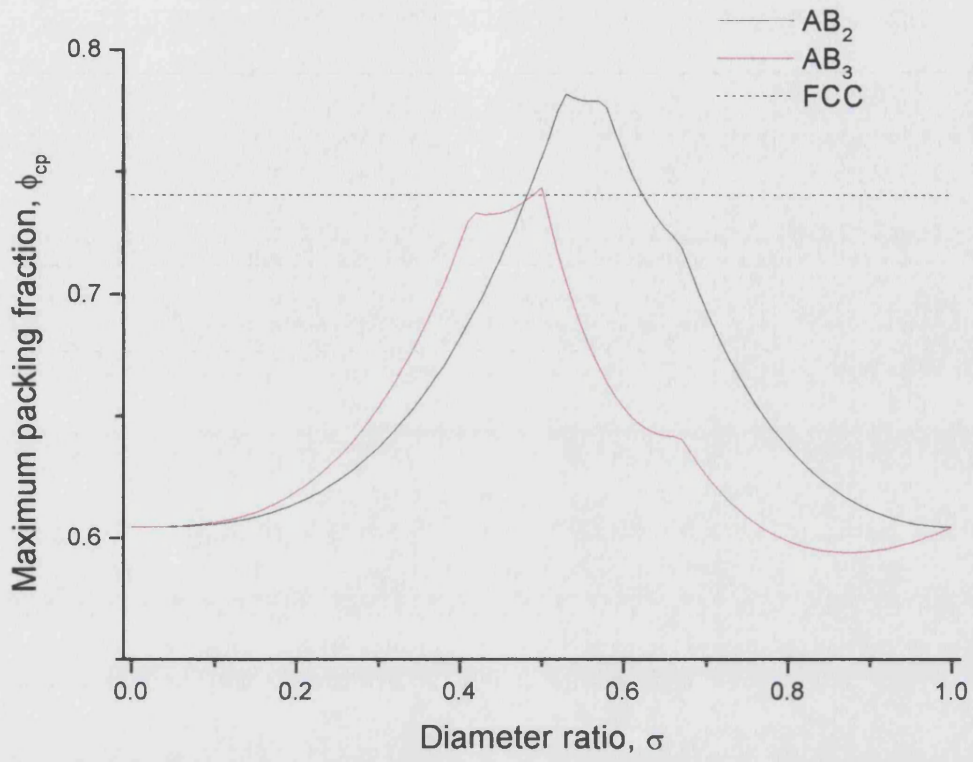

Figure 3.2.7 Close packing cure for two of the structures based upon a trigonal prismatic arrangement of large spheres, AB_2 and AB_3. The dotted line is the maximum packing fraction of a monodisperse FCC crystal and is shown for comparison.

3.2.5 AB_3 Structure and Close Packing Curve

The second of three structures based upon a trigonal prism, AB_3 is obtained by an alteration of the AB_2 structure. Instead of placing one small sphere at the centre of the trigonal prism, three small spheres are placed at the centres of the three rectangular faces of the prism. The purpose of this was to utilize the close packing characteristics of AB_2 at slightly lower diameter ratios. AB_3 has reasonably good close packing characteristics, peaking at diameter ratios near 0.5. In fact between the diameter ratios

0.465 and 0.48 it has the highest packing fraction of all structures considered (fig. 3.2.7).

The packing curve is determined by calculating the values of the cell parameters, a and c. These parameters are constrained by the need to avoid any overlap between neighbouring spheres. The greatest packing fraction is achieved by minimising the volume of the whole unit cell. As this volume is proportional to a^2c, the minimum will be achieved by finding, first, the smallest value of a, then of c.

Possible contacts in the basal plane are the first to be considered. Large spheres are separated by a distance, a, so

$$a \geq 1. \quad (3.2.1)$$

The gap between adjacent small spheres is $a/2$, therefore

$$a \geq 2\sigma. \quad (3.2.2)$$

There are no possible contacts between large and small spheres in the basal plane, so these two constraints are sufficient to determine a.

The separation of large spheres across the basal plane is c. The first constraint upon this cell parameter is therefore

$$c \geq 1. \quad (3.2.3)$$

This constraint makes it unnecessary to add a second to avoid overlap between small spheres across the basal plane. But it is necessary to avoid overlap between large and small spheres, which are separated by a distance $\sqrt{a^2/4 + c^2/4}$. Accordingly

$$\sqrt{a^2/4 + c^2/4} \geq \frac{1+\sigma}{2}. \qquad (3.2.4)$$

As a is already determined, this may be rearranged to give

$$c \geq \sqrt{(1+\sigma)^2 - a^2}\,. \quad (3.2.5)$$

The maximum packing fraction is then given by

$$\phi_{cp} = \frac{\pi(1+3\sigma^3)}{3\sqrt{3}a_{\min}{}^2 c_{\min}}. \quad (3.2.6)$$

The four branches of the packing curve corresponding to the four different sets of constraints which actually determine the values of a and c as shown in table 3.2.1.

Range	a	c
$0 \leq \sigma \leq \sqrt{2}-1$	$a=1$	$c=1$
$\sqrt{2}-1 \leq \sigma \leq 1/2$	$a=1$	$c=\sqrt{(1+\sigma)^2 - a^2}$
$1/2 \leq \sigma \leq 2/3$	$a=2\sigma$	$c=\sqrt{(1+\sigma)^2 - a^2}$
$2/3 \leq \sigma \leq 1$	$a=2\sigma$	$c=1$

Table 3.2.1 Constraints which apply to cell parameters for the unit cell of AB_3 at different diameter ratios.

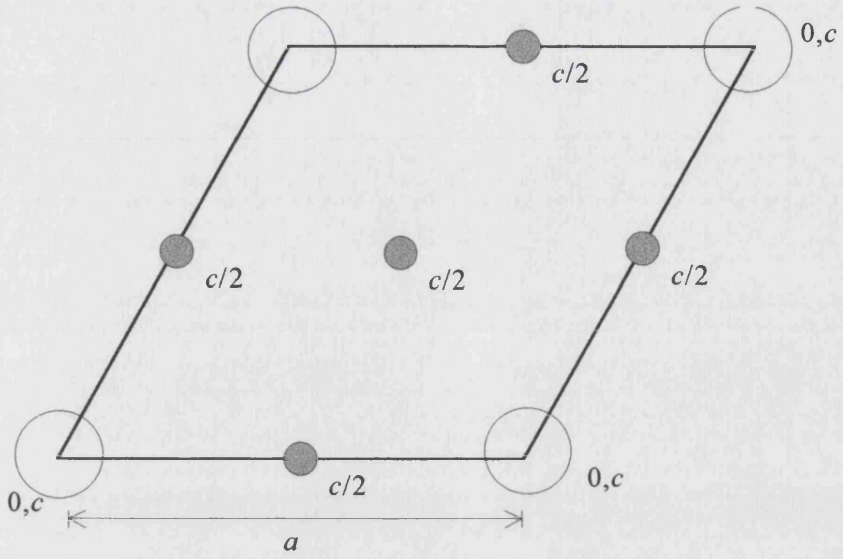

Figure 3.2.8 Diagram showing arrangement of large and small spheres in the unit cell of AB_3. The co-ordinates perpendicular to the plane of the diagram are given adjacent to the spheres.

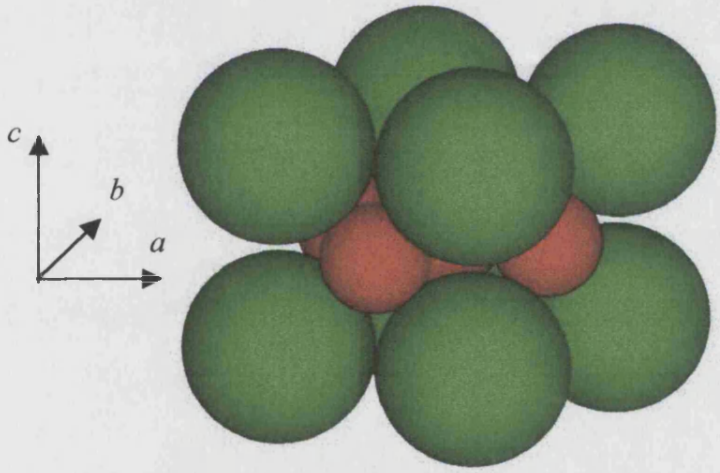

Figure 3.2.9 Unit cell for AB_3, (010) face.

3.2.6 $CaCu_5$ Structure and Close Packing Curve

This is one of two structures observed in systems of charged colloids with strongly screened coulombic attractions[49]. These systems were intended as approximations to hard sphere systems. However, the formation of the structures observed was possibly affected by the nature of the potential. Never the less, they were initially included for

completeness. It is not immediately apparent from the unit cell, but this structure is also based upon a trigonal prism arrangement of the larger spheres. The unit cell dimensions are given by a and c (fig. 3.2.10).

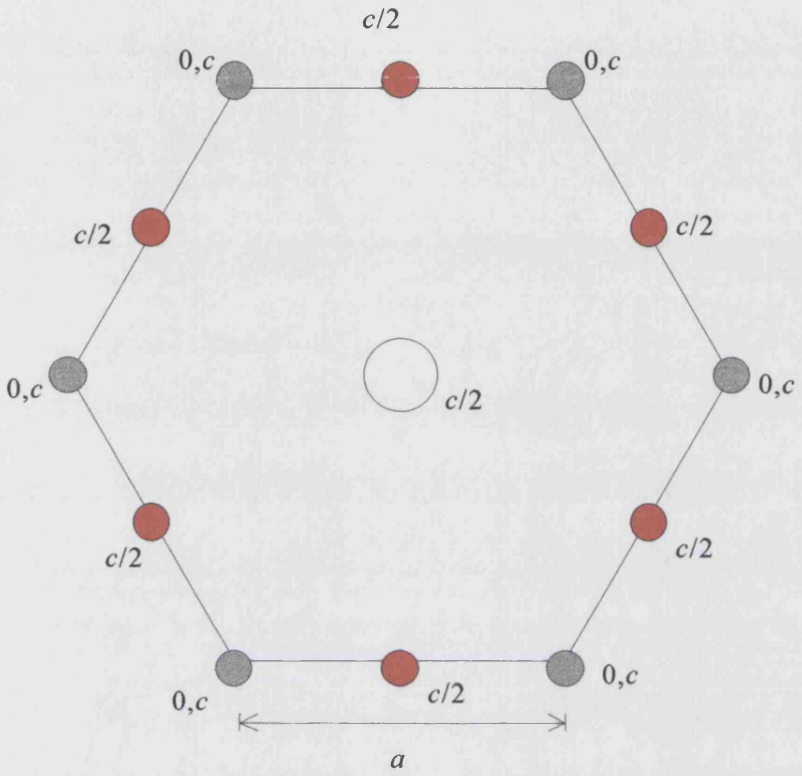

Figure 3.2.10 Diagram showing arrangement of large and small spheres in the unit cell of $CaCu_5$. The co-ordinates perpendicular to the plane of the diagram are given adjacent to the spheres. Note that the small spheres shown in red are in a distinct environment to those shaded grey.

The $CaCu_5$ structure contains small spheres in two distinct environments (fig. 3.2.10). Therefore the generalisation that packing curves have three branches does not apply. Close packing occurs when the cell parameters a and c are at their minima. As unit cell volume is proportional to a^2, this parameter is minimised first. The minimum value of c is then found given that a is already at its minimum possible value.

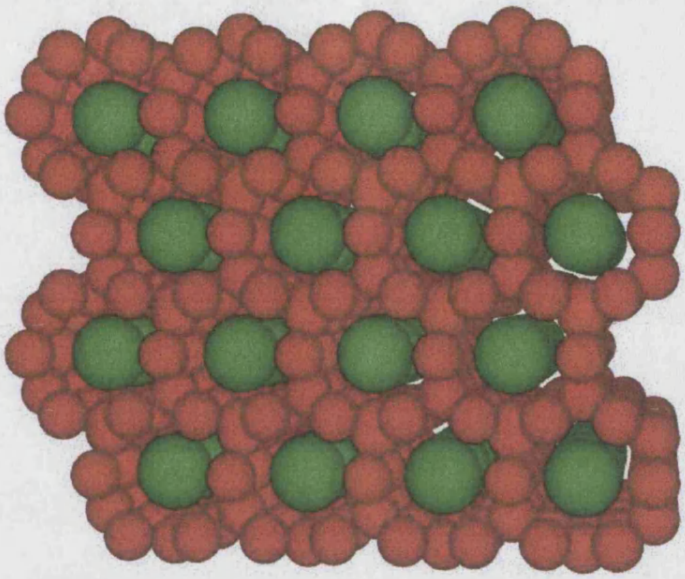

Figure 3.2.11 The $CaCu_5$ structure, (001) face.

There are two distinct layers shown in the unit cell. The first at height c/2 contains the large spheres. Adjacent hard spheres are separated by a distance $\sqrt{3}a$. Therefore

$$a \geq \frac{1}{\sqrt{3}}. \qquad (3.2.7)$$

In the same layer, the separation between the small and large spheres is a, so

$$a \geq \frac{1+\sigma}{2}. \qquad (3.2.8)$$

Small spheres are also separated by a distance a, which would give the constraint

$$a \geq \sigma \quad (3.2.9)$$

but as $\sigma \leq 1$ this constraint is satisfied as long as the other constraints are met and may be safely ignored.

By considering the layer which contains only small spheres at height 0 the final constraint upon the value of a is obtained. In this layer, small spheres are separated by a distance of $\frac{\sqrt{3}}{2}a$. Accordingly

$$a \geq \frac{2\sigma}{\sqrt{3}}. \qquad (3.2.10)$$

a may be determined by the set of relationships,

$$a = \frac{1}{\sqrt{3}} \text{ when } \sigma \leq \frac{2}{\sqrt{3}} - 1 \qquad (3.2.11)$$

$$a = \frac{1+\sigma}{2} \text{ when } \frac{2}{\sqrt{3}-1} \leq \sigma \leq \frac{\sqrt{3}}{4-\sqrt{3}} \qquad (3.2.12)$$

$$a = \frac{2\sigma}{\sqrt{3}} \text{ when } \sigma \geq \frac{\sqrt{3}}{4-\sqrt{3}} \qquad (3.2.13)$$

The second cell parameter may now be determined. The separation between the large spheres in alternate layers is c, so

$$c \geq 1. \qquad (3.2.14)$$

Contact between the large and small spheres is avoided as long as

$$c \geq \sqrt{(1+\sigma)^2 - 3a^2}. \qquad (3.2.15)$$

The final constraint upon c is in order to prevent small spheres in adjacent layers coming into contact. Their separation is $\frac{\sqrt{a^2+c^2}}{2}$, so that

$$c \geq \sqrt{4\sigma^2 - a^2}\,. \qquad (3.2.16)$$

In practise overlap of small and large spheres is avoided when overlap between spheres of the same size is. Therefore only the first and last constraints upon c apply. c is then determined by the pair of relationships,

$$c = 1 \text{ when } \sigma \leq \frac{2+\sqrt{154}}{30} \qquad (3.2.17)$$

$$c = \sqrt{4\sigma^2 - a^2} \text{ when } \sigma \geq \frac{2+\sqrt{154}}{30} \qquad (3.2.18)$$

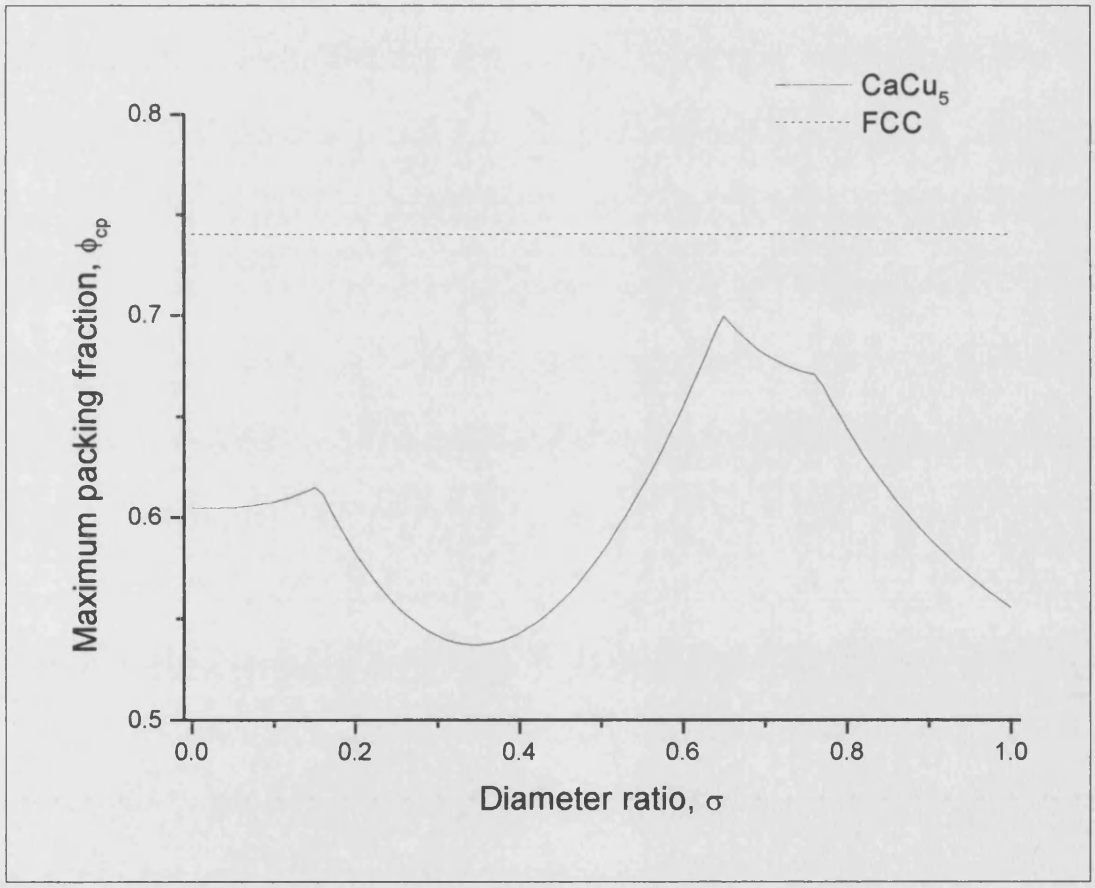

Figure 3.2.12 Close packing curve for $CaCu_5$. The dotted line is the maximum packing fraction of a monodisperse FCC crystal.

The set of three constraints upon a and two upon c bring about a total of four branches to the close packing curve, which is given by

$$\phi_{cp} = \frac{\pi(1+5\sigma^3)}{9\sqrt{3}a_{\min}{}^2 c_{\min}}. \quad (3.2.19)$$

As may be observed from its close packing curve, (fig. 3.2.12) $CaCu_5$ does not have a high packing fraction. Its greatest packing fraction is obtained at high diameter ratios where binary structures are less likely to occur.

3.2.7 $MgCu_2$ Structure and Close Packing Curve

$MgCu_2$ is the second of the structures examined that were observed in the systems of charged colloids[49].

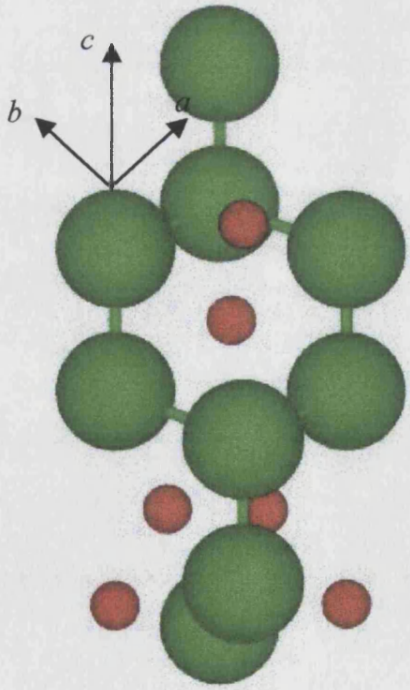

Figure 3.2.13 Unit cell for $MgCu_2$, (010) face.

The basis for this structure is the diamond lattice. The large spheres occupy the positions that in diamond are taken by carbon atoms. In this structure the large atoms form six membered rings with the same chair confirmation as cyclohexane. A small sphere sits in the middle of each of these rings (fig. 3.2.13). This is a poorly packed structure at diameter ratios below 0.8. Even at the optimum diameter ratios its close packed volume fraction barely exceeds 0.7. For this reason, it is not expected that this structure will be observed in systems of true hard spheres.

3.2.8 AB_6 Structure and Close Packing Curve

As with AB_{13}, the large spheres in the AB_6 arrangement form a primitive cubic array. The difference is that in this structure the small spheres form octahedral clusters to sit at the centre of each cube.

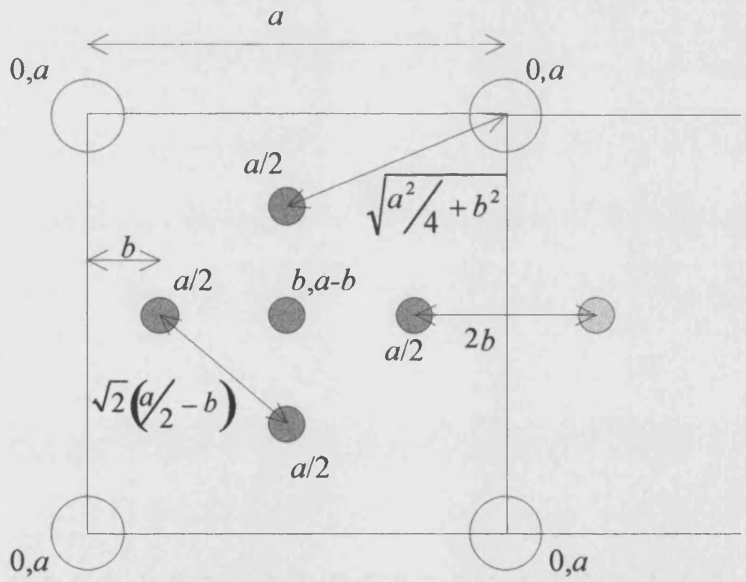

Figure 3.2.14 Diagram showing arrangement of large and small spheres in the unit cell of AB_6. The co-ordinates perpendicular to the plane of the diagram are given adjacent to the spheres.

This structure was included for consideration as it was thought to be a possible arrangement for binary crystals at diameter ratio, $\sigma = 0.36$ observed in experiments in Edinburgh by Pusey and Schofield[51].

Two parameters a and b define the unit cell for AB_6 (fig. 3.2.14). These are the width of the cubic unit cell, a, and the distance of the small spheres forming the octahedral cluster from the face of the unit cell, b. In the ideal structure b is fixed relative to a such that the distance between any two neighbouring small spheres is constant. That is

$$2b = \sqrt{2}\left(a/2 - b\right), \text{ which may be rearranged to give} \quad (3.2.20)$$

$$b = \frac{a}{2+2\sqrt{2}}. \quad (3.2.21)$$

As the separation between neighbouring large spheres is a, then

$$a \geq 1. \quad (3.2.22)$$

The separation between neighbouring small spheres being constant, we have

$$2b \geq \sigma, \text{ or in terms of } a, \quad (3.2.23)$$

$$\frac{2a}{2+2\sqrt{2}} \geq \sigma. \text{ Standard manipulation gives} \quad (3.2.24)$$

$$a \geq \left(1+\sqrt{2}\right)\sigma. \quad (3.2.25)$$

Finally, adjacent small and hard spheres give the constraint that

$$\sqrt{a^2/4 + b^2} \geq \frac{1+\sigma}{2}. \text{ Leading to} \quad (3.2.26)$$

$$a \geq (1+\sigma)\sqrt{\frac{3+\sqrt{2}}{4+\sqrt{2}}} \qquad (3.2.27)$$

The unit cell, being a cube with sides length a, contains six small spheres and eight eighths of large spheres. At close packing, the volume fraction is given by

$$\phi_{cp} = \frac{\pi(1+6\sigma^3)}{6a_{\min}^{\ 3}} \qquad (3.2.28)$$

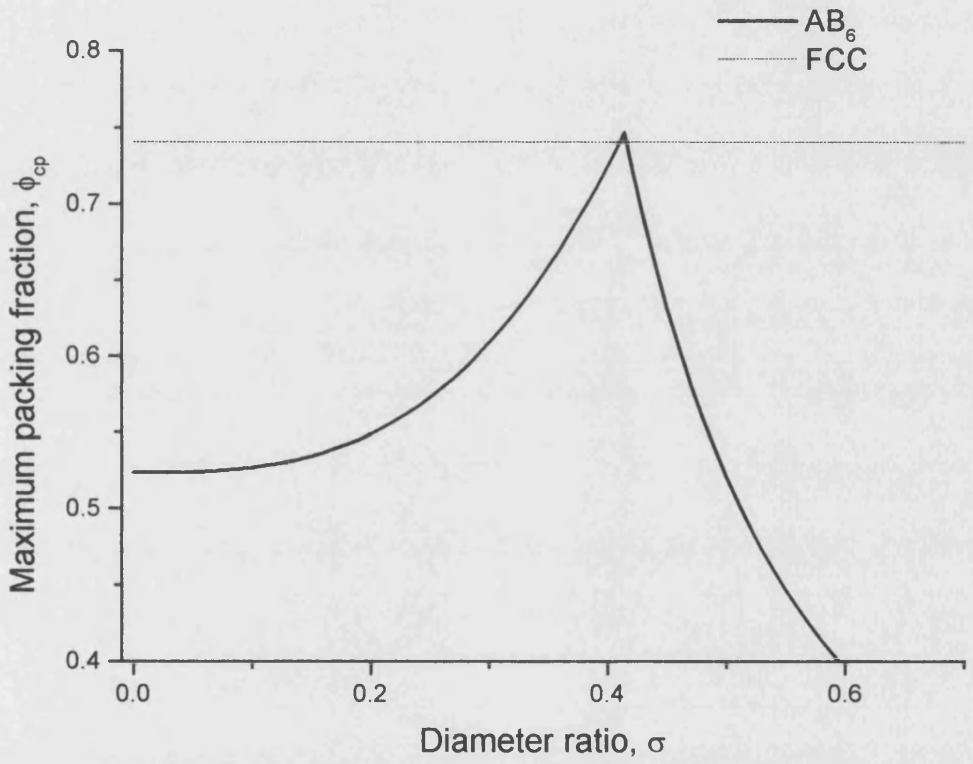

Figure 3.2.15 Close packing curve for AB_6. The dotted line is the maximum packing fraction of a monodisperse FCC crystal.

There are two branches to this close packing curve (fig 3.2.15). Each branch corresponds to a different constraint. At low diameter ratios it is the large spheres that are in contact, the small spheres are relatively free. a is determined by the constraint

$a \geq 1$. At higher diameter ratios, the small spheres come into contact and the important constraint becomes $a \geq \left(1+\sqrt{2}\right)\sigma$, as the large spheres have some space to "rattle about" in. In this case the small spheres never come into contact with the large spheres, so the third constraint becomes irrelevant. Hence there are only two branches to this packing curve. The peak in the curve occurs at the point where the two branches overlap. This corresponds to the case when neither the large nor the small spheres have any unused space to move about in. If the AB_6 arrangement is to occur at all, it is expected to be near this diameter ratio where packing is most efficient.

3.2.9 CsCl Structure and Close Packing Curve

The fourth and simplest of structures based upon the cubic arrangement of the large spheres, CsCl has only one small sphere at the centre of each cube.

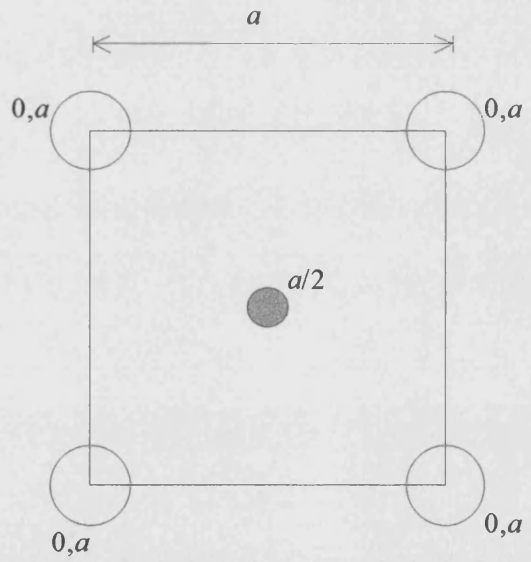

Figure 3.2.16 Diagram showing arrangement of large and small spheres in the unit cell of CsCl. The co-ordinates perpendicular to the plane of the diagram are given adjacent to the spheres.

Only one cell parameter, a, is needed to uniquely define the structure (fig. 3.2.16). The closest packing is obtained when $\sigma = \sqrt{3} - 1$. The close packed volume fraction is then 0.729009 (6dp), which is relatively low. The packing curve is determined by the constraints,

$$a \geq 1 \text{ and} \qquad (3.2.29)$$

$$a \geq \frac{1+\sigma}{\sqrt{3}}. \text{ Giving} \qquad (3.2.30)$$

$$\phi_{cp} = \frac{\pi(1+\sigma^3)}{6a_{\min}^{\ 3}} \qquad (3.2.31)$$

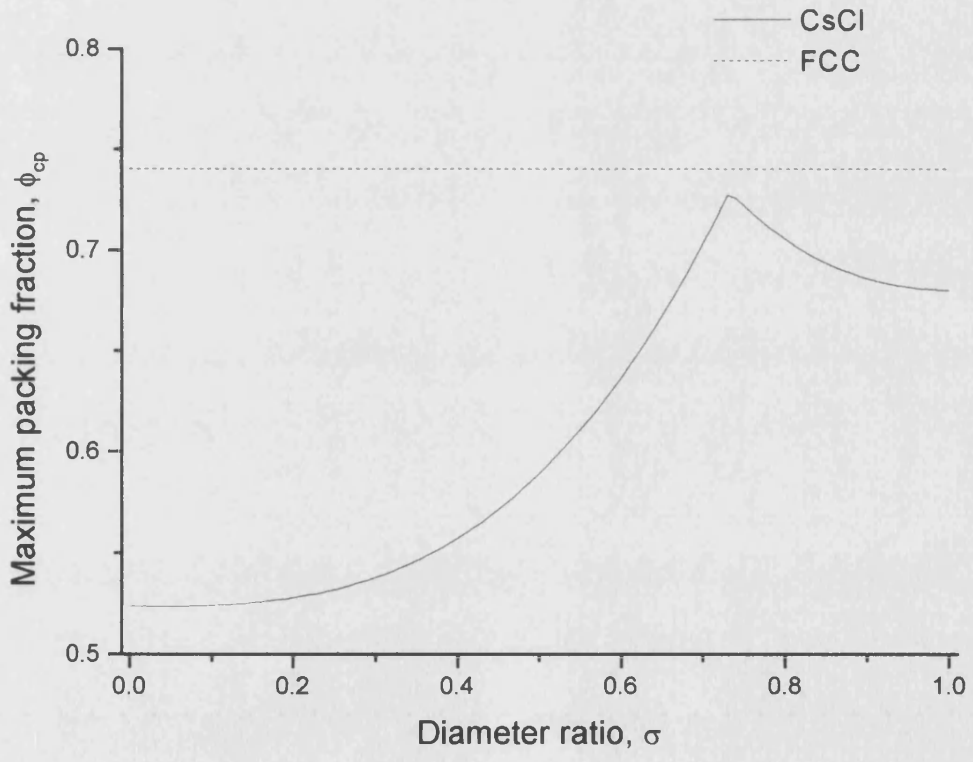

Figure 3.2.17 Close packing curve for CsCl. The dotted line is the maximum packing fraction of a monodisperse FCC crystal.

CsCl is another structure that does not pack well until higher diameter ratios (fig. 3.2.17). Consequently it was thought unlikely that this structure would be thermodynamically stable in a binary system.

3.2.10 NaCl Structure and Close Packing Curve

NaCl is one of three structures based upon a close packed arrangement of the large spheres. The large spheres form a face centred cubic arrangement, with the small spheres occupying the octahedral interstitial vacancies.

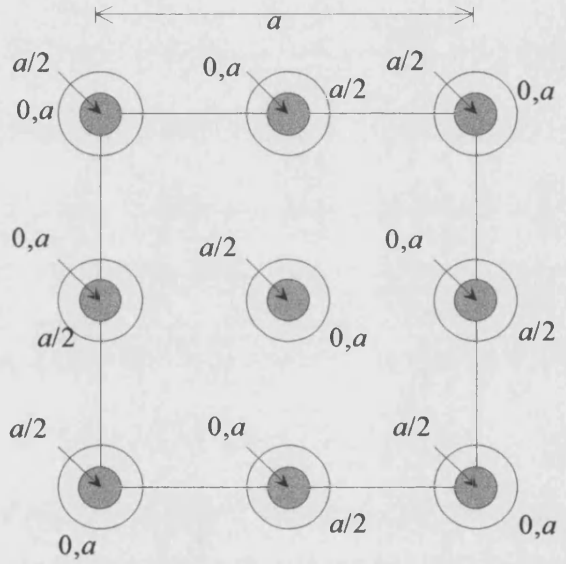

Figure 3.2.18 Diagram showing arrangement of large and small spheres in the unit cell of NaCl. The co-ordinates perpendicular to the plane of the diagram are given adjacent to the spheres.

There are only two constraints upon the cell parameter, a (fig. 3.2.18). The first prevents overlap between hard spheres,

$$a \geq \sqrt{2}. \qquad (3.2.32)$$

Whilst the second prevents any overlap in-between small and large spheres,

$$a \geq 1 + \sigma . \qquad (3.2.33)$$

Consequently the packing fraction is given by

$$\phi_{cp} = \frac{\pi(4 + 4\sigma^3)}{6a_{\min}^{\ 3}} \qquad (3.2.34)$$

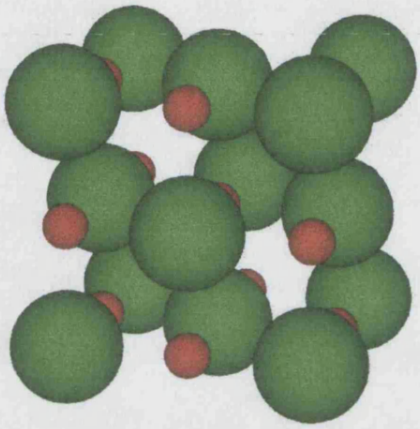

Figure 3.2.19 Unit cell for NaCl, (001) face showing.

The best packing arrangement is achieved when the two branches of the curve overlap. Clearly this will occur when $\sigma = \sqrt{2} - 1$, which corresponds to the diameter ratio where the small spheres exactly fill the octahedral holes. The packing fraction at this point is 0.7931. The characteristics of this structure would suggest that if any superlattice is to be observed at this diameter ratio, it should be this one. Along with NiAs it has the joint highest packing fraction of any of the structures examined in this study. However as monodisperse systems of hard spheres are known to prefer to form face centred cubic arrangement, it may be expected that NaCl will be more favoured than NiAs. This idea will be explored later (section 5.1.3).

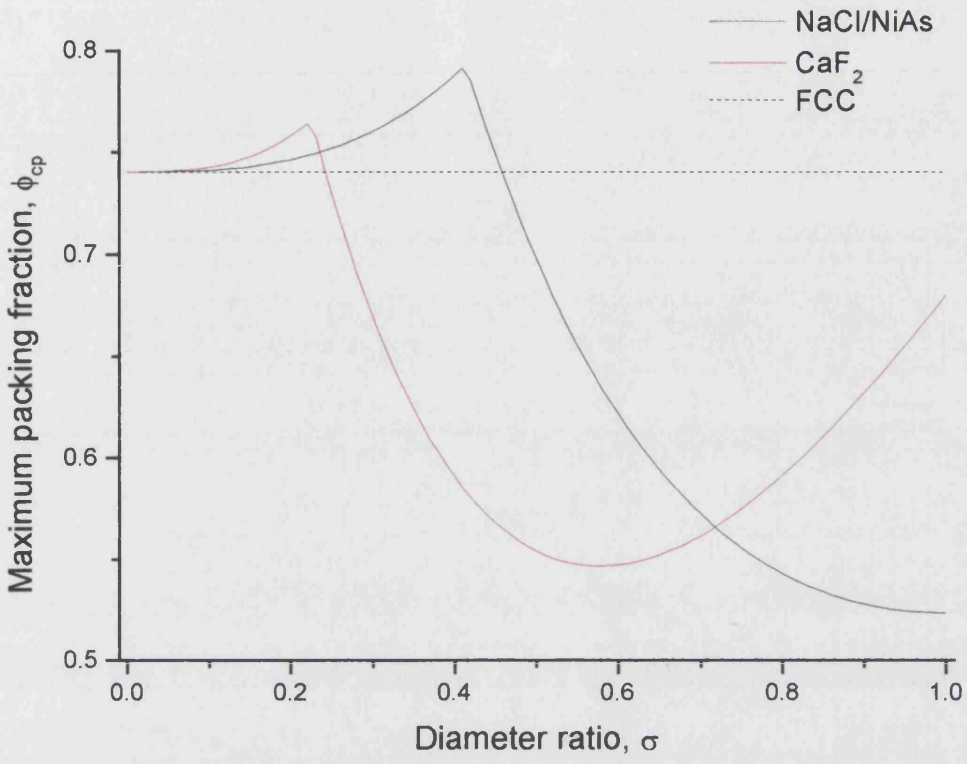

Figure 3.2.20 Close packing curve for the structures based upon a close packed arrangement of large spheres, NaCl, NiAs and CaF_2. The dotted line is the maximum packing fraction of a monodisperse FCC crystal.

3.2.11 NiAs Structure and Close Packing Curve

The second of the structures based upon the close packed arrangement of the large spheres, NiAs differs from NaCl in that the large spheres form an hexagonal close packed arrangement. Thus the large spheres form ABAB repeating layers. The small spheres still occupy the octahedral vacancies.

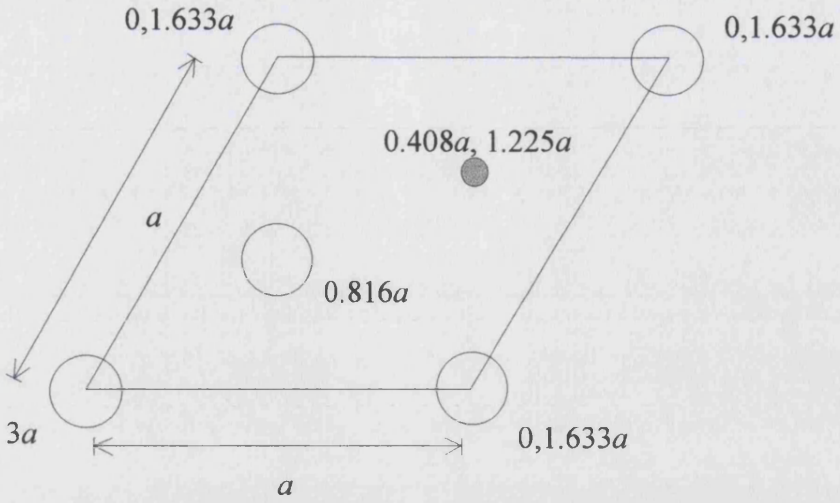

Figure 3.2.21 Diagram showing arrangement of large and small spheres in the unit cell of NiAs. The co-ordinates perpendicular to the plane of the diagram are given adjacent to the spheres.

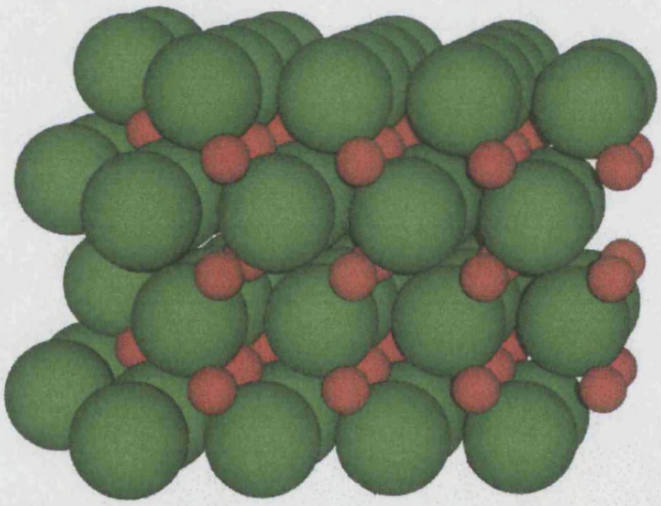

Figure 3.2.22 NiAs Structure, showing (001) face.

NiAs has exactly the same close packing characteristics as NaCl. The small spheres are also in the same environment as they are in NaCl, being situated at the centre of octahedral arrangement of large spheres. However in NaCl the large spheres are surrounded by an octahedral arrangement of small spheres, whilst in NiAs this arrangement takes the form of a triagonal prism.

3.2.12 CaF_2 Structure and Close Packing Curve

The third and perhaps the least likely of the structures based upon the close packing of the large spheres, CaF_2 has the small spheres occupying the tetrahedral vacancies. The diameter ratio favoured for this arrangement is 0.225. This structure does not seem likely, as there is no obvious reason why the small spheres should occupy the tetrahedral vacancies and leave the large octahedral vacancies unfilled. Never the less it is included for completeness. It was tested as a possible structure at low diameter ratios, but not predicted to be stable.

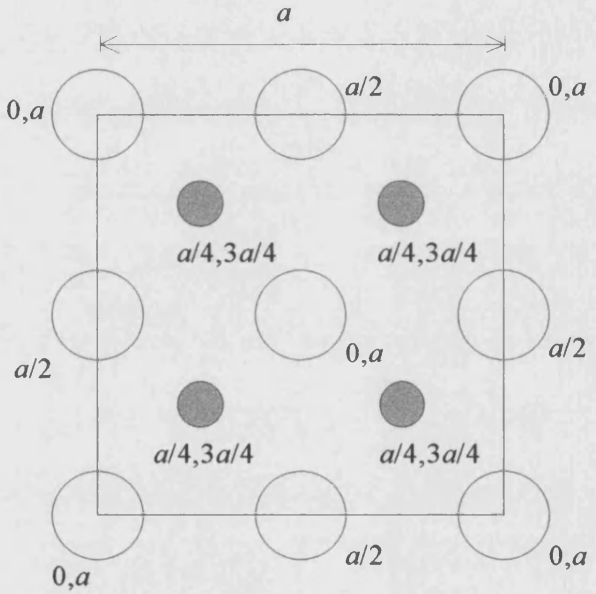

Figure 3.2.23 Diagram showing arrangement of large and small spheres in the unit cell of CaF_2. The co-ordinates perpendicular to the plane of the diagram are given adjacent to the spheres.

3.2.13 BCC-6 Structure and Close Packing Curve

Some pure elements are known to form the BCC structure. The following two structures have the large spheres in a BCC arrangement with the small spheres filling the vacancies. It is not immediately apparent where the vacancies are in the BCC

structure. When deciding where the small spheres should lie, care must be taken to ensure all large spheres remain in identical environments to maintain the true nature of the BCC arrangement. BCC-6 has a stochiometry of AB_6.

The packing curve for BCC-6 follows the typical three branch construction of AB_{13}. There is only one cell parameter, a, which is constrained by the need to avoid overlap.

Large spheres are separated by a distance of $\frac{\sqrt{3}a}{2}$. This gives the first constraint,

$$a \geq \frac{2}{\sqrt{3}}. \qquad (3.2.35)$$

Small spheres are quite close together, the smallest gap between them being only $\frac{a}{2\sqrt{2}}$. Consequently

$$a \geq 2\sqrt{2}\sigma. \qquad (3.2.36)$$

Finally the space between small and large spheres is $\frac{a\sqrt{5}}{4}$. Requiring that

$$\frac{a\sqrt{5}}{4} \geq \frac{1+\sigma}{2}, \text{ which is rearranged to give} \qquad (3.2.37)$$

$$a \geq \frac{2(1+\sigma)}{\sqrt{5}}. \qquad (3.2.38)$$

The packing fraction is given by

$$\phi_{cp} = \frac{\pi(1+6\sigma^3)}{3a_{\min}{}^3} \qquad (3.2.39)$$

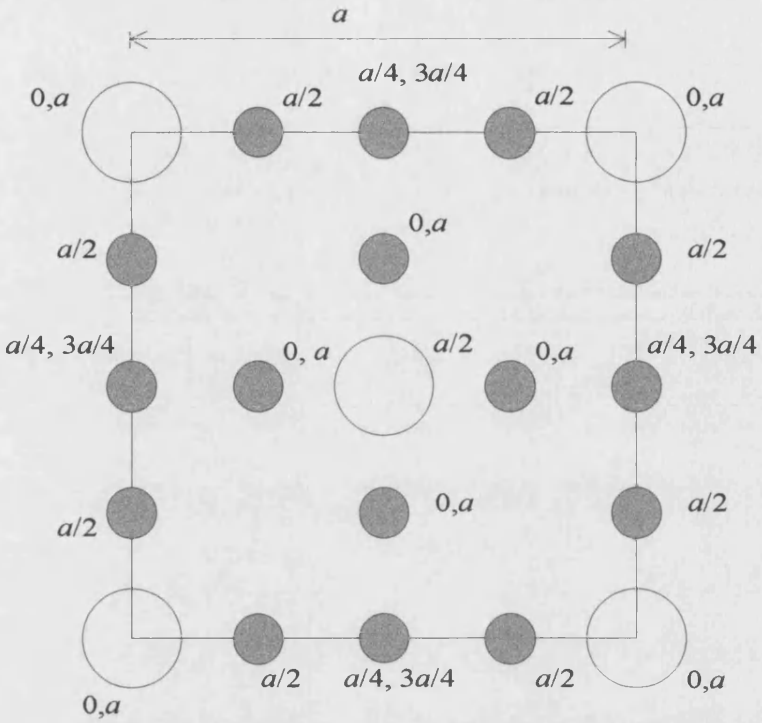

Figure 3.2.24 Diagram showing arrangement of large and small spheres in the unit cell of BCC(AB_6). The co-ordinates perpendicular to the plane of the diagram are given adjacent to the spheres.

Optimum packing occurs at when large spheres are in contact both with other large spheres and small spheres. This occurs when both of the constraints for these contacts are just satisfied. i.e.

$$a = \frac{2}{\sqrt{3}}, \text{ and} \quad (3.2.40)$$

$$a = \frac{2(1+\sigma)}{\sqrt{5}}. \text{ Giving} \quad (3.2.41)$$

$$\frac{2}{\sqrt{3}} = \frac{2(1+\sigma)}{\sqrt{5}}, \text{ or} \quad (3.2.42)$$

$$\sigma = \sqrt{\frac{5}{3}} - 1, \quad (3.2.43)$$

At this diameter ratio (~0.3) the close packed volume fraction approaches 0.78.

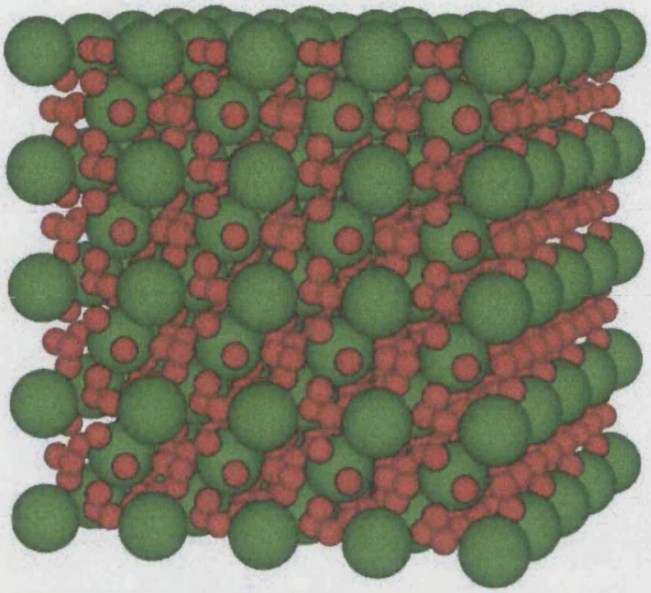

Figure 3.2.25 The BCC(AB_6) structure, showing (001) face.

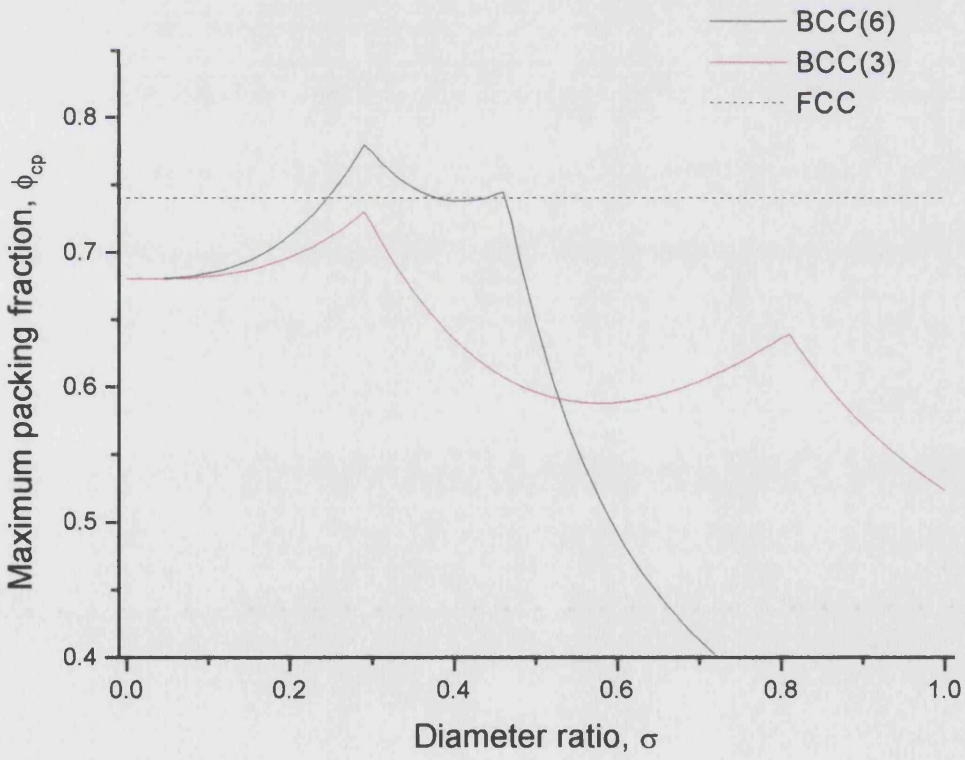

Figure 3.2.26 Close packing curves for BCC structures. The dotted line is the maximum packing fraction of a monodisperse FCC crystal.

3.2.14 BCC-3 Structure and Close Packing Curve

As the BCC-6 structure must expand in order to accommodate the small spheres, it was thought that more favourable packing characteristics might be obtained by removing some small spheres and freeing up the structure. The BCC-3 structure is formed by removing alternate small spheres from the BCC-6 structure. This does indeed allow the unit cell to be more compact at higher diameter ratios. However any advantaged gained is offset by the empty spaces left by the small spheres that are removed. BCC-3 only has a higher packing fraction than BCC-6 at fairly high diameter ratios, where neither has particularly good packing ability.

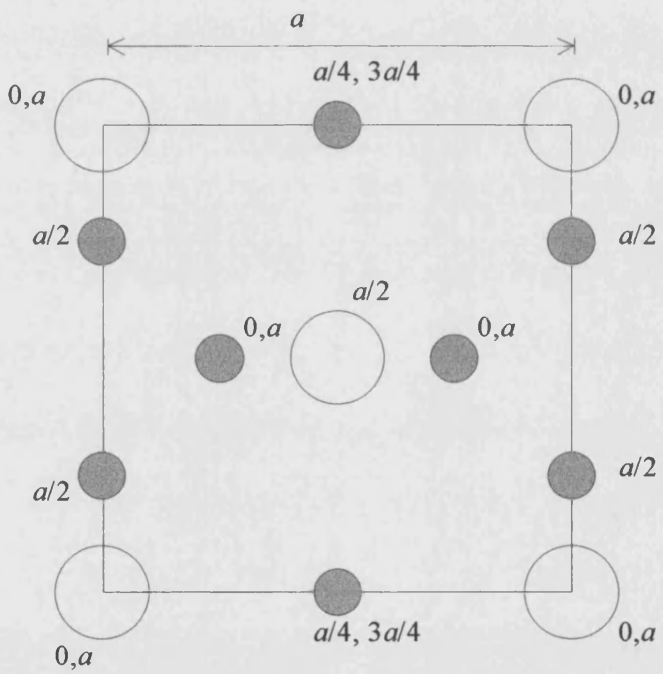

Figure 3.2.27 Diagram showing arrangement of large and small spheres in the unit cell of BCC(AB_3). The co-ordinates perpendicular to the plane of the diagram are given adjacent to the spheres.

As half the small spheres have been removed from the BCC-6 structure, the constraint to avoid overlap between small spheres becomes

$$a \geq 2\sigma . \qquad (3.2.44)$$

The packing curve for BCC-3 is given by

$$\phi_{cp} = \frac{\pi(1+3\sigma^3)}{3a_{\min}^{\ 3}}. \qquad (3.2.45)$$

3.2.15 The Arrangement of Neighbours Around Each Tagged Particle

In the cell model, the positions and sizes of the neighbouring hard spheres determine the free volume of the particle under consideration. It is important not to exclude any spheres from the calculations that may have an influence on the calculation of the free volume. The inclusion of spheres that have no relevance will not adversely affect the results. For this reason, if there is a possibility that a neighbour will influence the calculation, it was included. The small spheres become more relevant as the diameter ratio increases. Note it is not necessarily only the nearest neighbours that are included in the calculation.

After placing each "tagged" particle at the origin of its cell, the coordinates of the neighbours were calculated in terms of the unit cell dimensions. The unit cell dimensions depend on the diameter ratio and are thus variable. For this reason algorithms were written to generate the positions of the neighbours for each cell type considered. In most structures there were only two cell types to be considered. e.g. NaCl has two different cells, one for the large and one for the small spheres. AB_{13} is one of the few exceptions, having cells for the large, small vertex and small central spheres.

The positions of neighbours relative to the particle under consideration were calculated first at close packing. To analyse the stability at volume fractions less than

the close packing limit, the system is expanded uniformly until the required volume fraction is obtained. The monodisperse system first forms the solid at a volume fraction of 0.545. If Binary systems are to crystallise, it is expected to be at similar volume fractions. Allowing a generous margin either side, the properties of each structure were calculated between the volume fraction, $\phi = 0.45$ and the close packing limit.

The restriction of the free volume by the Voronoi polyhedron is of greatest relevance when considering cells containing small spheres at low diameter ratios. Without this restriction, the small sphere would be free to "escape" from the cage formed by its nearest neighbours. If it were to do this then that particle could not be said to be located on its lattice site, but would be free to wander throughout the crystal structure (fig. 3.2.28).

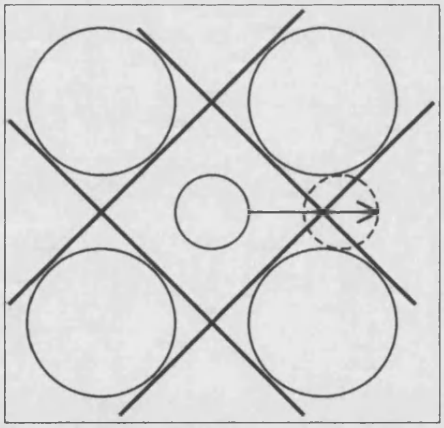

Figure 3.2.28 At low densities and low diameter ratios, the small sphere may be able to escape from the "cage" of large spheres. to escape from the "cage" of large spheres. In the calculations detailed here, the possible escape of the particle is removed by restricting the sphere to a Voroni polyhedron formed by the neighbouring spheres.

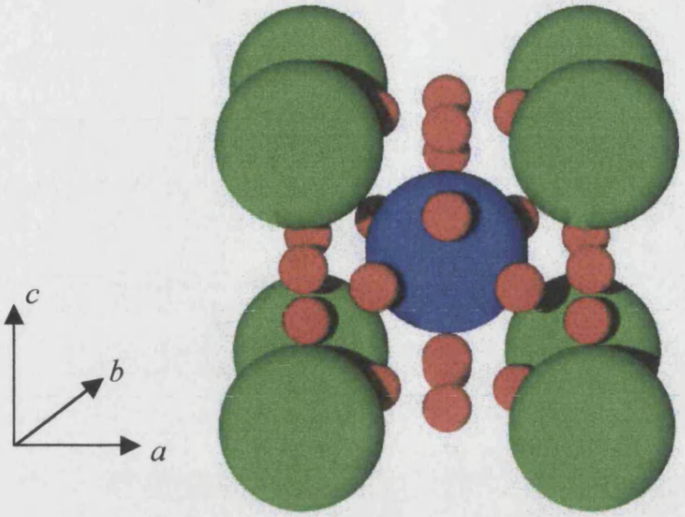

Figure 3.2.29 Arrangement of spheres used when calculating the free volume of the large sphere (shaded blue) in the BCC(AB_6) structure. The neighbours are shaded green (large) and red (small).

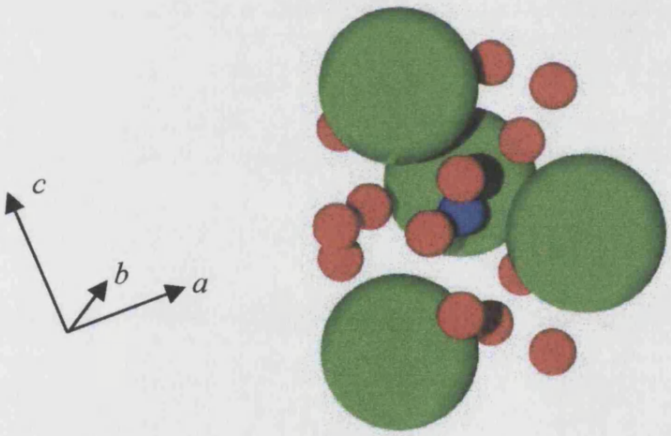

Figure 3.2.30 Arrangement of spheres used when calculating the free volume of the small sphere (shaded blue) in the BCC(AB_6) structure. The neighbours are shaded green (large) and red (small).

The arrangements of neighbours used for the BCC-6 arrangement are shown in figs. 3.2.29 and 3.2.30. In each case the tagged particle is shown in blue. The free volume may be determined by all the neighbours or by just a few depending on their size and proximity. The algorithm used to calculate the free volume allows for either situation.

3.3 Evaluation of Phase Behaviour

The properties of the binary superlattices, are on their own of limited interest. Rather, it is the phase behaviour of binary systems that is of most interest. In order to calculate this, the properties of the binary fluid phase must be obtained.

3.3.1 Binary Fluid Equation of State – MCSL

The equation of state of Mansoori, Carnahan, Starling and Leyland[60] (MCSL) has been tested against both Monte Carlo and molecular dynamics simulations[61] and found to be in good agreement. Although some alternatives are discussed in a later section (3.4), it is this equation of state that will be primarily used here in the evaluation of the phase behaviour. The pressure of the binary fluid is obtained using

$$\frac{p_f V_f}{(N_A+N_B)kT} = \frac{1+\phi_f+\phi_f^{\,2}-3\phi_f(y_1+\phi_f y_2)-\phi_f^{\,3}y_3}{(1-\phi_f)^3}, \qquad (3.3.1)$$

$$\text{where } y_1 = \frac{x_A x_B(\sigma_A-\sigma_B)^2(\sigma_A+\sigma_B)}{x_A\sigma_A^{\,3}+x_B\sigma_B^{\,3}},$$

$$y_2 = \frac{x_A x_B \sigma_A\sigma_B(\sigma_A-\sigma_B)^2(x_A\sigma_A^{\,2}+x_B\sigma_B^{\,2})}{(x_A\sigma_A^{\,3}+x_B\sigma_B^{\,3})^2} \qquad (3.3.2)$$

$$\text{and } y_3 = \frac{(x_A\sigma_A^{\,2}+x_B\sigma_B^{\,2})^3}{(x_A\sigma_A^{\,3}+x_B\sigma_B^{\,3})^2}.$$

Here V_f, ϕ_f and p_f are the volume, volume fraction and pressure of the binary fluid respectively. x_A and x_B are the mole fractions of the two species present.

The Helmholtz free energy for the fluid phase, A_f, may then be obtained by a straightforward integration as

$$p_f = -\left(\frac{\partial A_f}{\partial V_f}\right)_{T,N_A,N_B}, \quad (3.3.3)$$

$$\frac{A_f}{NkT} = -\int \frac{p_f}{NkT} dV_f + \frac{A_0}{NkT}. \quad (3.3.4)$$

But

$$dV_f \equiv -\frac{V_f}{\phi_f} d\phi_f, \quad (3.3.5)$$

$$\frac{A_f}{NkT} = \int \frac{p_f V_f}{NkT\phi_f} d\phi_f + \frac{A_0}{NkT}. \quad (3.3.6)$$

Standard manipulation leads to the expression,

$$\frac{A_f}{NkT} = (y_3 - 1)\ln(1-\phi_f) + \frac{2y_3 + 3y_2}{(1-\phi_f)} + \frac{3(1-y_1-y_2)-y_3}{2(1-\phi_f)^2} + \ln\phi_f + \frac{A_0}{NkT} \quad (3.3.7)$$

The integration constant, $\frac{A_0}{NkT}$, is obtained the low density limit, where the ideal free energy is approached.

$$\text{As } \phi_f \to 0, \ \frac{A_f}{NkT} \to \frac{A_{idf}}{NkT}. \quad (3.3.8)$$

With the standard state $\lambda_A = \lambda_B = \sigma_A$, used for the binary solid,

$$\frac{A_{idf}}{NkT} = x_A \ln(x_A\rho) + x_B \ln(x_B\rho) - 1, \quad (3.3.9)$$

where $\rho = \frac{N}{V_f}$. Then,

$$\phi_f \xrightarrow{\lim} 0, \frac{-A_o}{NkT} = \begin{bmatrix} (y_3 - 1)\ln(1-\phi_f) + \frac{2y_3 + 3y_2}{(1-\phi_f)} \\ + \frac{3(1-y_1-y_2) - y_3}{2(1-\phi_f)^2} + \ln\phi_f \\ - x_A \ln(x_A\rho) - x_B \ln(x_B\rho) + 1 \end{bmatrix}. \quad (3.3.10)$$

Evaluation of this expression leads to

$$\frac{A_0}{NkT} = \frac{3}{2}(y_1 - y_2 - y_3 - 1) + x_A \ln x_A + x_B \ln x_B \\ -1 - \ln\frac{\pi}{6} - \ln(x_A + x_B\sigma^3) \quad (3.3.11)$$

The final expression for the Helmholtz free energy is then

$$\frac{A_f}{NkT} = (y_3 - 1)\ln(1-\phi_f) + \frac{2y_3 + 3y_2}{(1-\phi_f)} + \frac{3(1-y_1-y_2) - y_3}{2(1-\phi_f)^2} \\ + \ln\rho + \frac{3}{2}(y_1 - y_2 - y_3 - 1) + x_A \ln x_A + x_B \ln x_B - 1 \quad (3.3.12)$$

The method detailed below for evaluating the phase behaviour does not directly require expressions for the chemical potentials of the individual species, but instead uses expressions for the Gibbs free energy per particle,

$$\frac{G_f}{NkT} = \frac{A_f}{NkT} + \frac{p_f V_f}{NkT}. \quad (3.3.13)$$

3.3.2 Common Tangent Construction

The three conditions that must be satisfied in order for fluid-solid equilibrium to be obtained are

$$\begin{aligned} p_s &= p_f \\ \mu_{Af} &= \frac{\partial G_f}{\partial N_A} = \frac{\partial G_s}{\partial N_A} = \mu_{As} \\ \mu_{Bf} &= \frac{\partial G_f}{\partial N_B} = \frac{\partial G_s}{\partial N_B} = \mu_{Bs} \end{aligned} \qquad (3.3.14)$$

As is demonstrated later in this section, these conditions may be satisfied "graphically" by plotting $\frac{G}{NkT}$ against x_A at constant pressure. In such a plot, the free energy of the fluid phase appears as a curve and that of the solid phases as points, as each solid has a constant mole fraction. Such a plot is shown in fig. 3.3.1, where in this example the diameter ratio under consideration is 0.39 and the dimensionless pressure, $\frac{p\sigma_A^3}{kT} = 150$.

Consider the diameter ratio of 0.39. Note first, that not every possible binary crystal has been considered. For instance, the CsCl structure is ignored, as at this diameter ratio it has a maximum packing fraction of only 0.5547, which is low when compared to the packing fractions obtainable by other structures. Table 3.3.1 shows the maximum packing fractions of various structures at a diameter ratio, $\sigma = 0.39$. All structures, with a maximum packing fraction greater than 0.65, were included in the calculations. The only exception being AB_{12} (the variant of the AB_{13} structure), as it was known that AB_{13} was unstable at diameter ratios in this region. The monodisperse FCC phases were always considered. In this way, the only structures that have been ignored to save calculation time are those with particularly low close packing

fractions and those known to be unstable. According to Murray and Saunders hypothesis, no structure with a close packing fraction below 0.745 should be stable. The results will prove that this is not the case.

Structure	Maximum packing fraction at diameter ratio, $\sigma = 0.39$	
NaCl/NiAs	0.784405	Considered
BCC (AB_6)	0.738893	Considered
AB_3	0.712193	Considered
AB_6	0.709955	Considered
AB_2	0.676328	Considered
AB_{12}	0.67419	Ignored
AB_{13}	0.673748	Considered
CaF_2	0.566625	Ignored
CsCl	0.554658	Ignored
$CaCu_5$	0.54098	Ignored
$MgCu_2$	0.380435	Ignored

Table 3.3.1 Structures chosen for consideration at diameter ratio, $\sigma = 0.39$

Secondly, note that the true value of $\frac{G}{NkT}$ ranges from 10 to 120. So, purely to ease visualisation, $\frac{G_{skew}}{NkT}$ is plotted, where

$$\frac{G_{skew}}{NkT} = \frac{G}{NkT} - \frac{G_A}{NkT} + x_A\left(\frac{G_A}{NkT} - \frac{G_B}{NkT}\right). \quad (3.3.15)$$

Here, $\frac{G_A}{NkT}$ and $\frac{G_B}{NkT}$ are the Gibbs free energies of the pure FCC phases of the large and small phases respectively. Consequently, the two pure FCC phases correspond to $\frac{G_{skew}}{NkT} = 0$. As this is a linear transformation, there is no effect upon the positions of any common tangents. This transformation is unnecessary in any computational calculations and was therefore not used in the algorithms written to determine the phase behaviour.

In the example shown (fig. 3.3.1), the points for the binary structures, AB_{13}, AB_2 and BCC(AB_6) lie above the fluid curve. Therefore, none of these crystals would exist under these conditions, as they remain thermodynamically unstable with respect to the corresponding fluid. The implication is that they have a higher free energy than the fluid with the same mole fraction and pressure. This is unsurprising in the case of AB_{13} and AB_2, as they do not have particularly high maximum packing fractions (ϕ_{cp} ~0.67 at this diameter ratio). The point for BCC(AB_6) lies above the curve even though BCC(AB_6) has a high maximum packing fraction (ϕ_{cp} ~0.739). AB_3, which has a lower maximum packing fraction (ϕ_{cp} ~0.712), lies below the fluid free energy curve. This demonstrates that crystal stability does not depend entirely upon the maximum packing fraction. The point for NaCl/NiAs lies well below the fluid curve,

as may be expected from the high maximum packing fraction seen in table 3.3.1. The free energies of these two structures are sufficiently close to be indistinguishable in fig. 3.3.1 (NiAs is more stable than NaCl by just 0.0007kT at these conditions).

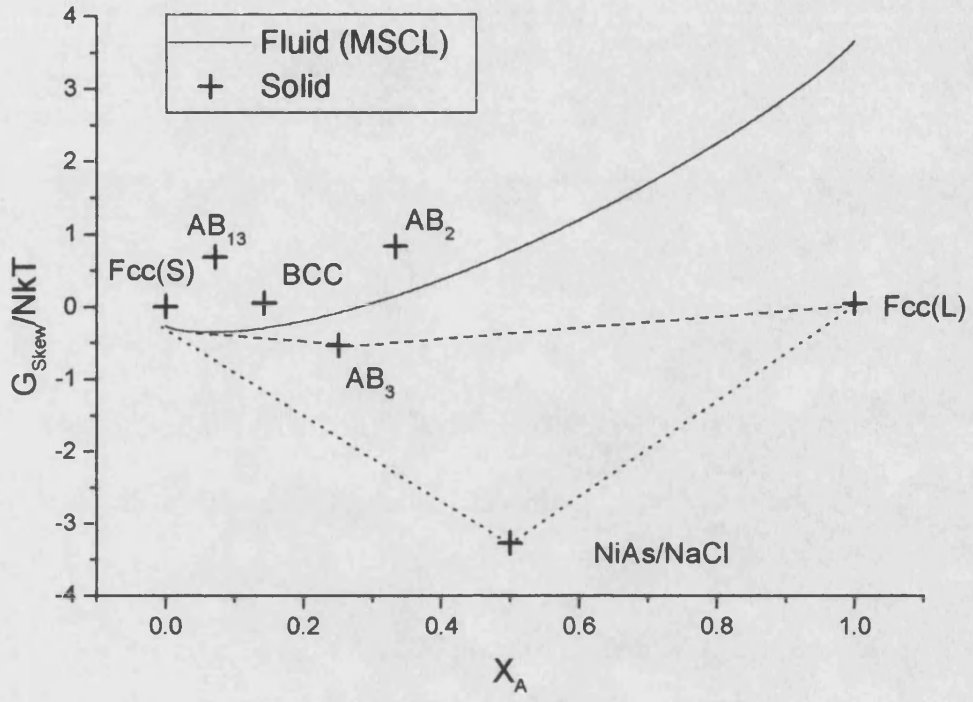

Figure 3.3.1 $\frac{G_{\text{skew}}}{NkT}$ vs. x_A for diameter ratio, $\sigma = 0.39$ and dimensionless pressure, $\frac{p\sigma_A^3}{kT} = 150$. The dotted line represent the lowest free energy path. The dashed line represent the lowest free energy path if NiAs/NaCl is ignored.

The Gibbs free energy for a binary fluid is given by,

$$\frac{G_f}{NkT} = x_A \frac{\mu_A}{kT} + (1 - x_A)\frac{\mu_B}{kT}. \quad (3.3.16)$$

The slope of the tangent to any point on the fluid curve may be determined using

$$\frac{d\left(\frac{G_f}{NkT}\right)}{dx_A} = \frac{\mu_A}{kT} - \frac{\mu_B}{kT}. \qquad (3.3.17)$$

The intercept of that tangent with the Y-axis then occurs at $\frac{\mu_B}{kT}$. The slope and intercept of the tangent to the curve at any point uniquely determine the chemical potentials of the two species at that point. If any two curves share a common tangent, then their chemical potentials must be equal. As the graph is plotted at constant pressure, all three necessary conditions are satisfied and equilibrium is established when this occurs.

In this representation the solid phases are shown as discrete free energy points rather than as curves. Since any deviation in the composition of the binary crystal leads to a steep increase in the free energy of that crystal, the solids are more accurately represented as steep parabolic curves with minima at the points plotted. Not having any information on the dependence of the free energy of the solid phases on composition, only the minima are shown, represented by points in fig. 3.3.1. Any line passing through such a point will form a tangent with the corresponding curve. Fluid-solid equilibrium is therefore established when any tangent to the fluid curve passes through a solid "point".

The positions of all fluid-solid equilibria are determined in this manner. Example phase equilibria and the corresponding tangent construction are shown in fig. 3.3.1. The behaviour of the fluid curve means that a common tangent is found for any free energy point beneath it. The existence of a common tangent, although necessary for two phases to co-exist, is not sufficient since a lower free energy equilibrium may exist with an alternative phase. The system will, of course, seek to minimise its free

energy for all mole fractions. The behaviour of the system at constant pressure and variable mole fraction is determined by the lowest "free energy path" from $x_A = 0$ to $x_A = 1$. This path consists of portions of the fluid curve, common tangents between the fluid and solid or in-between solid points.

The phase existing at $x_A = 0$ is determined solely by a comparison of the free energy of the fluid with composition $x_A = 0$ and the FCC phase of small spheres. In the example shown, the fluid phase has lower free energy and would be selected as the "initial" phase. Having determined the initial phase, the next step is to determine the lowest free energy equilibrium involving that phase. Of the possible fluid-solid equilibrium, the most favourable will be the first one, as tangents to the fluid always lie beneath the fluid curve and so will lead to the lowest free energy path. That is the NaCl/NiAs equilibrium in the example shown. The next step is to determine the solid-solid or solid-fluid equilibrium tangent with the most negative gradient. Only the equilibriums with increasing x_A are of interest. In the example, there is no further solid-fluid equilibrium and the only possible further equilibrium is with the pure FCC phase of large spheres. The "path" is therefore completed from $x_A = 0$ to $x_A = 1$.

In the example shown, the lowest "free energy path" commences with the fluid phase and moves onto the AB phase (either NaCl, NiAs or a hybrid, see section 5.1) before ending with the FCC phase of large spheres. This is shown in fig. 3.3.2 By varying the value of the constant pressure is it thus possible to construct a phase diagram in the pressure-mole fraction plane.

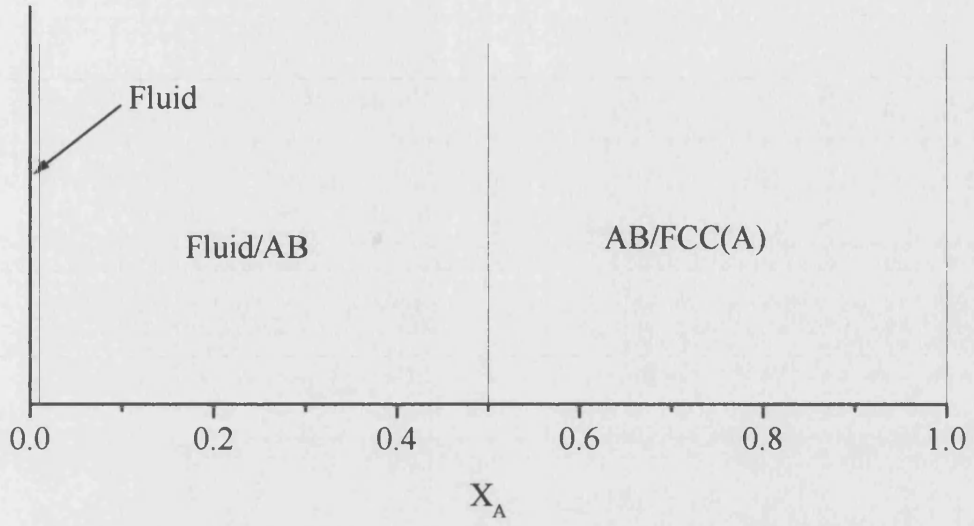

Figure 3.3.2 Phase behaviour at diameter ratio = 0.39 and dimensionless pressure, $\frac{P\sigma_A^3}{kT} = 150$.

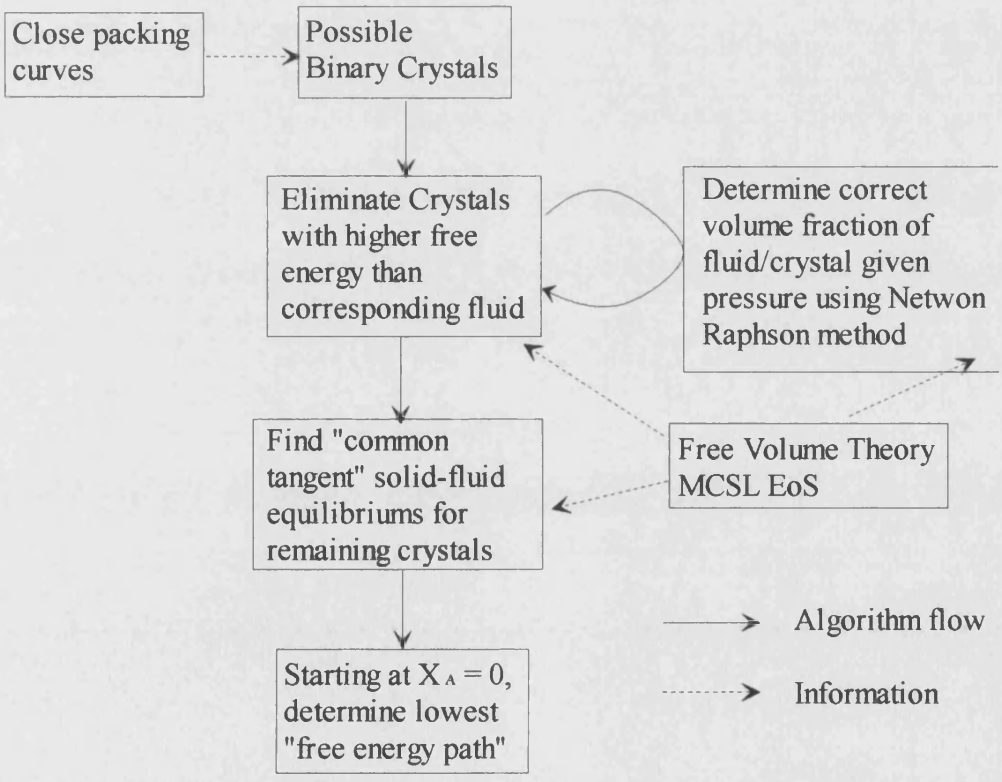

Figure 3.3.3 Flow diagram illustrating algorithm used to determine phase behaviour.

This whole process is illustrated in fig. 3.3.3

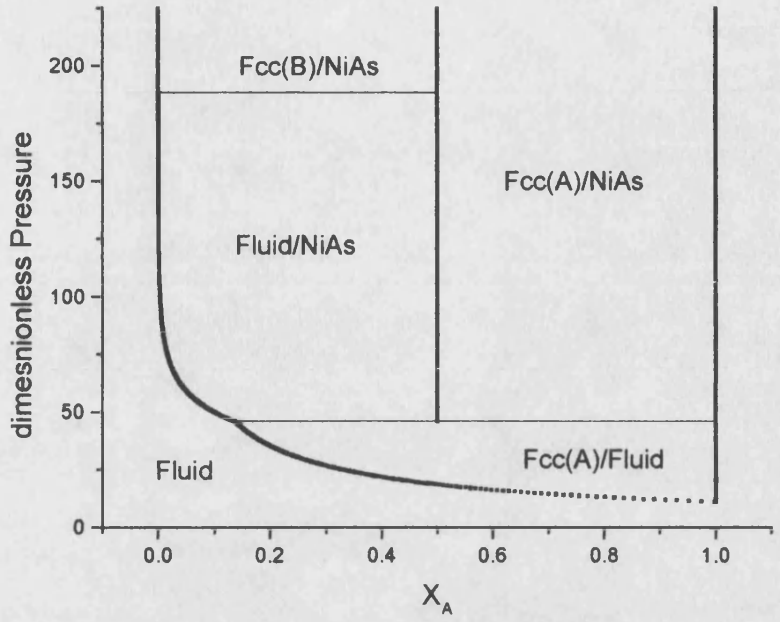

Figure 3.3.4 Phase behaviour for binary system with diameter ratio, $\sigma = 0.39$ in the pressure-mole fraction representation.

An example of a phase diagram constructed in this way is shown in fig. 3.3.4. The fluid phase appears as the section adjacent to the origin, bounded by a curve. The solid phases appear as vertical lines. Note that at dimensionless pressures below 188, the AB phase is in equilibrium with the fluid phase. At higher pressures, it is in equilibrium with the FCC phase of small spheres. The changeover occurs at 188.4 at which pressure all three phases are in equilibrium (AB, FCC(B) and fluid). On the phase diagram a horizontal line represents this triple "point".

When comparing these theoretical results to experiment, the phase diagram in the pressure-mole fraction plane is not immediately useful. Experimental results are more often presented in the volume fraction-volume fraction plane. It is easier to convert the theoretical phase diagram to that used by experimentalist than visa-versa. The corresponding phase diagram is shown in fig. 3.3.5.

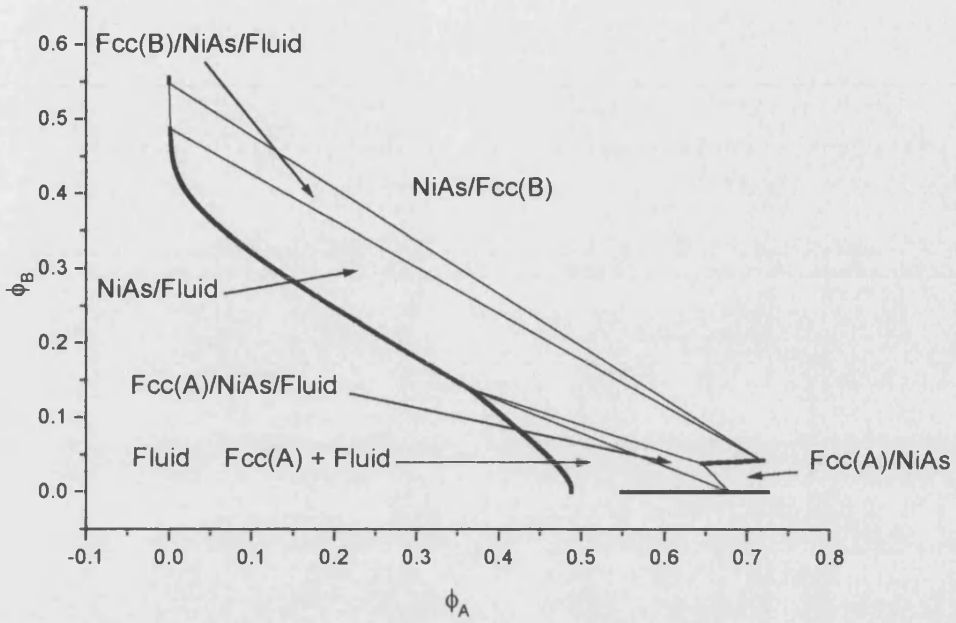

Figure 3.3.5 Phase behaviour for binary system with diameter ratio, $\sigma = 0.39$ in the volume fraction representation.

Again the section adjacent to the origin bounded by a curve represents the fluid. The lines radiating out from the origin represent the solid phases. Triple "points" are seen as triangles and correspond to the horizontal lines on the phase diagram in the pressure-mole fraction plane. The discussion of these results and others is reserved for section 5.2.

3.4 Equations of State for the Binary Hard Sphere Fluid

As mentioned in section 3.3.1, it is the MSCL equation of state that has been used to obtain the properties of the binary fluid. The accuracy of the calculated phase behaviour depends upon the accuracy of this equation of state as well as the cell model used to calculate the properties of the solid phases. In most cases the MSCL equation of state is sufficiently accurate over the range it is required. As will be shown the equation of state becomes less accurate at higher densities. But in most cases freezing occurs before these high densities are reached. A number of different equations of state have been proposed for the binary system of hard spheres[62-69]. In this section, just three alternatives to the MSCL equation of state are examined, in order to determine if there is any significant affect on the calculated phase behaviour.

3.4.1 The Rescaled Virial Expansion

For low densities, a virial expansion may be used to accurately represent the equation of state.

$$Z_{fv} = \sum_{n=1}^{\infty} B_n \rho^{n-1} = \sum_{n=1}^{\infty} b_n \phi_f^{\,n-1}, \text{ where (3.4.1)}$$

ϕ_f is the volume fraction of the fluid. The virial coefficient, B_n is dependent upon the composition of the binary mixture. b_n is the reduced virial coefficient and is related to B_n by

$$b_n = \frac{B_n}{\left(\frac{\pi}{6}\xi_3\right)^{n-1}}. \qquad (3.4.2)$$

ξ_k are the moment of the diameter distribution given by

$$\xi_k = x_1 + x_2\sigma^k \qquad (3.4.3)$$

The first three virial coefficients are known exactly.

$$\begin{aligned} b_1 &= 1 \\ b_2 &= 1 + 3\frac{\xi_1\xi_2}{\xi_3} \\ b_3 &= 1 + 6\frac{\xi_1\xi_2}{\xi_3} + 3\frac{\xi_2^3}{\xi_3^2} \end{aligned} \qquad (3.4.4)$$

The next two coefficients have been evaluated numerically by Saaji[64-65].

In region of density where freezing is expected to occur, the virial expansion is inaccurate. The form of the equation of state does not allow for any divergence as higher densities are reached. Coussaert and Baus[67] used a perturbation improvement of the MSCL equation of state in order to keep the divergent properties whilst taken the fourth and fifth virial coefficients into account. The form of the equation state became

$$Z_{fd} = Z_{mscl} + \xi_0^3\Delta\overline{B}_4 + \xi_0^4\Delta\overline{B}_5, \text{ where} \qquad (3.4.5)$$

$$\begin{aligned} \Delta\overline{B}_4 &= \overline{B}_4 - \overline{B}_{4mscl} \\ \Delta\overline{B}_5 &= \overline{B}_5 - \overline{B}_{5mscl} \\ \overline{B}_{4mscl} &= \overline{\xi}_0\overline{\xi}_3^3 + 9\overline{\xi}_1\overline{\xi}_2\overline{\xi}_3^2 + 8\overline{\xi}_2^3\overline{\xi}_3 \\ \overline{B}_{5mscl} &= \overline{\xi}_0\overline{\xi}_3^4 + 12\overline{\xi}_1\overline{\xi}_2\overline{\xi}_3^3 + 15\overline{\xi}_2^3\overline{\xi}_3^2 \end{aligned} \qquad (3.4.6)$$

In later studies, Coussaert and Baus[68] used a rescaled virial expansion, rather than the perturbed MSCL equation of state. This is given by

$$Z_{frs} = \frac{\sum_{n=1}^{\infty} c_n \phi_f^{n-1}}{(1-\phi_f)^3}, \text{ where} \qquad (3.4.7)$$

$$c_n = b_n - 3b_{n-1} + 3b_{n-2} - b_{n-3}. \qquad (3.4.8)$$

When $n < 1$, $b_n = 0$. The form of this equation of state means that Z_{frs} will diverge as $\phi_f \to 1$.

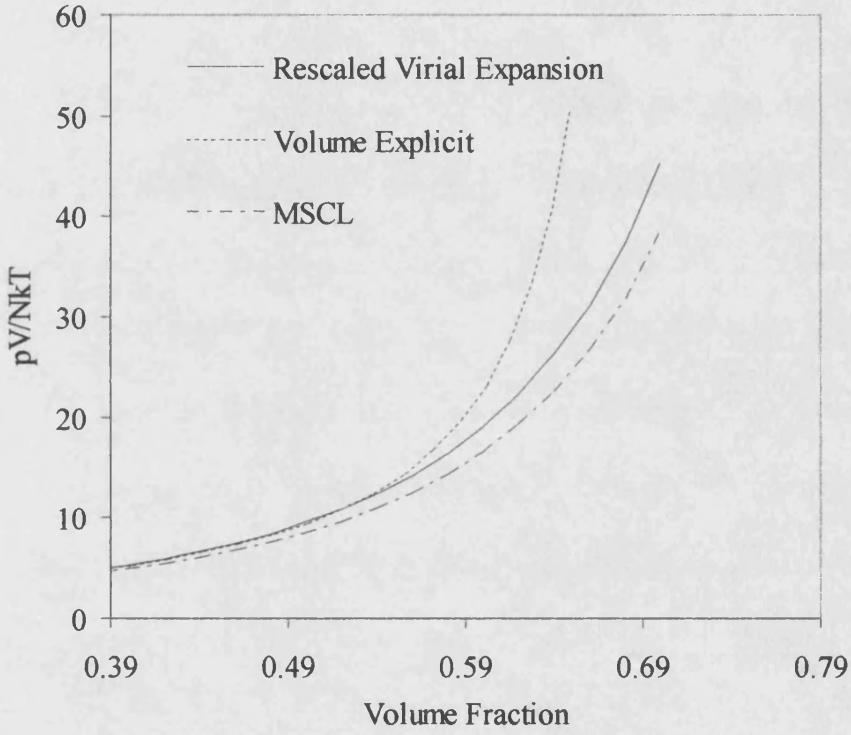

Figure 3.4.1 A comparison of the alternative binary hard sphere fluid, equations of state, at a diameter ratio, and a mole fraction of larger spheres, $X_A = 0.4$. See section 3.4.2 for explanation of the volume explicit equation of state.

As may be seen from fig. 3.4.1 the rescaled virial equation of state does not differ greatly from the MSCL equation of state. Consequently the position of phase boundaries are not greatly effected when either of these alternatives are used.

This is borne out in fig. 3.4.2 when the phase diagram for diameter ratio 0.36 is shown. Even the postion of the metastable AB_6 phase is not greatly effected (compare to fig. 5.2.5). This phase is only marginally stable relative to the binary fluid, so would be expected to be most sensitive to any change.

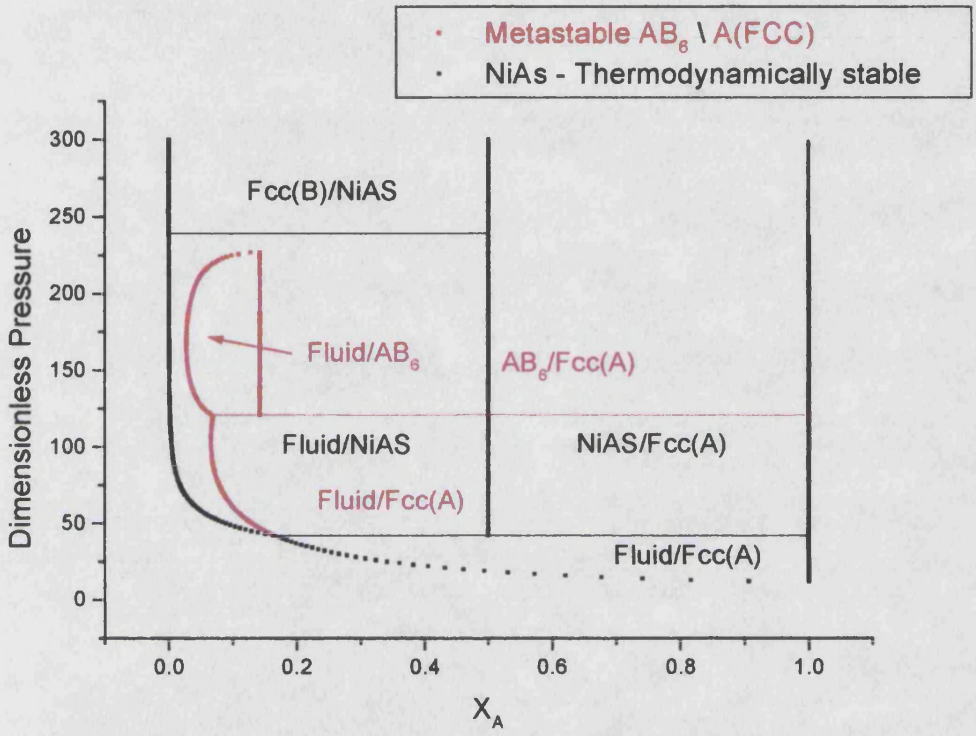

Figure 3.4.2 Phase diagram, diameter ratio, $\sigma = 0.36$. The Rescaled virial expansion equation of state[69] has been used to describe the binary fluid of hard spheres.

One change that the introduction of the alternative equations of state brings, is to the behaviour of the binary fluid. Analysis of the binary fluid shows that there is a demixing transition present under certain conditions. It was only when the fourth and fifth virial coefficient were calculated that this transition came to notice. However these transitions occur at very high pressures and are thus Metastable relative to the freezing transition. It was initially thought that these transitions occurred at much

lower pressures[67], but an error was found in the fifth virial coefficients used for these calculations[66].

Of more significance to these studies is the behaviour of the binary fluid at high densities. All the equations of state specified so far do not diverge until a volume fraction of unity is reached. In contrast the equations of state of all the solid phases diverge at their close packing fractions. The failure of the fluid equation of state to diverge at a lower volume fraction leads to some unreasonable phase behaviour being calculated. For instance, the phase behaviour of a binary system with diameter ratio 0.36 is calculated, where it is assumed that the AB phase is kinectically hindered. The fluid is calculated as being the most thermodynamically stable phase at volume fractions above 0.7. For a monodisperse fluid random close packing occurs at 0.63. Even allowing for the fact that a binary system can be expected to have a higher random close packing value, it is unreasonable to expect the fluid to still be stable at 0.7 or above.

3.4.2 The Volume Explicit Equation of State

The volume explicit equation of state of Hamed[69] addresses this problem. This equation of state, unlike those preceding, is based on a pressure expansion, rather than a density expansion.

The final form of the equation of state is given by

$$Z_{fve} = 1 + d_2\psi + \frac{3}{4} f\psi \ln\left(\frac{3+h\psi}{3+25h\psi}\right), \text{ where} \quad (3.4.9)$$

$$\psi = \frac{P_f}{kT}\frac{\pi}{6}$$
$$h = \frac{1}{4}(5\bar{\xi}_1\bar{\xi}_2 - \bar{\xi}_3)$$
$$f = 2\frac{\bar{\xi}_2^2(3\bar{\xi}_1^2 - \bar{\xi}_2)}{5\bar{\xi}_1\bar{\xi}_2 - \bar{\xi}_3} \quad , \quad (3.4.10)$$
$$d_2 = 3\bar{\xi}_1\bar{\xi}_2 + \bar{\xi}_3$$

Although this equation of state does diverge at volume fractions lower than unity and was compared favourably to some simulation data of Alder[70], this alone is not a proof of its accuracy. It is possible to calculate the volume fraction at which the equation will diverge for a given diameter ratio and mixture composition. As can be seen from fig. 3.4.5 even this equation of state predicts the stability of binary fluids at high volume fractions (>0.7).

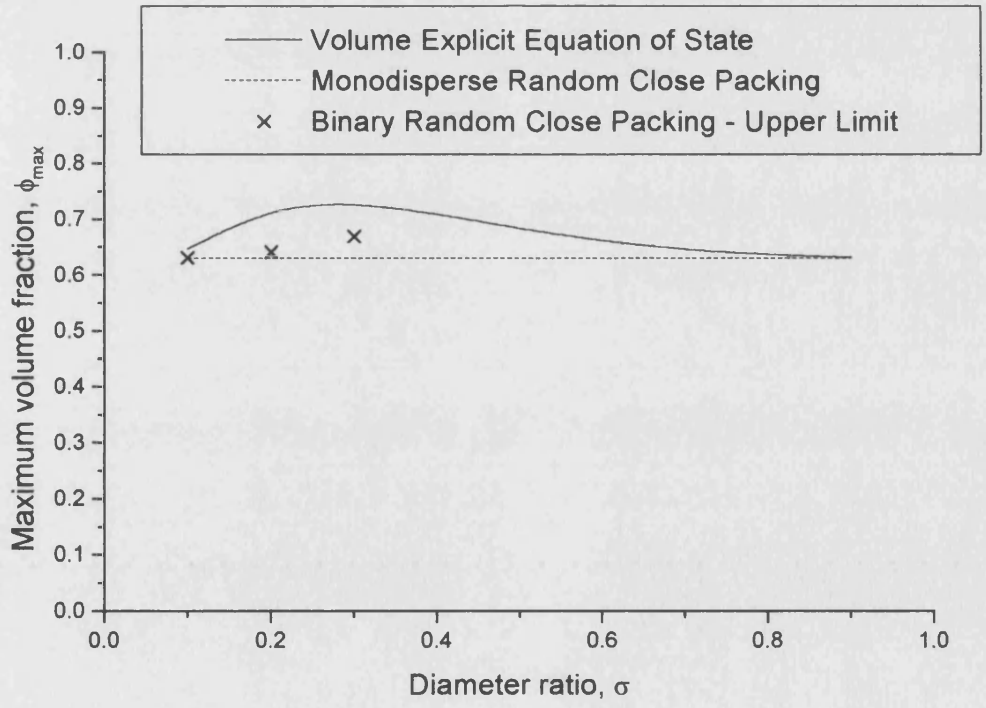

Figure 3.4.5 The volume fraction at which equation of state will diverge plotted against diameter ratio. The mole fraction of the larger spheres is 0.3. The upper limit

for binary random close packing is calculated by assuming that the small spheres randomly close pack in the void left by the randomly close packed large spheres. This crude model provides an upper limit to binary random close packing.

Changing the equation of state naturally brings about a change in the form of the curve in the constant pressure, Gibbs free energy vs. mole fraction plot (fig. 3.4.6). At diameter ratio 0.36, the effect of this is exclude the metastable AB_6 phase and to enlargen the size of the monodisperse FCC regions (fig. 3.4.7).

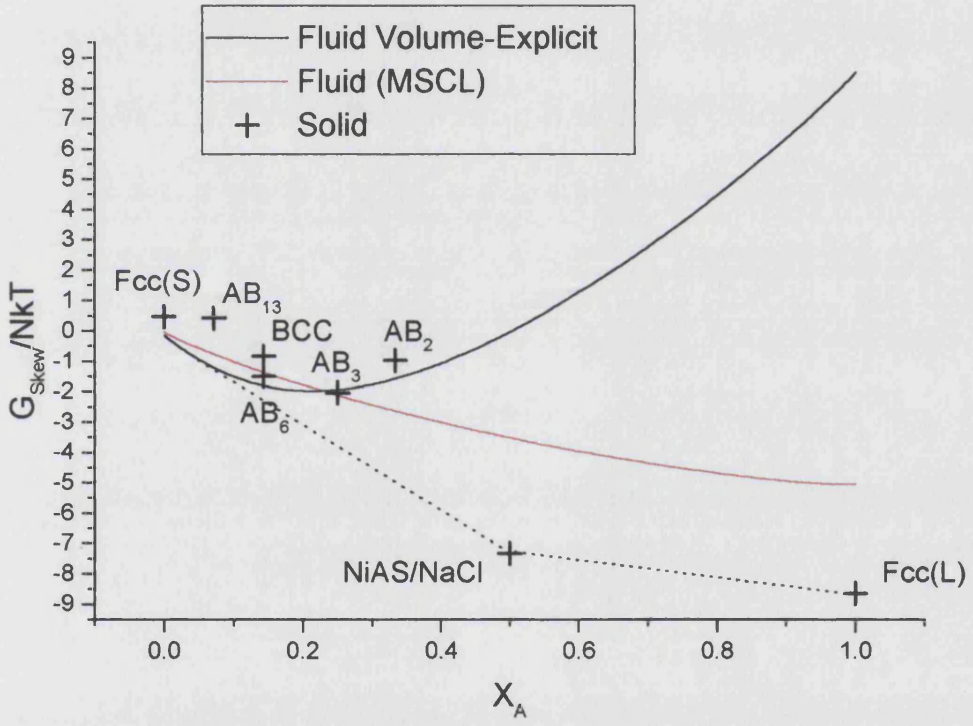

Figure 3.4.6 $\frac{G_{skew}}{NkT}$ vs. x_A for diameter ratio, $\sigma = 0.36$ and dimensionless pressure, $\frac{p\sigma_A^{\,3}}{kT} = 150$ (see section 3.3.2). The binary fluid is described by the volume explicit equation of state. The dotted line represents the lowest free energy path.

Although there may be some certainty as to the accuracy of the various binary fluid equations of state at high density. The accuracy of the MSCL equation of state at lower densities is not in question. Therefore the qualitative predictions made about the thermodynamic phase behaviour are not in doubt. It is the metastable phase behaviour which is effected by these differences.

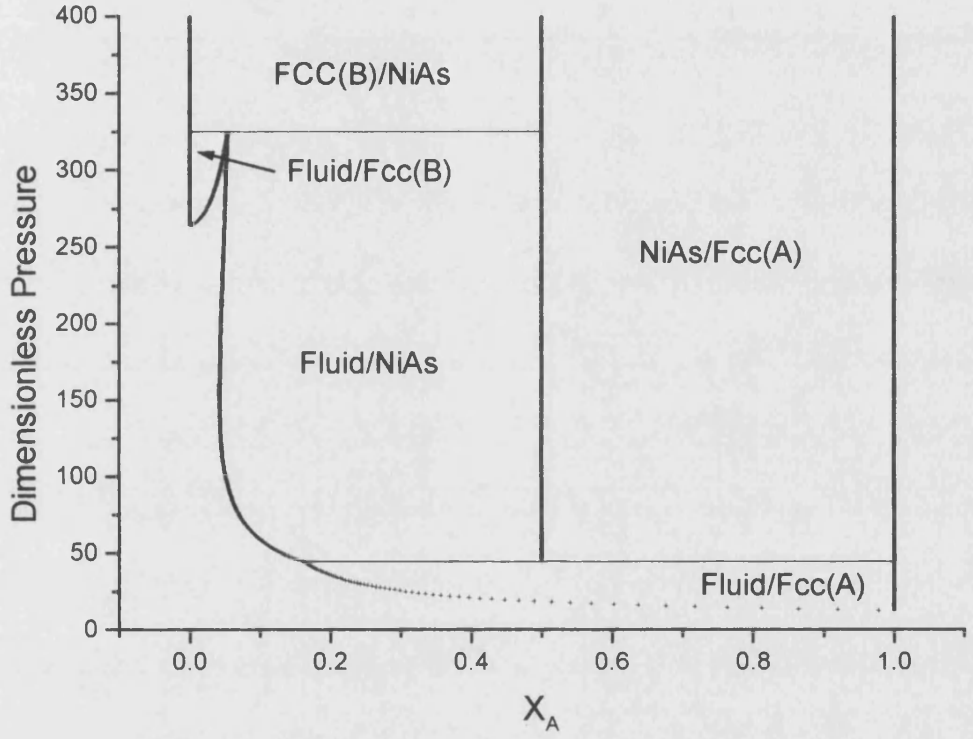

Figure 3.4.7 Phase diagram at diameter ratio 0.36. The volume explicit equation of state was used to describe the fluid. Note, there is no metastable AB_6 phase.

Chapter 4 The Calculation of Free Volume in a Binary System

In the case of the hard sphere system, the free volume is a shape that may be formed by constructive solid geometry. This volume may be calculated using methods that could be applied to any other shape, regardless of its final purpose. In this case the volume was calculated by a trapezium rule integration. The algorithms used to calculate the free volume are detailed in the following pages.

4.1 Geometrical Constraints

Recall that the free volume is that volume in which the centre of the tagged particle is free to wander about in (section 1.2). As no two particles may overlap, then the closest distance which the centres of two particles may approach is given by the sum of their radii. Consider a neighbour to the tagged particle. The centre of the tagged particle is excluded from a sphere, with the same centre as that neighbour and radii equal to the minimum approach distance. The diameter of this exclusion sphere being the sum of the tagged particle diameter and that of its neighbour. For each of the neighbours there is an equivalent exclusion sphere. The free volume is then that volume left at the centre of the arrangement of exclusion spheres (fig. 4.1).

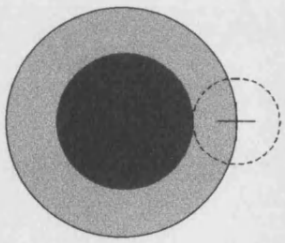

Figure 4.1 The centre of the tagged particle (cross) is excluded from a sphere (grey) that has radius equal to the sum of the radii of the tagged particle and the neighbour (black)

As the tagged particle is confined to its own cell, there is a set of planes beyond which the centre of the tagged particle may not pass. It is these planes, which together form a Voronoi Polyhedron, and the exclusion spheres that determine the geometry and extent of the free volume.

4.2 Determination of the Boundaries

There is no simple way to calculate each free volume analytically. It is necessary to determine the free volume numerically. Whether the Monte Carlo method (section 4.3) or trapezium rule method is used (section 4.4) , the extreme limits of the free volume must be estimated. It is important to obtain a good idea of the magnitude of the free volume as underestimation as well as overestimation may lead to errors in the numerical procedures used (fig. 4.2).

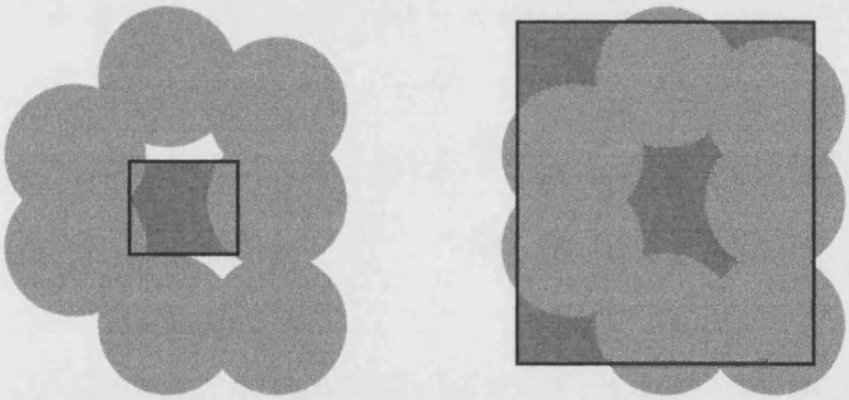

Figure 4.2 The correct choice of a boundary (black box) when determining the free volume avoids errors from either underestimation or overestimation (hatched areas).

As there are a large number of possible arrangements and neighbour diameters a general algorithm is needed to determine these limits.

The algorithm, "GAP" was designed for this task. The principal is that the tagged particle "walks" in a straight line towards the position that is the mean of the centres of groups of three or four particles (fig. 4.3). Any "gaps" in the cage of exclusion spheres are most likely to be found in this direction, as are the vertices. Periodically the tagged particle "wanders" off in a random direction to explore another section of the free volume. All walks are terminated when the tagged particle attempts to overlap with a neighbour or go beyond the bounds imposed by the Voronoi polyhedron. The furthest directions along the X,Y and Z axes in which the tagged particle was able to venture are then recorded. The limits thus obtained are expanded slightly and used in the determination of the free volume.

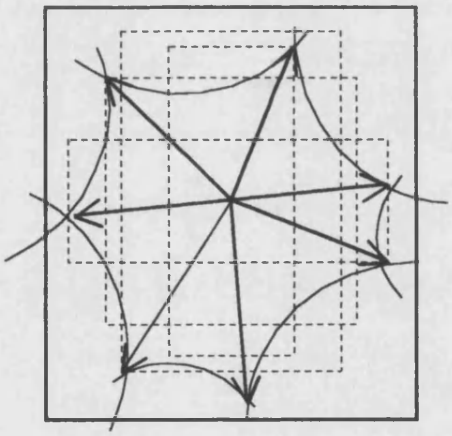

Figure 4.3 Boundary determination, the limits are set by the GAP algorithm, which searches for the extent of the free volume.

4.3 Calculations Using a Monte Carlo Algorithm

This simple method was used as a check on the more sophisticated (and potentially more error prone) method discussed in section 4.4.

The tagged particle is placed at a random point within a box with predetermined limits allocated by GAP (fig. 4.4). The distance from this point to each of the centres of the neighbours is then calculated. If the tagged particle has been placed at a "legitimate" site then firstly, the calculated distance must be greater than the radius of the associated exclusion sphere. Secondly the distance must also exceed that to the tagged particle's lattice site, the origin. This ensures that any overlap is avoided as well as confining the tagged particle to its Voronoi polyhedron. The successful "hits" and attempts are enumerated. The determined free volume, v_{fmc} ,is then given by

$$v_{fmc} = v_b \frac{n_h}{n}, \quad (4.1)$$

where v_b is the volume of the box, n_h is the number of successful hits and n the number of attempts.

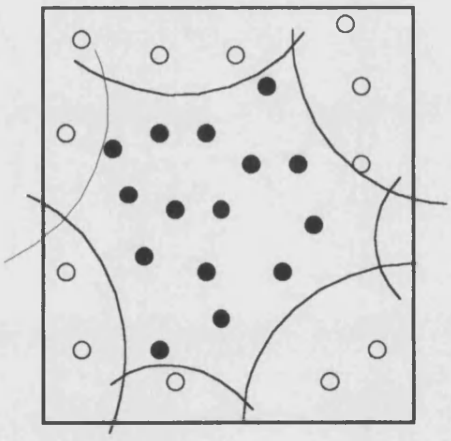

Figure 4.4 The Monte Carlo algorithm works by randomly selecting points within the boundaries to determine if they are part of the free volume.

If the true free volume is v_f then the probability of a "hit" is given by

$$p_h = \frac{v_f}{v_b}. \qquad (4.2)$$

Therefore n_h varies according to a binomial distribution. The standard deviation of n_h is the standard result

$$SD(n_h) = \sqrt{np_h(1-p_h)}. \qquad (4.3)$$

From this the standard deviation of the calculated free volume is obtained,

$$SD(v_{fmc}) = \frac{\sqrt{v_f(v_b - v_f)}}{\sqrt{n}}. \qquad (4.4)$$

The standard deviation of the calculated free volume, an indicator of the uncertainty of the result, is inversely proportional to $\sqrt{n}$. This means that a very large number of samples is needed to reduce the uncertainty of the result. This method is not particularly accurate when the number of samples is restricted by limited computing power. An error of 0.06% (relative to an analytical expression[40]) was recorded in a result that took one minute to compute using the Monte Carlo algorithm on a 486, 66Mhz PC. In comparison, using the following algorithm the error was only 0.01% and the calculation took just 0.06 seconds.

4.4 Calculation Using the Trapezium Algorithm

In this method the free volume is split into many sections according to a grid in the XY plane. The sections are made to be narrow enough that they approximate cuboids. The volume of each cuboid may then be calculated by determining the height of that cuboid along the Z-axis. This is illustrated in fig. 4.5. In practice the cuboids are far narrower, so that the error associated with this method is greatly reduced. The total

number of cuboids used in each calculation was 1,000,000, corresponding to the division of the X and Y-axes into 1000 parts each.

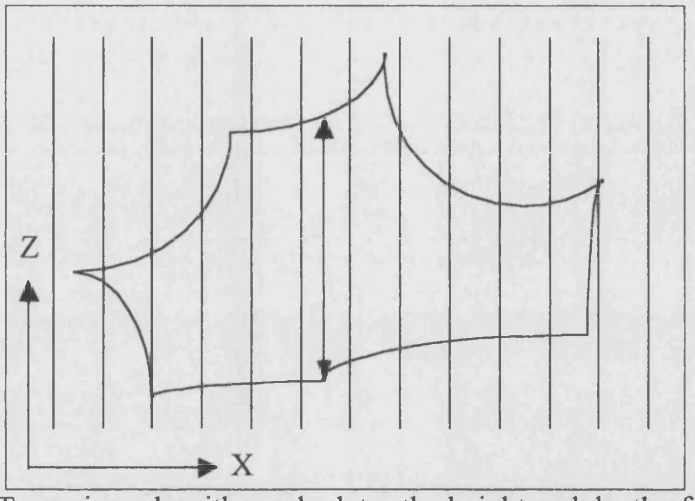

Figure 4.5 The Trapezium algorithm calculates the height and depth of the free volume across a grid.

The restriction of the tagged particle to a Voronoi polyhedron determines the initial height and depth of the cuboids under consideration. Each exclusion sphere is examined to see if it overlaps with the cuboid under consideration. If so, then an exclusion section is generated. The exclusion sections are then compared with each other and any duplication or overlap is eliminated to attain the minimum number of exclusion sections. Some exclusion sections lie partially outside the cuboid, in which case the height or depth of the cuboid is reduced such that the section is completely outside so that it may be ignored. The volume of the cuboid minus the sum of the exclusion sections is then calculated.

If the correct boundaries have been chosen then the sum of the volumes of the cuboids at the edge of the box will be zero. For this reason, as well as summing the volumes of all cuboids to determine the overall free volume, the sum of the volumes of cuboids at

the edge of the box is determined. If this latter sum is greater than zero then the calculation is redone with increased boundaries.

In the majority of cases the algorithm worked without any cause for further investigation, although there were a few exceptions. Problems occured at small diameter ratios when the shape of the free volume becomes significantly concave. In these cases the free volume may well be split into two parts joined by a narrow neck. Both parts are within the Voronoi polyhedron and may thus be considered as part of the free volume. However as the density increases, the neck may be broken, leaving two distinct parts of the free volume. Strictly speaking only the part that contains the lattice site of the tagged particle should be considered. Determining the boundary so as to only include this part involves some extra intervention. However, this generates a discontinuity in the free volume of the tagged particle in that particular arrangement. This is not to be mistaken for a phase transition of any sort. It is a product of the fixed neighbour cell model. The fitting functions used ensure that this data was smoothed out to avoid spurious results.

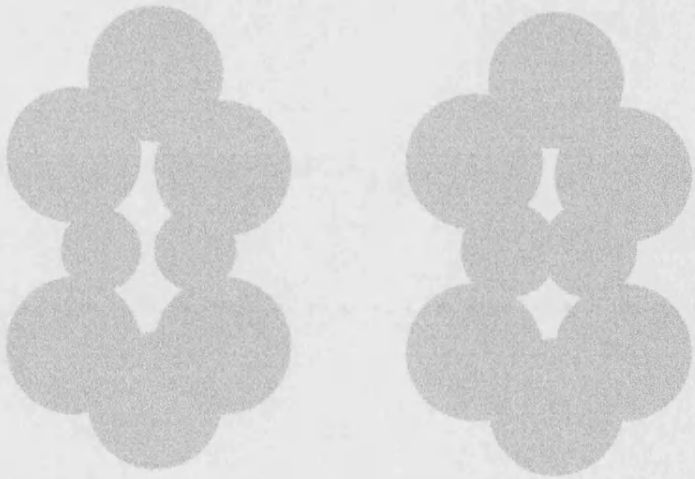

Figure 4.6 Given certain arrangements of neighbours, it is possible that the free volume is broken in two disconnected parts at high densities.

Chapter 5 Results for Binary Systems

5.1 Primary Results

The purpose of this section is to demonstrate how useful thermodynamic information is obtained from the initial free volume calculations. Results are compared to those obtained by molecular dynamics; a comparison is made between the NaCl and NiAS structures and the AB_6 structure is examined.

5.1.1 AB_2, A Comparison with Results from Molecular Dynamics

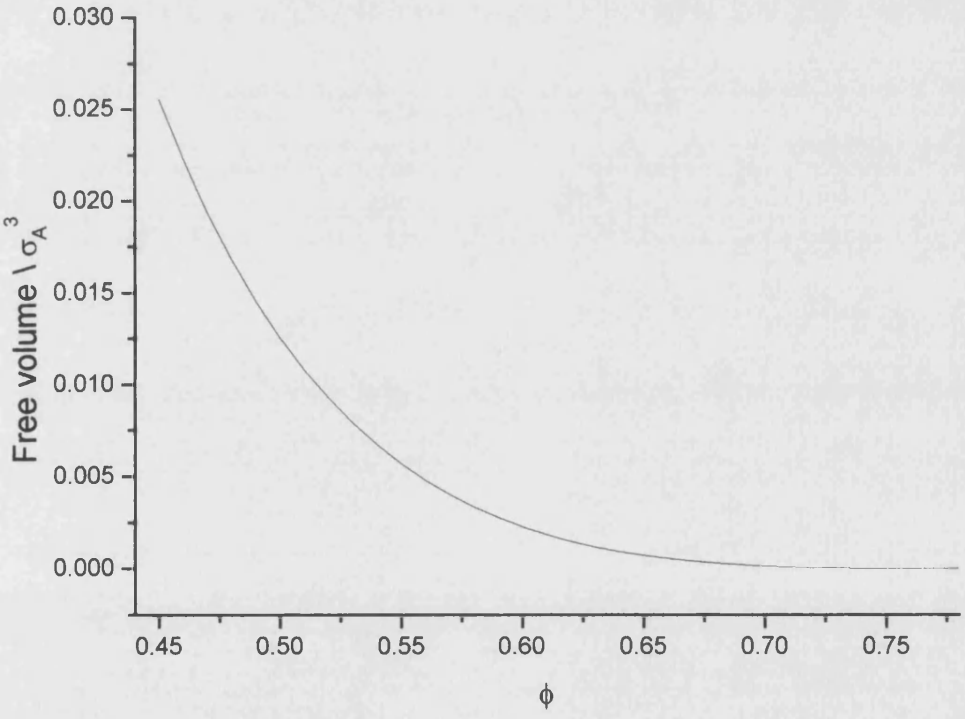

Figure 5.1.1 Free volume of the large spheres (A) in the AB_2 structure at a diameter ratio, $\sigma = 0.56$, vs. volume fraction, ϕ.

Calculations were performed on a Pentium II, 266 MHz running Windows NT Workstation™. For each structure and diameter ratio of interest, the free volume for

all distinct particles was calculated at volume fraction intervals of 0.0025. The lowest value of the volume fraction at which the calculation was run was 0.45, the highest value was determined by the close packing limit. All free volumes were measured in units of σ_A^3 (diameter of larger sphere cubed) and written out to disk. Results were saved in both "formatted" text and "unformatted" double precision (64bit) files. Double precision stores numbers precise to 14 or 15 significant places, which amply covers the accuracy of the original results.

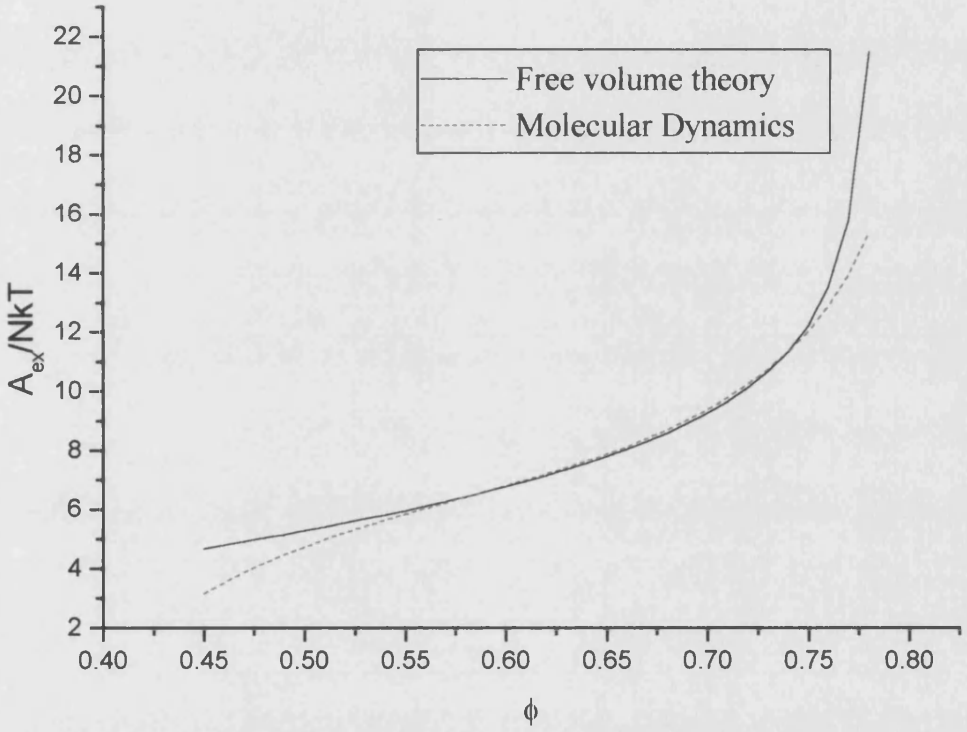

Figure 5.1.2 Excess Helmholtz free energy against volume fraction for AB_2 at a diameter ratio, $\sigma = 0.56$. The results calculated using free volume theory are compared to those from molecular dynamics[54].

The calculated free volume for the large spheres in AB_2 at diameter ratio 0.56 is shown in fig. 5.1.1. The free volume approaches zero near the close packing fraction,

which for a diameter ratio of 0.56, in AB_2, is at 0.779. The Helmholtz free energy may then be directly calculated from the free volume. As the free volume approaches zero, the Helmholtz free energy, which is dependent upon the logarithm of the free volume, approaches infinity.

In fig. 5.1.2 the excess Helmoltz free energy for AB_2 at a diameter ratio of 0.56 is plotted against the volume fraction, ϕ. The free volume theory results are compared to those obtained from molecular dynamics[54]. Agreement is very good, especially in the range where AB_2 may be expected to form, $0.55 \leq \phi \leq 0.70$. These results illustrate the accuracy of the simple free volume theory.

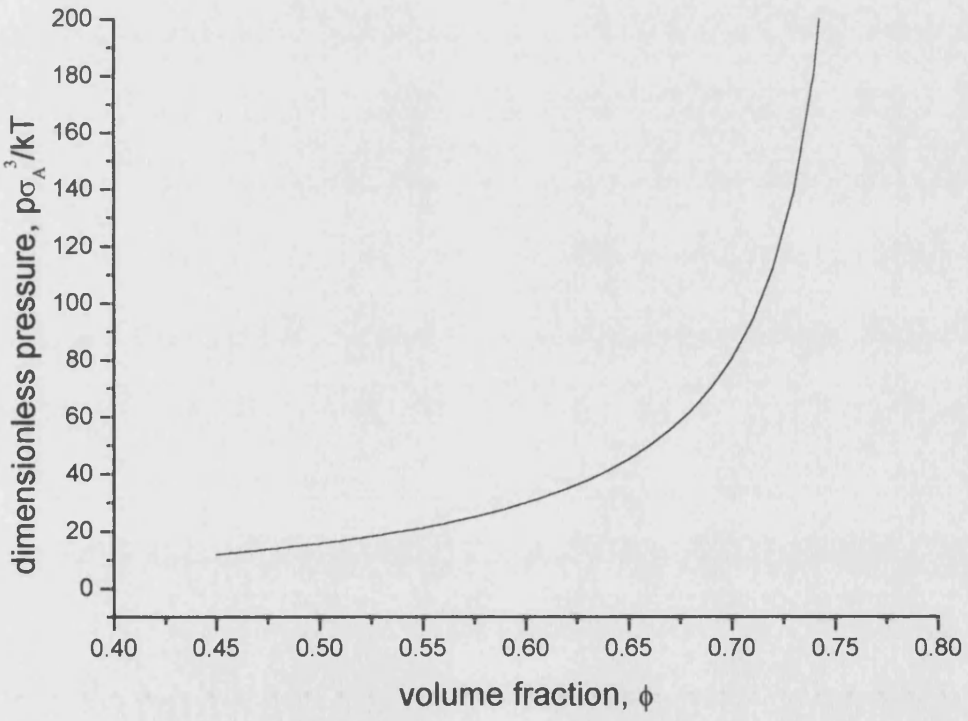

Figure 5.1.3 Dimensionless pressure of AB_2 vs. volume fraction at a diameter ratio, $\sigma = 0.56$.

The pressure was obtained by numerical differentiation after fitting the free volume to a cubic spline. The pressure was then obtained by differentiation of the fitted function. To avoid any erroneous results from function fitting the calculations were commenced at low volume fractions. Pressure is given in the dimensionless units, $\frac{p\sigma_A^3}{kT}$.

5.1.2 AB_{13}, A Comparison with Results from Molecular Dynamics

The second structure, for which molecular dynamical calculations have been performed is AB_{13}[55]. Here the diameter ratio used was 0.558. As is clear from fig. 5.1.4 the comparison between the results from the two different methods is very favourable. The comparison is, also near quantitative at a diameter ratio of 0.58.

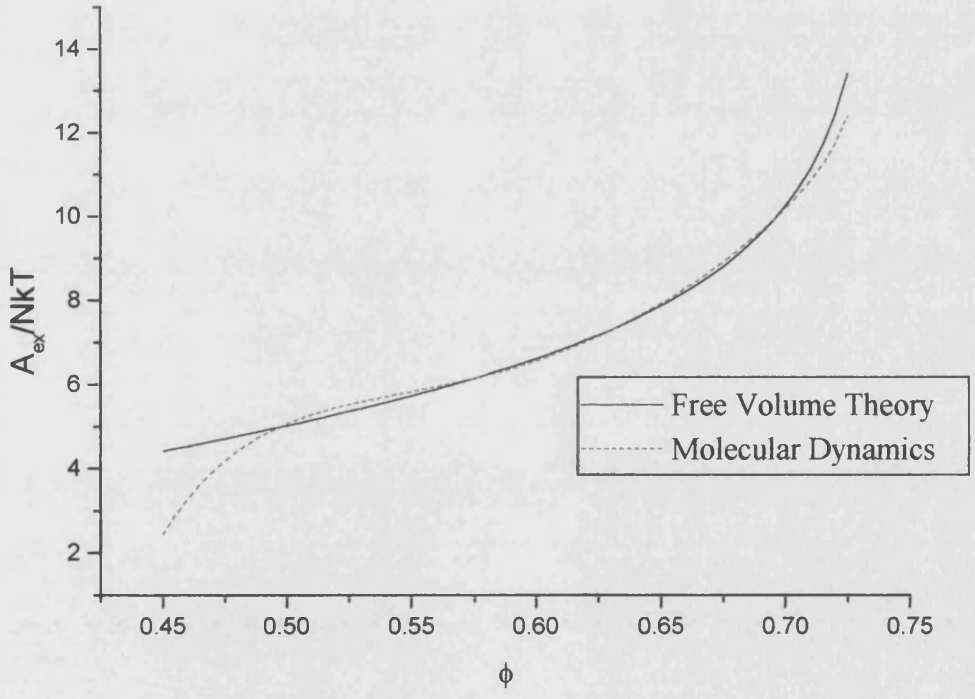

Figure 5.1.4 Excess Helmholtz free energy against volume fraction for AB_{13} at a diameter ratio, $\sigma = 0.558$. The results calculated using free volume theory are compared to those from molecular dynamics[55].

5.1.3 A Comparison of the NaCl and NiAs Structures.

In both NaCl and NiAs, the large spheres are arranged in hexagonally close packed layers, with small spheres occupying the octahedral vacancies (the interstitial gaps in the FCC or HCP crystal that are surrounded by six spheres). The differences between the two structures lie in the orientation of the close packed layers. In NaCl, the large spheres adopt the FCC structure, whilst in NiAs the large spheres are in the HCP arrangement (section 1.3).

Considering the debate over the relative stabilities of the one component FCC and HCP structures, as discussed in section 1.3, it is interesting to compare the stabilities of the binary analogues. Note that the free volume theory can find no difference between the monodisperse FCC and HCP crystals.

In the free volume model any difference between the two structures depends upon the difference between the cells occupied by the large spheres, as small spheres occupy identical octahedral vacancies in both cases. In the NaCl structure the large spheres are surrounded by an octahedral arrangement of small spheres (fig. 5.1.5.A). Whereas in the NiAs structure the arrangement is that of a trigonal prism (fig. 5.1.5.B). The corresponding arrangements of exclusion spheres are shown in figs. 5.1.5.C and 5.1.5.D respectively. The distance of the exclusion spheres from the centre of the free volume is identical at every diameter ratio and volume fraction. However, the trigonal prism arrangement leads to a greater overlap of exclusion spheres. The more exclusion spheres overlap with each other, the more the total amount of excluded volume decreases and hence the larger the free volume. This results in the free volume being marginally greater in the NiAs structure.

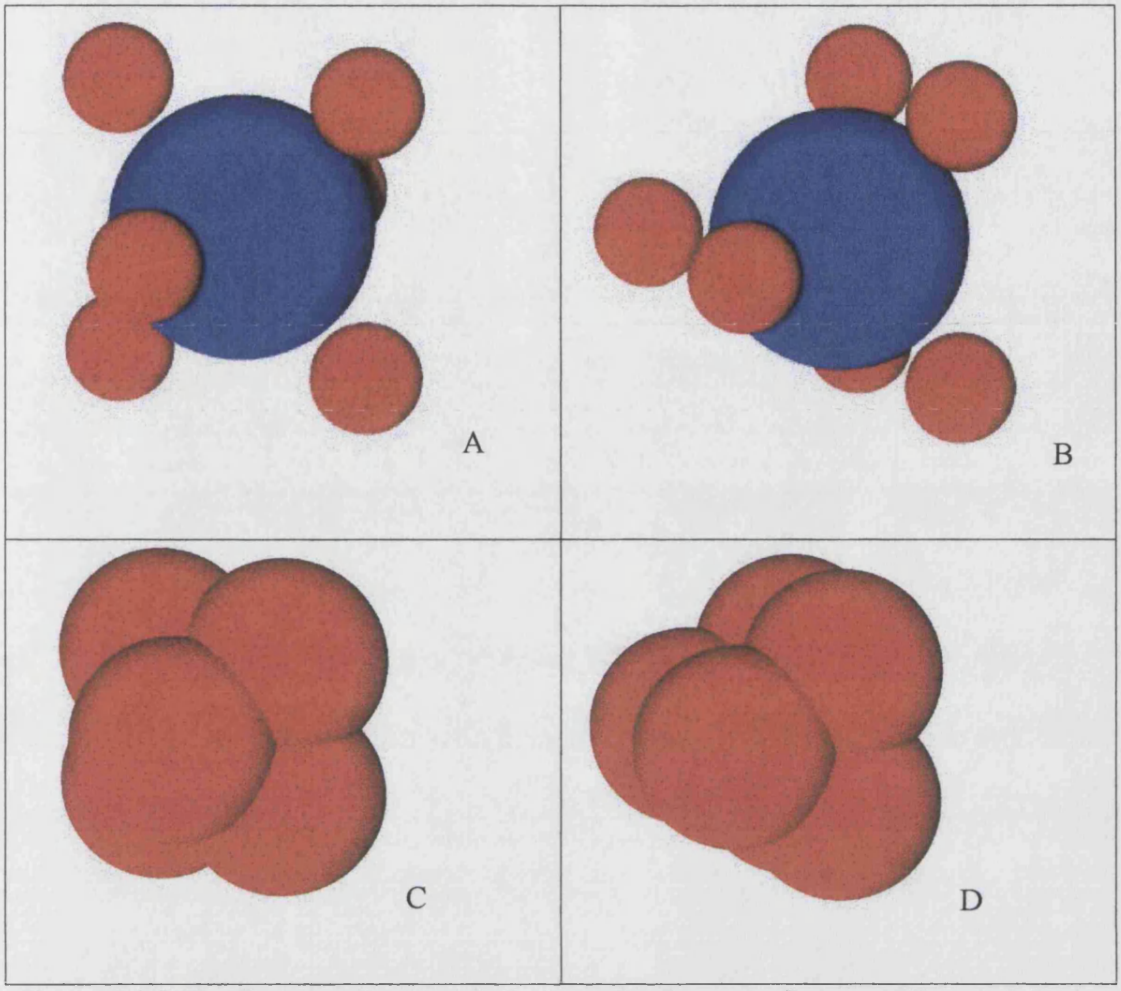

Figure 5.1.5 The first coordination shell of small spheres (red) surrounding each large sphere (blue) in the NaCl (A) and NiAs (B) structures. At a diameter ratio, $\sigma = 0.42$ and a volume fraction, $\phi = 0.685$ which is close to freezing. The corresponding arrangement of exclusion spheres for NaCl (C) and NiAs (D) are also shown.

In fig. 5.1.6 the free energy difference between the two structures is plotted against volume fraction. For comparison, the free energy difference between the monodisperse HCP and FCC structures is also shown. The entropic advantage gained by NiAs is indeed small, being of the order 0.038 kT at the volume fraction that NaCl or NiAs is first observed, 0.695. This is about seven times greater than the difference found by Woodcock[41] and over forty times that found by Bolhuis[42] for the

monodisperse case and is in the opposite direction. i.e. it is the structure where the large spheres are in the HCP arrangement that is more stable.

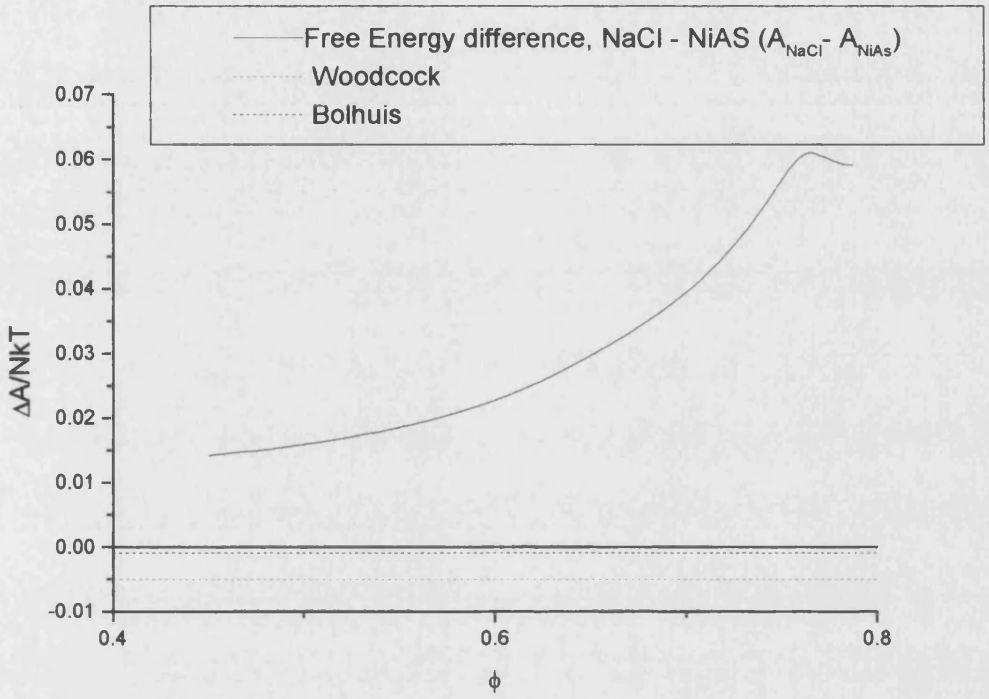

Figure 5.1.6 Difference in free energies of NaCl and NiAs as a function of volume fraction. The results are compared with the difference in free energy found in the monodisperse FCC and HCP structures by Woodcock and Bolhuis (in both cases FCC was found to have a lower free energy).

5.1.4 Stability

Having obtained the thermodynamic data, it is possible to predict whether or not a structure would be stable relative to the fluid phase, at a given volume fraction and diameter ratio. Of course this is not a prediction that this structure would be globally stable, as other solid phases may be more favoured. The Helmholtz free energy is plotted against volume fraction in fig. 5.1.7 for NiAs at a diameter ratio of 0.36. On the same graph the Helmholtz free energy for the corresponding fluid is plotted (The

MSCL equation of state was used for the binary fluid, section 3.3). i.e. the fluid with the same diameter ratio and mole fractions (in this case the mole fraction of both species is 0.5). Wherever the free energy of the fluid is lower than that of the solid, the solid cannot be stable. Whereas if the solid has a lower free energy, the solid may exist. Figure 5.1.7 predicts that in binary systems with a diameter ratio of 0.36, NiAs can only occur at volume fractions of 0.6 or above. In order to ascertain whether or not this is the case, the complete phase behaviour of a binary mixture, with this diameter ratio must be determined. This is covered in section 3.3.

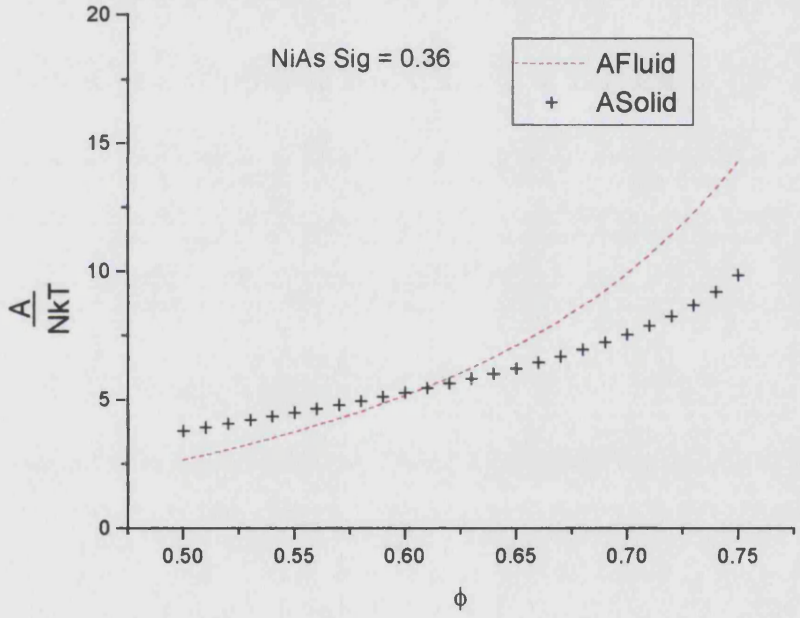

Figure 5.1.7 Free energy of NiAs at a diameter ratio of 0.36 compared with a binary hard sphere fluid with identical composition and volume fraction. The MSCL equation of state was used for the binary fluid.

Whilst, it is not possible to predict the existence of NiAs with certainty, it is possible to predict the instability of AB_2 at these diameter ratios as illustrated by fig. 5.1.8. The

solid free energy is never below the corresponding fluid. Hence any AB_2 solid would melt into the equivalent fluid rather than remain in its crystalline state.

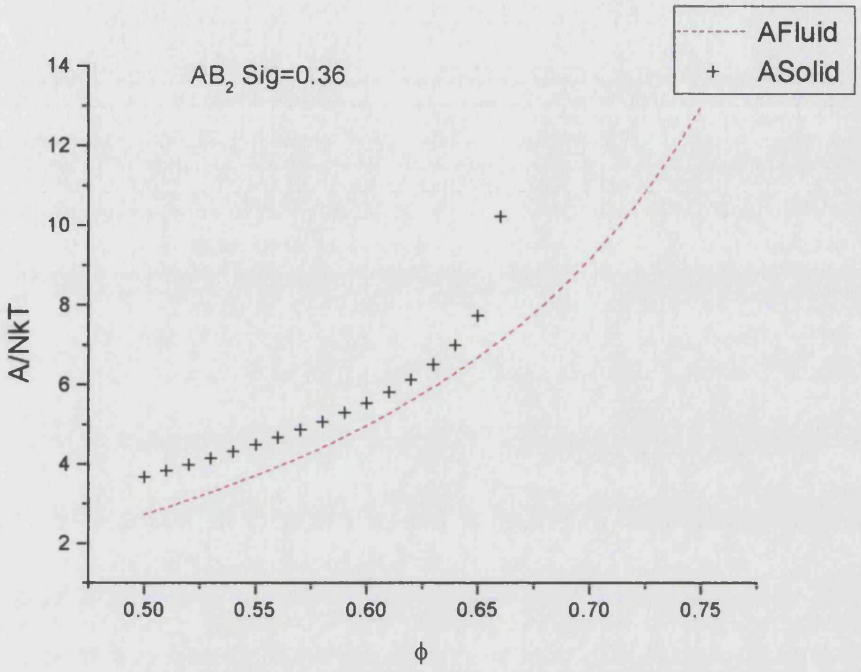

Figure 5.1.8 Free energy of AB_2 at diameter ratio 0.36 compared to binary fluid with same mole fractions of each species present. The MSCL equation of state was used for the binary fluid.

5.1.5 AB_6

AB_6 is an interesting case. The free energy was determined at a range of diameter ratios assuming an undistorted structure. In each of the diameter ratios studied AB_6 was less stable than the corresponding fluid. This can be seen in fig. 5.1.9, where for a diameter ratio of 0.36 the free energy difference between the solid and the corresponding fluid is plotted. For the undistorted structure the difference is always positive although it is close to zero at certain densities. However it is possible to distort AB_6 to lower the free energy of the crystal. Recall that AB_6 is based upon a

primitive cubic lattice of large spheres with octahedral clusters of small spheres (section 3.2.8). As long as each octahedral cluster remains inside its own cube, then it is possible to vary its dimensions. The properties of this cluster-expanded AB_6 crystal were also calculated. In this distorted structure each octahedral cluster was expanded to just slightly less than the maximum size possible. Although the free volume of the large spheres dropped, that of the more prevalent small spheres increased. The gain was sufficient to lower the free energy. As shown in fig. 5.1.9 the free energy of the cluster-expanded variant drops below that of the corresponding fluid, indicating that the variant is stable with respect to the fluid. The relevance of this is considered in section 5.2.

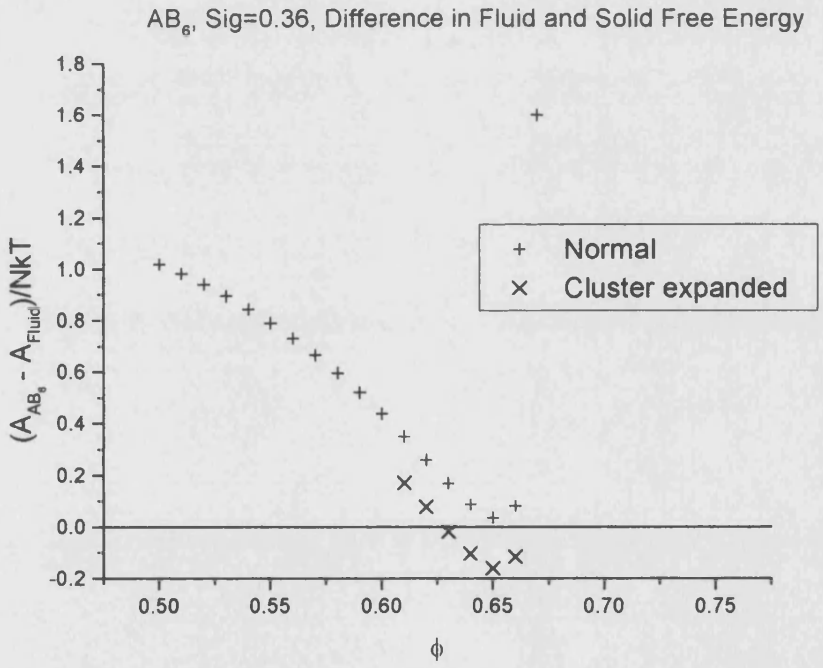

Figure 5.1.9 Difference in free energy of AB_6 at diameter ratio 0.36 and binary fluid with same mole fractions of each species present. Also shown are the results obtained for a distortion of the normal structure of AB_6.

5.2 Phase Diagrams

In the following section, the phase diagrams for binary systems with a range of diameter ratios are presented. In the majority of cases, the phase diagram is given in the pressure - mole fraction and volume fraction – volume fraction planes. The lowest diameter ratio for which a phase diagram is calculated is 0.33. Although it is possible to calculate phase diagrams for diameter ratios lower than this, they are not presented as they fail to take into account the possibility of a phase where the small spheres remain as a fluid inside the crystalline arrangement of large spheres. Again, emphasis is put on the fact that not every single possible binary arrangement has been considered in calculating these phase diagrams, but the ones that have been considered are that are those more likely ones to occur.

5.2.1 Diameter Ratios 0.33 to 35

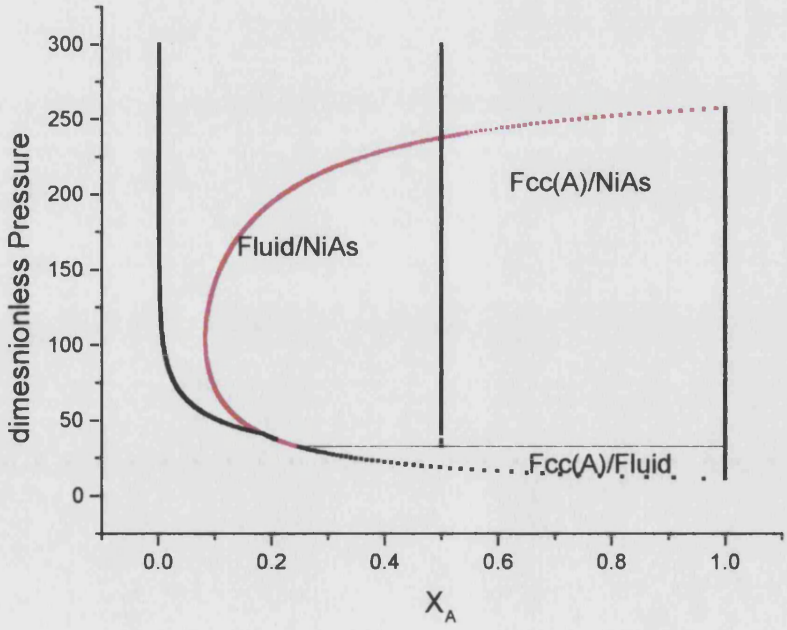

Figure 5.2.1 Phase diagram, diameter ratio 0.33, metastable phases shown in red occur when NiAs and NaCl are removed.

The only binary crystal phase that is predicted to be stable in this region is the AB (NaCl/NiAs) phase (fig. 5.2.1). Although this phase appears to be thermodynamically stable over a range of diameter ratios, until recently[53] it had never been observed in any experiments involving hard sphere like colloidal systems. For this reason, the "metastable phase diagram" is also shown. This is simply the predicted phase behaviour when the AB phase is excluded from the calculations, so that any metastable phases will emerge.

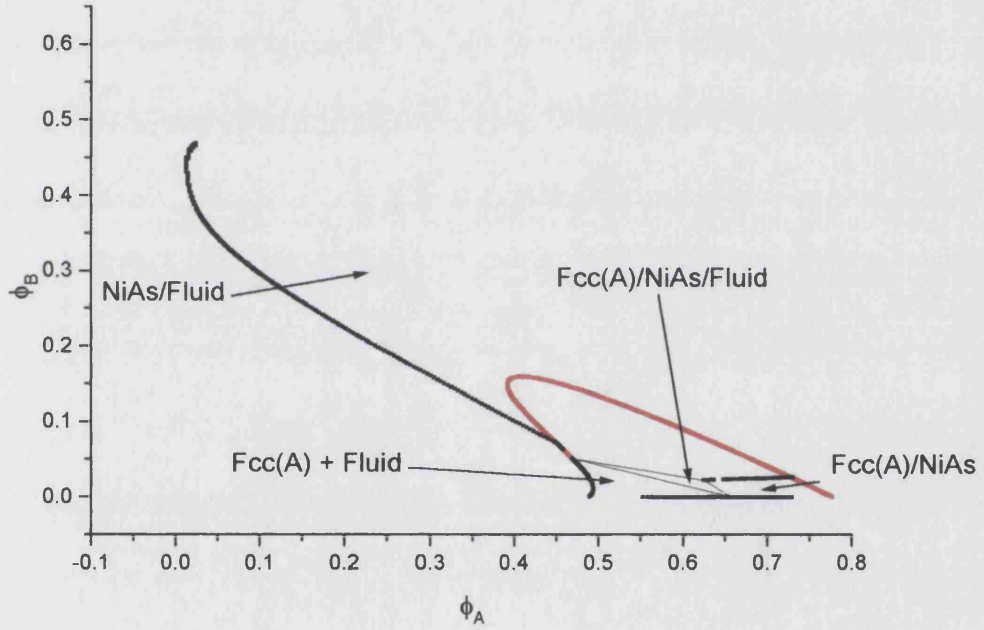

Figure 5.2.2 Phase diagram, diameter ratio 0.33, metastable phases marked in red occur when NiAs and NaCl are removed.

As expected at these small diameter ratios, the FCC phase of small spheres does not occur until quite high pressures.

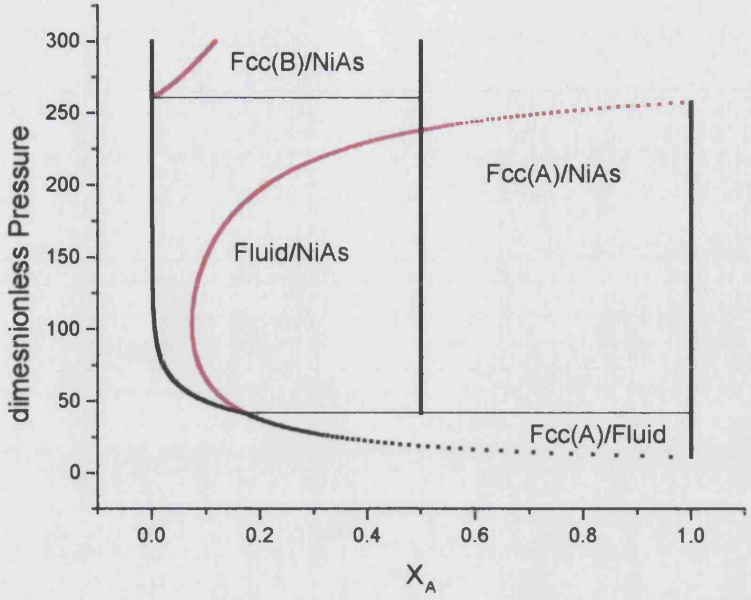

Figure 5.2.3 Phase diagram, diameter ratio 0.35, metastable phases marked in red occur when NiAs and NaCl are removed.

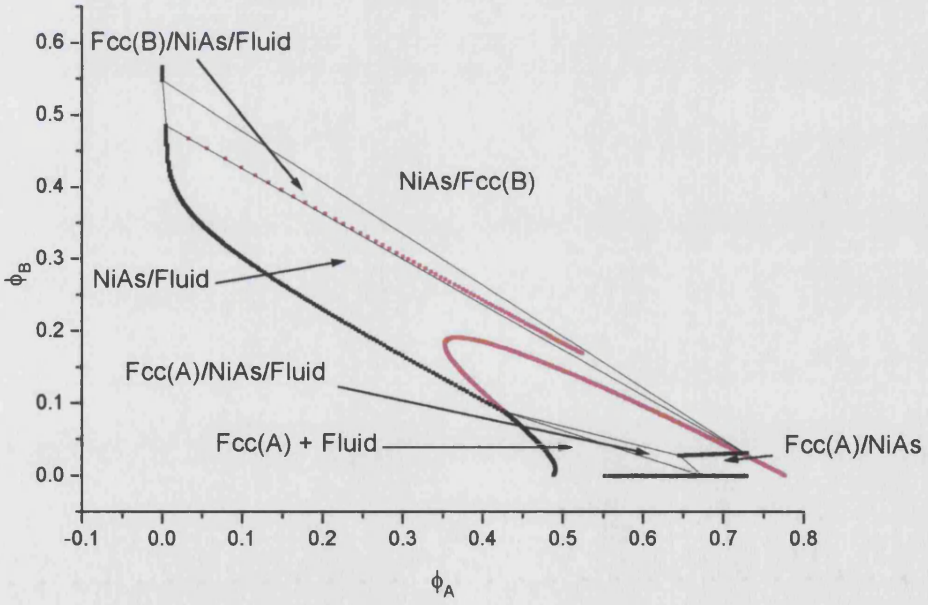

Figure 5.2.4 Phase diagram, diameter ratio 0.35, metastable phases marked in red occur when NiAs and NaCl are removed.

The phase behaviour at a diameter ratio of 0.35 is qualitatively the same as 0.33. Note that if the possibility of the existence of the AB phase is excluded, then there are some regions at quite high pressures and densities where the fluid phase would still exist (fig. 5.2.3). Though in reality it would be expected that a glassy phase would occur at high densities and pressures. The list of structures considered at these diameter ratios is AB_6, AB_{13}, AB_{12}, AB_3, AB (NaCl, NiAs), BCC (AB_6). None of these apart from the AB phase was found to be stable.

5.2.2 Diameter Ratio 0.36

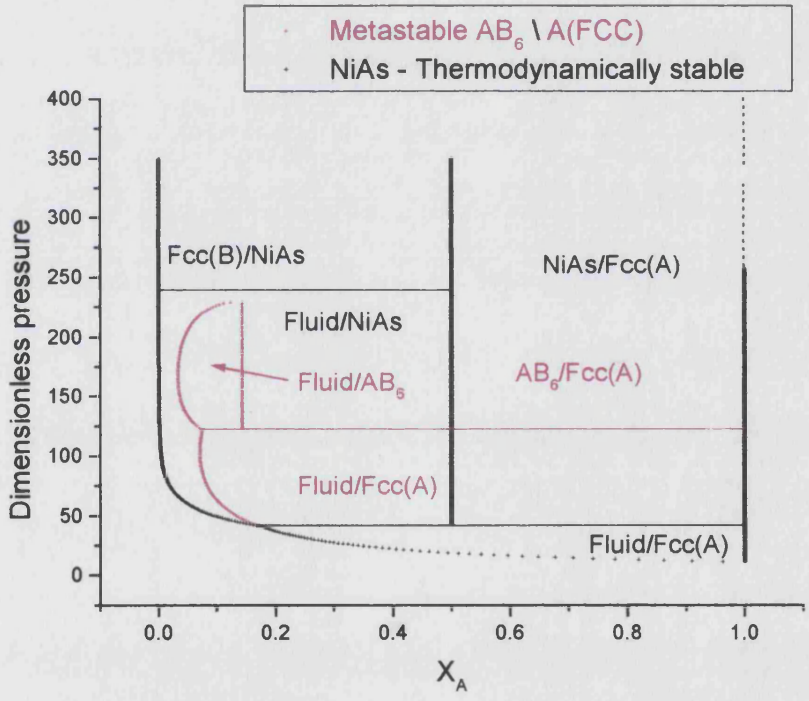

Figure 5.2.5 Phase diagram, diameter ratio 0.36, metastable phases marked in red occur when NiAs and NaCl are removed.

As the diameter ratio is increased from 0.35 to 0.36, the metastable phase behaviour changes. At this diameter ratio, the AB_2 structure was considered as a possibility. Again the AB phase is predicted to be the most stable. But when this phase is excluded, the AB_6 phase emerges. Note that this is the variant of the AB_6 structure discussed in section 5.1. This AB_6 phase is only stable for a small region, so that the metastable phase diagram is incomplete (fig. 5.2.5 and 5.2.7). This is the only diameter ratio where AB_6 is predicted to be stable in any form. It is interesting to note that AB_6 only has a packing fraction of ~0.670 at this diameter ratio. Its highest packing fraction of 0.747 occurs at diameter ratios of 0.414 ($\sqrt{2}-1$), where AB_6 is unstable relative to the corresponding fluid over all volume fractions (fig. 5.2.6).

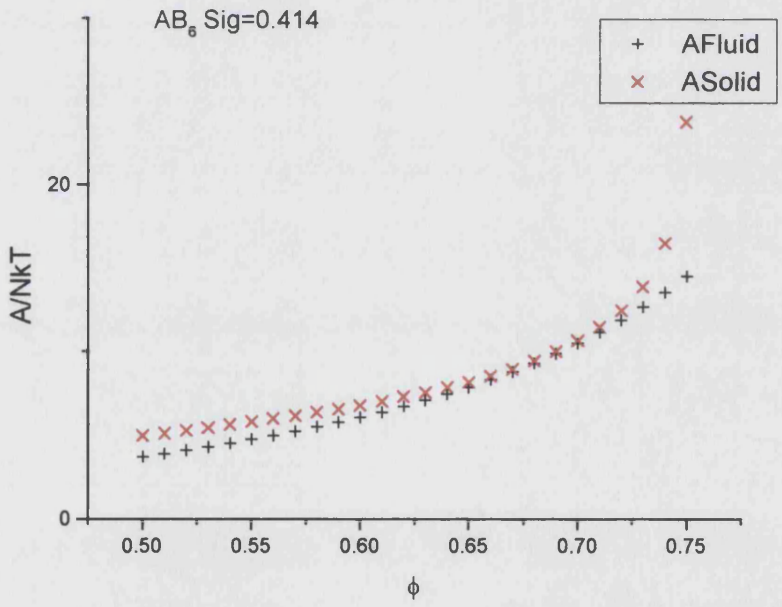

Figure 5.2.6 Helmholtz free energy for AB_6 at diameter ratio 0.414 and the corresponding fluid phase.

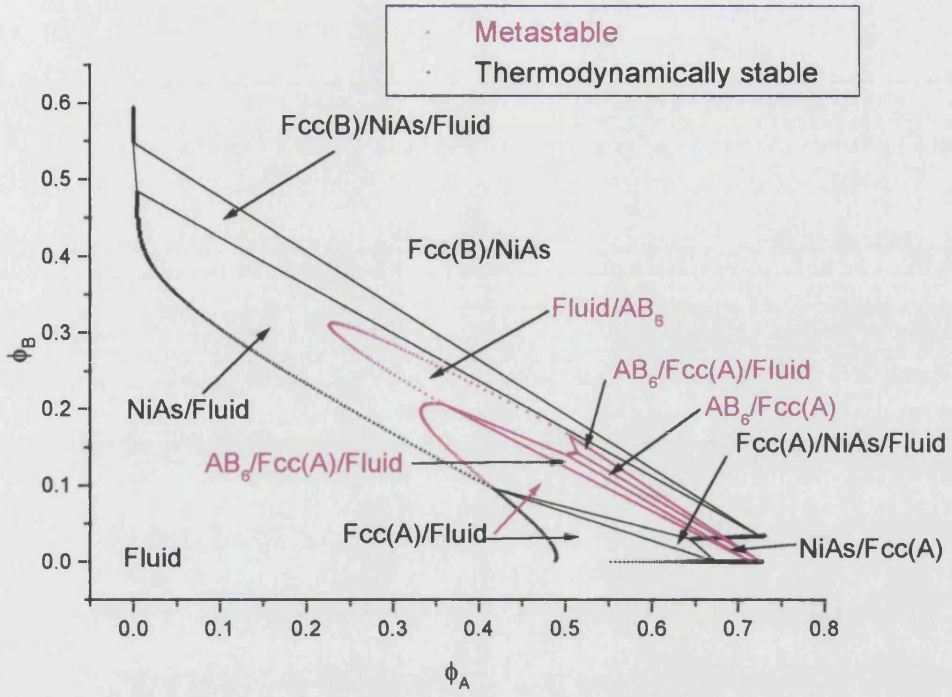

Figure 5.2.7 Phase diagram, diameter ratio 0.36, metastable phases marked in red occur when NiAs and NaCl are removed.

5.2.3 Diameter Ratio 0.39-0.42

The AB phase continues to dominate as the diameter ratio reaches 0.39. The predicted thermodynamically stable phase behaviour is qualitatively the same as that at lower diameter ratios. Of more interest is the metastable phase behaviour shown in figs. 5.2.8 and 5.2.9.

When the AB phase is excluded the AB_3 phase emerges. Unlike AB_6 at diameter ratio 0.36, AB_3 remains stable at higher pressures and densities. It is not possible to predict that the AB_3 phase will be observed from these calculations alone. It would only be observed if the AB phase is indeed hindered from forming and the AB_3 phase does not suffer from similar hindrance.

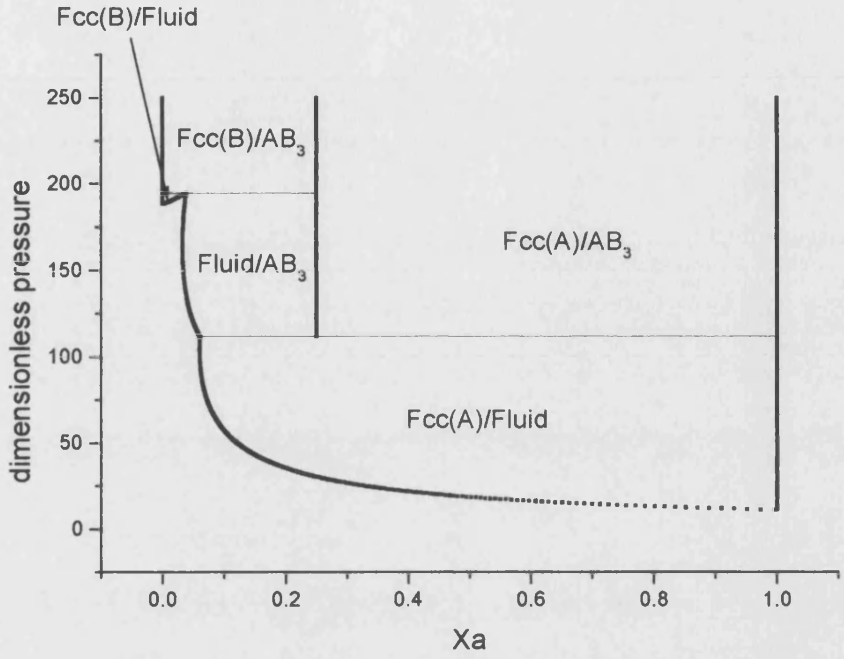

Figure 5.2.8 Phase diagram, diameter ratio 0.39, showing the metastable phases that occur when NiAs and NaCl are removed.

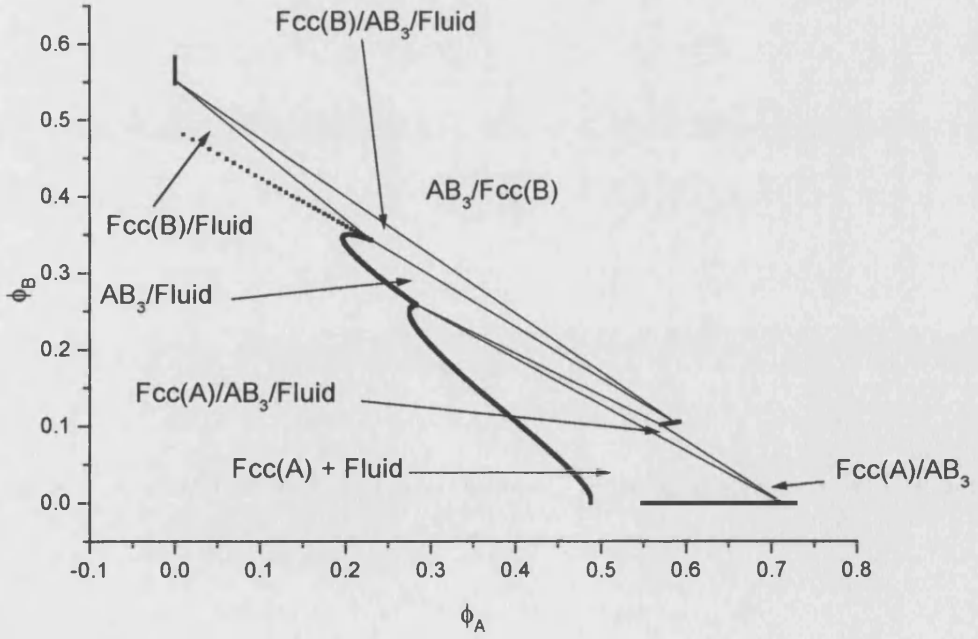

Figure 5.2.9 Phase diagram, diameter ratio 0.39, showing the metastable phases that occur when NiAs and NaCl are removed.

The phase behaviour at diameter ratio 0.414 is of particular interest because a number of structures have their highest possible packing fractions. The AB phases have a packing fraction of 0.7931 at this diameter ratio, the highest packing fraction of all binary structures at all diameter ratios considered. Notably even though AB_6 has a packing fraction of 0.7469 at this diameter ratio (the second highest at this ratio) it is not observed. In figs. 5.2.10 and 5.2.11, the thermodynamically stable and metastable phase diagrams are overlaid. There is a third possible phase at this diameter ratio. If all the AB_3 and AB phases are excluded, then the BCC(AB_6) phase is seen to emerge. This is the only diameter ratio where there is any suggestion that the BCC(AB_6) phase will be at all stable.

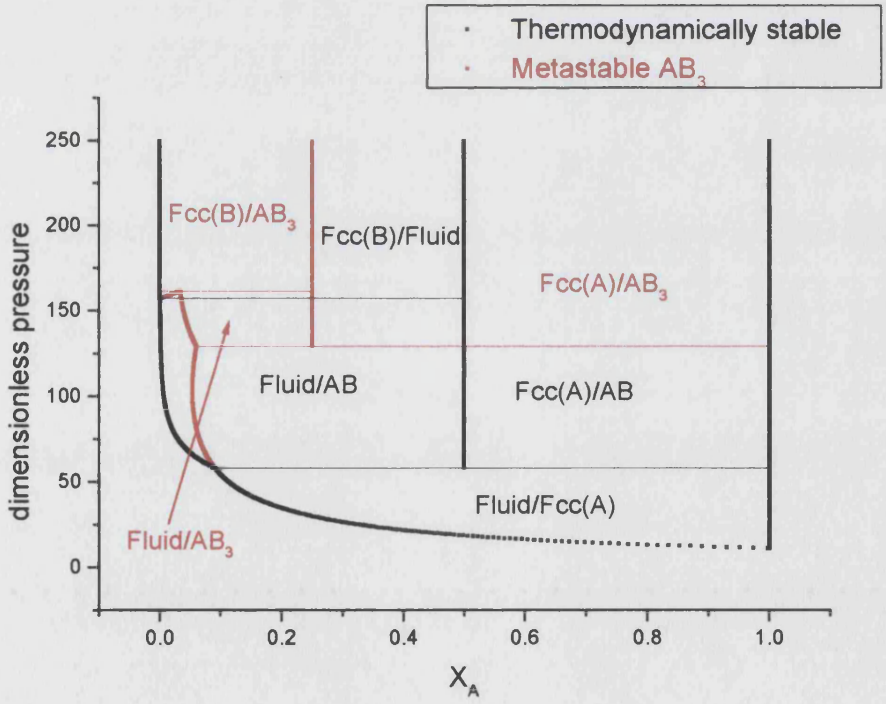

Figure 5.2.10 Phase diagram, diameter ratio 0.414, metastable phases marked in red occur when NiAs and NaCl are removed.

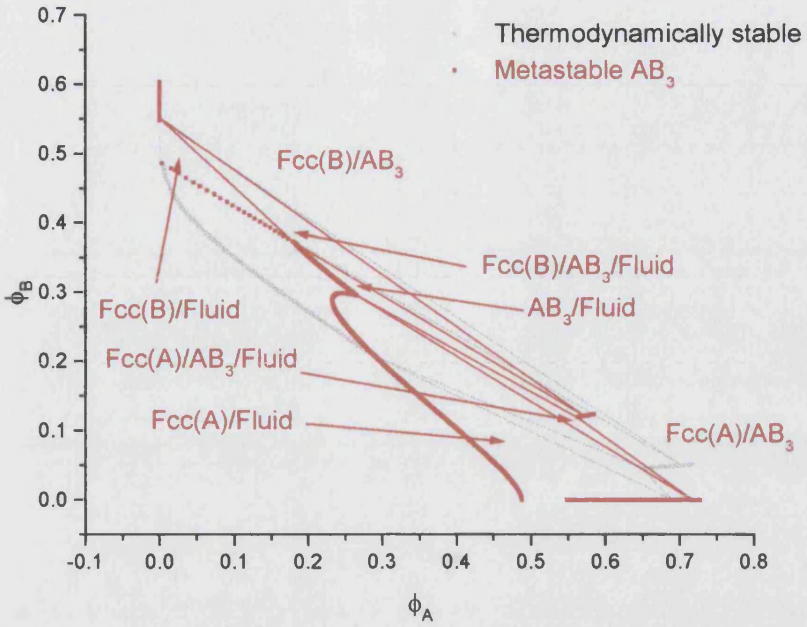

Figure 5.2.11 Phase diagram, diameter ratio 0.414, metastable phases marked in red occur when NiAs and NaCl are removed.

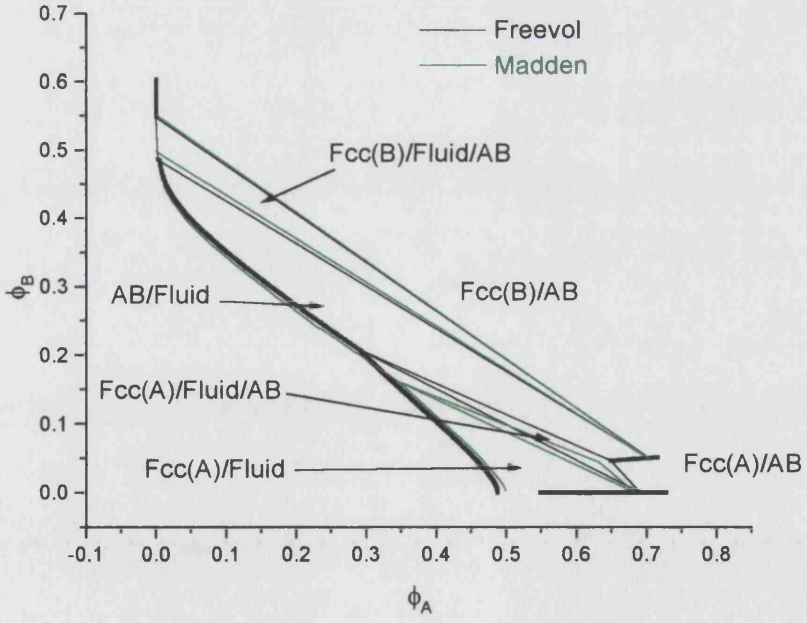

Figure 5.2.12 Diameter ratio 0.414, comparison of phase diagrams obtained using free volume theory and molecular dynamical calculations[71].

In fig. 5.2.12 a comparison is made between the phase behaviour calculated using free volume theory and that calculated using molecular dynamics by Trizac et al[71]. The agreement between the two different methods is excellent.

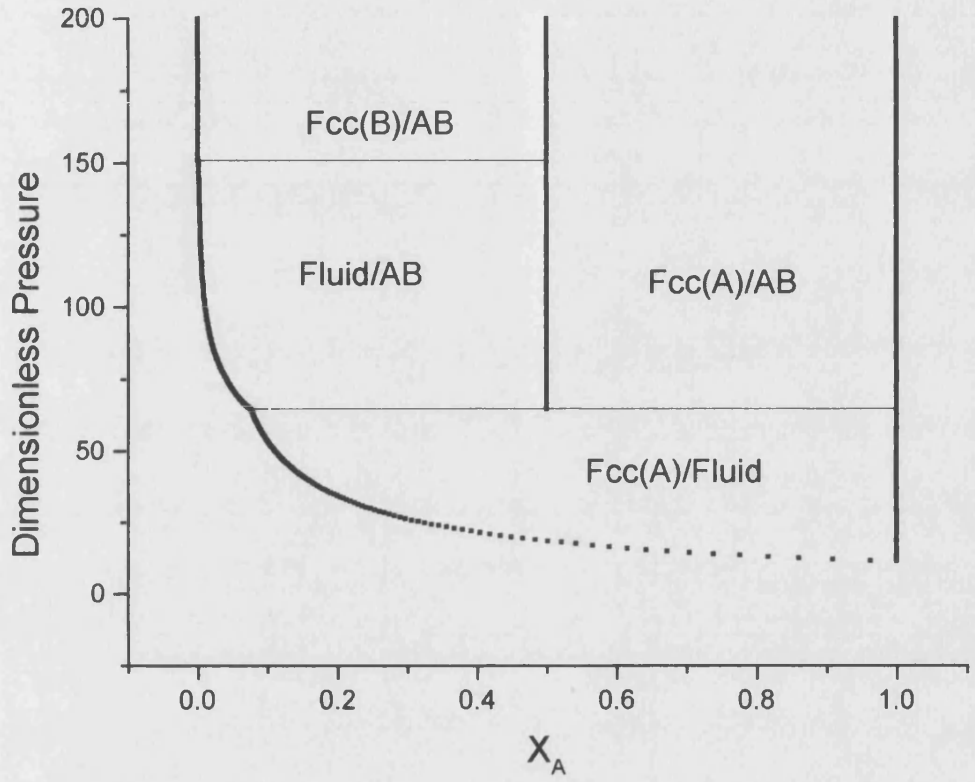

Figure 5.2.13 Phase diagram, diameter ratio 0.42.

At a diameter ratio of 0.42 the AB phase is still the only phase to be thermodynamically stable, as shown in figs. 5.2.13 and 5.2.14 Again the AB_3 phase is predicted to be metastable at this diameter ratio.

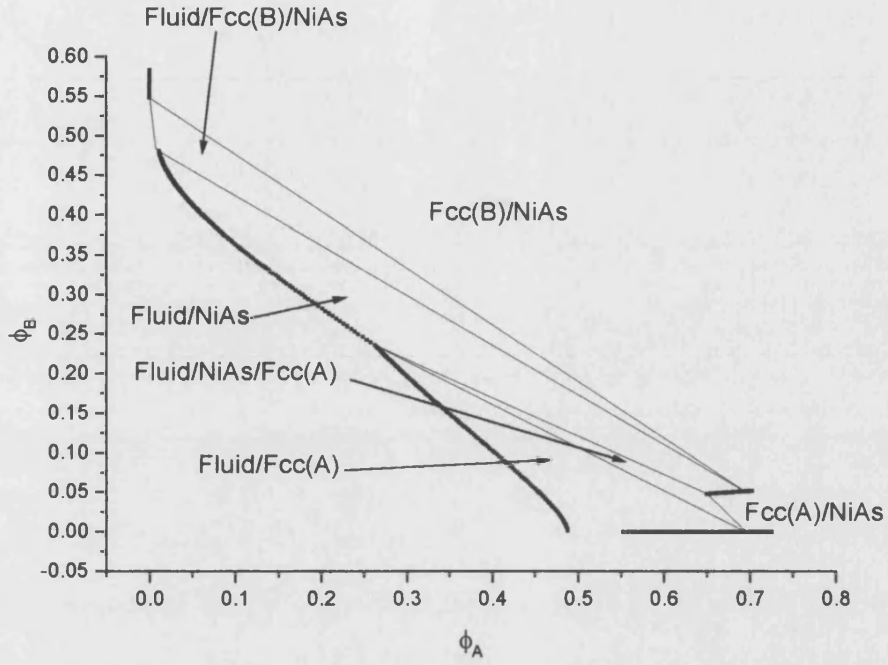

Figure 5.2.14 Phase diagram, diameter ratio 0.42

5.2.4 Diameter Ratios 0.43 to 0.44

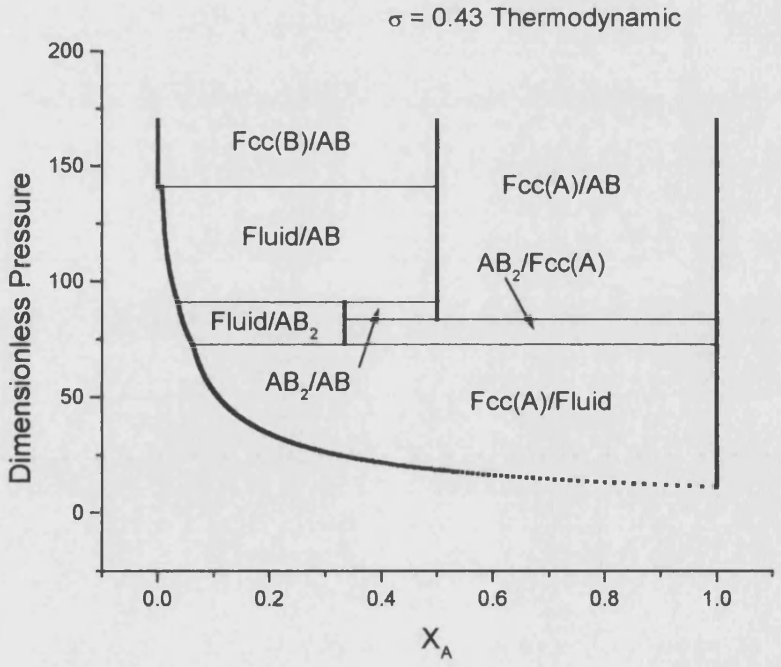

Figure 5.2.15 Phase diagram, diameter ratio 0.43

Once the diameter ratio is increased from 0.42 to 0.43 a new thermodynamically stable phase is seen to appear alongside the AB phases. This is the AB_2 phase, which, unlike the AB phases, has been observed in experiments with colloidal hard spheres[26]. But at this diameter ratio, the AB phase still dominates, being favoured at higher pressures and densities (figs. 5.2.15 and 5.2.16). There is no equilibrium between the AB_2 phase and the FCC phase of small spheres.

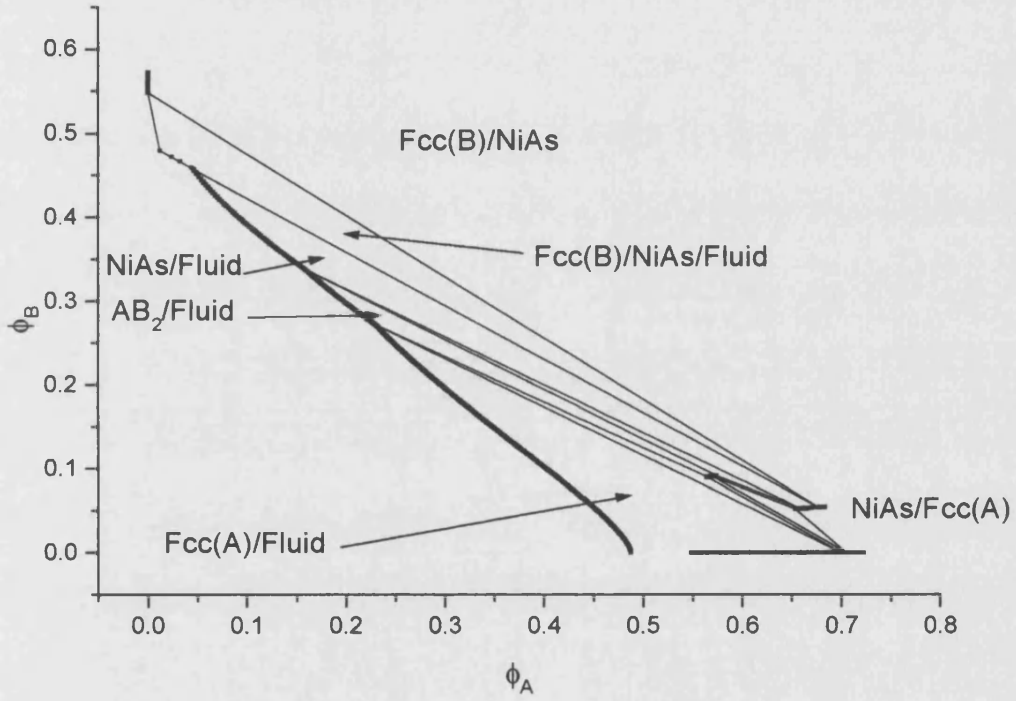

Figure 5.2.16 Phase diagram, diameter ratio 0.43

As the diameter ratio is increased further still to 0.44, a transition is seen to begin to occur as the domination of the AB phases decreases (figs. 5.2.17 and 5.2.18). At this diameter ratio equilibrium between AB_2 and the FCC phase of small spheres may be observed. However the AB phase continues to dominate at higher pressures.

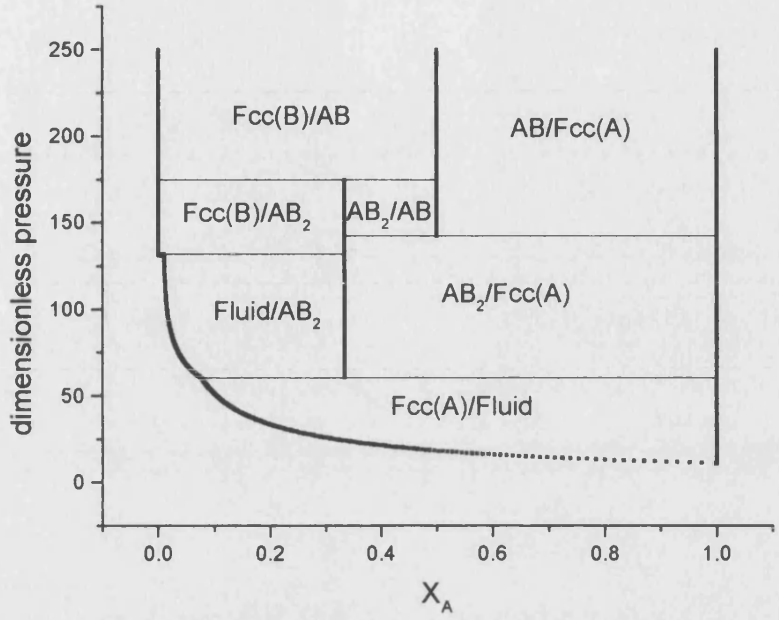

Figure 5.2.17 Phase diagram, diameter ratio 0.44

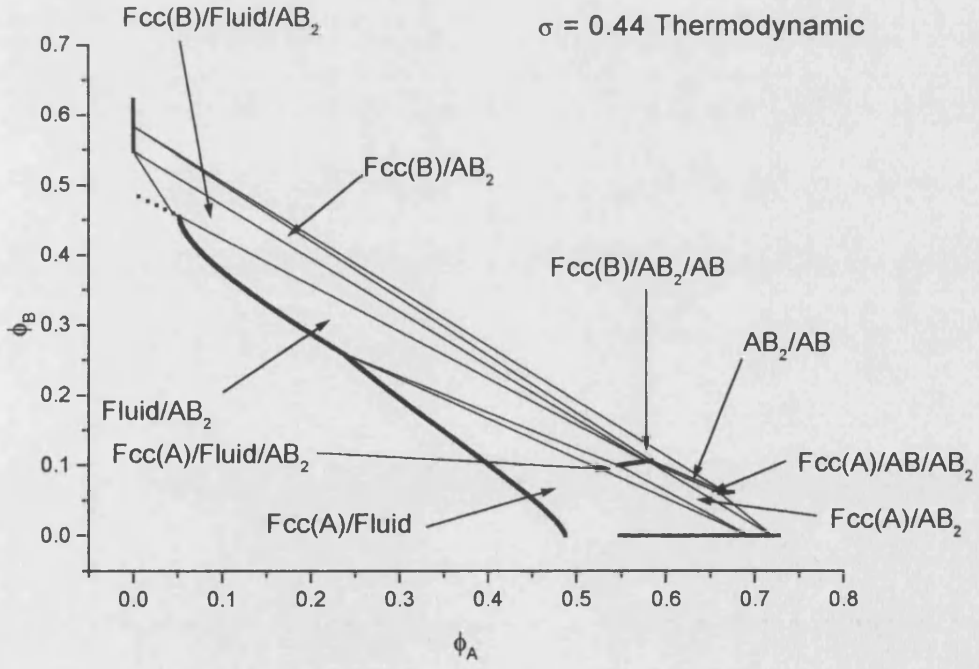

Figure 5.2.18 Phase diagram, diameter ratio 0.44.

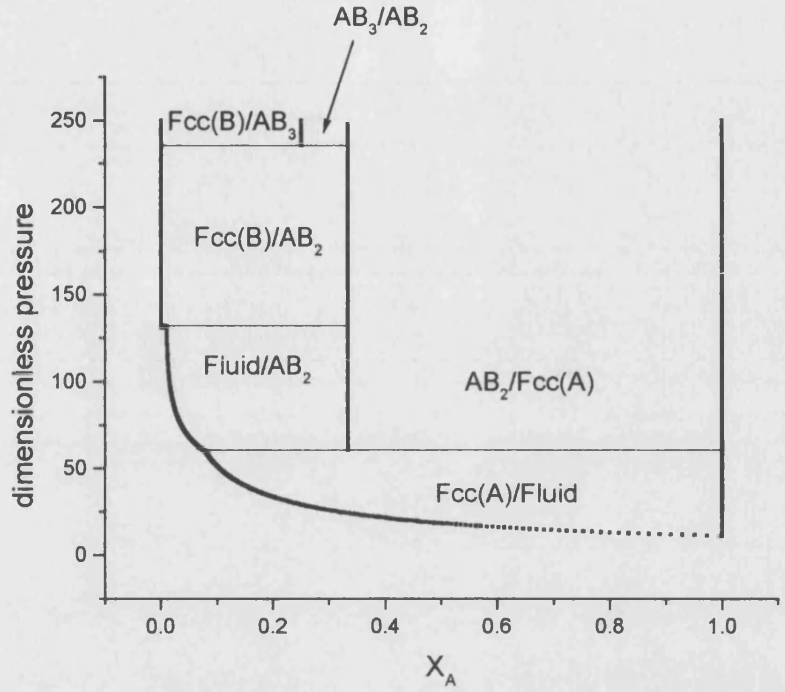

Figure 5.2.19 Phase diagram, diameter ratio 0.44, showing metastable phases that occur when NiAs and NaCl are removed.

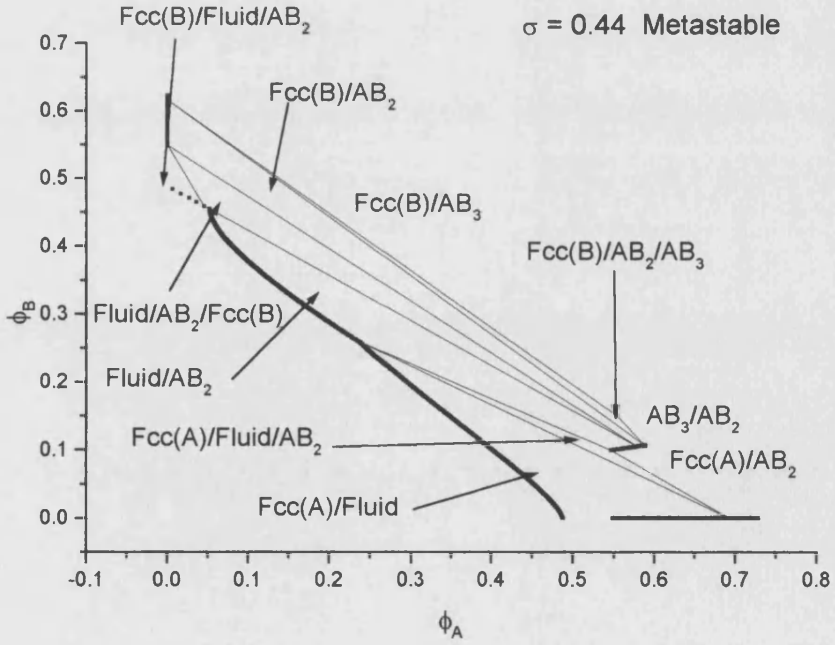

Figure 5.2.20 Phase diagram, diameter ratio 0.44, showing metastable phases that occur when NiAs and NaCl are removed.

In keeping with the phase diagrams for lower diameter ratios, the metastable phase behaviour is also considered. When the AB phase is excluded at these diameter ratios, the AB_3 phase once more emerges. There is little purpose in excluding the AB_2 phase, as this is known to occur. The metastable behaviour for diameter ratio 0.44 is shown in figs. 5.2.19 and 5.2.20. Note that the metastable AB_3 phase is only seen at high pressures and densities. This is the highest diameter ratio at which AB_3 is seen in any form. It is only ever seen as a metastable phase, the AB phase if it were allowed to form, would always exclude it.

5.2.5 Diameter Ratios 0.45 to 0.48

The range from 0.45 to 0.48 is straightforward, in that there are no metastable phases to be considered. The only phase present is the experimentally observed AB_2 phase. There is no significant difference between the phase behaviour at the two diameter ratios. In this range none of the structures have very high packing fractions. AB has a packing fraction of ~0.75 at diameter ratio 0.45, whilst AB_2 has a packing fraction of only ~0.715. The other structure considered at diameter ratio 0.45, AB_3, has a packing fraction of ~0.733. In this case, of the three structures considered, it is the one with the lowest close packing fraction, AB_2, not the highest, AB that is found to be stable.

At diameter ratio 0.48, none of the binary structures have a packing fraction higher than the monodisperse FCC structure, but AB_2 is still predicted to be stable.

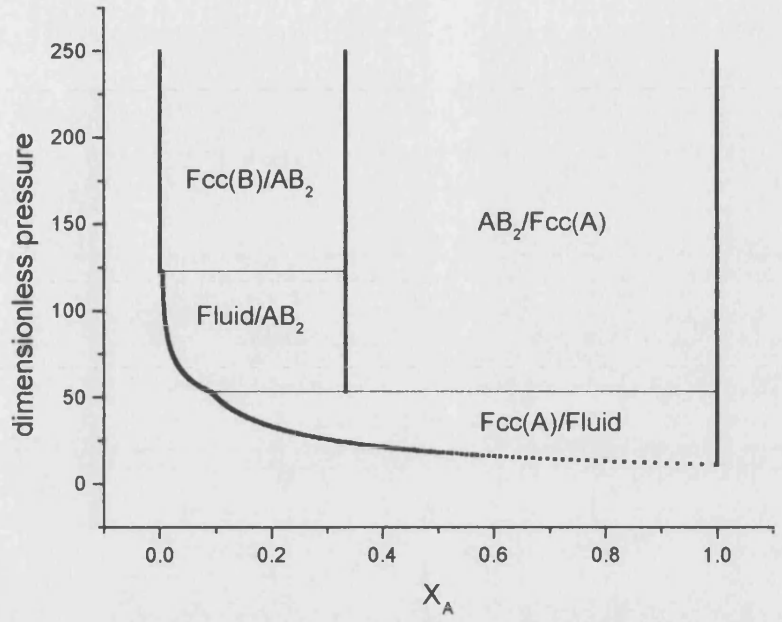

Figure 5.2.21 Phase diagram, diameter ratio 0.45

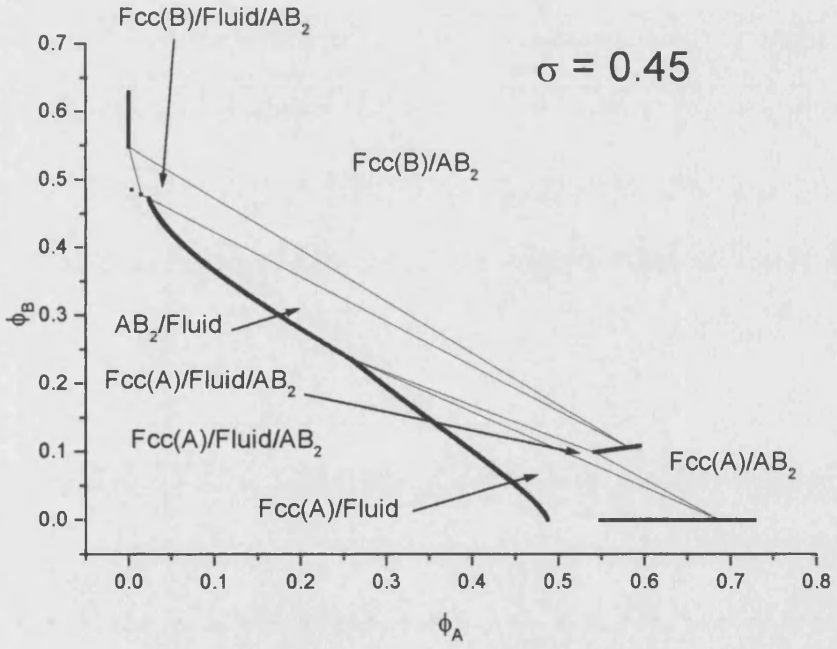

Figure 5.2.22 Phase diagram, diameter ratio 0.45

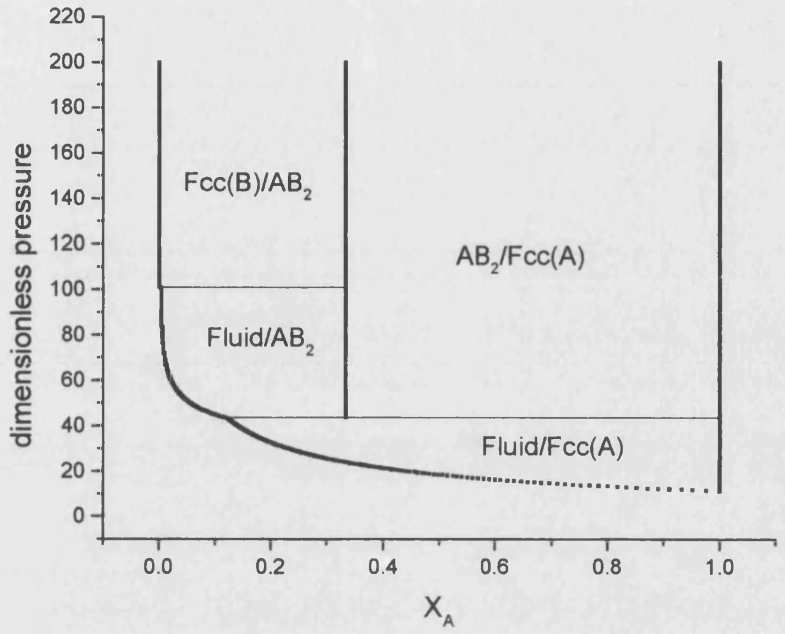

Figure 5.2.23 Phase diagram, diameter ratio 0.48

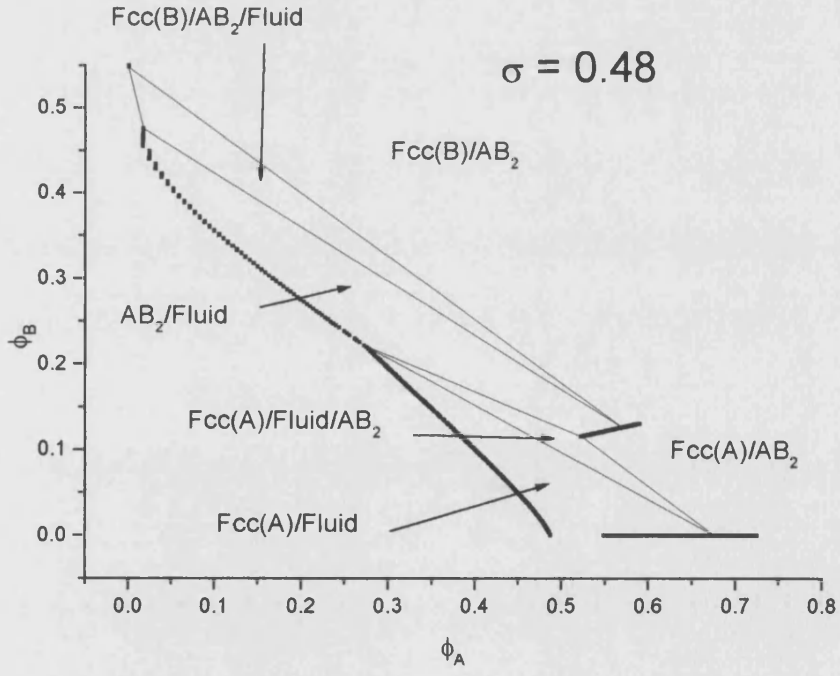

Figure 5.2.24 Phase diagram, diameter ratio 0.48

5.2.6 Diameter Ratio 0.52

As at diameter ratios 0.45-0.48, it is AB_2 that is predicted to be the most stable phase at diameter ratio 0.52. However it is interesting to note the emergence of the AB_{13} phase when AB_2 is artificially excluded. AB_{13} is, perhaps, the most unusual of the binary structures considered and has a packing fraction of ~0.714 at this diameter ratio. Although it is not expected to form at this diameter ratio due to the presence of the AB_2 phase, the position of the metastable AB_{13} phase is shown on the pressure - mole fraction plane phase diagram (fig. 5.2.25). Only the thermodynamically stable AB_2 phase is shown on the volume fraction – volume fraction diagram (fig. 5.2.26).

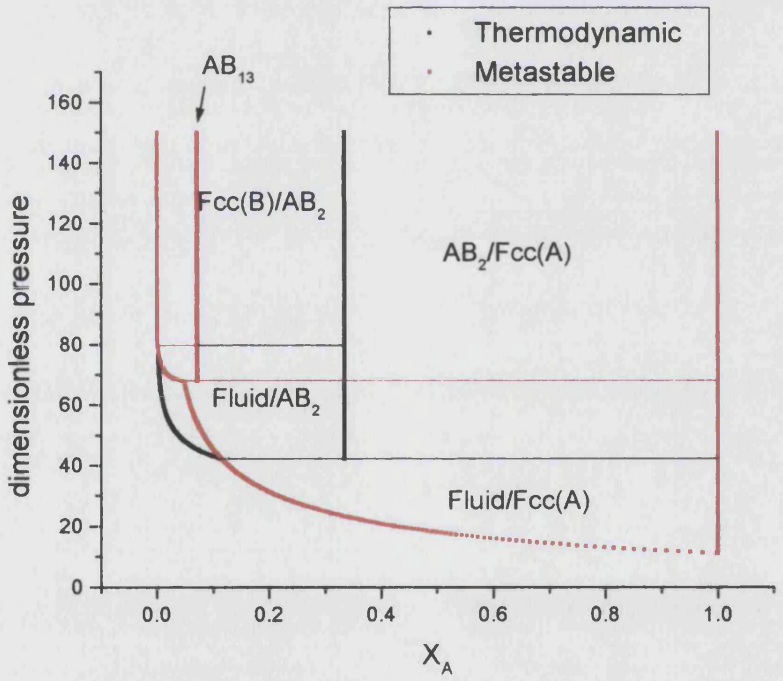

Figure 5.2.25 Phase diagram, diameter ratio 0.52, metastable phases marked in red occur when AB_2 is removed.

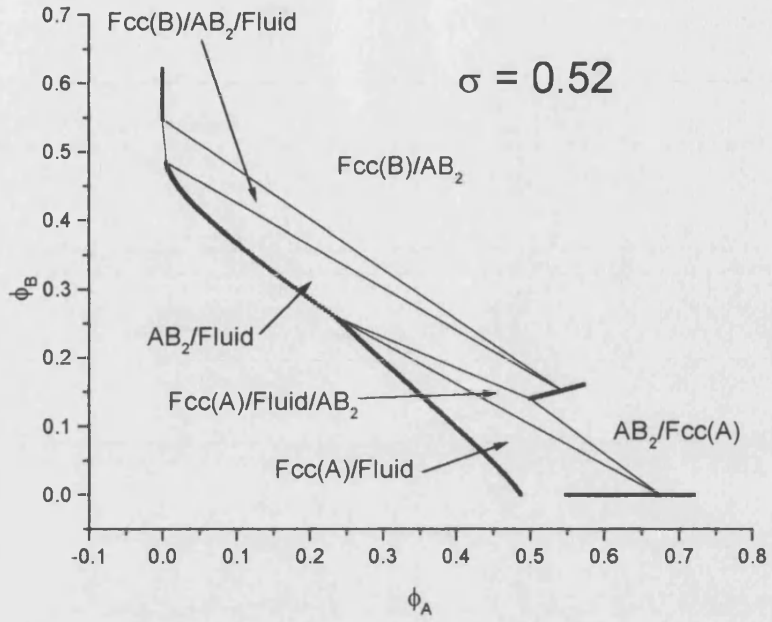

Figure 5.2.26 Phase diagram, diameter ratio 0.52.

5.2.7 Diameter Ratio 0.558 to 0.6

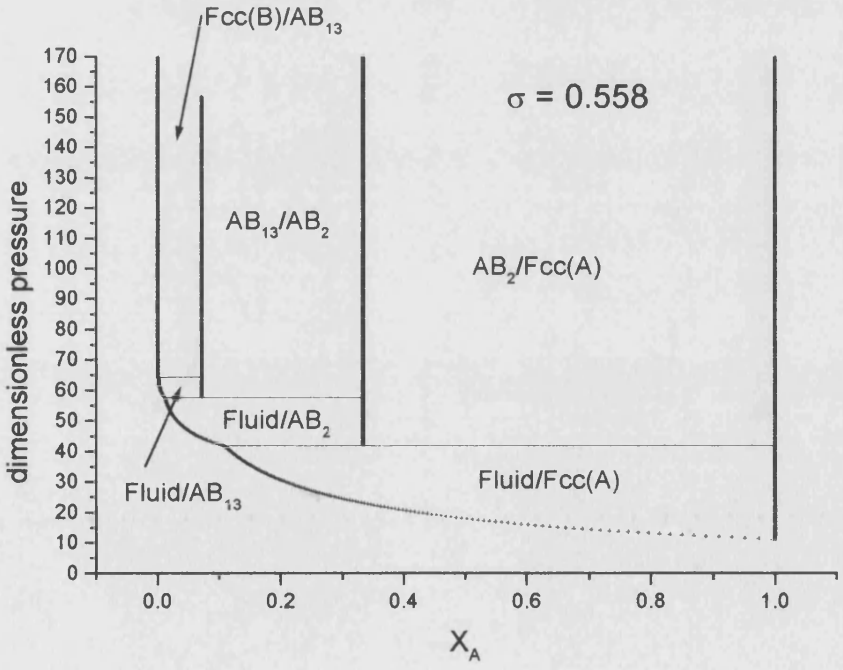

Figure 5.2.27 Phase diagram, diameter ratio 0.558.

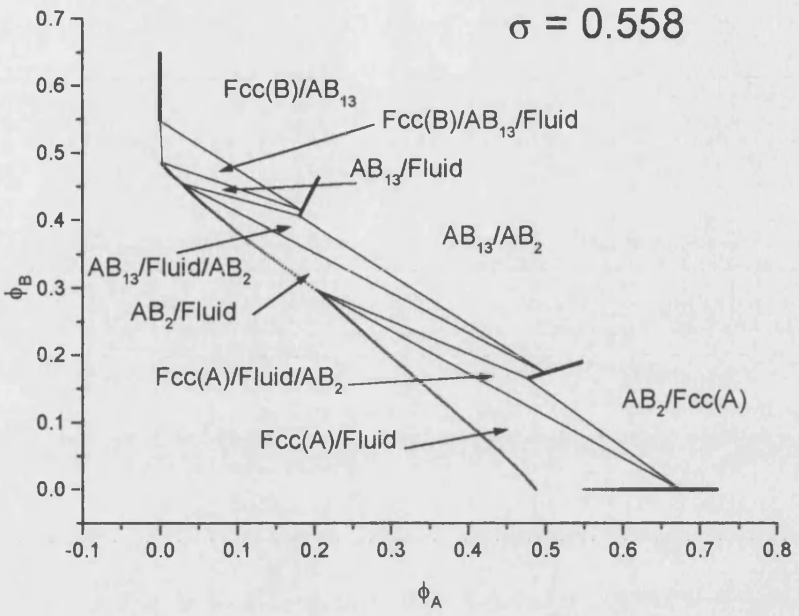

Figure 5.2.28 Phase diagram, diameter ratio 0.558.

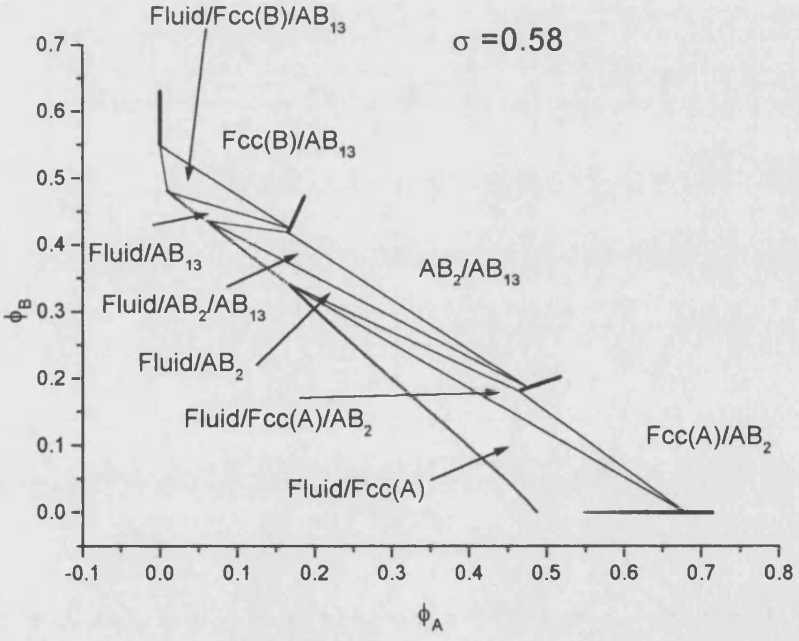

Figure 5.2.29 Phase diagram, diameter ratio 0.58.

In the ratio of diameter ratios from 0.558-0.6, there is a rich variety of phases. At the diameter 0.558, AB_{13} has a packing fraction of 0.738. This is the highest packing

fraction that AB_{13} can achieve and it is less than the packing fraction of the FCC phase. Murray and Saunders[48] suggested that a distortion from the ideal structure was needed to increase the packing fraction of AB_{13}, so that it could form. No such distortion has been carried out in these calculations; AB_{13} is predicted to form even though it has a relatively low packing fraction.

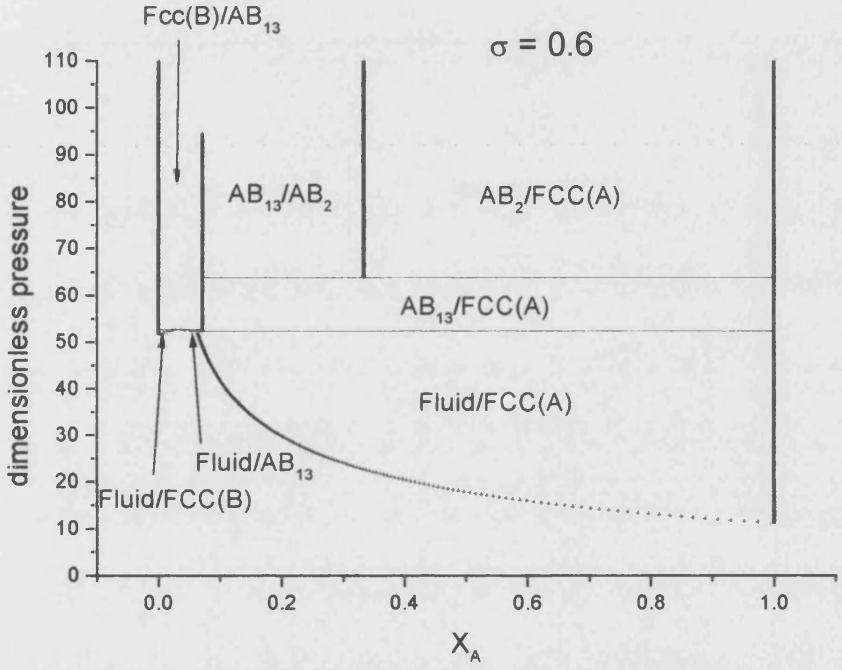

Figure 5.2.30 Phase diagram, diameter ratio 0.6.

As the diameter ratio increases to 0.6, the AB_{13} phase begins to diminish on the phase diagram (figs. 5.2.30 and 5.2.31). The equilibrium between the fluid and the AB_2 phase also disappears as the binary phases are pushed to higher pressures and densities.

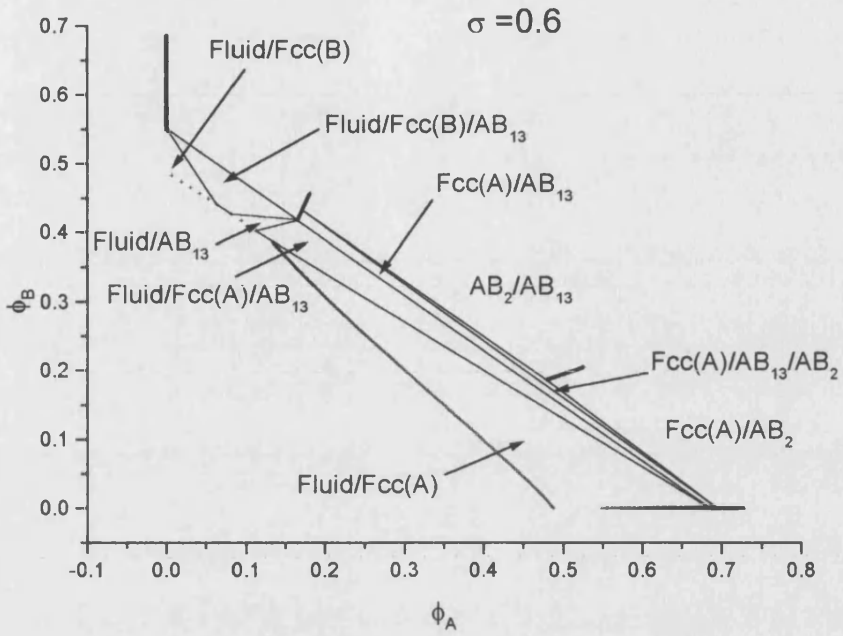

Figure 5.2.31 Phase diagram, diameter ratio 0.6.

5.2.8 Diameter ratio 0.61

The diameter ratio 0.61 marks the transition from binary phases to monodisperse phases. The only binary phase present in the AB_2 phase, which only appears at high pressures and densities. The fluid is only in equilibrium with the monodisperse phases and for the first time, the two monodisperse phases are seen to be in equilibrium with each other. Note that these diagrams give the most thermodynamically stable phases. The presence of a phase on any of these diagrams by no means indicates that it will certainly occur, as kinetic effects, amongst others may hinder its formation. None of the binary structures in this study have very good packing fractions at diameter ratios greater than 0.61.

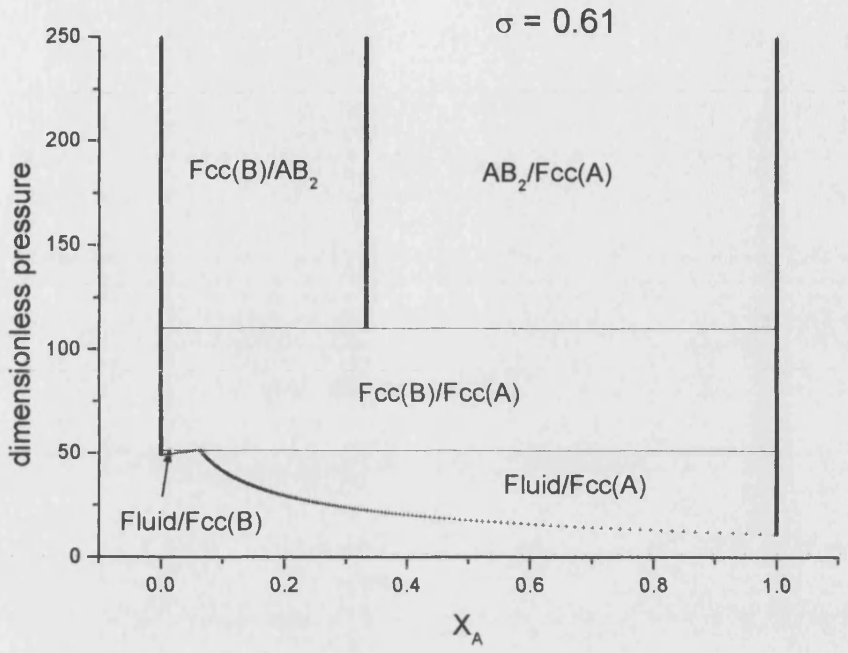

Figure 5.2.32 Phase diagram, diameter ratio 0.61.

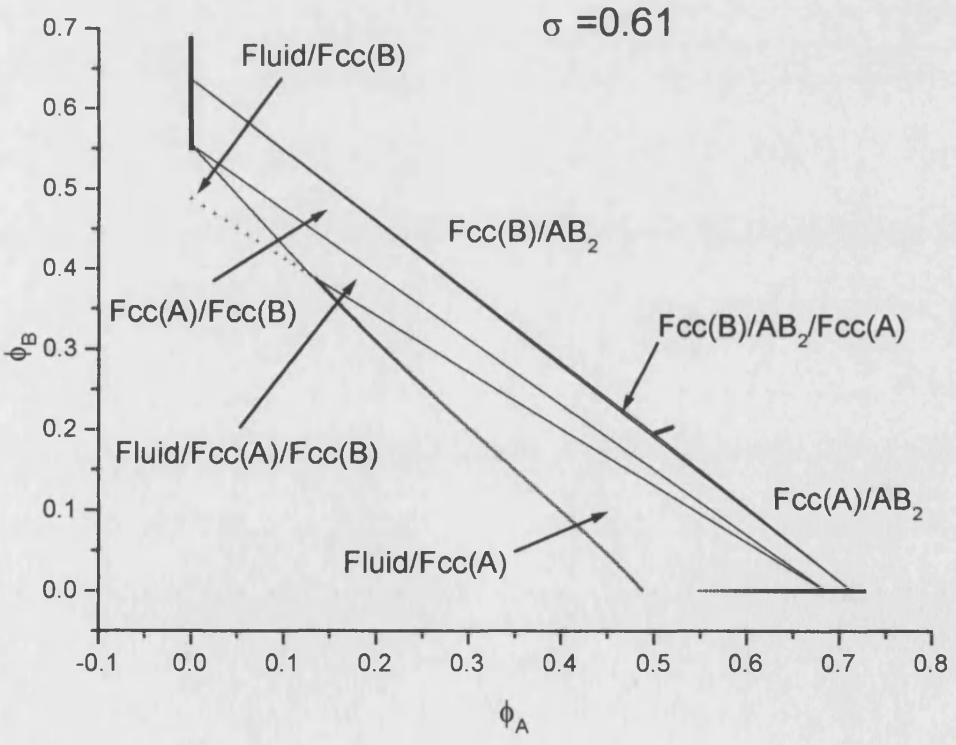

Figure 5.2.33 Phase diagram, diameter ratio 0.61.

5.2.9 Diameter Ratio 0.62 and Higher

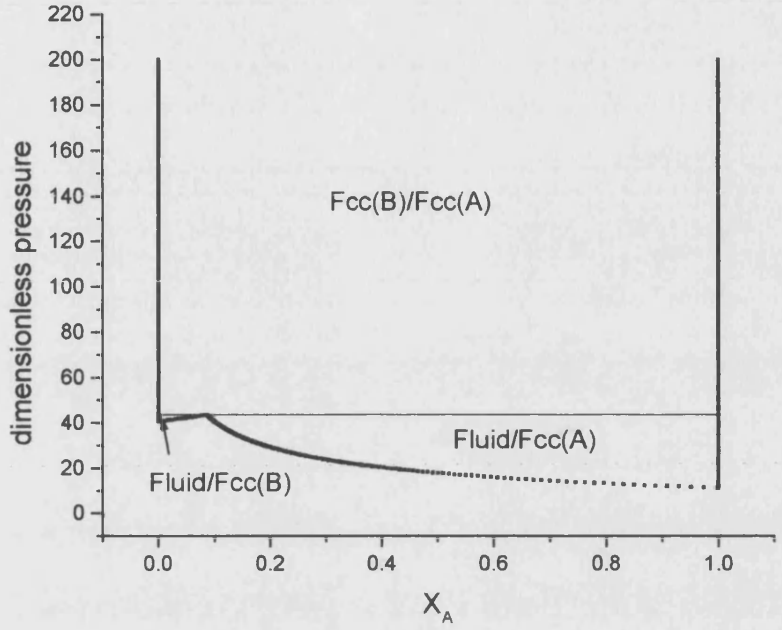

Figure 5.2.34 Phase diagram, diameter ratio 0.65.

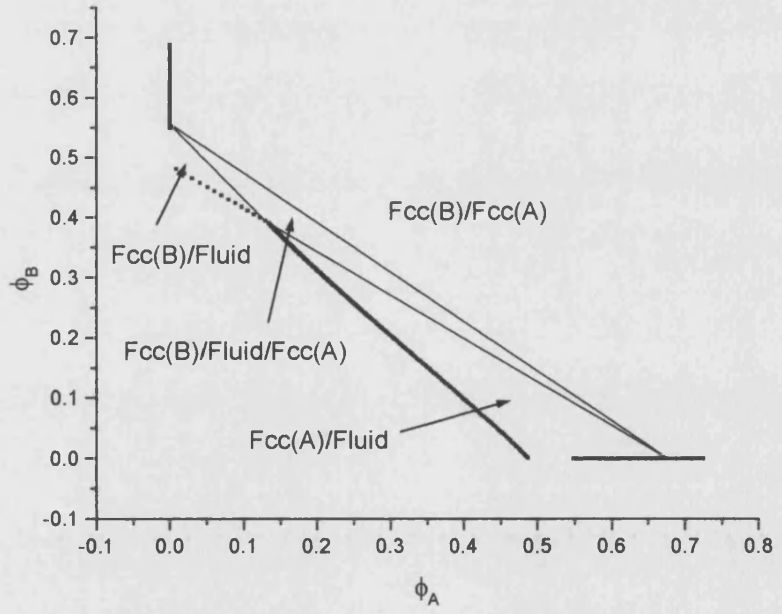

Figure 5.2.35 Phase diagram, diameter ratio 0.65.

No binary structures are observed in the phase diagrams for diameter ratios greater than 0.62. The only crystalline phases present are the two FCC phases (large and

small spheres). The only change noted as the diameter ratio increases further is the position of the eutectic, which approaches a mole fraction of 0.5. However, this study has not taken into account the possibility of a substitutionally disordered FCC phase. This phase has been considered by Cottin and Monson[72] and is only applicable at higher diameter ratios.

5.2.10 Summary and Conclusions

Diameter Ratio	Structures Tested	Phase Behaviour [Metastable]
0.33	AB_6,AB_{13},AB_{13},AB_3,AB,BCC(AB_6)	AB
0.36	AB_6,AB_{13},AB_3,AB,BCC(AB_6),AB_2	AB [AB_6]
0.39	AB_6,AB_{13},AB_3,AB,BCC(AB_6),AB_2	AB [AB_3]
0.414	AB_6,AB_{13},AB_3,AB,BCC(AB_6),AB_2	AB [AB_3,BCC(AB_6)]
0.42	AB_3,AB,BCC(AB_6),AB_2	AB [AB_3]
0.43	AB_3,AB,AB_2	AB_2,AB [AB_2,AB_3]
0.44	AB_3,AB,AB_2	AB_2,AB [AB_2,AB_3]
0.45	AB_3,AB,AB_2	AB_2
0.48	AB_{13},AB_2,AB	AB_2
0.52	AB_{13},AB_2,AB	AB_2 [AB_{13}]

0.558	AB_{13},AB_{13},AB_2	AB_2,AB_{13}
0.56	AB_{13},AB_2	AB_2,AB_{13}
0.58	AB_{13},AB_2	AB_2,AB_{13}
0.6	AB_{13},AB_2	AB_2,AB_{13}
0.61	AB_{13},AB_2	FCC(L),FCC(S),AB_2
0.62	AB_2	FCC(L),FCC(S)
0.65-0.75		FCC(L),FCC(S)

Table 5.2.1

Calculations have been performed over a range of diameter ratios, $0.33 \leq \sigma \leq 0.75$. At each diameter ratio at which calculations were performed, the thermodynamic properties of a number of structures was calculated using the Lennard-Jones cell model. The thermodynamically stable phase behaviour was then calculated using the MSCL equation of state to represent the binary fluid. The list of structures tested is listed in table 5.2.1. As some structures may be kinectically hindered, the metastable phase behaviour has also been calculated. The predictions of this thesis are summarised in figure 5.2.36. These may be compared to the predictions made in chapter 2 that are summarised in figure 2.1.

Using cell theory, AB_2 is predicted to be stable over a range of diameter ratios, $0.43 \leq \sigma \leq 0.61$. This is consistent with the observations of AB_2 at diameter ratios of $\sigma = 0.58$ by Bartlett[50] and $\sigma = 0.52$ by Hunt and Jardine[53]. These results are also in agreement with the predictions made by Eldridge and Madden[54,55].

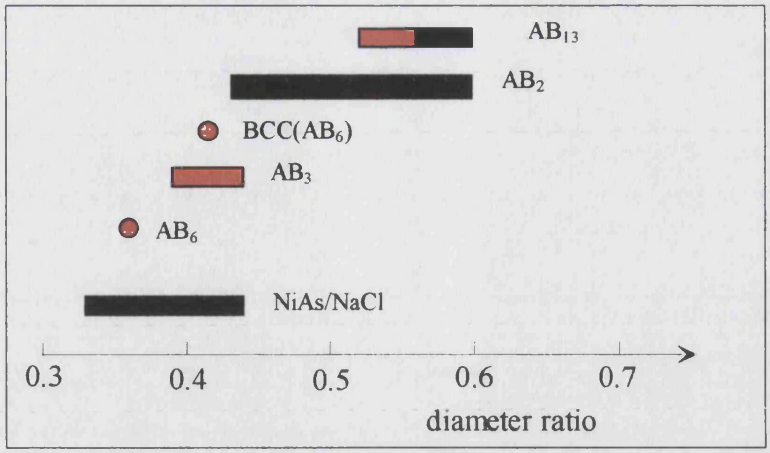

Figure 5.2.36 The predictions of the cell model. Thermodynamically stable phases are shown in black, while Metastable phases are shown in red. Compare this to figure 2.1.

Eldridge and Madden predicted that AB_{13} would be stable in the range, $0.54 \leq \sigma \leq 0.625$. Again the results of the cell theory are in quite good agreement with these findings. AB_{13} is predicted to be thermodynamically stable in the range $0.558 \leq \sigma \leq 0.6$ and metastable with respect to the AB_2 phase in the range $0.52 \leq \sigma \leq 0.558$. The predictions of cell theory are also consistent with the observation of AB_{13} at $\sigma = 0.58$ by Bartlett[50]. Hunt and Jardine[53] observed AB_{13} at $\sigma = 0.52$, these results would suggest that this is a metastable structure.

The observation of NaCl/NiAs structures at $\sigma = 0.39$ by Hunt and Jardine[53] is consistent with the predictions made. The NiAs/NaCl structures are predicted to be thermodynamically stable in the range, $0.33 \leq \sigma \leq 0.44$. This is also in agreement with the results of Trizac et al[57], who predicted that NaCl would be stable at $\sigma = 0.414$. They predicted that NaCl would also be stable at $\sigma = 0.45$, which is just outside the limit predicted by cell theory.

AB_6 has been observed at a diameter ratio of $\sigma = 0.36$ by Pusey et al.[51]. The results of these calculations would suggest that this is a metastable phase being observed, relative to the more stable NaCl/NiAs phase.

These results also suggest the possibility of metastable BCC(AB_6) and AB_3 structures occurring. But it is difficult to predict their formation with any certainty.

These calculations have found no evidence of binary superlattices at diameter ratios greater than 0.62. This is in disagreement with the observation of $MgCu_2$ and $CaCu_5$ in systems of charged colloids by Hachisu et al[49]. However the observation of these structures may well be due to the nature of the charged potential.

Schofield[52] observed the formation of a binary hard crystal with the CsCl structure at a diameter ratio, $\sigma = 0.736$. No evidence is found of any structures at these diameter ratios. These results would concur with the suggestion that CsCl is metastable. The absence of any binary superlattices at higher diameter ratios is also consistent with the observations of Hunt and Jardine[53] at $\sigma = 0.72$.

Chapter 6 Polydisperse Systems

6.1 Polydisperse Experimental Systems

As mentioned in the introduction there is great deal of interest in systems of colloidal hard spheres. Theories that have been successfully applied to the hard sphere model have also been applied to these suspensions in order to predict, amongst, other things their phase behaviour.

However although colloidal particles may have a near hard sphere potential, there is significant difference between colloidal systems and the theoretical hard sphere systems discussed in chapter 1. Simulated hard spheres are made to be monodisperse (i.e. they are uniform in size), whilst colloidal particles have a continuous distribution of particle diameters.

Experimentalists are not able to produce colloidal hard spheres that are monodisperse. There is always some degree of polydispersity (i.e. there is a variation in size). If colloidal systems are to be modelled by a hard sphere system, then the effects of polydispersity upon that system must first be understood. Polydispersity may, potentially, alter the entire phase behaviour of hard spheres. This may in some cases be used to an advantage. For instance it may be possible to prevent crystallisation by increasing the polydispersity. If it is the aim to form hard spheres crystals, then it is important to know the degree of polydispersity that will be tolerated.

Polydispersity, ψ, is defined as the standard deviation of the distribution of particle diameters divided by the mean.

$$\psi = \frac{\sqrt{\langle D^2 \rangle - \langle D \rangle^2}}{\langle D \rangle} \quad (6.1)$$

It might naively be assumed that the effects of small degrees of polydispersities are negligible. However even relatively low polydispersities, $\psi < 0.05$, may have a significant effect on the position and width of the freezing transition. Freezing occurs because a crystalline arrangement of spheres utilises the available space most efficiently, giving individual particles greater freedom to move about and consequently maximises their entropy. Any variation in particle diameter reduces the efficiency of packing of an ordered array so that the entropy of the crystal is reduced. Thus the crystal becomes less favourable than before. Increasing polydispersity favours the disordered fluid phase.

6.2 The Freezing Of Polydisperse Fluids

Barrat and Hansen[73] were the first to theoretically analyse this problem. In 1986 they applied a density functional theory of freezing to polydisperse colloidal crystals. They considered the effects of a triangular diameter distribution. They found that there was a polydispersity above which the crystal was unstable at all packing fractions. Above a "terminal" polydispersity of 0.067 the crystal was predicted to be mechanically stable but thermodynamically unstable. Calculations using a rectangular diameter distribution gave similar results. For both of these calculations it was assumed that the distribution of diameters was the same in the fluid and solid phases.

McRae and Haymet[74] applied density functional theory to the freezing of a polydisperse fluid of hard spheres. Interestingly they considered the formation of both FCC and HCP

crystals (sections 1.3 and 9.3). The used both the Schulz (section 7.1.1) and Gaussian distributions to describe the diameters of the particles. They found a terminal polydispersity of 0.05, above which no freezing took place. As this polydispersity was approached, the densities of the phases in the freezing transition were found to increase markedly. Bolhuis and Kofke[75] have carried out a Monte Carlo study of the freezing of polydisperse hard spheres. They imposed a chemical potential distribution on the hard spheres. They then used an isobaric semi-grand ensemble, where the identities (diameters) of particles were changed. This avoided the problems with particle insertion at high densities associated with the grand canonical ensemble. Gibbs-Duhem integration was used to trace the phase boundary from the well-known monodisperse transition to the unknown polydisperse transitions. They did not assume that the diameter distribution was identical in the two phases. Instead they found that there was a higher degree of polydispersity in the fluid than in the solid. They also found there was a terminal polydispersity above which no solid formed. They found this polydispersity to be 0.057, whilst the corresponding polydispersity in the fluid was 0.118.

Bartlett[76] has made a calculation based upon the assumption that the thermodynamic properties of a polydisperse distribution depend on the number, mean diameter, surface area and volume of the particles. These properties depend on the zeroth to third moments of the diameter distribution. This method has been labelled "scaled particle theory". The basis of this approximation is that the energy required to insert a particle into a given phase (i.e. the chemical potential) will depend only upon these four properties. Using this assumption, a polydisperse distribution may be approximated by a binary mixture. Binary mixtures of hard spheres have been well studied[77]. Using results for the solid phase and

the Mansoori, Carnahan, Starling and Leland (MCSL) equation of state of the fluid phase; the phase behaviour was evaluated. The terminal polydispersity was found to be 0.083. No evidence was found for any substantial difference in the distribution of diameters in the two phases.

Phan and Russel[78] performed a molecular dynamics simulation of 500 polydisperse hard spheres. Diameters were distributed according to a Gaussian distribution. By finding the intersect of the maximum packing fractions of the polydisperse solid and fluid, they predicted an upper limit to the terminal polydispersity of 0.12. In the polydisperse crystal it was found that larger particles tended to be surrounded by smaller ones. i.e. there was some degree of substitutional ordering occurring.

6.3 Other Effects of Polydispersity

Polydispersity may well have more effects than altering the location of or preventing the freezing transition. A number of studies have concerned themselves with other effects.

Sear[79] calculated that a fluid of hard spheres with polydispersity above 0.082 might phase separate and crystalise leading to two solid factions with polydispersities approximately half of the original. However, it was pointed out that such a transition may not be seen in experiment due to the intervention of the glass transition.

Cuesta[80] examined the behaviour of polydisperse fluids following the Boublik-Mansoori-Carnahan-Straling-Leland equation of state. He predicted that a system where the particle diameters followed a log-normal size distribution would demix if polydisperse enough. The threshold for demixing was estimated to be 0.12 polydispersity.

Bartlett[81] found similarly to Sear that if a fluid was sufficiently polydisperse (greater than 0.085), then crystallisation would occur simultaneously with fractionation. As the polydispersity increased, it was predicted that the fluid would split into a greater number of fractions.

Bartlett and Warren[82] carried out calculations that predicted an interesting phenomenon. At low polydispersities a single fluid to crystal transition is expected. However, as higher polydispersities, near to the terminal polydispersity are reached, it was predicted that there would exist a density above which the crystal would melt back into an amorphous phase. These re-entrant transitions were found to converge at the terminal polydispersity.

Williams et al.[83] used molecular dynamics to investigate the possibility that the formation of a hard sphere colloidal glass is as a result of polydispersity. They discovered that polydispersity decreased the speed of crystallisation and in some cases prevented it, so that a glassy phase was formed.

Evans et al.[84] predicted that a polydisperse colloidal system would never reach its true equilibrium state. As the smaller particles will diffuse more quickly through a system, they are more likely to incorporated into the crystal. They argued that once a crystal has been formed, steric hindrance prevents further particle movement, so that the mean size of the particles in the crystal will be smaller than that predicted.

Elliot et al.[85] examined the effects of polydispersity on the geometrical packing of spherical particles.

It is the intention of this study to apply Lennard-Jones Cell theory to a polydisperse crystal of hard spheres.

6.4 Plan of Action

The purpose of these calculations is twofold.

i) To develop a simple yet robust computational approach to calculate the properties of a polydisperse solid as a function of volume fraction and polydispersity.

ii) To develop a technique to handle polydisperse phase equilibrium.

Of particular interest will be the value obtained for the terminal polydispersity using this model.

There are a number of issues to consider in the application of Lenanrd-Jones cell theory to a polydisperse system. In section 7.1 the choice of diameter distribution is discussed. The specifics of the application of the cell model to a polydisperse system are detailed in section 7.2.

As the calculation of free volume in a polydisperse system proved to be expensive, techniques to reduce the calculation time are examined in sections 8.1 and 8.2.

Primary results are given in section 9.1 and the phase behaviour of a polydisperse system is examined in section 9.2.

Finally, in section 9.3 the influence of polydispersity upon the relative stability of the FCC and HCP structures is considered.

Chapter 7 Theory of Polydisperse Systems

7.1 Diameter Distributions

7.1.1 The Schulz Distribution

In order to perform any meaningful calculations on a polydisperse system, a mathematical description for the distribution of particle sizes is required. Two different distributions were initially considered. One of these was the Schulz distribution (fig. 7.1.1). The distribution of the diameters being given by

$$f(D)=\frac{1}{z!}\left(\frac{z+1}{\overline{D}}\right)^{z+1} D^{z} e^{\frac{-(z+1)D}{\overline{D}}},\ 0 \le D < \infty \quad (7.1.1)$$

$$z=\frac{1}{\psi^{2}}-1 \quad (7.1.2)$$

The Schulz distribution is preferable to a simple triangular or rectangular distribution in that it is more likely to accurately reproduce the distribution of diameters of a natural system. But it does have one unrealistic feature, as the distribution tails off to infinity, there is always a finite probability that a diameter may be unusually large. At a given volume fraction it is possible to calculate the separation distance, c between two neighbouring hard spheres.

$$c=\sqrt[3]{\frac{\pi\langle D^{3}\rangle}{3\sqrt{2}\phi}}(1), \quad (7.1.3)$$

where ϕ is the volume fraction and $\langle D^{3}\rangle$ is the mean of the cube of the diameter distribution.

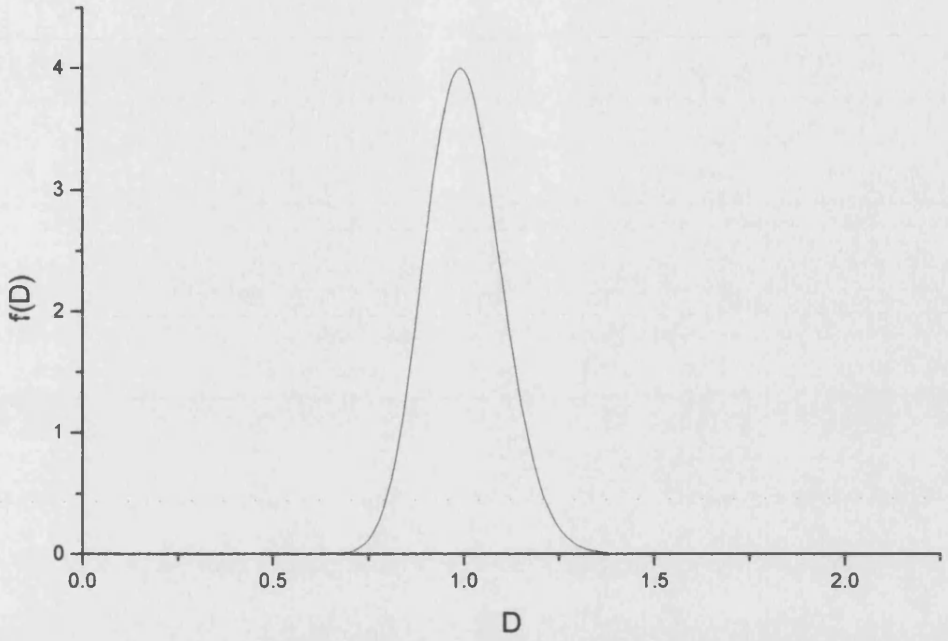

Figure 7.1.1 The Schulz Distribution, $\psi = 0.1$, $\overline{D} = 1$

From this the probability that two neighbours will overlap may be calculated. As the particles are hard spheres, any overlap is forbidden. To avoid overlap between neighbours there should be zero probability of a particle diameter being greater than the separation distance between particles. However there will always be a finite probability of particle overlap with any "long tailed" distribution. To overcome these problems a truncated Shultz distribution was considered. A cut-off point for the distribution was predetermined to ensure no particle overlap occurred. This presented two problems. Firstly this created a distribution that was irregular. At high volume fractions, the cut off point was quite close to the distribution peak. Secondly, calculations using a truncated Schulz distribution proved to be intractable. Consequently truncating the distribution was abandoned.

7.1.2 The Triangular Distribution

As an alternative the triangular distribution was considered. The triangular distribution (fig. 7.1.2) is given by

$$f(D) = \frac{1}{W^2}(1 - |1 - D|) \qquad 1 - W < D < 1 + W \qquad (7.1.4)$$
$$= 0 \qquad \text{Otherwise}$$

$$W = \sqrt{6}\sigma \qquad (7.1.5)$$

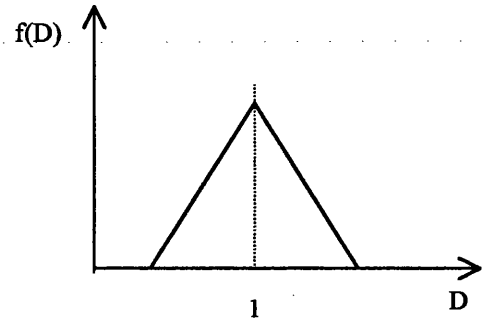

Figure 7.1.2 – The triangular distribution.

But this distribution, whilst avoiding the possibility of any overlap, is not one that may be expected to accurately describe an experimental system. Consequently the Shultz distribution was retained as the distribution used to describe the diameters of the particles.

7.1.3 Numerical Integration

As will be discussed in section 7.2.1. the Helmholtz free energy is given by

$$\frac{A^{ex}}{NkT} = -\sum_i P_i \ln v_{fi}, \quad (7.1.6)$$

where P_i is the probability of observing a cell of type i. Cells are characterized by the diameters of the tagged particle and its neighbours. In each FCC or HCP cell there are, in total, thirteen particles. Each particle, labelled 0 to 12 has a diameter that comes from the distribution. Hence 7.1.6 becomes

$$\frac{A^{ex}}{NkT} = -\iiint\iiint\iiint\iiint\int \ln v_f \prod_{j=0}^{12} dD_j \quad (7.1.7)$$

Such an expression may not be readily evaluated. It is necessary to resort to a form of numerical integration (effectively a summation),

$$\int f(D)dD \cong \sum_{x_i} w_i f(x_i) \quad (7.1.8)$$

The continuous distribution of particle sizes is approximated by a distribution with a finite number of discrete diameters, where w_i is the probability of observing a particle with diameter x_i.

As it is still necessary to perform the summation over each particle present in the cell, it is not possible to use a large number of discrete diameters to approximate the continuous distribution. The number of different cells generated by n discrete particle diameters being n^{13}. As only a few discrete diameters may be used, it is important to choose them carefully.

A distribution, continuous or discrete, is characterised by its moments. The moments, c_j are defined by

$$c_j = \int_{-\infty}^{\infty} f(D)D^j dD, \quad (7.1.9)$$

for a continuous distribution, where $f(D)$ is the distribution function. For a discrete distribution, with n points, they are given by

$$c_j = \sum_{i=1}^{n} w_i x_i^{\,j} \text{ ,(7.1.10).}$$

The discrete diameters are chosen in such a way as to match as many moments of the discrete distribution to the continuous.

Gaussian Quadrature is utilized to match the first $2n-1$ moments of the distributions using n discrete points.

In this method, the roots of one of a series of orthogonal polynomials determine the discrete diameters. The polynomials, P_J are generated by a recurrence relationship.

$$P_{-1} = 0, \qquad (7.1.11)$$

$$P_0 = 1, (7.1.12)$$

$$P_{J+1} = (x - a_j)P_j - b_j P_{J-1}, \qquad (7.1.13)$$

$$\text{where } a_J = \frac{\langle xP_j | P_J \rangle}{\langle P_J | P_J \rangle} \quad (7.1.14)$$

$$\text{and } b_J = \frac{\langle P_J | P_J \rangle}{\langle P_{J-1} | P_{J-1} \rangle}. \quad (7.1.15)$$

The series of polynomials depends on the original distribution used. Some notation used is

$$\langle P_J | P_K \rangle = \int_{-\infty}^{\infty} f(x) P_J P_K dx . \qquad (7.1.16)$$

Once the polynomials had been generated and the roots found, the weights, w_i, corresponding to the discrete diameters, x_i, were found by solving the set of linear equations.

$$\sum_{i=1}^{n} w_i x_i^{\,j} = c_j \qquad j = 0,1...2n-1 \qquad (7.1.17)$$

Initially an attempt was made to generate the polynomials numerically. Whilst this is theoretically possible, problems were encountered when attempting to evaluate expressions like a_2. a_2 is given by

$$a_2 = \frac{\langle xP_2 | P_2 \rangle}{\langle P_2 | P_2 \rangle}. \qquad (7.1.18)$$

$$\text{In practise } \langle xP_2 | P_2 \rangle = \langle P_2 | P_2 \rangle, \qquad (7.1.19)$$

$$\text{so } a_2 = 1. \qquad (7.1.20)$$

But the algorithm used was evaluating the numerator and denominator numerically. Although the calculation was accurate to about six significant figures, slight inaccuracies were present. The calculation proved to be very sensitive to these inaccuracies and larger errors were thus produced. In order to get around this problem it was decided to do the calculations analytically. These analytical calculations are reproduced in appendix A.

Once the continuous distribution is approximated by a discrete one, the possibility of overlap between particles with larger diameters is removed for most cases. This was another reason why it was decided to stick with the non-truncated Schulz distribution to describe the particle diameters in the polydisperse system. Note that there always remains a possibility of particle overlap at high densities and polydispersities. This issue is considered in section 9.1.4.

If three diameter points are used (using the roots of P_3), then the number of cells that are generated is $3^{13} = 1{,}594{,}323$. Initially the calculations were performed on a 486\66Mhz P.C. The algorithm used to calculate the free volumes was the "Trapezium rule", which was used when calculating the free volume of binary systems (chapter 4). In this algorithm the free volume is split into sections by a grid in the XY plane. The height of each section is then determined analytically to obtain an approximate free volume. To obtain even approximate results requires an absolute minimum of 150^2 sections. 1000^2 sections are required for accurate results. As there were 1,594,223 free volumes to calculate for each set of values of the polydispersity and free volume, this meant that it would have taken 18 days to compute approximate results for each set of values.

7.2 The Application of the Cell Model

7.2.1 Statistical Mechanics

The cell model was introduced in section 1.2, so here we details its application to a polydisperse system.

In the binary case the different types of cells present had to be accounted for (section 3.1). This was not a large obstacle for the binary system as there were at most three different types of cells. In the polydisperse case, there is an infinite number of different types of possible cells. Even after the continuous distribution is split into a number of different size components there remain a large number of different cells.

For an N-component mixture, the semi-classical partition function, Z_N is used. If there are N_j molecules of type j then the total number of particles, N, is given by

$$N = \sum_{j=1}^{n} N_j \qquad (7.2.1)$$

and the partition function (assuming the occupation of each cell is independent of its neighbours)

$$Z_N = \frac{N!}{N_1!N_2!....N_n!} \prod_i z_i^{NP_i}, \quad (7.2.2)$$

where z_i is the semi-classical partition function of cell i. z_i is given by the standard result

$$z_i = \frac{1}{\lambda_{ci}^{\,3}} \int d^3 r e^{-\beta \Phi_i(r)} \quad (7.2.3)$$

where $\beta = \frac{1}{k_B T}$, Φ is the potential energy function and λ_{ci}, the thermal wavelength is given by

$$\lambda_{ci} = \frac{h}{\sqrt{2\pi m k_B T}}. \qquad (7.2.4)$$

P_i is the probability of observing a cell of type i. If no substitutional ordering is assumed then

$$P_i = x_1^{S_{1i}} x_2^{S_{2i}} \ldots x_n^{S_{ni}}, \quad (7.2.5)$$

where S_{ij} is the number of particles of type j in cell $\underline{i}$ (including the tagged particle) and x_j is the mole fraction (or weight) of particle j. Since each cell is the unit cell of the FCC or the HCP structure,

$$\sum_{j=1}^{n} S_{ij} = 13. \quad (7.2.6)$$

The cell configurational integral, q_i is defined as

$$q_i = \int d^3 r e^{-\beta \Phi_i(\underline{r})}. \text{ So } (7.2.7)$$

$$Z_n = \frac{N!}{N_1! \ldots N_n!} \prod_i \left(\frac{q_i}{\lambda_{ci}^{\ 3}} \right)^{NP_i}. \quad (7.2.8)$$

As discussed in the introduction, the cell configurational integral, q_i is equivalent to the free volume, v_{fi}.

To calculate the pressure and the chemical potentials the excess Helmholtz free energy,

$$A^{ex} = A - A_{ideal}, \qquad (7.2.9)$$

$$\text{where } A_{ideal} = \sum_i x_i \ln x_i \lambda_i^3, \qquad (7.2.10)$$

was calculated.

Standard statistical mechanics gives the result

$$\frac{A^{ex}}{NkT} = -\sum_i P_i \ln v_{fi} \qquad (7.2.11)$$

The pressure is given by

$$p = -\left(\frac{\partial A}{\partial V}\right)_{T,n_i} \qquad (7.2.12)$$

This gives the result

$$\frac{p}{NkT} = \left(\frac{\partial \sum_i P_i \ln v_{fi}}{\partial V}\right) \qquad (7.2.13)$$

The volume fraction, ϕ is given by

$$\phi = \frac{N\pi\langle D^3\rangle}{6V}, \text{ so} \qquad (7.2.14)$$

$$\frac{d\phi}{dV} = \frac{-N\pi\langle D^3\rangle}{6V^2}, \qquad (7.2.15)$$

$$\frac{d}{dV} \equiv \frac{-N\pi\langle D^3\rangle}{6V^2}\frac{d}{d\phi} \qquad (7.2.16)$$
$$\frac{d}{dV} \equiv -\frac{\phi}{V}\frac{d}{d\phi}$$

So that the pressure may be obtained by

$$\frac{pV}{NkT} = -\phi\frac{d}{d\phi}\sum_i P_i \ln v_{fi}. \qquad (7.2.17)$$

This differential was evaluated numerically from a two point calculation where the separation of the two volume fractions were carefully chosen to give an accurate representation of the gradient at the mid-point.

The pressure can also be obtained by differentiation of the cell model free volume. This gives the expression for the pressure[86]

$$\frac{pV}{NkT} = 1 + \frac{1}{3}\left\langle \frac{s_f}{v_f} \right\rangle, \qquad (7.2.18)$$

where s_f is the surface area of the free volume.

This expression was the motivation for the development of the analytical algorithm discussed in section 8.2. Note all volumes and areas are measured relative to the mean diameter $\langle D \rangle$.

The chemical potential of a species i is given by

$$\mu_i = \left(\frac{\partial A}{\partial N_i}\right)_{T,V,\{N_j\}} \qquad (7.2.19)$$

$$x_i = \frac{N_i}{\sum_j N_j} \qquad (7.2.20)$$

$$\frac{\partial x_i}{\partial N_i} = \frac{1}{\sum_j N_j} - \frac{N_i}{\left(\sum_j N_j\right)^2} \qquad (7.2.21)$$
$$= \frac{1}{N}(1 - x_i)$$

$$\frac{\partial x_i}{\partial N_j} = \frac{-x_i}{N}, i \neq j \qquad (7.2.22)$$

$$\frac{\partial}{\partial N_k} = \sum_i \frac{\partial x_i}{\partial N_k}\frac{\partial}{\partial x_i}, \text{ so} \qquad (7.2.23)$$

$$\frac{\partial}{\partial N_k} = \frac{1}{N}(1 - x_k)\frac{\partial}{\partial x_k} + \sum_{i \neq k} -\frac{x_i}{N}\frac{\partial}{\partial x_i} \qquad (7.2.24)$$

$$\beta A = N\left\{\sum_{j=1}^{n} x_j \ln x_j - \sum_{i=1}^{Nlcell} P_i \ln\left(\frac{q_i}{\lambda_{ci}{}^3}\right)\right\} \qquad (7.2.25)$$

$$\beta \frac{\partial A}{\partial N_k} = \frac{\beta A}{N} + N\frac{\partial}{\partial N_k}\left\{\sum_{j=1}^{n} x_j \ln x_j - \sum_{i=1}^{N_{cell}} P_i \ln\left(\frac{q_i}{\lambda_{ci}{}^3}\right)\right\} \qquad (7.2.26)$$

$$\beta\mu_k = \frac{\beta A}{N} + (1 - x_k)(\ln x_k + 1) - \sum_{j \neq k} x_j(\ln x_j + 1) - N\frac{\partial}{\partial N_k}\left\{\sum_{i=1}^{N_{cell}} P_i \ln\left(\frac{q_i}{\lambda_{ci}{}^3}\right)\right\}$$
$$= \ln x_k - \sum_{i=1}^{Nlcell} P_i \ln\left(\frac{q_i}{\lambda_{ci}{}^3}\right) - N\frac{\partial}{\partial N_k}\left\{\sum_{i=1}^{Nlcell} P_i \ln\left(\frac{q_i}{\lambda_{ci}{}^3}\right)\right\}$$

(7.2.27)

as the cell partition functions q_i are independent of N_k then

$$\beta\mu_k = \ln x_k - \sum_{i=1}^{N_{cell}} \left(P_i + N \frac{\partial}{\partial N_k} P_i \right) \ln\left(\frac{q_i}{\lambda_{ci}^{\ 3}} \right) \quad (7.2.28)$$

The probability of observing a cell, i is given by

$$P_i = x_1^{\ S_{i1}} x_2^{\ S_{i2}} \ldots . x_n^{\ S_{in}}, \quad (7.2.29)$$

where S_{ik} is the number of particles of type k in cell i (including the centre tagged particle). So

$$\begin{aligned} N \frac{\partial}{\partial N_k} P_i &= (1 - x_k) \left[x_1^{\ S_{i1}} \ldots . x_k^{\ S_{ik}-1} \ldots . x_n^{\ S_{in}} \right] S_{ik} \\ &\quad + \sum_{j \neq k} - x_j \left[x_1^{\ S_{i1}} \ldots . x_j^{\ S_{ij}-1} \ldots . x_n^{\ S_{in}} \right] S_{ij} \quad (7.2.30) \\ &= S_{ik}(1 - x_k) \left(\frac{P_i}{x_k} \right) - \sum_{j \neq k} S_{ij} P_i \end{aligned}$$

$$\begin{aligned} P_i + N \frac{\partial}{\partial N_k} P_i &= S_{ik} \frac{P_i}{x_k} - \sum_{\text{all } j} S_{ij} P_i + P_i \\ &= P_i \left\{ \frac{S_{ik}}{x_k} - Z \right\} \end{aligned} \quad (7.2.31)$$

$$\text{as } \sum_{\text{all } j} S_{ij} = Z + 1, \text{ so } \quad (7.2.32)$$

$$\beta\mu_k = \ln x_k - \sum_{i=1}^{N_{cell}} \left(P_i \left\{ \frac{S_{ik}}{x_k} - Z \right\}_i \right) \ln\left(\frac{q_i}{\lambda_{ci}^{\ 3}} \right) \quad (7.2.33)$$

where Z is the nearest neighbour number. In this current case $Z = 12$.

7.2.2 Moment Chemical Potentials

As phase equilibria in polydisperse systems is complex, it is initially convenient to focus on just on the cloud and shadow boundaries. The shadow curve represents the line of the minority phase that just separates from the majority phase, described by the cloud curve. In these studies, the polydisperse fluid was chosen as the majority phase, with the polydisperse solid the emerging minority phase. For completeness the Schultz distribution was chosen. The mean diameter of the particles in the majority phase is used as the unit of length throughout the calculations.

To establish the conditions under which the phases coexist, the particle chemical potentials must be matched as well as the osmotic pressure. Given the infinite number of species present in a polydisperse system, this is not a trivial task. Sollich and Cates[87] proposed a method to reduced the dimensionality of polydisperse systems, thus making them more manageable. They suggested that the original multi-dimensional free energy surface might be projected onto a reduced subspace of variables. The moment densities,

$$m_j = \int_{-\infty}^{\infty} \rho(D) D^j dD = \rho c_j \qquad (7.2.34)$$

being the most convenient set of variables.

As

$$\begin{aligned} \mu_i &= \left(\frac{\partial A}{\partial N_i} \right)_{T,V,\{N_j\}} \\ &= \sum_k \frac{\partial a}{\partial m_k} D_i^k \qquad (7.2.35) \\ &= \sum_k \mu_{mk} D_i^k \end{aligned}$$

the equality of particle chemical potentials implies also the equality of "moment" chemical potentials,

$$\mu_{mk} = \frac{\partial a}{\partial m_k}, \quad (7.2.36)$$

in coexisting phases. As Sollich and Cates indicated, equilibrium may be established by equating these moment chemical potentials in the analogous to the conventional methods by which "normal" chemical potentials are balanced.

There being an infinite number of moment densities, this is still however not a trivial problem. Sollich and Cates argued that the most important moments were those that affect the excess free energy. Accordingly the infinite-dimensional space was split into two subspaces, a "moments" subspace and an orthogonal "transverse subspace" containing the remaining degrees of freedom. Phase equilibria was determined by establishing coexistence planes in the moments subspace, while free energy was minimized in the transverse subspace.

In particular it was suggested that the zeroth and first moment of the diameter distribution be used to define a moment space. The zeroth moment being equivalent to the particle density, ρ. As only these two moments are used, the shape of the distribution is identical in the coexisting phases.

Since $\mu_i = \sum_k \mu_{mk} D_i^k$, then the moment chemical potentials are the coefficients of the polynomial describing the relationship between the chemical potential of a species and its diameter.

In this study, the continuous distribution is approximated by a discrete one, the excess portion of the chemical potentials of particles with certain diameters are obtained from the calculations. The excess portion of the moment chemical potentials is therefore readily obtained by fitting a suitable polynomial to the data obtained.

Finding the ideal portion of the moment chemical potentials is not so straightforward, it being necessary to project the ideal free energy surface onto the reduced subspace. This was done by maximizing the entropy whilst assuring the two moments of the distribution being used are fixed. Warren has derived analytical results for the one and two moment cases[88], we use these to find the ideal portion of the moment chemical potentials. For the Schulz distribution,

$$\mu_0^{id} = \ln\rho - \alpha\ln\langle D\rangle \quad (7.2.37)$$

$$\mu_1^{id} = -\alpha\langle D\rangle \quad (7.2.38)$$

$$\alpha = 1/\sigma^2 \quad (7.2.39)$$

7.2.3 Calculating Equilibrium Conditions

Using a projected free energy surface, we are now able to establish the conditions for the cloud-shadow curve by satisfying just three equations.

$$p_s = p_f \quad (7.2.40)$$

$$\mu_{sm0} = \mu_{fm0} \quad (7.2.41)$$

$$\mu_{sm1} = \mu_{fm1} \quad (7.2.42)$$

The properties of the fluid phase are obtained by use of the well known MSCL equation of state already discussed in sections 3.3 and 3.4.

As there are three equations to be satisfied, there must of course be three thermodynamic variables to describe the position of equilibrium. The number densities of the fluid and solid phases are two of them. The third variable is the mean particle diameter of the emerging solid phase, relative to the fluid phase. This will give a measure of the degree of fractionation that accompanies the phase transition. Strictly speaking this should be fixed at unity so that the shape of the distribution is the same as in the majority phase. But this rule is only broken infinitesimally by the emerging solid phase.

Chapter 8 Calculation of Free Volume in a Polydisperse System

8.1 Use of the Symmetry to Reduce the Length of the Calculations

Given the large number of cells that are generated by three diameter points, it is very necessary to avoid any duplication of effort when calculating the free volume. This may be done by taking the high degree of symmetry, present in the FCC and HCP arrangements, into account.

8.1.1 Symmetry of a Face Centred Cubic Arrangement

There are twelve neighbours that surround the tagged particle in its cell. The tagged particle's diameter varies, as do the neighbours'. The positions of the neighbours may be labelled from 0 to 11 (fig. 8.1.1). As the diameter of the particle at each position changes in turn, a new "arrangement" is formed. The total number of arrangements generated in this way is 3^{12}.

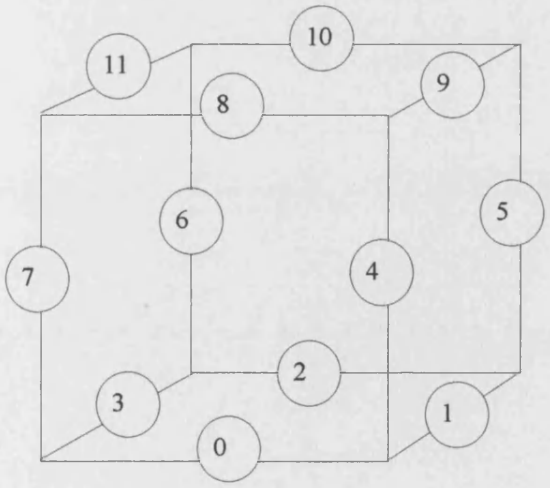

Figure 8.1.1 The labelling used for neighbour positions in the FCC arrangement

It is possible to perform a variety of transformations on an arrangement of neighbours that only changes the labelling of the positions not the actual positions in space themselves. Such a transformation will have no effect on the magnitude or shape of the free volume. Therefore an arrangement that may be produced by a transformation on another arrangement will lead to the same free volume as the original. i.e. The free volumes will be similar. Consequently, methodically stepping through all possible arrangements leads to many unnecessary calculations being performed. To avoid this replication of effort, the set of arrangements that produces no similar free volumes, was compiled as follows.

For the FCC cell, there are a total of 48 different possible transformations that only alter the labelling.

Every arrangement (0 to 11) may be rotated in one of twelve ways, such that each neighbour ends up in a predefined position (position 0). Following this one of four "secondary" transformations may be performed (fig. 8.1.2).

i) Unitary transformation (no change)

ii) Reflection (mirror plane going through positions 0,2,8,10)

iii) Two-fold rotation (axis of rotation going through positions 0,10)

iv) Combined transformation, reflection (ii) followed by rotation (iii).

By combining each of the twelve rotations with each of the other four secondary transformations, a total of $12 \times 4 = 48$ combined transformations are thus possible.

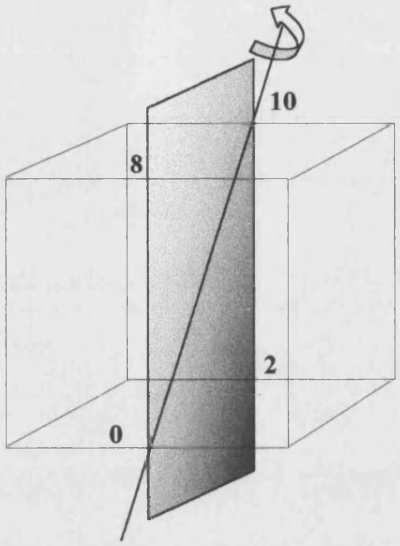

Figure 8.1.2 Transformations (mirror & rotation) performed on the arrangements.

Using a spreadsheet a matrix was produced to perform these transformations. Each particle size was given a digit to identify it. When using the three-point Gaussian Quadrature approximation, the smallest was 0, the largest 2. An identification number was then calculated for each cell arrangement. If d_i is the digit of the particle at position i then the identification number is given by

$$w = \sum_{i=0}^{11} d_i \times 3^i \,. \qquad (8.1.1)$$

This is equivalent to writing out the arrangement as a ternary number, $d_{11}d_{10}d_9d_8d_7d_6d_5d_4d_3d_2d_1d_0$.

Every possible arrangement was then stepped through starting from $w = 0$ and ending up at $w = 3^{12} - 1$. This was done using a recursive subroutine. i.e. The particle size at position 0 was varied, then for each variation the subroutine called itself to vary position 1 and so on. The 48 transformations were performed on each arrangement generated. If the lowest identification number achievable was that of the arrangement started with then that arrangement was added to a list. Else, if it was possible to

generate an arrangement with a lower identification number than the original then that arrangement was found in the list (using a quick search) and the count for that arrangement incremented (fig. 8.1.4).

In this way a unique set of arrangements of neighbours was produced. The total set of arrangements and their counts was written to a file in binary format to be used by the algorithm doing the main calculation.

In this fashion it was discovered, there are 12111 ways of arranging twelve neighbours for a FCC cell, when each neighbour may be one of three sizes. This means that the total number of cells that had to be considered was $3 \times 12111 = 36333$, as the tagged particle had to be varied as well. At this rate each data point would have taken 10 hours to compute (reduced from 18 days). Since at least 250 data points were required, this constituted an impracticably long time.

8.1.2 Symmetry of a Hexagonal Close Packed Arrangement

HCP does not have as high a degree of symmetry as FCC. The arrangement of neighbours and the labelling of their positions used is shown in fig. 8.1.3. The positions were classified into two types, "end types" (0,1,4,6,10,11) and "middle types" (2,3,5,7,8,9).

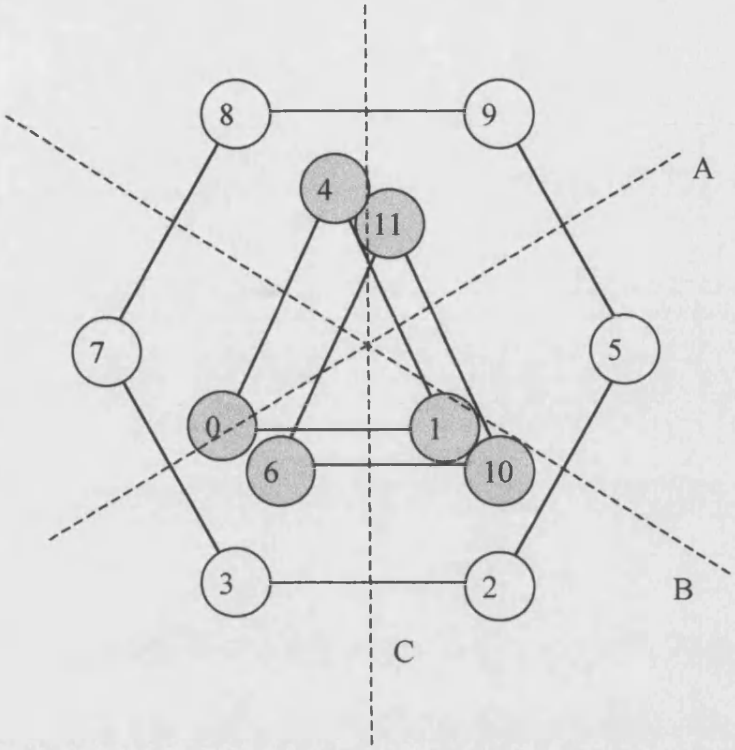

Figure 8.1.3 The labelling used for neighbour positions in the HCP arrangement and three of the mirror planes present.

The transformations that were used to generate the list of arrangements were

i) Three-fold rotation (axis perpendicular to plane containing middle types)

ii) Reflection (mirror is plane containing middle types)

iii) Reflection (mirror plane A in fig. 8.1.3)

iv) Reflection (mirror plane B in fig. 8.1.3)

v) Reflection (mirror plane C in fig. 8.1.3)

Combining these transformations gives a total of 24 unique transformations. Using the same algorithm that was used for the FCC arrangement, it was discovered the total number of ways of arranging three distinct diameters in a HCP cell is 46674.

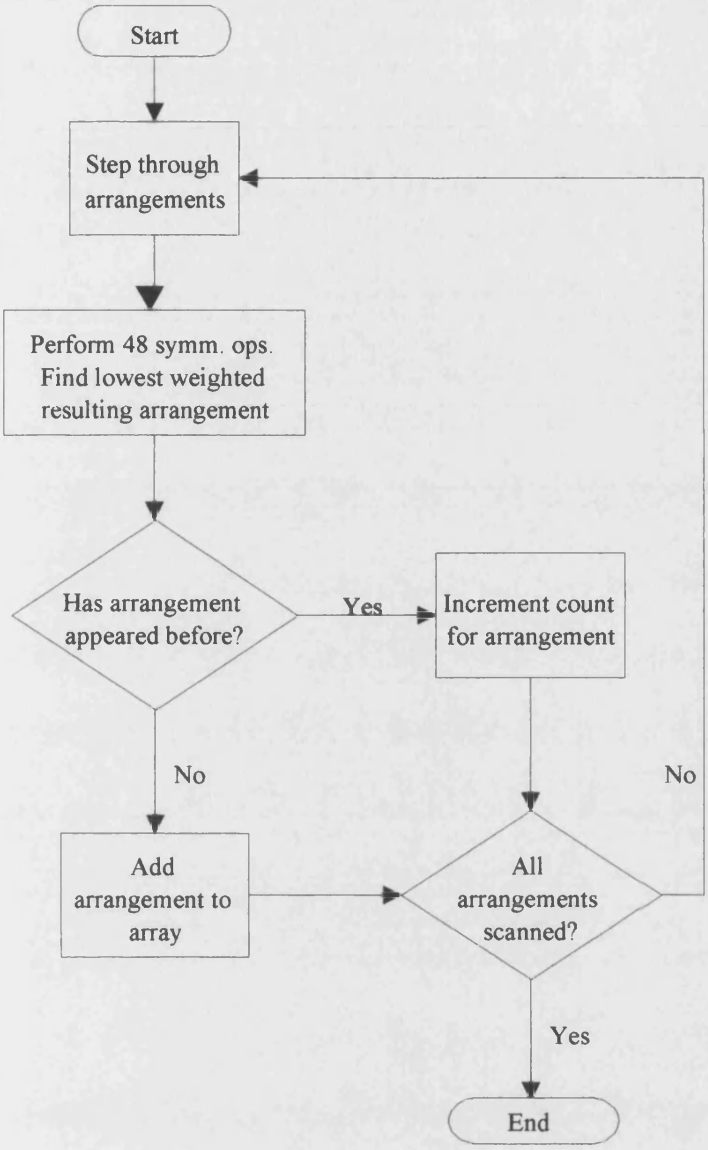

Figure 8.1.4 Flow diagram illustrating the algorithm used to search for congruent arrangements of neighbours.

8.2 The Calculation of Free Volume in a Polydisperse System

8.2.1 Techniques to Calculate Free Volume

The free volume of a polydisperse system of spheres was calculated by the trapezium rule method detailed in section 2.4.4.The free volume is split up into many sections with a rectangular grid in the XY plane (fig. 8.2.1). The height of each section was then calculated analytically, while integration in the X and Y planes was evaluated using the trapezium rule. This method provides more accurate results than the Monte Carlo method (section 4.3). The Monte Carlo method converged very slowly with the number of points used. Note that in the trapezium rule method, an analytical calculation is performed over one dimension and approximate integration is used over the remaining two. The code for the algorithm that performed the trapezium rule integration, TRAPINT, is given in appendix C.1.

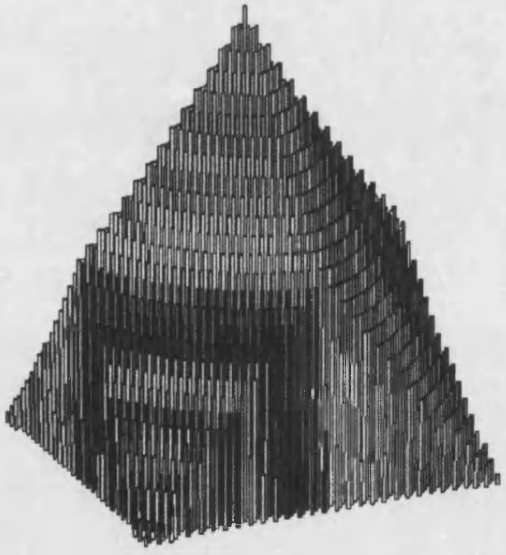

Figure 8.2.1 When using the trapezium rule integration method, the free volume is effectively approximated by set of cuboids. The set of cuboids corresponding to the upper half of the free volume is shown.

A brief attempt was also made at developing a method that split the free volume into slices. The idea being that the area of each slice was calculated analytically with a numerical integration along one dimension. This method, however, proved to be too complicated. The shape of each slice is determined by a number of overlapping circles and it is not trivial to calculate the area.

While the trapezium rule is notably faster than the Monte Carlo method it however was not sufficiently computationally efficient considering the number of free volume calculations necessary. Typically it takes, of order, one second to calculate each free volume (using 150^2 sections). Since each polydisperse sample required the calculation of 36,333 free volumes, this was taking in excess of ten hours (twenty to calculate the pressure by numerical differentiation). Even then, numerical differentiation was not proving to be a very favourable method to calculate the pressure. Consequently it was decided to evaluate the pressure via an alternative more rapid route.

8.2.2 Calculation of the Pressure in a Polydisperse Face Centred Cubic Crystal

As discussed in section 7.2, the pressure is dependent on the ratio of the free area to the free volume, where the free area is the surface area of the free volume shape. The trapezium rule method did not appear to be suitable to accurately calculate the free area. For this reason it was decided to develop an analytical method to calculate the free area. Having started to develop this method it was decided to extend it to calculate the free volume analytically as well.

The analytical algorithm was first developed to calculate the free volume of a particle in an FCC arrangement.

As there are twelve exclusion spheres in each arrangement, there are twelve concave faces to the free volume. Each face was examined separately and the associated free volume and free area calculated. The other eleven exclusion spheres determine the shape and thus the contribution each face makes to the free volume/area. In fig. 8.2.2 the face under consideration is the face belonging to the sphere shaded in black. The only sphere, which does not affect this face, is the sphere shaded in yellow.

It was initially envisaged that only the four spheres shown in blue in fig. 8.2.2 would affect the face of the free volume of the sphere in black (fig. 8.2.3). The view shown is the view looking from the centre of the arrangement towards the black sphere. The exclusion spheres overlap with each other to form circles. It is these circles whose arcs form the edges to each face. The characteristic shape of the face is shown in fig. 8.2.3.

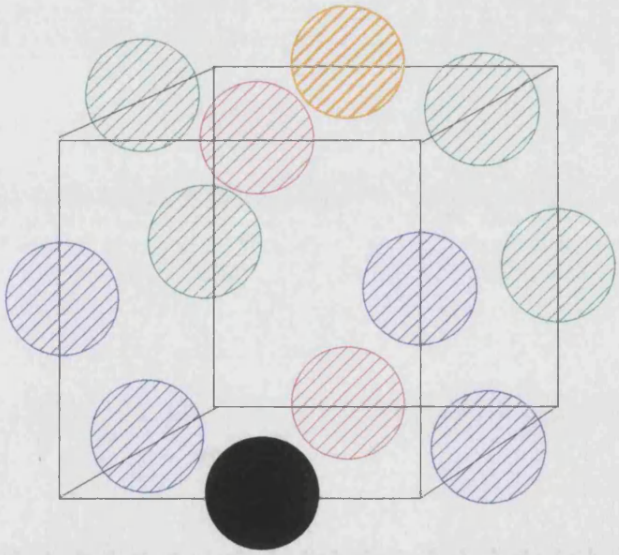

Figure 8.2.2 The arrangement of twelve exclusion spheres that determine the shape of the free volume. There are twelve faces corresponding to each of the exclusion spheres. The shape of each face is determined by the other eleven exclusion spheres.

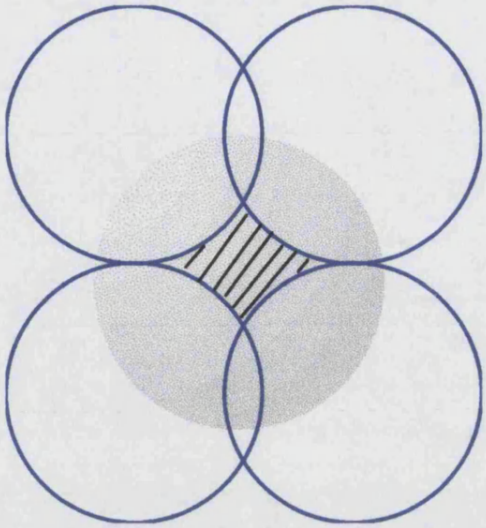

Figure 8.2.3 The hatched regions shows the shape of one face of the free volume. The shape is determined by the overlapping exclusions spheres from the four spheres outlined in blue.

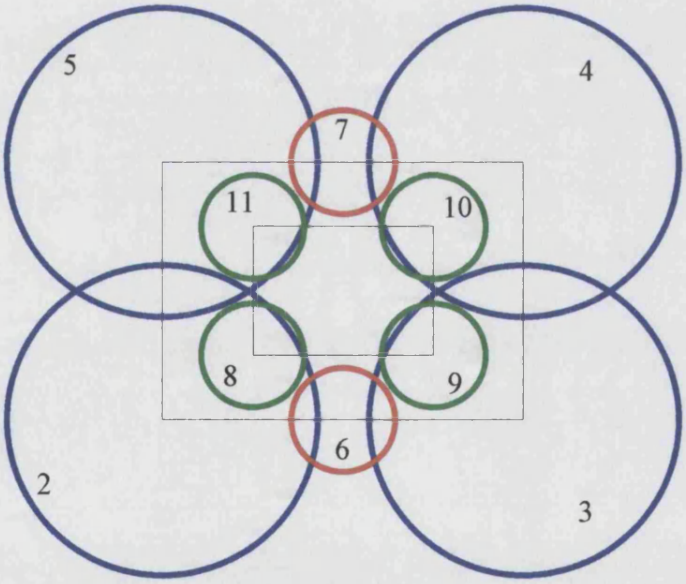

Figure 8.2.4 The positions of the overlapping circles which define the characteristic shape of each face.

Non-Euclidean spherical geometry was used to analyse the area of each face[89]. The principle axis was defined as the line going from the centre of each sphere towards the centre of the arrangement. Figure 8.2.4 shows the view looking from the centre of the arrangement towards the black sphere. It shows the positions of the various circles

that make up the edges of the face. The positions and distance between the centres of the circles are measured in terms of the angles subtended at the centre of the sphere of interest (in this case the black sphere). These angles remain unchanged throughout all calculations and were thus calculated and supplied as constants in the algorithm.

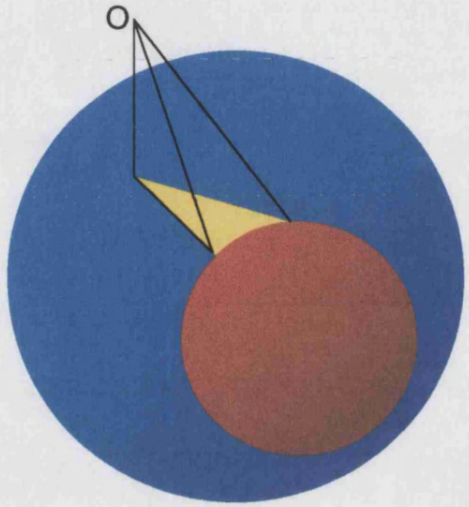

Figure 8.2.5 A section of the free volume. The area shaded yellow is part of the face of the free volume and lies on the face of the exclusion sphere, shown in blue. The red circle is an overlapping exclusion sphere that determines the shape of the face. The section of the free volume is the pyramid with base shaded yellow and vertex at O.

In order to calculate the free volume and area it is necessary to know the exact details of the arcs, which bound each face. Each arc is split by the line radiating out from the centre of the face to its own centre. Each half arc encompasses a section of the face of the free volume (fig. 8.2.4). Once all the dimensions shown in fig. 8.2.6 are known, as well as the distance, c between neighbours, the radius, R_n of each exclusion sphere and the angle β_i, then the contribution to the free volume and free area of that section may be calculated.

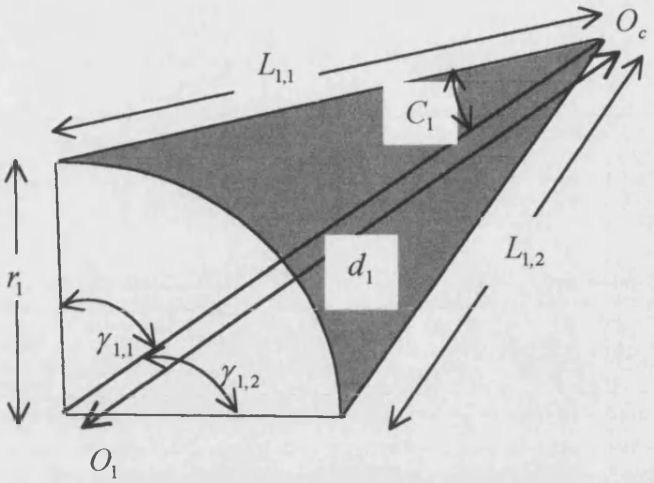

Figure 8.2.6 Dimensions of concave face of section of free volume. The free area is hatched. O_c is the centre of the face and O_1 is the centre of the arc with radius r_1.

The first step of the algorithm is to form a complete loop out of the circles, which bound each face. To do this the algorithm starts at circle 2 or 8 if it is not covered by 2 (fig. 8.2.4). It then calculates the overlap with all circles up to, but not including the circles diagonally opposite. The circle, which forms the next part of the loop, is the one, which overlaps the most with the original circle. The algorithm then moves onto this circle and proceeds until a complete loop has been formed (fig. 8.2.8).

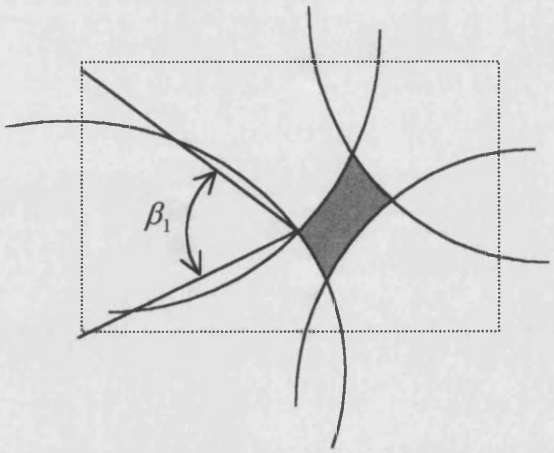

Figure 8.2.7 The angle β formed by the triangle whose points are the centres of two overlapping circles and the point at which they overlap. The free area is hatched.

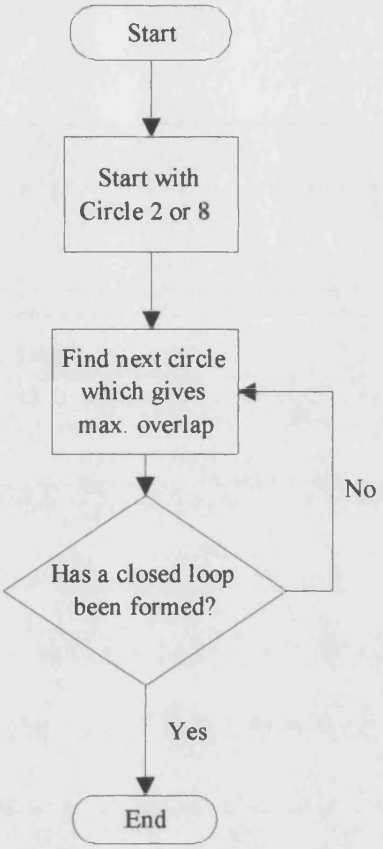

Figure 8.2.8 Algorithm used to form a complete loop out of the circles bounding the face.

It is possible that two opposing circles may overlap. If this occurs then either the face is split into two or the face is completely covered over (fig. 8.2.9). The algorithm checks for both of these possible conditions and adjusts the calculation to compensate. After considering and allowing for any possible combinations of overlaps between circles, the algorithm finally calculates the free volume and area for each section. The free surface area s_f is given by

$$s_f = \sum_n \left[2\pi + \left(\sum_i (\gamma_{i,1} + \gamma_{i,2}) \mathrm{Cos}\, r_i - \beta_i \right) \right] \times R_n^{\,2} \qquad (8.2.1)$$

where n labels the face and i the sections.

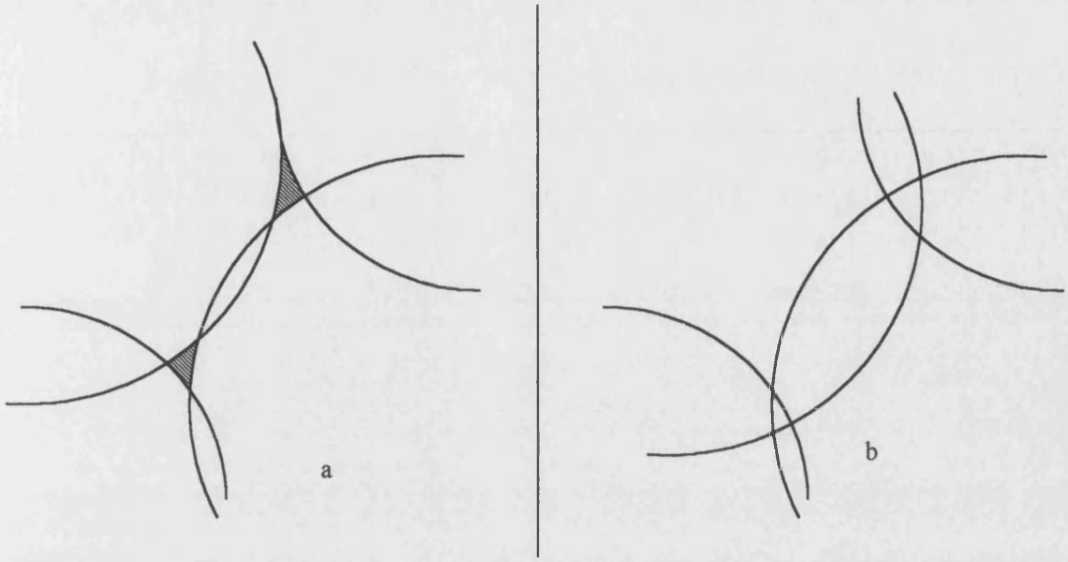

Figure 8.2.9 If the overlapping circles are large enough then it is possible that either one face of the free volume is a) split into two halves (hatched) or b) disappears completely.

The free volume, v_f is given by

$$v_f = \sum_n \left[\sum_i \left(\begin{array}{l} \sum_{k=1,2} \left(\begin{array}{l} \left(\mathrm{Tan}^{-1}\left(\dfrac{\mathrm{Cot}\,\mu_{i,k}}{S_{i,k}} \right) - \mathrm{Tan}^{-1}\left(\dfrac{\mathrm{Cot}(\mu_{i,k} + C_{i,k})}{S_{i,k}} \right) \right) \dfrac{1}{2S_{i,k}} \\ + \dfrac{(\mathrm{Cos}\,2r_i - 1)\gamma_{i,k}\,\mathrm{Cos}\,d_i}{4} \\ - \mathrm{Sin}\,\gamma_{i,k}\left(r_i - \dfrac{\mathrm{Sin}\,2r_i}{2} \right) \dfrac{\mathrm{Sin}\,d_i}{2} \end{array} \right) \times cR_N^{\,2} \\ - \left((\gamma_{i,1} + \gamma_{i,2})\,\mathrm{Cos}\,r_i - \beta_i \right) \times R_N^{\,3} \end{array} \right) - 2\pi R_N^{\,3} \right] \times \frac{1}{3}$$

(8.2.2)

where

$$S_{i,k} = \sqrt{1 + K_{i,k}^{\,2}}, \qquad (8.2.3)$$

$$K_{i,k} = \frac{1}{\mathrm{Tan}\, L_{i,k}\, \mathrm{Sin}\, \mu_{i,k}}, \qquad (8.2.4)$$

$$\mathrm{Tan}\, \mu_{i,k} = \mathrm{Sin}\, C_{i,k} \Big/ \left(\frac{\mathrm{Tan}\, L_{i,k}}{\mathrm{Tan}\, d_i} - \mathrm{Cos}\, C_{i,k} \right) \qquad (8.2.5)$$

The derivation of these expressions is detailed in appendix B. The code for the algorithm that performed this calculation is given in appendix C.2.

8.2.3 Analytical Technique to Calculate the Free Volume in a Polydisperse Hexagonal Close Packed Crystal

The analytical algorithm used to calculate the free volume for an HCP arrangement is different to that used for the FCC arrangement in a number of respects.

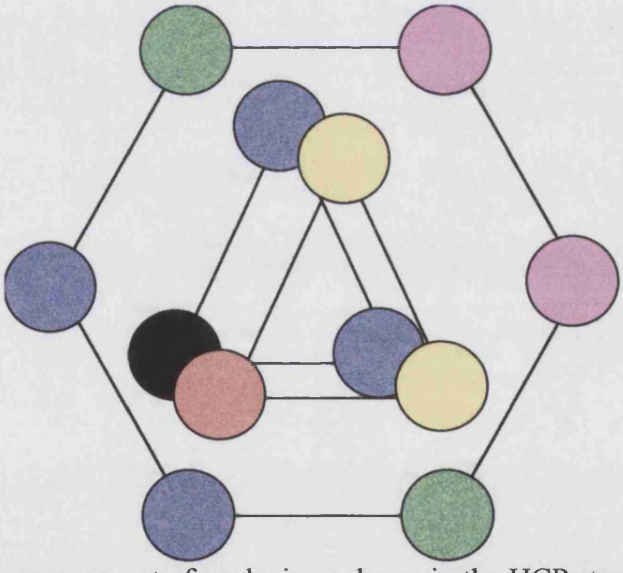

Figure 8.2.10 The arrangement of exclusion spheres in the HCP structure. The face under consideration is that of the black sphere, which is one of the spheres in the "end" group.

Firstly, the twelve neighbours are split into two distinct groups according to the symmetry of the HCP arrangement. The two groups were labelled "middle" and

"end". The distinction between the groups lies in the relative positions of the other neighbours. The positions of the other neighbours determines the shape of the face of the free volume and so the groups are treated differently.

As with FCC, each face is considered individually. The positions of the circles, which determine the nature of the face, are calculated from the positions of the spheres by the algorithm. The positions of the spheres which determine the shape of each face and their corresponding circles are shown in figs. 8.2.10 - 8.2.13.

The range of possible overlaps between the circles needs to be considered for each case and is more complex than for the FCC arrangement. Once all possible overlaps have been taking intro consideration, the algorithm again calculates the contribution towards the free volume and area made by each section.

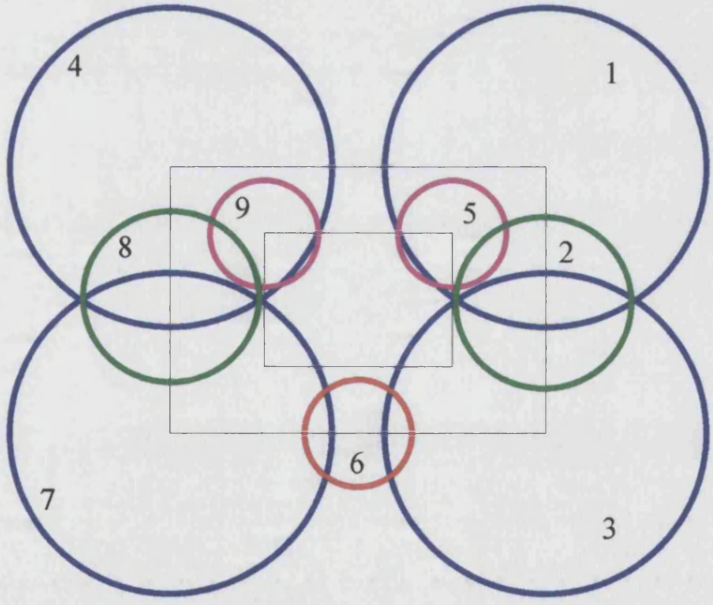

Figure 8.2.11 The position of overlap circles for spheres from the "end" group, see fig. 8.2.10

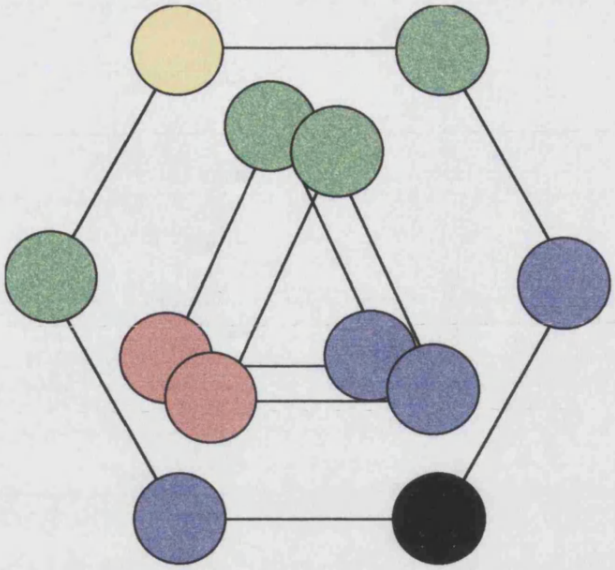

Figure 8.2.12 The arrangement of exclusion spheres in the HCP structure. The face under consideration is that of the black sphere, which is a sphere from the "middle" group.

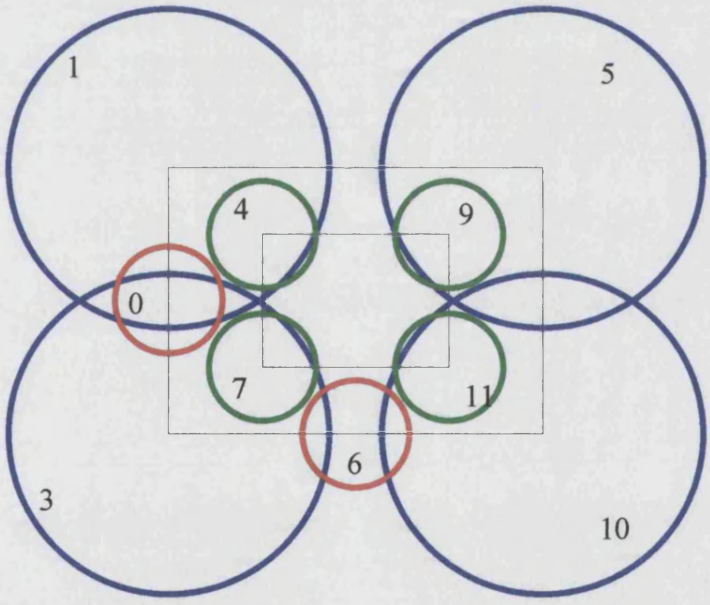

Figure 8.2.13 The position of overlap circles for spheres from the "middle" group, see fig. 8.2.12

9.1 Primary Results

9.1.1 The Accuracy of Analytical Calculations

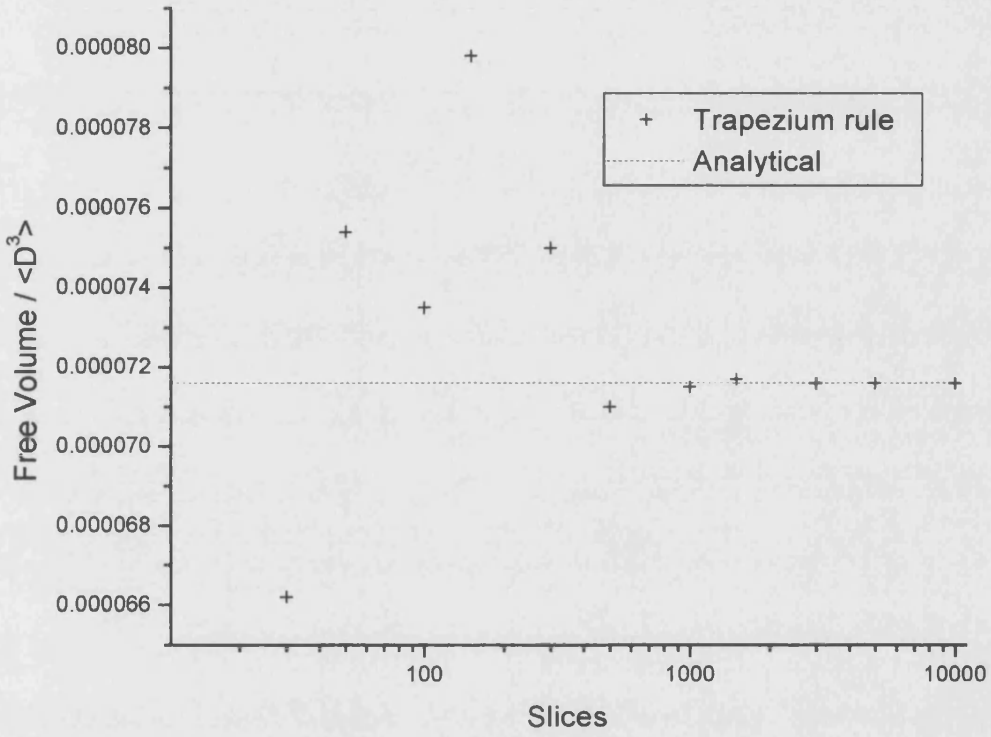

Figure 9.1.1 Graph showing the calculated free volume vs. the number of slices used for the trapezium rule. The dotted line represents the analytical result. This calculation was performed at a polydispersity of 0.04 and volume fraction of 0.6 using an arbitrary arrangement.

Before the analytical algorithm to calculate the free volume was developed, the trapezium rule method was used. This uses the same method to calculate the free volume as used for the binary systems. The accuracy of the calculation depends on the number of sections used. The calculated results converge when the free volume is

split into a thousand slices across both the X and Y planes. The total number of sections being one million. Even after Gaussian quadrature is used and symmetry is taken into account, there are a large number of possible arrangements of neighbours in a polydisperse system. Therefore to use this number of sections is unfeasible. A calculation using a million sections would have taken years to complete using the available resources (initially a 486 66 Mhz PC).

It would have been necessary to compromise the accuracy of the calculations in order to reduce the time it took to complete them. A practical number of slices would have been just 150, giving a reduced total of 22500 sections. Each free volume took one second to compute using this number of slices. The length of time required to calculate the properties of the polydisperse system under any given conditions was ten hours.

The analytical algorithm was of immense use as it was able to very accurately calculate the free volume in a fraction of the time. It also provided a method to calculate the pressure of the system without relying on numerical differentiation.

The analytical algorithm was able to calculate the free volumes at a rate of 65 per second on the same computer. When a Pentium II (266Mhz) became available, this rate increased to about 400 per second. The combination of improved software and hardware made it more practical to perform these calculations using three diameter points. It also made it possible to calculate the thermodynamic properties using four diameter points.

9.1.2 Number of Points Used in Gaussian Quadrature

The convergence of the results with the number of diameter points used is examined next.

As previously discussed, the continuous distribution of particle sizes associated with a polydisperse suspension of colloid particles was approximated by a finite number of discrete particles. The number of different particle sizes used to make this approximation is naturally important.

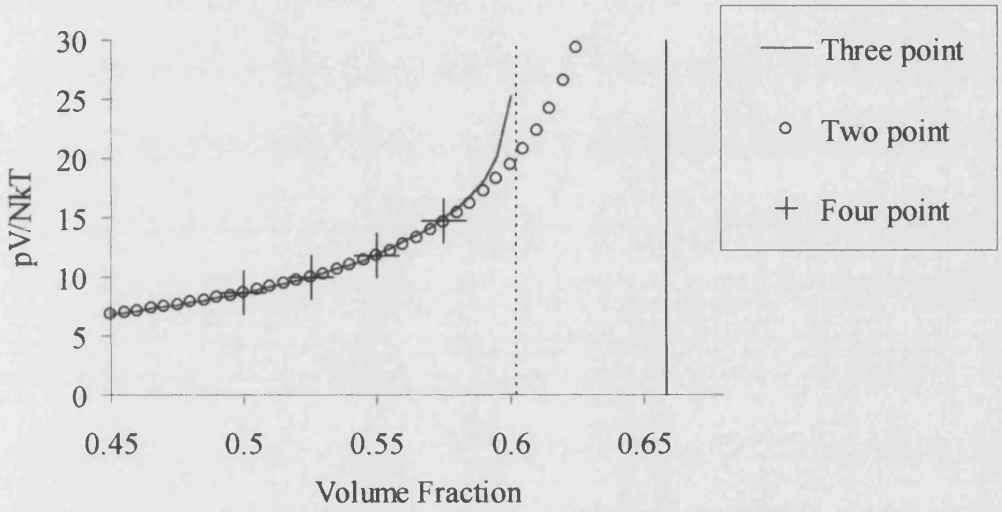

Figure 9.1.2 Graph of pressure vs. Volume fraction at constant polydispersity of 0.04, showing difference between various calculations. Dashed and solid vertical lines mark maximum volume fractions for three and two point system respectively.

The pressure was calculated at 0.04 polydispersity over a few volume fractions using two, three and four different particle sizes. The results of this calculation are shown in fig. 9.1.2.

Note that at lower volume fractions, up to 0.57, the results are in good agreement, differing by less than 0.02. There is a clear divergence at higher volume fractions. This difference is due to the size of the particles used to approximate the continuous

distribution. When using two points, the size of the larger particle is 4.2% larger than the mean particle diameter. In the three-point approximation, the particle diameters are spread further apart, the largest being 7.3% larger than the mean particle diameter. It has been assumed that neighbouring particles are fixed at their lattice sites. Accordingly there is a volume fraction at which the largest hard spheres would begin to overlap. This leads to asymptotic behaviour in the pressure. Further, the position of this asymptote depends on the number of particle diameters used in the approximation. As will be seen, this difference becomes increasingly important at higher polydispersities.

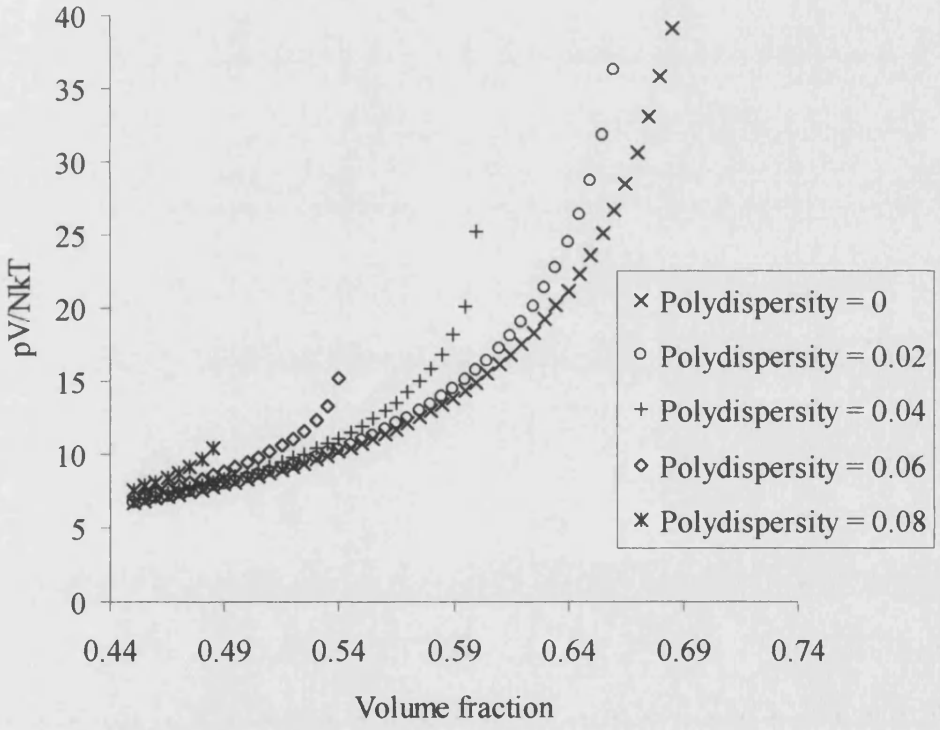

Figure 9.1.3 Graph showing pressure against volume fraction at increasing levels of polydispersity.

Recall that using Gaussian quadrature the first five moments of the polydisperse distribution are matched, when using three points and the first three when using two points.

The pressure, excess Helmholtz free energy and chemical potentials were calculated for a range of polydispersities and volume fractions. The polydispersity was varied from 0 to 0.097 in steps of 0.001. For all polydispersities, the initial volume fraction was 0.45. This was increased in steps of 0.05 until the density was reached where it was no longer possible to pack the hard spheres together. This limit decreases as the polydispersity increases. Due to the fact that it is assumed that neighbours are fixed on their lattice sites, this limit is, again, dependent on the size of the largest particles.

In fig. 9.1.3 the pressure is plotted against the volume fraction for a number of polydispersities. For comparison the pressure for a polydispersity of 0, that is monodispersity, is also shown. As expected, pressure increases more rapidly at higher polydispersities. Even at lower volume fractions, where particles have plenty of space, the pressure is higher as the system is more polydisperse.

In fig. 9.1.4 the excess moment chemical potentials are plotted for 0.03 polydispersity. The results obtained using a two and a three point Gaussian quadrature approximation are compared. There is good agreement between the results at lower volume fractions, which is encouraging as it supports the hypothesis that the properties of polydisperse systems depend only on the first few moments of the distribution. However, the results diverge at higher volume fractions. This may be attributed to the difference in the maximum volume fraction obtainable, using the different approximations.

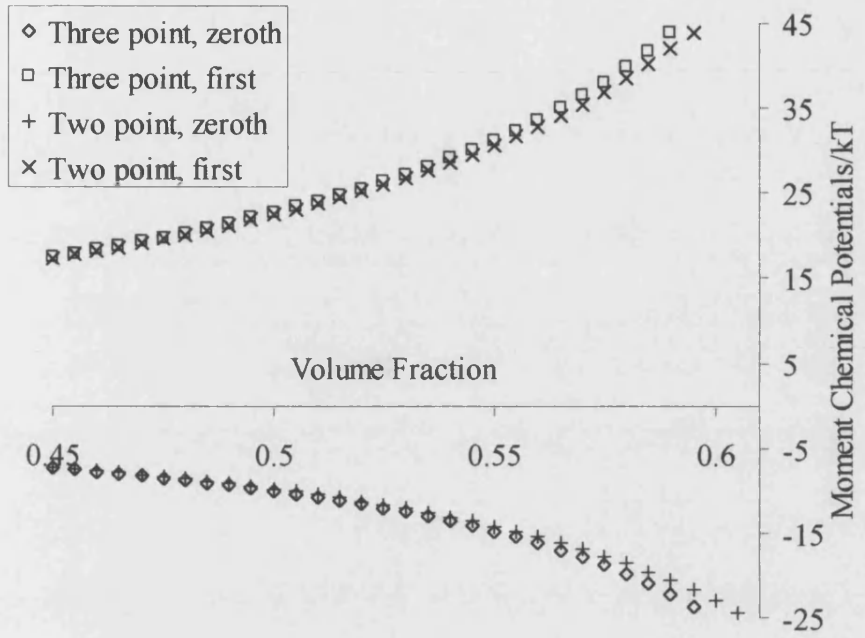

Figure 9.1.4 A comparison of the excess moment chemical potentials at 0.03 polydispersity, calculated using a two and a three point approximation.

9.1.3 Geometric Constraints

The maximum found in the three-point approximation is not a true reflection of a real system. It is a result of the "inability" of particles to move, even slightly from their lattice sites. The limit upon the volume fraction is unrealistic.

Consider the two-dimensional analogy. In the three-point approximation, the largest particles account for at most 15% of the particles. So the probability of finding two adjacent large particles is low. However, when this does happen they may well overlap if the volume fraction is high enough. Only a very slight distortion of the crystal lattice would be required to allow the large particles to move apart, as may be seen by comparing figs. 9.1.5 and 9.1.6.

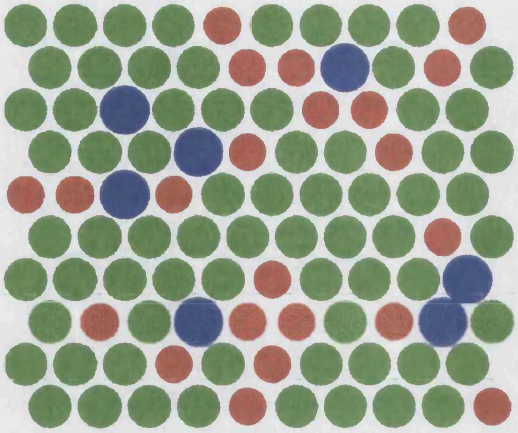

Figure 9.1.5 Two-dimensional crystal of polydisperse (approximated with three differently sized points) hard disks. Note the two overlapping large disks at the bottom right.

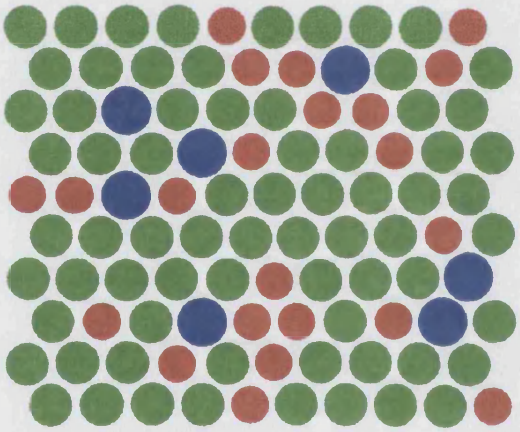

Figure 9.1.6 Two-dimensional crystal of polydisperse hard disks that has been "relaxed" so that no overlap is taking place.

By "relaxing" the rule that neighbours are fixed at their lattice sites, it should be possible to reach higher, more realistic volume fractions. This was done in the two dimensional case.

Particles of different sizes were randomly placed in a two-dimensional crystal array. A very simple algorithm was used to randomly move particles to ensure they were as

evenly spaced as possible. In fig. 9.1.7 pressure is plotted against number density for a relaxed system. For comparison the "original" fixed system is shown. Note that the relaxed system does not reach as high a pressure as the fixed system.

This demonstrates the principal of relaxing a system. However relaxing a three dimensional system proved to be far more complicated. Moving one particle away from another could often lead to overlap with another. Calculating the free volume for particles in a distorted array was not trivial. The algorithm used previously, relied on the neighbours being fixed. It appeared that without carrying out a full Monte Carlo simulation, it would not be possible to relax the system in the same way the two-dimensional system was. This was not the original intention, so this was carried no further.

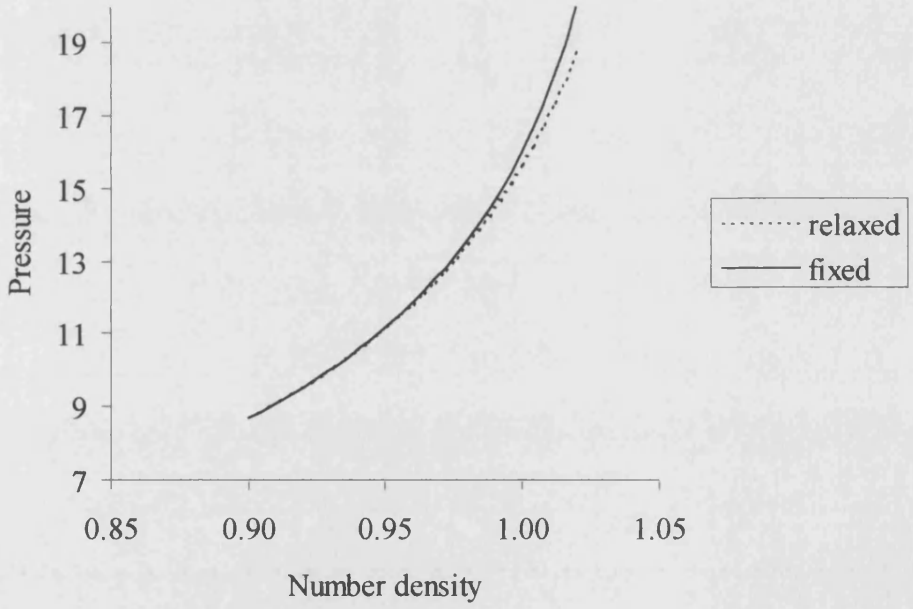

Figure 9.1.7 Pressure against number density at 0.04 polydispersity, comparing a fixed and a relaxed two-dimensional crystal.

9.2 Phase Behaviour

9.2.1 Evaluation of Phase Behaviour

Having obtained the thermodynamic properties of a crystal of polydisperse hard spheres, it was then possible to evaluate the phase behaviour of a polydisperse system. Recall that the phase behaviour of monodisperse hard spheres is very simple (section 1.1). The phase behaviour of a polydisperse system is potentially far more complicated, but is simplified by the use of the projected free energy surface (section 7.2).

The properties of the polydisperse solid, as calculated by the application of the cell model, were exported to a file in binary format. The algorithm that calculated the phase behaviour imported the data in this file. Recall that it is the cloud-shadow curve that is been determined. It was assumed the shape of the distribution and hence the polydispersity of the emerging solid phase matched that of the fluid. Equilibrium between the fluid and solid was then calculated at any given polydispersity. The properties of the solid phase at each polydispersity were fitted to a cubic spline to enable interpolation of the data.

Recall that the excess portions of the moment chemical potentials are the coefficients of the polynomial describing the relationship between the chemical potential of a particle and its diameter. Given that just two moment chemical potentials are required, then it is a linear relationship that is being used. It is trivial to find the coefficients and hence the moment chemical potentials when the two point approximation is used. However when the three-point approximation is used, there are various options to consider. It would be possible to use a quadratic to describe the relationship. This may

seem appealing as a quadratic could be fitted exactly to the data. However, as only two moment chemical potentials are being used it may be more sensible to fit the data directly to a line. There still remain two ways to do this for three points. A straightforward line of best fit is a simple option. The alternative is a weighted line of best fit, where the mole fractions of the species present are taken into account. As the particle with the medium diameter has the highest mole fraction, this will have the effect of lowering the position of the line, as is seen from fig. 9.2.1. The consequences of both of these approaches will be considered.

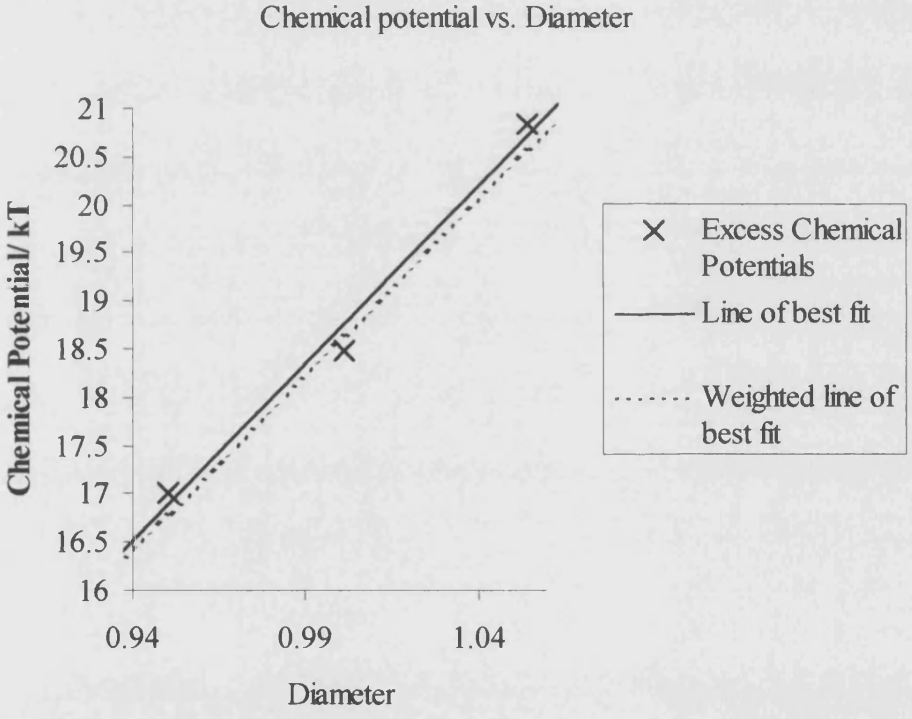

Figure 9.2.1 The use of two moment chemical potentials is equivalent to fitting the excess chemical potentials to a line of best fit. The weighted line of best fit takes the mole fractions into account.

The algorithm that established the conditions of equilibrium did so by first finding the number densities of the fluid and solid phase where the moment chemical potentials

were matched. Secondly the mean diameter of the particles in the emerging solid phase was determined by equating the pressure to that of the fluid phase.

9.2.2 Phase Diagrams

As the polydispersity gets higher the densities of the fluid and solid phases in equilibrium with each other increase, this is to be expected as polydispersity decreases the stability of the ordered crystal (fig. 9.2.3). Of much interest, is the terminal polydispersity, the polydispersity above which the crystal is found to be thermodynamically unstable at all densities.

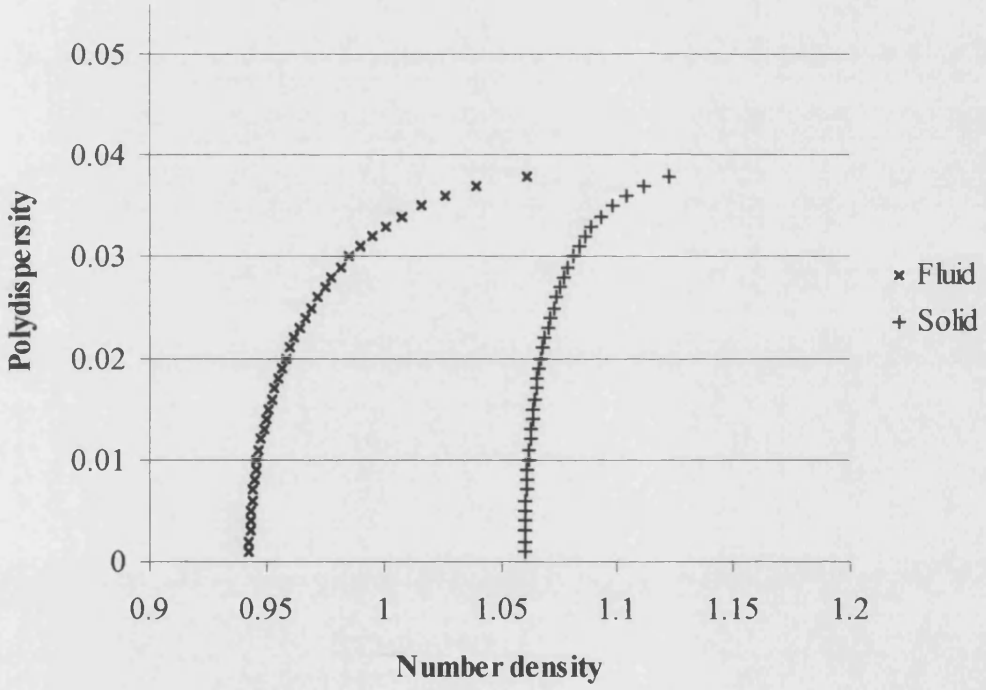

Figure 9.2.3 Phase diagram, tielines are horizontal. Using a three point approximation for the polydisperse solid.

Using the data obtained using the three point Gaussian quadrature approximation and a line of best fit to describe the diameter dependence of the chemical potential, the

highest polydispersity at which co-existence of a solid and fluid phase could be established was just 0.038, considerably lower than the values predicted by other studies[73-76,78].

However as this "terminal" polydispersity is approached, the volume fraction of the solid phase (0.595) found to be in equilibrium with the fluid phase nears the maximum possible (0.608 at 0.038 polydispersity). As discussed previously, this maximum is dependent on the properties of the model used. These results may therefore be distorted. Hence we consider the results obtained using a two-point approximation.

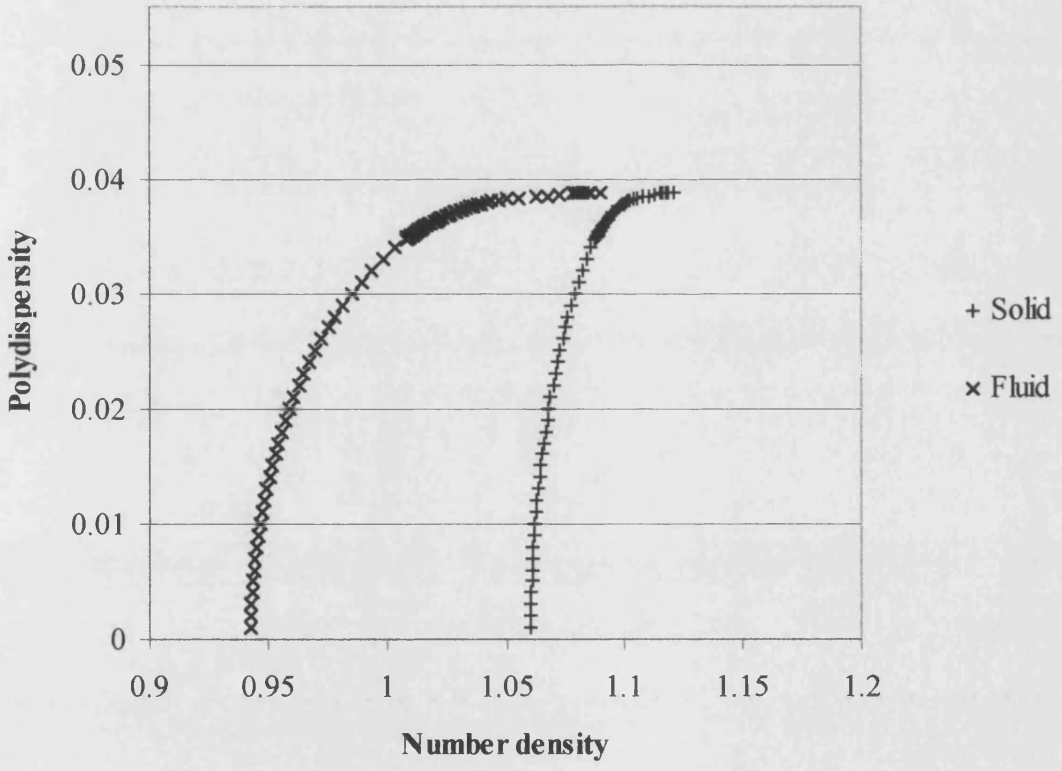

Figure 9.2.4 Phase diagram, tielines are horizontal. Using a two point approximation for the polydisperse solid.

The two-point approximation has the advantage that the maximum packing density is much higher. Interestingly, there is no significant difference the two and three point results at polydispersities below 0.03 and only a minor difference above 0.03.

With the two-point approximation the "terminal" polydispersity is found to be at 0.0388, only slightly higher than the value obtained using the three-point approximation and a line of best fit. Above this polydispersity, no equilibrium may be established. Note that the density of the solid phase is significantly lower than the maximum packing value for this model.

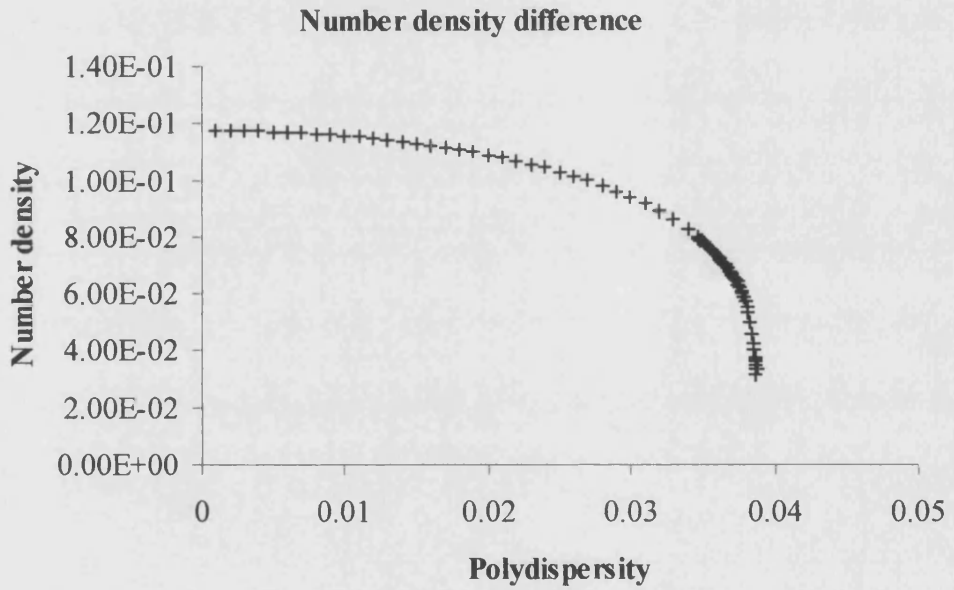

Figure 9.2.5 Number density difference between the solid and fluid phase, two point approximation. Converges to zero at 0.0388 polydispersity.

As the terminal polydispersity is approached, the number densities of the fluid and solid phase in equilibrium rapidly come close to equality, as shown in fig. 9.2.5 This is not analogous to a critical point as the transition from a disordered fluid to an ordered solid is generally first order. It is a point of equal concentration[90]. At

polydispersities higher than the terminal polydispersity the model would predict only the existence of the fluid or an amorphous glass at higher densities.

Recall that the mean diameter of particles in the solid phase is a variable. In fig. 9.2.6 the ratio of solid phase mean diameter to fluid phase mean diameter is plotted against polydispersity. Note that as polydispersity increases, the mean diameter of particles in the emerging solid phase is marginally larger.

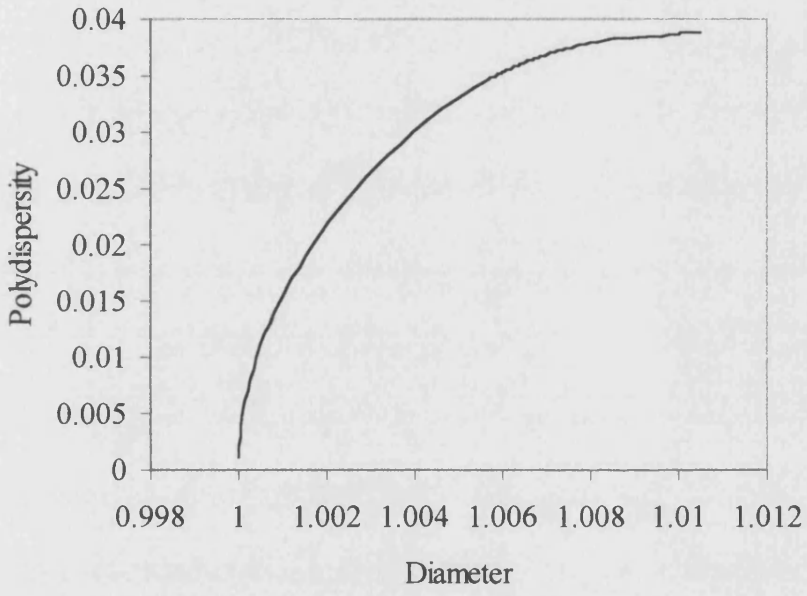

Figure 9.2.6 Mean diameter ratio, solid to fluid phase, two point approximation.

The phase behaviour shown in fig. 9.2.4 is shown in the polydispersity-volume fraction plane in fig. 9.2.7.

Now we consider the results obtained by using a weighted line of best fit to describe the diameter dependence of the chemical potentials, using the data from the three-point approximation.

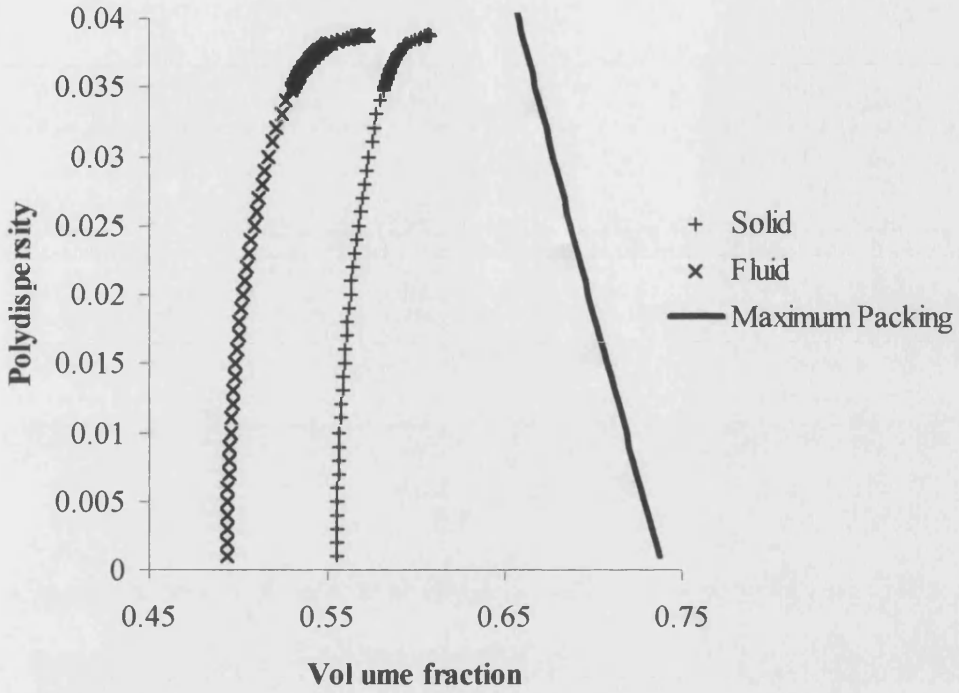

Figure 9.2.7 Phase diagram, two point approximation used for the polydisperse solid.

The results obtained are significantly different. The deviation of the number densities of the co-existing phases to higher values is less prominent. Also the value obtained for the terminal polydispersity is higher. As a first estimate for this value, it was found that it was not possible to establish equilibrium at polydispersities higher than 0.0498.

However, once more the maximum packing obtainable with this particular model has an influence on these results. This is best seen in fig. 9.2.9, where the phase diagram is plotted in the polydispersity – volume fraction plane. At 0.05 polydispersity, the maximum packing fraction for the three point approximation model is just 0.572. The volume fraction of the phase in equilibrium is found to be 0.563.

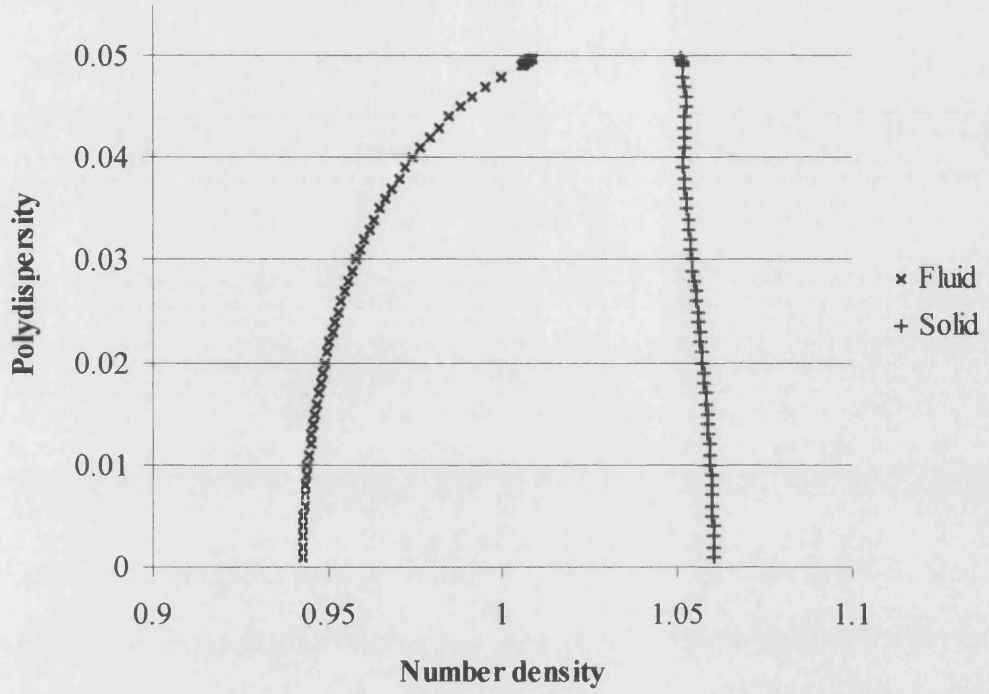

Figure 9.2.8 Phase diagram, three point approximation used for the polydisperse solid.

A weighted best fit was used to calculate the moment chemical potentials.

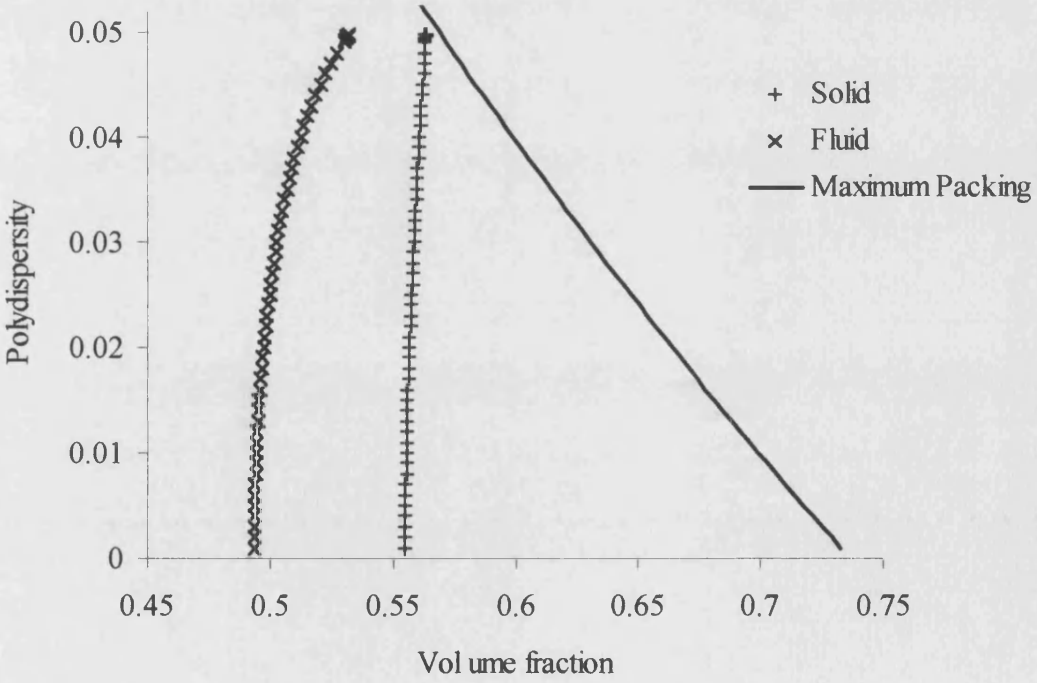

Figure 9.2.9 Phase diagram, three point approximation used for the polydisperse solid.

A weighted best fit was used to calculate the moment chemical potentials.

In order to get a better estimate for the terminal polydispersity, in fig. 9.2.10 the number density difference between the two phases in equilibrium is plotted. When this graph is extrapolated, the number densities are in equality at 0.055. This value is a more realistic estimate of the terminal polydispersity.

In fig. 9.2.11 the diameter ratio of the solid phase to the fluid phase. Once more, it may be noted that the emerging solid phase has a marginally higher mean diameter at higher polydispersities.

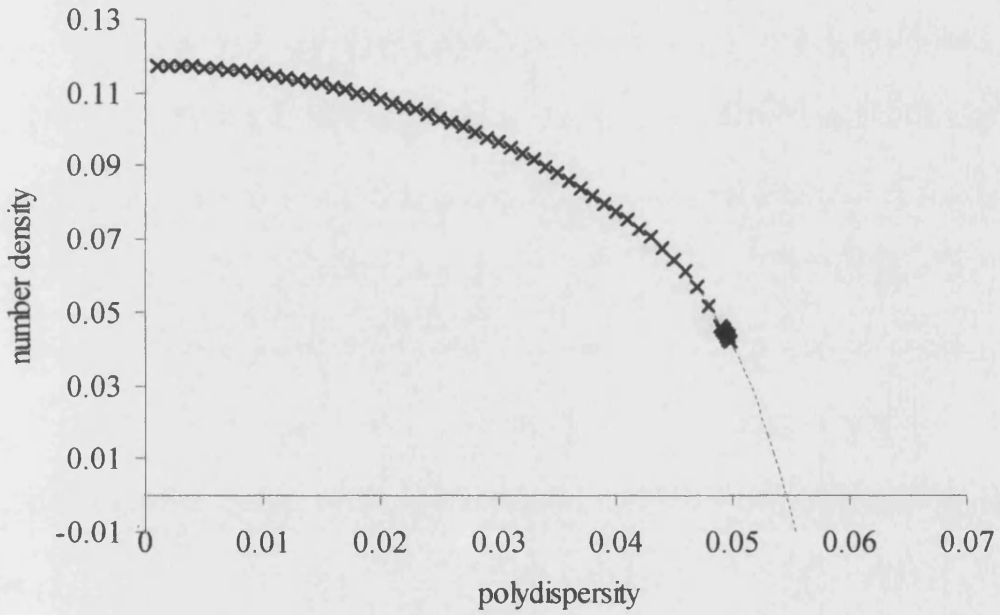

Figure 9.2.10 Number density difference between the solid and the fluid phase. three point approximation used for the polydisperse solid. A weighted best fit was used to calculate the moment chemical potentials. The difference converges to zero at a polydispersity of 0.055

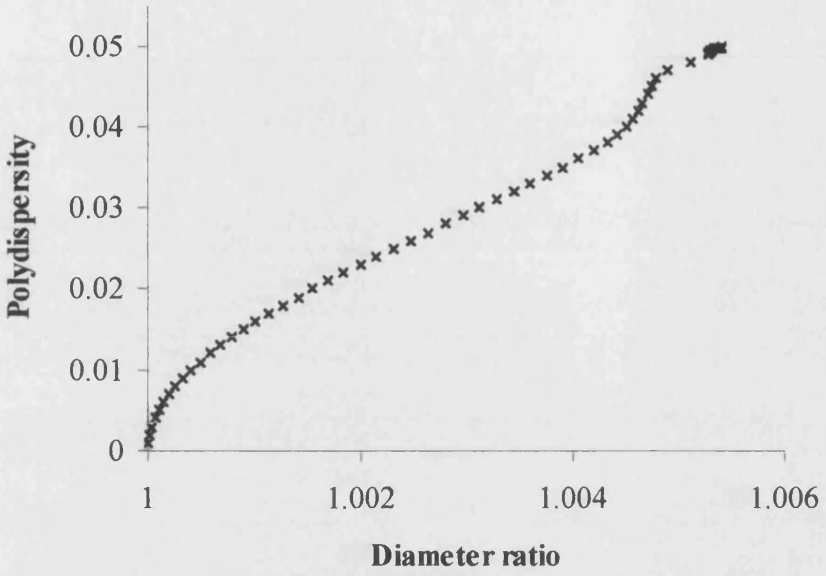

Figure 9.2.12 Mean diameter ratio, solid to fluid phase, three point approximation

9.2.3 Summary and Conclusion

The properties of a polydisperse FCC crystal have been calculated using the Lennard-Jones cell model. The continuous distribution of particle diameters was approximated by a finite number of discrete points. In order to perform the calculation efficiently, symmetry was taken into account and a fast analytical algorithm was used to calculate the pressure and Helmholtz free energy. The advantage of the cell model is its simplicity. However the application to a polydisperse system is non-trivial. In this application of the cell model, particles are fixed at their lattice sites in a systematic manner. While it may be possible to adapt the cell model to allow substitutional ordering and some relaxation of the crystal, to do so would make a simple model excessively complicated.

Using the cell model a terminal polydispersity of about 0.055 is predicted, however the different results obtained show their sensitivity to variations in method. Any

advantage the three-point approximation may have had over the two-point approximation is lost in the low maximum packing fraction, which appears to distort the results. The value obtained for the terminal polydispersity is therefore amongst the lower values predicted in literature. It is in agreement with the value predicted by McRae and Haymet[74] using density functional calculations and that predicted by Bolhuis and Kofke[75] using Monte Carlo calculations. However it is much lower than the value of 0.083 predicted by Bartlett[76]. It is also significantly different to the result of Phan and Russel[78], who performed a simulation of polydisperse hard spheres and predicted the terminal polydispersity to have an upper limit of 0.12.

Polydisperse phase behaviour is potentially very complex. The use of the projected free energy surface is an attempt to simplify it. The nature in which any approximation is made is bound to affect the outcome of the results. The relationship between the chemical potential of a particle and its diameter is not truly linear as may be seen in fig. 9.2.12. A number of different methods could have been used to derive a linear relationship, of which two have been considered. While it may be argued that the weighted line of best fit is the best method, it is still an approximation.

While these difficulties may have prevented good quantitative results being obtained. The results still give a good qualitative indication of the polydisperse phase behaviour of hard spheres.

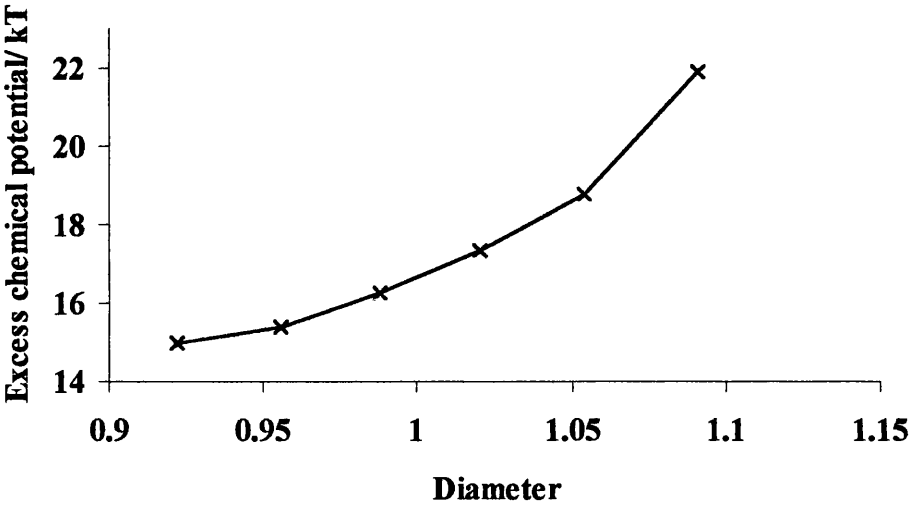

Figure 9.2.12 Excess chemical potential against diameter at 0.03 polydispersity and volume fraction 0.55. These results were obtained using an eight point approximation, where the central six points are shown. A randomly generated 20x20x20 crystal of polydisperse hard spheres was used to calculate this data. Not enough data was generated to accurately calculate the chemical potentials of the two outlying points.

9.3 The Effect of Polydispersity on the Relative Stability of FCC and HCP

In section 1.3 these two structures and their relative stability were discussed. As was pointed out, the structures formed by monodisperse hard spheres are equally as stable according to the free volume model, but the FCC structure is marginally more stable according to molecular dynamics.

9.3.1 Basis for a Distinction

In their density functional theory studies of the freezing of polydisperse hard spheres, McRae and Haymet[74] observed that close to the terminal polydispersity there was "persistent numerical evidence" that the HCP structure was more stable than the FCC structure. They felt unable to make any conclusive predictions on the grounds of their calculations alone.

The application of free volume theory to this interesting problem may be able to provide a basis for the HCP structure being more stable.

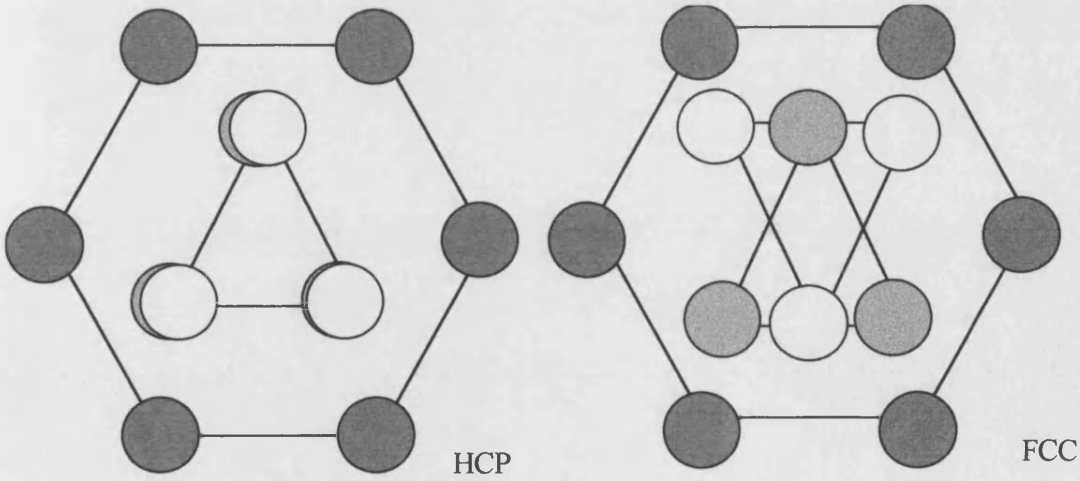

Figure 9.3.1 the arrangements of neighbours in the HCP and FCC structures. The top layer is non-shaded, the middle layer is hatched and the bottom layer is grey.

In fig. 9.3.1 the arrangements of neighbours for the HCP and FCC structures are shown. Recall it is these neighbours that determine the free volume. Note the only difference is in the position of the spheres in the top layer (non shaded).

Consider the hypothetical arrangement of exclusion spheres in fig. 9.3.2. In A and B the sum of the areas of the exclusion spheres in the box is the same. However the remaining free area is greater in B because the exclusion spheres are overlapping to a greater extent.

In D there is more overlap between exclusion spheres occurring than in C. However, the free area is D is not greater than that in C, because this additional overlap occurred in a region where overlap was already occurring.

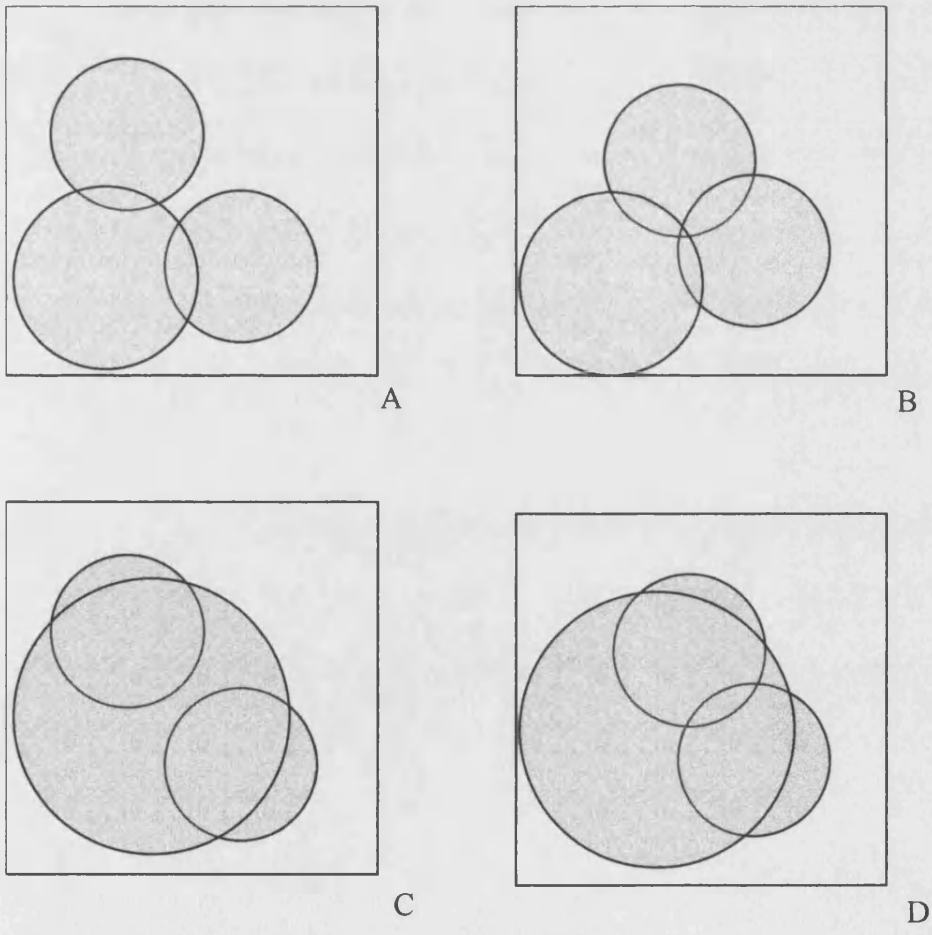

Figure 9.3.2 A hypothetical arrangement of exclusion spheres.

The potential for difference between the polydisperse FCC and HCP structures lies in the overlap of the exclusion spheres from the top and bottom layers. When the spheres are monodisperse all overlap between these exclusion spheres occurs in regions where overlap with the middle layer is already occurring (case D). When the spheres and hence the exclusion spheres are polydisperse then it is possible that the exclusion spheres from the top and bottom layers may overlap in a region where there is no overlap with the middle layer (case B). This requires there to be larger spheres in the top and bottom layers and smaller spheres in the middle layer. The exclusion spheres in the top and bottom layers are closer together in the HCP structure than in the FCC structure. This means that this is more likely to happen in the HCP structure. If this does occur, then this would lead to an additional stability of the polydisperse HCP structure over the corresponding HCP structure.

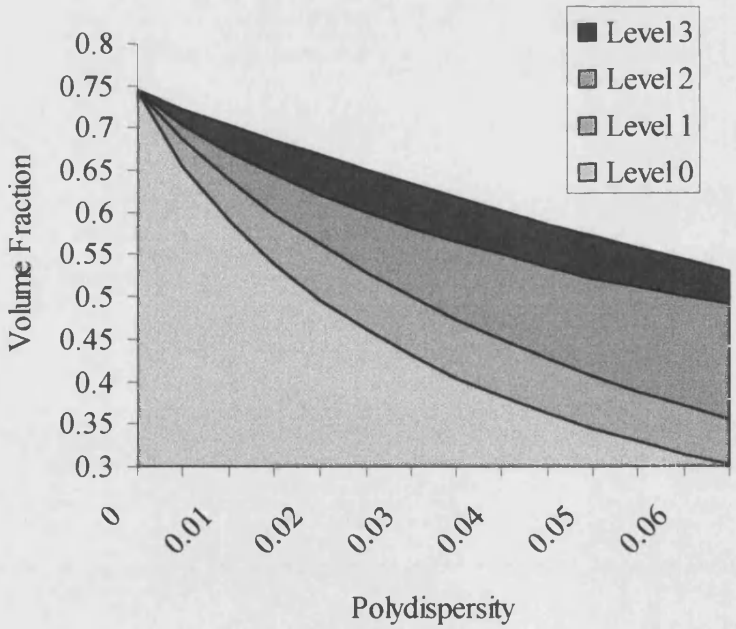

Figure9.3.3 The levels of the overlap effect.

This effect, which from now on will be referred to as the overlap effect, is dependent on the size of the exclusion spheres. As a two or three point Gaussian quadrature

approximation is being used, then it is possible to calculate at what densities and polydispersities it is likely to be noticed. In fig. 9.3.3 the progressive levels of the overlap effect are shown for a three-point Gaussian quadrature approximation. At level 0 there will be no effect. At level 1 a small effect will start to be seen due to large spheres in the top and bottom layers and small spheres in the middle layer. At level 2 an additional effect caused by large top and bottom spheres and medium spheres in the middle layer will begin to emerge. At level 3 medium sized spheres in the top and bottom layers and small spheres in the middle layer will start to contribute to the overlap effect. Note for a true polydisperse system, this influence of the overlap effect would be gradual, not stepped.

9.3.2 Results

In order to make this comparison it was necessary to first analytically calculate the free volume for polydisperse arrangements in the HCP structure. The overlap effect is very small and would have been lost in the uncertainties associated with any approximate technique used.

In fig. 9.3.4 a plot is made of the difference in stability of the FCC and HCP structures at a volume fraction of 0.545 as the polydispersity increases. The volume fraction of 0.545 was chosen, as this is the volume fraction at which hard spheres crystallise when monodisperse. The overlap effect is significant in comparison to the results calculated by Woodcock[41] and Bolhuis[42]. At 0.032 polydispersity the HCP structure is about 0.0046 RT more stable than the FCC structure. This is in contrast to the values of 0.005 RT and 0.0009 RT in the opposite direction found by Woodcock and Bolhuis respectively.

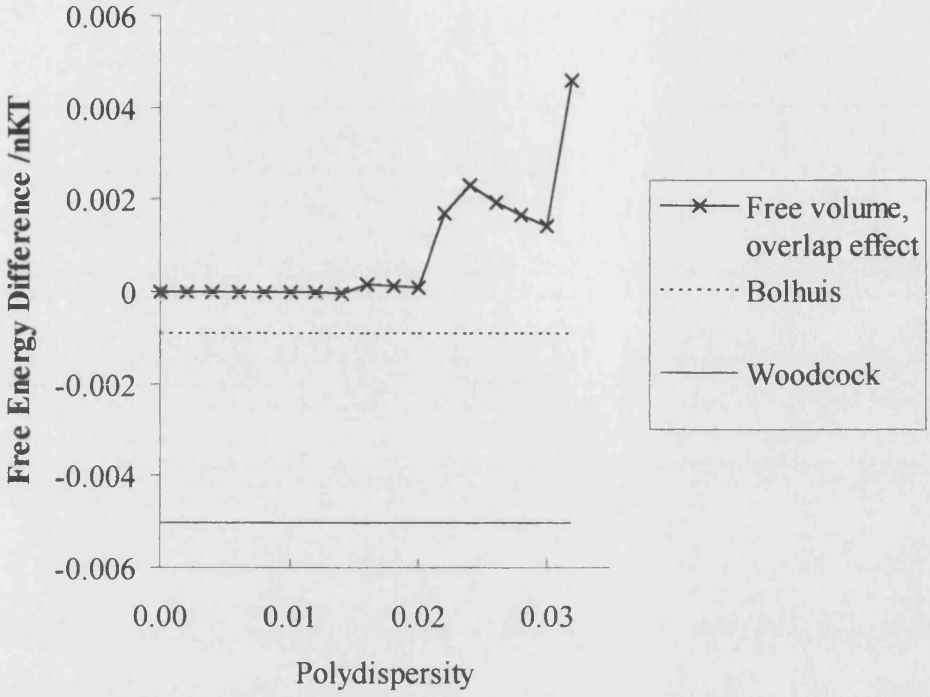

Figure 9.3.4 Free energy difference of the polydisperse FCC structure against the polydisperse HCP structure. Note the values plotted for Woodcock and Bolhuis are for the monodisperse structures.

Note the stepped nature of the energy difference plot. According to calculations based upon the size of the exclusion spheres, the overlap effect should first be noticed at 0.015 polydispersity, then increase first at 0.023 polydispersity and then again at 0.042. The steps are consistent with these predictions. Difficulties with the analytical calculations for the HCP structure prevented higher polydispersities being examined.

From these results, it may be concluded that the overlap effect is significant. It is difficult to put a qualitative value on it due to the nature of the three-point approximation being used in these calculations. However the effect is of the same order of magnitude as the difference found by Woodcock and Bolhuis. More over it is in the opposite direction. Accordingly the HCP structure should be more stable as polydispersity increases.

Appendix A Gaussian Quadrature Method

A.1 Gaussian Quadrature for a Triangular Distribution

The Triangular distribution is defined by

$$\begin{aligned} f(D) &= \frac{1}{W^2}(1-|1-D|) \qquad 1-W < D < 1+W \\ &= 0 \qquad\qquad\qquad\quad \text{Otherwise} \end{aligned} \tag{A.1}$$

where $2W$ is the width of the distribution. An expression for the moments, c_j may be obtained.

$$\begin{aligned} c_j &= \int_{1-W}^{1+W} f(D)D^j dD \\ &= \frac{1}{W^2}\int_{1-W}^{1+W}(W-|1-D|)D^j dD \quad \text{sub } y = D-1 \\ &= \frac{1}{W^2}\int_{-W}^{+W}(W-|y|)(y+1)^j dy \\ &= \frac{1}{W^2}\int_{-W}^{0}(W+y)(y+1)^j dy + \frac{1}{W^2}\int_{0}^{W}(W-y)(y+1)^j dy \\ &= \frac{2}{W^2}\left[\sum_{n=0,n\,\text{even}}^{j}\left(\frac{Wy^{n+1}}{n+1}p_{n,j} - \frac{y^{n+2}}{n+2}p_{n,j}\right)\right]_0^W \\ &= 2\sum_{n=0,n\,\text{even}}^{j}\frac{W^n p_{n,j}}{(n+1)(n+2)} \end{aligned} \tag{A.2}$$

$p_{n,j}$ is n,j th coefficient from Pascal's triangle

$$\begin{matrix} p_{1,1} & & 1 & & \\ p_{1,2}\ p_{2,2} & \equiv & 1 & 1 & \\ p_{1,3}\ p_{2,3}\ p_{3,3} & & 1 & 2 & 1 \end{matrix} \tag{A.3}$$

Therefore

$$c_0 = 1$$
$$c_1 = 1$$
$$c_2 = 1 + \frac{1}{6}W^2 \quad \text{(A.4)}$$
$$c_3 = 1 + \frac{1}{2}W^2$$

The following recurrence relationship was used to evaluate the polynomial whose roots are required.

$$P_{-1} = 0 \text{ (A.5)}$$

$$P_0 = 1 \quad \text{(A.6)}$$

$$P_{J+1} = (x - a_j)P_j - b_j P_{J-1} \text{ J=0,1,2..... (A.7)}$$

$$a_J = \frac{\langle xP_J | P_J \rangle}{\langle P_J | P_J \rangle} \quad J \geq 0 \qquad \text{(A.8)}$$

$$b_J = \frac{\langle P_J | P_J \rangle}{\langle P_{J-1} | P_{J-1} \rangle} \quad J \geq 1 \qquad \text{(A.9)}$$

$$b_0 = 0 \text{ (A.10)}$$

From these relationships it follows that

$$\langle P_0 | P_0 \rangle = 1 \qquad \text{(A.11)}$$

and $\langle xP_0 | P_0 \rangle = 1,$ (A.12)

therefore $P_1 = x - 1.$ (A.13)

The next polynomial in the series was evaluated as follows.

$$\begin{aligned}\langle P_1|P_1\rangle &= \int f(x)P_1P_1dx \\ &= \int f(x)P_1(x-1)dx\end{aligned} \quad \text{(A.14)}$$

But a property of orthogonal polynomials is

$$\int f(x)P_J x^I = 0 \text{ when } I < J \quad \text{(A.15)}$$

$$\begin{aligned}\langle P_1|P_1\rangle &= \int f(x)P_1 x dx \\ &= \int f(x)(x^2 - x)dx \\ &= c_2 - c_1 \\ &= 1 + \frac{1}{6}W^2 - 1 \\ &= \frac{1}{6}W^2\end{aligned} \quad \text{(A.16)}$$

$$b_1 = \frac{\langle P_1|P_1\rangle}{\langle P_0|P_0\rangle} = \frac{1}{6}W^2 \quad \text{(A.17)}$$

$$\begin{aligned}\langle xP_1|P_1\rangle &= \int f(x)P_1(x^2 - x)dx \\ &= \int f(x)\left[x^3 - 2x^2 + x\right]dx \\ &= c_3 - 2c_2 + c_1 \\ &= \frac{1}{6}W^2\end{aligned} \quad \text{(A.18)}$$

$$a_1 = \frac{\langle xP_1|P_1\rangle}{\langle P_1|P_1\rangle} = 1 \quad \text{(A.19)}$$

Which means that

$$
\begin{aligned}
P_2 &= (x-a_1)P_1 - b_1 P_0 \\
&= (x-1)P_1 - \frac{1}{6}W^2 P_0 \\
&= (x-1)(x-1) - \frac{1}{6}W^2 \\
&= \left(x - \left[1+\sqrt{\frac{1}{6}}W\right]\right)\left(x - \left[1-\sqrt{\frac{1}{6}}W\right]\right)
\end{aligned}
\qquad \text{(A.20)}
$$

So the roots of P_2 are given by.

$$x_{1,2} = 1 \pm \sqrt{\frac{1}{6}}W \qquad \text{(A.21)}$$

It is these roots that are used as points in the Gaussian Quadrature method. The corresponding weights w_1 and w_2 may be found by applying the relationship-

$$\sum_{i=1}^{n} w_i x_i^{\,j} = c_j, \; j = 0,1...2n-1 \text{ (A.22)}$$

This gives the weights for the two-point formula as

$$w_1 = w_2 = \frac{1}{2}. \text{ (A.23)}$$

It was found that

$$\langle xP_J \,|\, P_J \rangle = \langle P_J \,|\, P_J \rangle, \text{ (A.24)}$$

$$\text{so that } a_J = 1 \text{ all J.} \quad \text{(A.25)}$$

$$b_2 = \frac{7}{30}W^2, \quad \text{(A.26)}$$

$$P_3 = x^3 - 3x^2 + \left(3 - \frac{2}{5}W^2\right)x + \left(\frac{2}{5}W^2 - 1\right)$$

therefore

$$= (x-1)\left(x - \left[1 - \sqrt{\frac{2}{5}}w\right]\right)\left(x - \left[1 + \sqrt{\frac{2}{5}}w\right]\right). \qquad \text{(A.27)}$$

The roots of P_3 are

$$x_1 = 1 - \sqrt{\frac{2}{5}}W,\ x_2 = 1,\ x_3 = 1 + \sqrt{\frac{2}{5}}W, \qquad \text{(A.28)}$$

$$w_1 = w_3 = \frac{5}{24},\ w_2 = \frac{14}{24} \qquad \text{(A.29)}$$

are the corresponding weights.

The polynomials, their roots and weights were evaluated applying the above method for the polynomials P_1 to P_4.

No. Points		1	2	3	4
Two	Pts.	$1-\sqrt{\frac{1}{6}W}$	$1+\sqrt{\frac{1}{6}W}$		
	Wts.	$\frac{1}{2}$	$\frac{1}{2}$		
Three	Pts.	$1-\sqrt{\frac{2}{5}W}$	1	$1+\sqrt{\frac{2}{5}W}$	
	Wts.	$\frac{5}{24}$	$\frac{14}{24}$	$\frac{5}{24}$	
Four	Pts.	$1-\sqrt{\frac{31}{98}+\sqrt{\frac{2943}{48020}}W}$	$1-\sqrt{\frac{31}{98}-\sqrt{\frac{2943}{48020}}W}$	$1+\sqrt{\frac{31}{98}-\sqrt{\frac{2943}{48020}}W}$	$1+\sqrt{\frac{31}{98}+\sqrt{\frac{2943}{48020}}W}$
	Wts.	$\frac{1}{4}-\sqrt{\frac{5}{327}}\times\frac{11}{9}$	$\sqrt{\frac{5}{327}}\times\frac{11}{9}+\frac{1}{4}$	$\sqrt{\frac{5}{327}}\times\frac{11}{9}+\frac{1}{4}$	$\frac{1}{4}-\sqrt{\frac{5}{327}}\times\frac{11}{9}$

A.2 Gaussian Quadrature for a Schultz Distribution

For a given polydispersity, σ, the Schultz distribution is defined by

$$z = \frac{1}{\sigma^2} - 1 \qquad \text{(A.30)}$$

$$f(R) = \frac{1}{z!}\left((z+1)R\right)^z e^{-(z+1)R} \qquad R \geq 0 \qquad \text{(A.31)}$$

The general procedure for finding the appropriate points and weights for a Gaussian quadrature summation is the same as for the triangular distribution.

The moments, c_j are given by

$$\begin{aligned}
c_0 &= 1 \\
c_1 &= 1 \\
c_2 &= \frac{z+2}{z+1} \\
c_3 &= \frac{(z+3)(z+2)}{(z+1)^2} \\
c_4 &= \frac{(z+4)(z+3)(z+2)}{(z+1)^3} \\
c_5 &= \frac{(z+5)(z+4)(z+3)(z+2)}{(z+1)^4}
\end{aligned} \qquad \text{(A.32)}$$

As with the triangular distribution,

$$P_1 = x - 1. \qquad \text{(A.33)}$$

So that,

$$\begin{aligned}\langle P_1|P_1\rangle &= c_2 - c_1 \\ &= \frac{z+2}{z+1} - 1 \\ &= \frac{1}{z+1}\end{aligned} \qquad \text{(A.34)}$$

$$\begin{aligned}\langle xP_1|P_1\rangle &= c_3 - 2c_2 + c_1 \\ &= \frac{(z+3)(z+2)}{(z+1)^2} - 2\frac{(z+2)}{(z+1)} + 1 \\ &= \frac{z+3}{(z+1)^2}\end{aligned} \qquad \text{(A.35)}$$

The calculation then proceeds as follows

$$\begin{aligned}b_1 &= \frac{\langle P_1|P_1\rangle}{\langle P_0|P_0\rangle} \\ &= \frac{1}{z+1}\end{aligned} \qquad \text{(A.36)}$$

$$\begin{aligned}a_1 &= \frac{\langle xP_1|P_1\rangle}{\langle P_1|P_1\rangle} \\ &= \frac{z+3}{z+1}\end{aligned} \qquad \text{(A.37)}$$

Which means that

$$\begin{aligned}P_2 &= (x-a_1)P_1 - b_1P_0 \\ &= \left(x - \frac{z+3}{z+1}\right)(x-1) - \frac{1}{z+1} \\ &= x^2 - 2\left(\frac{z+2}{z+1}\right)x + \frac{z+2}{z+1}\end{aligned} \qquad \text{(A.38)}$$

$$\begin{aligned}\langle P_2|P_2\rangle &= c_4 - 2\left(\frac{z+2}{z+1}\right)c_3 + \frac{z+2}{z+1}c_2 \\ &= 2\frac{z+2}{(z+1)^3}\end{aligned} \qquad \text{(A.39)}$$

$$\langle xP_2 | P_2 \rangle = 2\frac{(z+2)(z+5)}{(z+1)^4} \quad \text{(A.40)}$$

$$a_2 = \frac{z+5}{z+1} \quad \text{(A.41)}$$

$$b_2 = 2\frac{z+2}{(z+1)^2} \quad \text{(A.42)}$$

$$P_3 = x^3 - 3\frac{(z+3)}{(z+1)}x^2 + 3\frac{(z+3)(z+2)}{(z+1)^2} - \frac{(z+3)(z+2)}{(z+1)^2} \quad \text{(A.43)}$$

A pattern emerges so that the other polynomials may be found using the general expressions,

$$a_n = \frac{(z+2n+1)}{(z+1)} \quad \text{(A.44)}$$

$$b_n = \frac{n(z+n)}{(z+1)^2} \quad \text{(A.45)}$$

Once the roots of the required polynomial have been found, the weights may be calculated using equation A.22.

Appendix B Analytical Expression for the Free Volume

B.1 Breakdown of a Section of the Free Volume

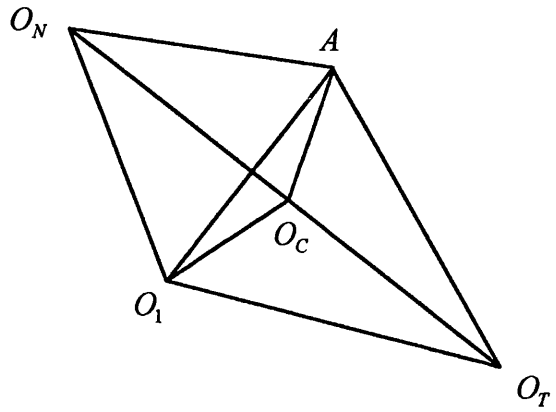

Figure B.1 The triangular based bypryramid (irregular tetrahedron) from which each section of the free volume is calculated.

When deriving an analytical expression for the free volume, the starting point is the triangular bypyramid $O_T O_C O_1 A O_N$. Strictly speaking this is an irregular tetrahedron as the vertex O_c lies along the edge $O_T O_N$. But for convenience it is treated as a bypyramid. The vertex O_T is the lattice site of the tagged particle, whose free volume is under consideration. It is therefore also the centre of the free volume. The free volume is first split into twelve faces corresponding to the twelve neighbours. The lattice site of the neighbour being considered is labelled O_N. Each face is bounded by edges, which are arcs. The centre of the arc having radius, r, being labelled O_1. The arc itself is labelled AB. Each face of the free volume is concave, being formed out a portion of the surface of the exclusion sphere whose centre lies at O_N, having radius, R_N (referred to as sphere O_N hereafter). For this reason it is necessary to use non-Euclidean spherical geometry when analysing the areas and deriving expressions for the volume. The centre of each face, O_C, is defined by the intersect of the line $O_T O_N$

and the exclusion sphere centred at O_N. Thus all the points shown in fig. B.1 lie on the surface of the sphere O_N. Accordingly, all "lengths" are measured in terms of the angles subtended at the centre of sphere O_N. Any straight lines in these diagrams are in fact arcs of shortest possible length on the surface of the sphere.

The length of the line $O_T O_N$ is given by c and is the separation between neighbouring spheres.

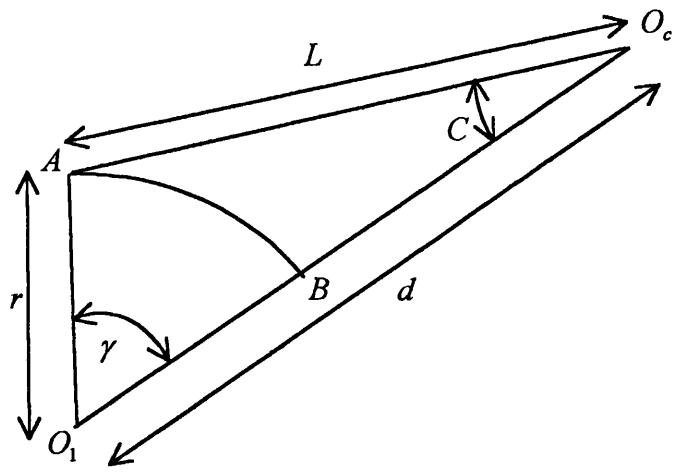

Figure B.2 The triangular base of the bypyramid. Triangle lies on surface of the sphere O_N.

The portion of the free area is $O_C AB$. This area may be calculated using

$$\text{Area } O_C AB = \text{Area Spherical Triangle } O_C AO_1 \qquad \text{(B.1)}$$

$$\text{- Area Sector } O_1 AB.$$

The area of the spherical triangle $O_C AO_1$ is a standard result, given by

$$(C + \gamma + O_C \hat{A} O_1 - \pi) R_N{}^2 \qquad \text{(B.2)}$$

The expression for the area of the sector, which lies on the surface of the sphere, was derived by integration. In fig. B.3, the area of the infinitesimal increment is given by

$$dA_s = \gamma R_N^{\,2} \operatorname{Sin} x dx. \quad \text{(B.3)}$$

The area of the whole sector, A_S is obtained using

$$\begin{aligned} A_S &= \int_0^r \gamma R_N^{\,2} \operatorname{Sin} x dx \\ &= \gamma R_N^{\,2} [-\operatorname{Cos} x]_0^r \quad \text{(B.4)} \\ &= \gamma R_N^{\,2} (1 - \operatorname{Cos} r) \end{aligned}$$

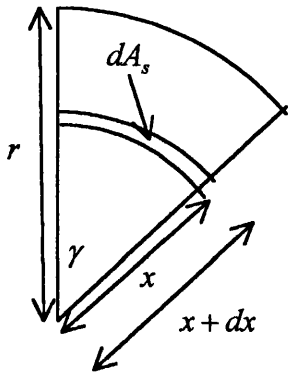

Figure B.3 Sector on surface of sphere O_N.

The final expression for the portion of the free area is thus given by

$$\begin{aligned} \text{Area } O_C AB &= (C + \gamma + O_C\hat{A}O_1 - \pi) R_N^{\,2} - \gamma R_N^{\,2} (1 - \operatorname{Cos} r) \\ &= (C + O_C\hat{A}O_1 - \pi + \gamma \operatorname{Cos} r) R_N^{\,2} \end{aligned} \quad \text{(B.5)}$$

The section of the free volume may be thought of as a pyramid with concave base $O_C AB$ and vertex O_T. This volume may be calculated using

$$\begin{aligned} \text{Volume } O_C ABO_T = &\text{ Volume bypyramid } O_N AO_1 O_C O_T \\ &- \text{Volume bypyramid } O_N O_1 AB \\ &- \text{Volume spherical sector } O_N O_C AB \end{aligned} \quad \text{(B.6)}$$

The spherical sector $O_N O_C AB$ has a base $O_C AB$ that is the portion of the free area previously calculated. The volume is given by

$$\text{Volume spherical sector } O_N O_C AB = (C + O_C \hat{A} O_1 - \pi + \gamma \operatorname{Cos} r) R_N^{\,3}. \qquad \text{(B.7)}$$

The volume of a pyramid is normally given by the formula,

$$\text{Volume} = \tfrac{1}{3} \times \text{area of base} \times \text{perpendicular height}. \qquad \text{(B.8)}$$

But the base is assumed to be flat. This is not the case with the two bypyramids being considered, where the bases are curved. The volumes of both by-pyramids are therefore obtained by integration.

B.2 Volume of By-pyramid Whose Base is a Triangle on the Surface of a Sphere

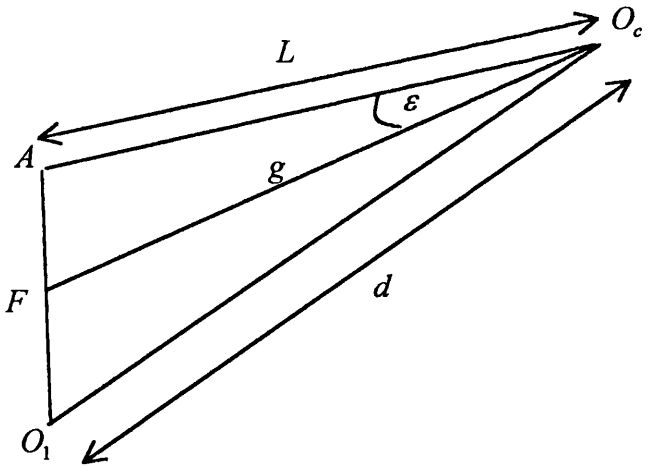

Figure B.4 Triangle on surface of sphere O_N, where one point is at O_C.

The point F lies along the line AO_1 such that $FO_C A = \varepsilon$. The length of the line $O_C F$ that cuts through the by-pyramid is given by g. The cross sectional view of the pyramid cut by the plane $O_N O_C O_T F$ may be seen in fig. B.5.

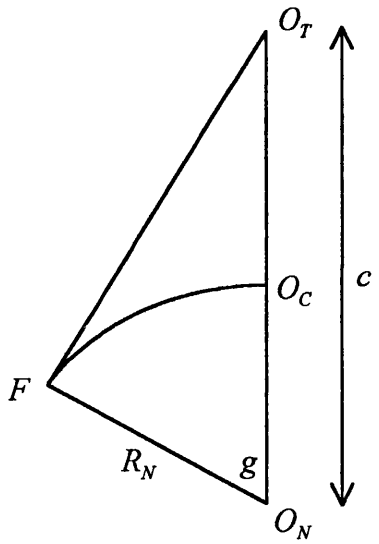

Figure B.5 Cross sectional view of bypyramid, where base is triangle lying on surface of sphere.

The area of triangle $O_N F O_T$ is given by

$$\text{Area } O_N F O_T = \tfrac{1}{2} R_N c \operatorname{Sin} g . \qquad \text{(B.9)}$$

The volume of the slice formed as ε is increased by $\delta\varepsilon$ is given by

$$\delta V_T = \tfrac{1}{6} c R_N{}^2 \operatorname{Sin}^2 g \delta\varepsilon . \qquad \text{(B.10)}$$

The total volume of the by-pyramid may therefore be obtained by integrating over ε. But first the function which maps ε onto g must be found.

Using standard trigonometry it is possible to derive the relationship,

$$\operatorname{Cot} g = K \operatorname{Sin}(\varepsilon + \mu), \text{(B.11)}$$

where K and μ are constants whose values may be found by a consideration of the values of g when $\varepsilon = 0$ and $\varepsilon = C$. Leading to

$$Tan\mu = \frac{SinC}{\frac{TanL}{Tand} - CosC}$$
$$K = \frac{1}{TanL \times Sin\mu} \qquad \text{(B.12)}$$

A standard results in trigonometry is

$$\mathrm{Sin}^2 g = \frac{\mathrm{Tan}^2 g}{1 + \mathrm{Tan}^2 g}. \quad \text{(B.13)}$$

This may be manipulated to give

$$\mathrm{Sin}^2 g = \frac{1}{K^2 \mathrm{Sin}^2(\varepsilon + \mu) + 1} \quad \text{(B.14)}$$

We can now write

$$V_T = \int_o^C \tfrac{1}{6} c R_N{}^2 \mathrm{Sin}^2 g \delta\varepsilon$$
$$= \int_o^C \frac{\tfrac{1}{6} c R_N{}^2}{K^2 \mathrm{Sin}^2(\varepsilon + \mu) + 1} \delta\varepsilon \qquad \text{(B.15)}$$

Let $y = \mathrm{Cot}(\varepsilon + \mu)$, so that

$$\mathrm{Sin}^2(\varepsilon + \mu) = \frac{1}{1 + y^2}$$
$$d\varepsilon \equiv \frac{-dy}{1 + y^2} \qquad \text{(B.16)}$$

By substitution it is now possible to obtain the expression for the volume of the bypyramid with its base on the surface of the sphere O_N.

$$
\begin{aligned}
V_T &= \int_{\mathrm{Cot}\,\mu}^{\mathrm{Cot}(C+\mu)} \frac{-\frac{1}{6}R_N c^2}{(1+y^2)\left(\frac{K^2}{1+y^2}+1\right)}dy \\
&= \int_{\mathrm{Cot}(C+\mu)}^{\mathrm{Cot}\,\mu} \frac{\frac{1}{6}R_N c^2}{K^2+1+y^2}dy \\
&= \frac{1}{6}R_N c^2\left[\frac{1}{\sqrt{1+K^2}}\mathrm{Tan}^{-1}\left(\frac{y}{\sqrt{1+K^2}}\right)\right]_{\mathrm{Cot}(C+\mu)}^{\mathrm{Cot}\,\mu} \\
&= \frac{R_N c^2}{6\sqrt{1+K^2}}\left[\mathrm{Tan}^{-1}\left(\frac{\mathrm{Cot}\,\mu}{\sqrt{1+K^2}}\right)-\mathrm{Tan}^{-1}\left(\frac{\mathrm{Cot}(C+\mu)}{\sqrt{1+K^2}}\right)\right]
\end{aligned}
\qquad \text{(B.17)}
$$

B.3 Volume of By-pyramid Whose Base is a Sector on the Surface of a Sphere

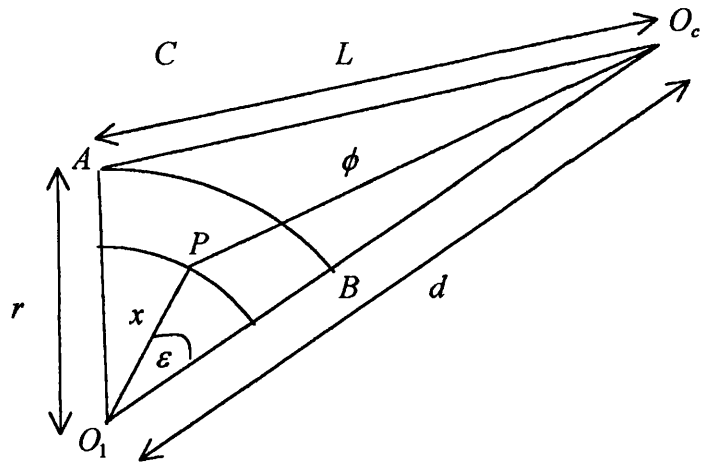

Figure B.6 Sector AO_1B lying on the surface of sphere O_N, the base of a by-pyramid.

Consider some sector AO_1B lying on the surface of the sphere O_N. Note that none of the three points lie along the line $O_N O_T$. A point P is defined such that $O_1P = x$, $O_C P = \phi$ and $BO_1P = \varepsilon$ (fig. B.6). The cross sectional view is shown in fig. B.7.

ϕ is related to x by the spherical trigonometric relationship,

$$\mathrm{Cos}\,\phi = \mathrm{Cos}\,x\,\mathrm{Cos}\,d + \mathrm{Sin}\,x\,\mathrm{Sin}\,d\,\mathrm{Cos}\,\varepsilon. \qquad \text{(B.18)}$$

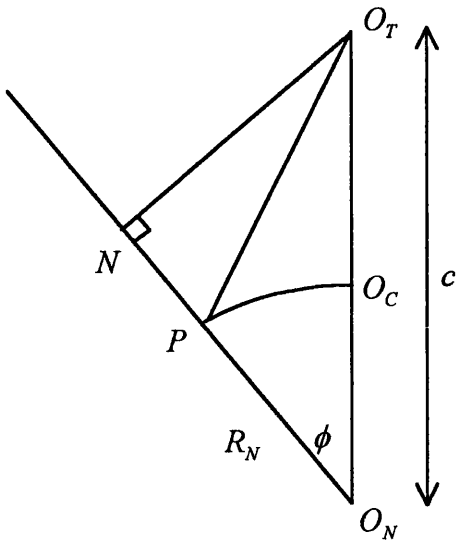

Figure B.7 Cross sectional view of bypyramid, where base is sector lying on surface of sphere.

The area on the surface of the sphere formed by an infinitesimally small increase of ε and x is given by

$$\delta A_S = \mathrm{Sin}\, x R_N{}^2 \delta x \delta \varepsilon . \quad \text{(B.19)}$$

The volume of the by-pyramid with base at P having area δA_S and vertices at O_N and O_T is then given by

$$\delta V_S = \tfrac{1}{3} c \,\mathrm{Cos}\, \phi \delta A_S \quad \text{(B.20)}$$

Substituting in equations B.18 and B.19 gives

$$\delta V_S = \tfrac{1}{3} c(\mathrm{Cos}\, x \,\mathrm{Cos}\, d + \mathrm{Sin}\, x \,\mathrm{Sin}\, d \,\mathrm{Cos}\, \varepsilon)\,\mathrm{Sin}\, x R_N{}^2 \delta\varepsilon\delta x \text{ (B.21)}$$

The volume of the by-pyramid may then be obtained by integrating over ε and x. So that

$$
\begin{aligned}
V_S &= \int_0^{\gamma}\int_0^{r} \tfrac{1}{3} c(\mathrm{Cos}\,x\,\mathrm{Cos}\,d + \mathrm{Sin}\,x\,\mathrm{Sin}\,d\,\mathrm{Cos}\,\varepsilon)\,\mathrm{Sin}\,x R_N^{\,2}\,\delta x\,\delta\varepsilon \\
&= \tfrac{1}{3} c R_N^{\,2} \int_0^{\gamma}\int_0^{r} (\mathrm{Sin}\,x\,\mathrm{Cos}\,x\,\mathrm{Cos}\,d + \mathrm{Sin}^2\,x\,\mathrm{Sin}\,d\,\mathrm{Cos}\,\varepsilon)\,\delta x\,\delta\varepsilon \qquad \text{(B.22)} \\
&= \tfrac{1}{3} c R_N^{\,2} \int_0^{\gamma}\int_0^{r} \left(\frac{\mathrm{Sin}\,2x}{2}\mathrm{Cos}\,d + \frac{1-\mathrm{Cos}\,2x}{2}\mathrm{Sin}\,d\,\mathrm{Cos}\,\varepsilon \right) \delta x\,\delta\varepsilon
\end{aligned}
$$

Carrying out the integration over x leads to

$$
\begin{aligned}
V_S &= \tfrac{1}{3} c R_N^{\,2} \int_0^{\gamma} \left[\frac{-\mathrm{Cos}\,2x}{4}\mathrm{Cos}\,d + \frac{2x-\mathrm{Sin}\,2x}{4}\mathrm{Sin}\,d\,\mathrm{Cos}\,\varepsilon \right]_0^{r} \delta\varepsilon \\
&= \tfrac{1}{3} c R_N^{\,2} \int_0^{\gamma} \left(\frac{-(\mathrm{Cos}\,2r-1)}{4}\mathrm{Cos}\,d + \frac{2r-\mathrm{Sin}\,2r}{4}\mathrm{Sin}\,d\,\mathrm{Cos}\,\varepsilon \right) \delta\varepsilon
\end{aligned} \qquad \text{(B.23)}
$$

Finally integrating over ε gives

$$
\begin{aligned}
V_S &= \tfrac{1}{3} c R_N^{\,2} \left[\frac{-(\mathrm{Cos}\,2r-1)}{4}\mathrm{Cos}\,d \times \varepsilon + \frac{2r-\mathrm{Sin}\,2r}{4}\mathrm{Sin}\,d\,\mathrm{Sin}\,\varepsilon \right]_0^{\gamma} \\
&= \tfrac{1}{3} c R_N^{\,2} \left[\frac{-(\mathrm{Cos}\,2r-1)}{4}\mathrm{Cos}\,d \times \gamma + \frac{2r-\mathrm{Sin}\,2r}{4}\mathrm{Sin}\,d\,\mathrm{Sin}\,\gamma \right]
\end{aligned} \qquad \text{(B.24)}
$$

Combining the various parts according to equation B.6 gives the final expression for one portion of the free volume,

$$
\begin{aligned}
V_{fp} &= \frac{R_N c^2}{6\sqrt{1+K^2}} \left[\mathrm{Tan}^{-1}\left(\frac{\mathrm{Cot}\,\mu}{\sqrt{1+K^2}} \right) - \mathrm{Tan}^{-1}\left(\frac{\mathrm{Cot}(C+\mu)}{\sqrt{1+K^2}} \right) \right] \\
&\quad - \tfrac{1}{3} c R_N^{\,2} \left[\frac{-(\mathrm{Cos}\,2r-1)}{4}\mathrm{Cos}\,d \times \gamma + \frac{2r-\mathrm{Sin}\,2r}{4}\mathrm{Sin}\,d\,\mathrm{Sin}\,\gamma \right] \qquad \text{(B.25)} \\
&\quad - (C + O_C \hat{A} O_1 - \pi + \gamma\,\mathrm{Cos}\,r) R_N^{\,3}
\end{aligned}
$$

$$Tan\mu = \frac{SinC}{\frac{TanL}{Tand} - CosC}$$
$$K = \frac{1}{TanL \times Sin\mu} \qquad \text{(B.26)}$$

This expression for just one portion of the free volume is the basis of the equation for the whole of the free volume given in section 8.2.

Appendix C Algorithm Code

All code presented here is written in FORTAN 90.

C.1 Code for TRAPINT Algorithm

```
SUBROUTINE TRAPINT(BOUND,MINSQ,FREEV,SLCS)
DOUBLE PRECISION BOUND
DOUBLE PRECISION X,Y,Z,FREEV,FREEZ
DOUBLE PRECISION WID,XYAREA,MINSQ(12)
INTEGER SLCS

FREEZ=0D0
WID=2*BOUND/SLCS
XYAREA=WID**2
X=-BOUND
DO WHILE (X.LT.BOUND)
        Y=-BOUND
        DO WHILE (Y.LT.BOUND)
                CALL ZVAL(X,Y,BOUND,Z,MINSQ)
                FREEZ=FREEZ+ZY=Y+WID
                ENDDOX=X+WID
        ENDDO
FREEV=FREEZ*XYAREA
RETURN
END

SUBROUTINE ZVAL(X,Y,ZBOUND,Z,MINSQ)
DOUBLE PRECISION ZBOUND,X,Y,Z,SR,SQ,HIGH,LOW,DELTAM
INTEGER NUM
DOUBLE PRECISION POSN(12,3),MINSQ(12),A,PI,ASQ,HIGHQ,LOWQ
LOGICAL MIDD
COMMON/XTAL/POSN,A,PI,ASQ

MIDD=.FALSE.
DELTAM=0D0
HIGH=ZBOUND
LOW=-ZBOUND
NUM=12
DO N=1,4
SQ=MINSQ(N+4)-((X-POSN(N+4,1))**2+(Y-POSN(N+4,2))**2)
        IF (SQ.GE.0D0) THEN
                MIDD=.TRUE.
                SR=SQRT(SQ)
                IF (SR.GT.DELTAM) DELTAM=SR
        ENDIF
        SQ=MINSQ(N)-((X-POSN(N,1))**2+(Y-POSN(N,2))**2)
        IF (SQ.GE.0D0) THEN
                SR=SQRT(SQ)
                HIGHQ=POSN(N,3)-SR
                IF (HIGHQ.LT.HIGH) HIGH=HIGHQ
        ENDIF
        SQ=MINSQ(N+8)-((X-POSN(N+8,1))**2+(Y-POSN(N+8,2))**2)
        IF (SQ.GE.0D0) THEN
                SR=SQRT(SQ)
```

```
                LOWQ=POSN(N+8,3)+SR
                IF (LOWQ.GT.LOW) LOW=LOWQ
        ENDIF
ENDDO
IF (.NOT.MIDD) THEN
        IF (HIGH.GT.LOW) THEN
                Z=HIGH-LOW
                RETURN
        ELSE
                Z=0D0
                RETURN
        ENDIF
        ELSE    IF (HIGH.LT.(DELTAM)) THEN
                HIGH=-DELTAM
        ELSEIF (LOW.GT.(-DELTAM)) THEN
                LOW=DELTAM
        ELSE
                Z=HIGH-LOW-(2D0*DELTAM)
                RETURN
        ENDIF
        IF (HIGH.GT.LOW) THEN
                Z=HIGH-LOW
                RETURN
        ELSE
                Z=0D0
                RETURN
        ENDIF
ENDIF
END
```

C.2 Code for FREEAREA Algorithm

```
FREEAREA(C,EXC,AREA,VOL,ERR)
DOUBLE PRECISION RA,GAP(10),THTPOSS,GAPOSS,RADPOSS
DOUBLE PRECISION AREA,NAREA,SA,C,CRNR(2:11),SINPOSSSQ
DOUBLE PRECISION PI,EXC(0:11),RAD(2:11),THT(2,2:15),ALF,BETA(2:15)
DOUBLE PRECISION TANMU,K,GAM,CEN,MU,SQ1PK,SINPID3
DOUBLE PRECISION INTCOS,VOL,NVOL,SQ2,SMCOS,MXTHT,MXSA,MXGAP   ,MXRAD
DOUBLE PRECISION
COSGAM,COSRA,SINRA,COSLNG,COSCEN,TANCEN,TANLNG,CENGAP
DOUBLE PRECISION MXTHTPLUS,ANGLE(11),SINPOSS,TANCPMU,KAP,BACKTHT
LOGICAL INC(2:15),CLOSED,INCSM(8:11),AFT,OPPOVR(2),ZERO,OVRLAP,ERR,ERRGPN,
                                                                TWICEROUND
INTEGER(1) ROTOP(11,12),N,GPN,PN,POSSOVR(4,2:11),PSTHP(4,2:11)
INTEGER(1) CNTPOSS,NXT,INIT,PSTHPRV(4,2:11),PSGAP(4,2:11),CIREF,CENGAPTYP(2:11)
INTEGER(1) HFCNRTYP(2,2:11),MXNXT,AFTSH,CCNTDATA
ROTOP/0,1,3,7,4,2,8,5,6,11,9,&
&1,2,0,4,5,3,9,6,7,8,10,&
&2,3,1,5,6,0,10,7,4,9,11,&
&3,0,2,6,7,1,11,4,5,10,8,&
&4,9,1,0,8,5,7,10,2,3,11,&
&7,3,11,8,0,6,4,2,10,9,1,&
&5,9,1,2,10,4,6,8,0,3,11,&
&6,3,11,10,2,7,5,0,8,9,1,&
&8,9,11,7,4,10,0,5,6,3,1,&
&9,10,8,4,5,11,1,6,7,0,2,&
&10,11,9,5,6,8,2,7,4,1,3,&
&11,8,10,6,7,9,3,4,5,2,0/&
```

```
&POSSOVR/6,3,9,8,&
&4,10,7,9,&
&7,5,11,10,&
&2,8,6,11,&
&3,9,4,10,&
&5,11,2,8,&
&2,6,3,9,&
&3,4,10,7,&
&4,7,5,11,&
&5,2,8,6/&
& PSTHP/1,1,2,3,&
& 1,4,4,5,&
& 1,1,2,3,&
& 1,4,4,5,&
& 1,6,6,7,&
& 1,6,6,7,&
& 1,8,9,10,&
& 1,8,9,10,&
& 1,8,9,10,&
& 1,8,9,10/&
 &PSGAP/1,2,3,4,&
& 5,6,2,4,&
& 1,2,3,4,&
& 5,6,2,4,&
& 1,7,2,8,&
& 1,7,2,8,&
& 4,7,3,9,&
& 4,6,10,8,&
& 4,7,3,9,&
& 4,6,10,8/&
 &PSTHPRV/1,1,9,1,&
& 1,8,6,1,&
& 1,1,9,1,&
& 1,8,6,1,&
& 1,8,4,10,&
& 1,8,4,10,&
& 5,6,2,10,&
& 3,4,9,7,&
& 5,6,2,10,&
& 3,4,9,7/&
&CENGAPTYP/5,5,5,5,1,1,4,4,4,4/&
&HFCNRTYP/3,5,5,3,3,5,5,3,&
& 8,8,8,8,11,11,11,11,11,11,11,11/

ERR=.FALSE.
PI=ASIN(1D0)*2D0
SQ2=SQRT(2D0)
SINPID3=SQRT(3D0)/2D0
CRNR=ACOS(-1D0/SQRT(3D0))
CRNR(6)=PI
CRNR(7)=PI
CRNR(8)=2D0*PI
CRNR(9)=2D0*PI
CRNR(10)=2D0*PI
CRNR(11)=2D0*PIANGLE(1)=0D0
ANGLE(2)=ACOS(3D0/SQRT(11D0))
ANGLE(3)=ACOS(1D0/SQRT(3D0))
ANGLE(4)=ACOS(SQRT(2D0/3D0))
ANGLE(5)=ACOS(1D0/3D0)
ANGLE(6)=PI/4D0
```

```
ANGLE(7)=ACOS(1D0/SQRT(5D0))
ANGLE(8)=PI/2D0
ANGLE(9)=ACOS(-SQRT(3D0/11D0))
ANGLE(10)=ACOS(-1D0*SQRT(3D0/5D0))
ANGLE(11)=PIGAP(1)=PI/4D0
GAP(2)=PI/2D0
GAP(3)=ACOS(1D0/(2D0*SQRT(3D0)))
GAP(4)=PI/6D0
GAP(5)=PI/3D0
GAP(6)=ACOS(1D0/SQRT(3D0))
GAP(7)=ACOS(SQRT(2D0/3D0))
GAP(8)=ACOS(1D0/SQRT(6D0))
GAP(9)=ACOS(2D0/3D0)
GAP(10)=ACOS(5D0/6D0)
AREA=0D0
VOL=0D0
DO N=1,12
        NAREA=2D0*PI
        INTCOS=0D0
        INC=.FALSE.
        CLOSED=.FALSE.
        DO GPN=2,5
                RAD(GPN)=ACOS((C**2+EXC(ROTOP(1,N))**2-EXC(ROTOP(GPN,N))**2)&
                &/(2D0*C*EXC(ROTOP(1,N))))
                SMCOS=(3D0*C**2+EXC(ROTOP(1,N))**2-EXC(ROTOP((GPN+6),N))**2)&
                &/(2D0*SQRT(3D0)*C*EXC(ROTOP(1,N)))
                SMCOS=SMCOS-INT(SMCOS)*(SMCOS-1D0)
                RAD(GPN+6)=ACOS(SMCOS)
                INCSM(GPN+6)=((RAD(GPN+6)-RAD(GPN)+PI/6D0).GT.0D0)
        ENDDO
        DO GPN=6,7
                RAD(GPN)=ACOS((2D0*C**2+EXC(ROTOP(1,N))**2-
                        EXC(ROTOP(GPN,N))**2)/(2D0*SQRT(2D0)*C*EXC(ROTOP(1,N))))
        ENDDO
        NXT=2
        IF (INCSM(8)) NXT=8
        INIT=NXT
        THT=0D0
        AFT=.FALSE.
        AFTSH=0CCNT=1
        TWICEROUND=.FALSE.
        DO WHILE (.NOT.CLOSED)
                CCNT=CCNT+1
                IF (CCNT.GT.20) TWICEROUND=.TRUE.
                RA=RAD(NXT)
                MXTHT=0D0
                MXNXT=0
                DO CNTPOSS=1,4
                        IF (((NXT.GT.5).OR.(CNTPOSS.LE.3).OR.(.NOT.AFT)).AND.&
&((POSSOVR(CNTPOSS,NXT).NE.6).OR.INC(6).OR.(MOD(NXT,6).NE.5))) THEN
                                GAPOSS=GAP(PSGAP(CNTPOSS,NXT))
                                RADPOSS=RAD(POSSOVR(CNTPOSS,NXT))
                                SA=(RA+RADPOSS+GAPOSS)/2D0
                                SINPOSSSQ=SIN(SA-GAPOSS)*SIN(SA-RA)/&
                                & (SIN(GAPOSS)*SIN(RA))
                                IF ((SINPOSSSQ.LE.1D0).AND.(SINPOSSSQ.GE.0D0))
                                                                        THEN
                                SINPOSS=SQRT(SINPOSSSQ)
                                THTPOSS=2D0*ASIN(SINPOSS)+
                                                ANGLE(PSTHP(CNTPOSS,NXT))
```

```
                        IF (THTPOSS.GT.MXTHT) THEN
                            MXTHT=THTPOSS
                            MXNXT=POSSOVR(CNTPOSS,NXT)
                            MXSA=SA
                            MXGAP=GAPOSS
                            MXRAD=RADPOSS
                            MXTHTPLUS=ANGLE(PSTHPRV(CNTPOSS
                                                        ,NXT))
                        ENDIF
                    ENDIF
                ENDIF
            ENDDO
            THT(1,NXT+AFTSH)=MXTHT
            BETA(NXT+AFTSH)=2D0*ASIN(SQRT(SIN(MXSA-MXRAD)*
                                SIN(MXSA-RA)/(SIN(MXRAD)*SIN(RA))))
            BACKTHT=2D0*ASIN(SQRT(SIN(MXSA-MXGAP)*SIN(MXSA-MXRAD)/&
            & (SIN(MXGAP)*SIN(MXRAD))))+MXTHTPLUS
            AFT=((MXNXT.LE.5).AND.(INCSM(MXNXT+6)).AND.
                            (BACKTHT.GT.ANGLE(HFCNRTYP(2,MXNXT))))
            IF (AFT) THEN
                AFTSH=10
            ELSE
                AFTSH=0
            ENDIF
            THT(2,MXNXT+AFTSH)=BACKTHT
            INC(MXNXT+AFTSH)=.TRUE.
            CLOSED=((MXNXT.EQ.INIT).OR.((MXNXT.EQ.6).&
            &AND.(NXT.NE.2).AND.(NXT.NE.8))&
            &.OR.((MXNXT.EQ.2).AND.(NXT.NE.8).AND.(AFT))&
            &.OR.(TWICEROUND))
            NXT=MXNXT
        ENDDO
        OPPOVR(1)=((RAD(2)+RAD(4)).GT.(2D0*PI/3D0))
        OPPOVR(2)=((RAD(3)+RAD(5)).GT.(2D0*PI/3D0))
        ZERO=(OPPOVR(1).AND.OPPOVR(2))
        IF (.NOT.ZERO) THEN
            IF (OPPOVR(1)) THEN
                IF ((.NOT.INC(2)).OR.(.NOT.INC(4))) THEN
                    ZERO=.TRUE.
                ELSE
                    INC(12)=.TRUE.
                    THT(1,12)=THT(1,2)
                    SA=(RAD(2)+RAD(4))/2D0+PI/3D0
                    KAP=2D0*ASIN(SQRT(SIN(SA-2D0*PI/3D0)*SIN(SA-
                                RAD(2))/(SIN(2D0*PI/3D0)*SIN(RAD(2)))))
                    THT(1,2)=ANGLE(3)+KAP
                    THT(2,12)=ANGLE(5)+KAP
                    BETA(12)=BETA(2)
                    BETA(14)=BETA(4)
                    BETA(2)=2D0*ASIN(SQRT(SIN(SA-RAD(4))*SIN(SA-
                                    RAD(2))/(SIN(RAD(4))*SIN(RAD(2)))))
                INC(14)=.TRUE.
                THT(1,14)=THT(1,4)
                KAP=2D0*ASIN(SQRT(SIN(SA-2D0*PI/3D0)*SIN(SA-
                                RAD(4))/(SIN(2D0*PI/3D0)*SIN(RAD(4)))))
                THT(1,4)=ANGLE(3)+KAP
                THT(2,14)=ANGLE(5)+KAP
                BETA(4)=BETA(2)
                IF (((THT(2,12)+THT(1,12)).GE.CRNR(2)).
                            OR.((THT(2,4)+THT(1,4)).GE.CRNR(4))) THEN
```

```
                INC(12)=.FALSE.
                INC(4)=.FALSE.
                INC(6)=.FALSE.
                INC(8)=.FALSE.
                INC(3)=.FALSE.
                INC(9)=.FALSE.
                INC(13)=.FALSE.
        ENDIF
        IF (((THT(2,2)+THT(1,2)).GE.CRNR(2)).OR.
                        ((THT(2,14)+THT(1,14)).GE.CRNR(4))) THEN
                INC(2)=.FALSE.
                INC(14)=.FALSE.
                INC(7)=.FALSE.
                INC(10)=.FALSE.
                INC(5)=.FALSE.
                INC(11)=.FALSE.
                INC(15)=.FALSE.
        ENDIF
        IF (INC(2).AND.INC(4)) THEN
                NAREA=4D0*PI
        ELSEIF (INC(2).OR.INC(4)) THEN
                NAREA=2D0*PI
        ELSE
                ZERO=.TRUE.
        ENDIF
    ENDIF
ELSEIF (OPPOVR(2)) THEN
    IF ((.NOT.INC(3)).OR.(.NOT.INC(5))) THEN
        ZERO=.TRUE.
    ELSE
        INC(13)=.TRUE.
        THT(1,13)=THT(1,3)
        SA=(RAD(3)+RAD(5))/2D0+PI/3D0
        KAP=2D0*ASIN(SQRT(SIN(SA-2D0*PI/3D0)*SIN(SA-
                        RAD(3))/(SIN(2D0*PI/3D0)*SIN(RAD(3)))))
        THT(1,3)=ANGLE(5)+KAP
        THT(2,13)=ANGLE(3)+KAP
        BETA(13)=BETA(3)
        BETA(15)=BETA(5)
        BETA(3)=2D0*ASIN(SQRT(SIN(SA-RAD(5))*SIN(SA-
                        RAD(3))/ (SIN(RAD(5))*SIN(RAD(3)))))
        INC(15)=.TRUE.
        THT(1,15)=THT(1,5)
        KAP=2D0*ASIN(SQRT(SIN(SA-2D0*PI/3D0)*SIN(SA-
                        RAD(5))/(SIN(2D0*PI/3D0)*SIN(RAD(5)))))
        THT(1,5)=ANGLE(5)+KAP
        THT(2,15)=ANGLE(3)+KAP
        BETA(5)=BETA(3)
        IF (((THT(2,15)+THT(1,15)).GE.CRNR(5)).OR.
                        ((THT(2,3)+THT(1,3)).GE.CRNR(3))) THEN
                INC(15)=.FALSE.
                INC(3)=.FALSE.
                INC(6)=.FALSE.
                INC(9)=.FALSE.
                INC(2)=.FALSE.
                INC(8)=.FALSE.
                INC(12)=.FALSE.
        ENDIF
        IF (((THT(2,5)+THT(1,5)).GE.CRNR(5)).OR.
                        ((THT(2,13)+THT(1,13)).GE.CRNR(3))) THEN
```

```
                        INC(5)=.FALSE.
                        INC(13)=.FALSE.
                        INC(7)=.FALSE.
                        INC(11)=.FALSE.
                        INC(4)=.FALSE.
                        INC(10)=.FALSE.
                        INC(14)=.FALSE.
                ENDIF
                IF (INC(3).AND.INC(5)) THEN
                        NAREA=4D0*PI
                ELSEIF (INC(3).OR.INC(5)) THEN
                        NAREA=2D0*PI
                ELSE
                        ZERO=.TRUE.
                ENDIF
        ENDIF
    ENDIF
ENDIF
IF (.NOT.ZERO) THEN
        OVRLAP=.TRUE.
        DO GPN=2,15
                ERRGPN=.FALSE.
                IF (INC(GPN)) THEN
                        CIREF=MOD((GPN-2),10)+2
                        CENGAP=GAP(CENGAPTYP(CIREF))
                        RA=RAD(CIREF)
                        ALF=CRNR(CIREF)-(THT(1,GPN)+THT(2,GPN))
                        IF (ALF.GE.0D0) THEN
                                OVRLAP=.FALSE.
                                COSRA=COS(RA)
                                SINRA=SIN(RA)
                                DO PN=1,2
                                        GAM=ANGLE(HFCNRTYP(PN,CIREF))-
                                                                THT(PN,GPN)
                                        COSGAM=COS(GAM)
                                        COSLNG=COSRA*COS(CENGAP)+SINRA
                                                        *SIN(CENGAP)*COSGAM
                                        COSCEN=(COSRA*SIN(CENGAP)-
                                                SINRA*COSGAM*COS(CENGAP))
                                                        /SQRT(1D0-COSLNG**2)
                                        COSCEN=COSCEN-INT(COSCEN)
                                                                *(COSCEN-D0)
                                        CEN=ACOS(COSCEN)
                                        IF (CEN.NE.0D0) THEN
                                                TANCEN=TAN(CEN)
                                                TANLNG=SQRT(1D0/
                                                        (COSLNG**2)-D0)

                                                TANMU=SIN(CEN)/(TANLNG/
                                                        TAN(CENGAP)-COSGAM)
                                                MU=ATAN(TANMU)
                                                K=1D0/(TANLNG*SIN(MU))
                                                SQ1PK=SQRT(1D0+K*K)
                                                TANCPMU=(TANCEN+TANMU)
                                                        /(1D0-TANCEN*TANMU)
                                                INTCOS=INTCOS+SIGN((ATAN(D0
                                        /(SQ1PK*TANMU))-ATAN(1D0/(SQ1PK*
                                                TANCPMU)))/(SQ1PK*2D0),GAM)+
                                                        (COS(2D0*RA)-1D0)*GAM*
```

```
                                                        COS(CENGAP)/4D0-
                                                SIN(GAM)*(RA-SIN(2D0*RA)/2D0)
                                                        *SIN(CENGAP)/2D0
                                    ENDIF
                                ENDDO
                            ENDIF
                            NAREA=NAREA+ALF*COS(RA)-BETA(GPN)
                            IF (ALF.LE.-2D-15) ERRGPN=.TRUE.
                        ENDIF
                ENDDO
                IF (.NOT.OVRLAP) THEN
                        AREA=AREA+NAREA*EXC(ROTOP(1,N))**2
                        NVOL=(C*INTCOS-EXC(ROTOP(1,N))*NAREA)/3D0
                        IF ((NAREA.LT.0D0).OR.(ERRGPN)) THEN
                            ERR=.TRUE.
                        ENDIF
                        VOL=VOL+EXC(ROTOP(1,N))**2*NVOL
                ENDIF
        ENDIF
ENDDO
RETURN
END
```

References

1 Wang, S. G., H. W. Xiang, et al., Chinese Chemical Letters, **11**, 989, 2000

2 Pavlyukhin, Y. T., Journal of Structural Chemistry, **41**, 809, 2000

3 Yelash, L. V. and Kraska, T., Phys. Chem. Chem. Phys., **3**, 3114, 2001

4 Mulero, A., C. Galan, et al., Phys. Chem. Chem. Phys., **3**, 4991, 2001

5 Pronk, S. and D. Frenkel , Phys. Chem.B, **105**, 6722, 2000

6 Anishchik, S.V., Medvedev, N., N., Phys. Rev. Lett, **75**, 4314, 1995

7 Dixit, N. M. and Zukoski, C. F., Phys. Rev.E, **64**, 1604, 2001

8 Wild, R. and Harrowell, P. , J. Chem. Phys., **114**, 9059, 2001

9 Davidchack, R. L. and Laird, B. B., J. Chem. Phys., **108**, 9452, 1998

10 Morrell, W.E., and Hilderbrand, J.H., J. Chem. Phys., **4**, 224, 1936

11 Wood, W. W., J. Chem. Phys., **20**, 1334, 1952

12 Kirkwood, Maun, and Alder, J. Chem. Phys., **18**, 1040, 1950

13 Zwanzig, Kirkwood, Stripp and Oppenheim, J. Chem. Phys., **21**, 1268, 1953

14 Hirschfelder, Stevenson, Eyring, J. Chem. Phys., **5**, 896, 1937

15 Metropolis, N., Rosenbluth, A. W., Rosenbluth, M. N., Teller, A. H., Teller, E., J. Chem. Phys., **21**, 1087, 1953

16 Rosenbluth, M. N., Rosenbluth, A. W., J. Chem. Phys., **22**, 881, 1953

17 Alder, B. J., Wainwright, T. E., J. Chem. Phys., **31**, 459, 1959

18 Alder, B. J., Wainwright, T. E., J. Chem. Phys., **27**, 1208, 1957

19 Wood, W. W., Jacobson, J. D., J. Chem. Phys, **27**, 1207, 1957

20 Baus, M., Collot, J. L. Mol. Phys., **55**, 653, 1985

21 Oxtoby, D.W., Crystallization of liquids: a density functional approach, in Liquids, Freezing and Glass Transitions, Les Houches, session L1, July 3-28, 1989, Hansen, J.P., Levesque, D., and Zinn-Justin, J., Eds., Elsevier/North-Holland, Amerstadam, 1991, 147-191.

22 Pieranski, P., Malecki, J., kuczynski, W., Wojciechowski, K., Phil. Mag. A, **37**, 107, 1978

23 Jardine, R. S. (2001). Interactions in colloidal systems. Chemistry, University of Bath.

24 Hachisu, S., Yoshimura, S., Physics of Complex and supermolecular fluids, 221, John Wiley & Sons, New York, 1987

25 Pusey, P. N., van Megen, W., Nature (London), **320**, 340, 1986

26 Bartlett, P., van Megen, W., Granular Matter, 195, Springer-Verlang, New York, 1994

27 Bartlett, P., Pusey, P. N., and Ottewill, R. H., 1991, Langmuir, **7**, 213

28 Zhu, J., Li, M., Rogers, R. Meyer, W. Ottewill, R. H., STS-73 Space Shuttle Crew, Russel, W. B., Chalkin, P. M., Nature, **387**, 883, 1997

29 Cheng, Z. D., Zhu J. X., et al., Applied Optics, **40**, 4146, 2001

30 Elliot, M. S., Haddon, S. B., et al., J. Phys. Cond. Matt., **13**, 553, 2001

31 Gasser, U., Weeks, E. R., et al., Science **292**, 258, 2001

32 Lennard-Jones, J. E., Devonshire, A. F., Proc. Roy. Soc., **163A**, 53, 1937

33 Kirkwood, J. G., J. Chem. Phys, **18**, 380, 1950

34 Cottin, X., Monson, P. A., J. Chem. Phys., **99**, 8914, 1993

35 Cottin, X., Monson, P. A., J. Chem. Phys., **105**, 10022, 1996

36 Wojciechowski, K.W., Branka, A. C., J. Phys. Chem. Solids, **45**, 913, 1984

37 Schmidt, M., Lowen, H., Phys. Rev. Lett., **76**, 4552, 1996

38 J. P. Voisey, Computer Calculations on Hard Spheres, University of Bath, 1996

39 Hoover, W. G., Ashurst, W. T., Grover, R., J. Chem. Phys., **57**, 1259, 1972

40 Buehler, R. J., Wentorf, JR., R. H., Hirschfelder, J. O. and Curtiss, C. F., J. Chem. Phys. **19**, 61, 1950

41 Woodcock, L. V., Nature, **385**, 141, 1997

42 Bolhuis, P. G., Frenkel, D., Mau, S., Huse, D. A., Nature, **388**, 235, 1997

43 Kiely, C. J., Fink J., et al., Nature, **396**, 444, 1998

44 Andres, R.P., Bielefeld, J.D., Henderson, J.I., Janes, D.B., Kolagunta, V.R., Kubiak, C.P., Mahoney, W.J., Osifchin, R.G., Science, **273**, 1690, 1996

45 Biswas, R., Sigalas, M. M., et al.,Phys. Rev. B, **57**, 370, 1998

46 Elghanian, R., Storhoff, J.J., Mucic, R.C., Letsinger, R.L., Mirkin, C.A., Science, **277**, 1078, 1997

47 Sanders, J. V., Phil. Mag. A, **42**, 705, 1980

48 Murray, M. J., and Sanders, J. V., Phil. Mag. A., **42**, 721, 1980

49 Hachisu, S., Yoshimura, S., Physics of Complex and supermolecular fluids, 221, John Wiley & Sons, New York, 1987

50 Bartlett, P., Ottewill, R. H., Pusey, P. N., Phys. Rev. Lett., **68**, 3801, 1992

51 Pusey, P. N., Schofield, A. B., private communication.

52 Schofield, A. B., Phys. Rev. E., **64**, 1403, 2001

53 Hunt, N., R. Jardine, et al., Phys. Rev. E, **62**, 900, 2000

54 Eldridge, M. D., Madden, P. A., Frenkel, D., Molec. Phys., **79**, 105, 1993

55 Eldridge, M. D., Madden, P. A., Frenkel, D., Molec. Phys., **80**, 987, 1993

56 Eldridge, M. D., Madden, P. A., Pusey, P. N., Bartlett, P., Molec. Phys., **84**, 395, 1995

57 Trizac, E., Eldridge, M. D., Madden, P. A., Molec. Phys., **90**, 675, 1997

58 Davidchack, R. L. and B. B. Laird, B.B., Molec. Phys., **97**, 833, 1999

59 Williams, S. R. and W. van Megen, W., Phys. Rev. E, **64**, 1502,2001

60 Mansoori, G. A., Carnahan, N. F., Starling, K. E. and Leland, T. W., J. Chem. Phys., **54**, 1523, 1971

61 Bartlett, P., J. Phys. C., **2**, 4979, 1990

62 Ghotbi, C. and Vera, J.H., Canadian J. Chem. Eng., **79**, 678, 2001 Page: 6

63 Santos, A.., Yuste S. B., et al., Molec.. Phys., **99**, 1959, 2001

64 Saija, F., Fiumura, G., and Giaquinta, P. V., Molec. Phys., **87**, 991, 1996

65 Saija, F., Fiumura, G., and Giaquinta, P. V., Molec. Phys., **90**, 679, 1997

66 Saija, F., Fiumura, G., and Giaquinta, P. V., Molec. Phys., **92**, 1089, 1997

67 Coussaert, T., and Baus, M., Phys. Rev. Lett., **79**, 1881, 1997

68 Coussaert, T., and Baus, M., J. Chem. Phys, **109**, 6012, 1998

69 Hamad, E. Z., Ind. Eng. Chem. Res., **36**, 4385, 1997

70 Alder, B. J., J. Chem. Phys., **40**, 2724, 1964

71 Trizac, E., Edridge, M. D., Madden, P. A., Molec. Phys., **90**, 675, 1997

72 Cottin, X., and Monson, P. A., J. Chem. Phys., **99**, 8914, 1993

73 Barrat, J. L. and Hansen, J. P., J. Phys. France, **47**, 1547, 1986

74 McRae, R and Haymet, A. D. J., J. Chem. Phys., **88**, 1114, 1988

75 Bolhuis, P. G. and Kofke, D. A., Phys. Rev. E, **54**, 634, 1996

76 Bartlett, P., J. Chem. Phys., **107**, 188, 1997

77 W. G. T. Kranendonk and D. Frenkel, Mol. Phys. **72**, 679, 1991; **72**, 669 1991; **72**, 715, 1991

78 Phan, S and Russel, W. B., J. Chem. Phys., **108**, 1998

79 Sear, R. P., Europhys Lett, **44**, 531, 1998

80 Cuesta, J. A., Europhys Lett, **46**,197,1999

81 Bartlett, P., Molec. Phys., **97**, 685, 1999

82 Bartlett, P. and Warren, P. B., Phys. Rev. Lett., **82**, 1979, 1999

83 Williams, S. R., Snook I. K., et al., Phys. Rev. E, **64**, 1506, 2001

84 Evans, R. M. L. and Holmes, C. B., Phys. Rev. E, **64**, 1404, 2001

85 Elliott, J. A. Windle, A.H., J. Chem. Phys., **113**, 10367, 2000

86 Hoover, W. G., J. Chem. Phys., **70**, 1837, 1979

87 Sollich, P. and Cates, M. E., Phys. Rev. Lett., **80**, 1369, 1998

88 Warren, P.B., Phys. Rev. Lett. **80**, 1369, 1998

89 Granville, W.A., Smith, P.F. and Mikesh, J.S.: Spherical Trigonometry, Ginn 1943.

90 Bartlett, P. and Warren, P. B., Phys. Rev. Lett., **82**, 1979, 1999